A Petrophysical Study on the Influence of Effective Stress and Fluid Saturation on Acoustic Velocities in Sandstones

Abbas Khaksar

BSc. Mining Eng. (Tehran University)
MSc. Petrol. Geol. & Geophy. (University of Adelaide)

National Centre for Petroleum Geology & Geophysics

Thesis submitted to the University of Adelaide in fulfillment of the requirement for the degree Doctor of Philosophy

January 1999

Dedicated to Adeleh, Sina, Neeka
and
to my family in Iran

A Petrophysical Study on the Influence of Effective Stress and Fluid Saturation on Acoustic Velocities in Sandstones

Abstract

Hydrocarbon production may cause changes in dynamic reservoir properties including pressure and fluid saturation. Laboratory measurements of acoustic properties of representative rock samples, simulating in situ effective stress and fluid saturation, prove useful for the calibration and interpretation of seismic and sonic log data. The aim of this study was to investigate the relationship between the acoustic velocities and petrographical and petrophysical character of low to medium porosity sandstone cores from the Cooper Basin, South Australia, identified as medium to low porosity gas-bearing shaly sandstones.

Systematic laboratory measurements of the velocity of compressional and shear elastic waves were undertaken on 22 Cooper Basin core samples under dry (air-saturated), partial and fully water-saturated conditions. The measurements were conducted at ultrasonic frequencies under controlled pore pressure and confining stress conditions using a pulse-echo technique. Petrographic information and rock properties including porosity, permeability and capillary pressure curves were necessary to interpret the experimental results. The velocity-effective stress and velocity-saturation relationships for the studied samples were investigated. The role of other rock properties on these relationships was examined and the results compared to other studies. The implications of the experimental results for hydrocarbon exploration and development have been discussed with examples from the Cooper Basin reservoir rocks.

Velocities and quality factors (V_p, V_s, Q_p and Q_s) in the Cooper Basin sandstones depend on effective stress, defined as $P_e = P_c - nP_p$, with $n \leq 1$. The value of the effective stress coefficient, n, for V_p and V_s approaches unity at high differential pressures P_d, $P_d = P_c - P_p$, whereas the pore pressure dependency of Q_p and Q_s increases as the differential pressure, P_d increases. The deviation of effective stress coefficient from unity for velocities and quality factors is attributed to the heterogeneity in elastic properties of the main rock components (quartz and clay).

Experimental results show that acoustic velocities in dry and water-saturated samples increase non-linearly with effective stress over the stress range from 5 to 60 MPa. A regression equation in the form of $V = A - Be^{-DP}$ describes empirically the velocity-effective stress relationship for the sampled Cooper Basin rocks under both dry and water-saturated conditions. In this equation; V is the wave velocity and P is effective stress, A is the crack free velocity, D shows the rate of crack closure, and the difference between A and B is the velocity at zero effective stress. The change of velocity with stress is

attributed mainly to the closure of microcracks which hardly affects the total porosity but significantly increases the elastic moduli of the rocks. The stress sensitivity of Cooper Basin sandstones is relatively large in comparison with data reported in the literature.

There is no significant correlation between porosity, clay content and stress sensitivity of acoustic velocities at high pressures for the studied samples. The difference in stress sensitivity of the samples may primarily be explained by variations in pore geometry, grain contacts conditions and the distribution and location of clay particles within the sample skeleton (quartz grains). At elevated effective stresses, porosity is the rock property best correlated with velocity. Although considering a clay content term in velocity-porosity transforms in shaly sandstones is essential, the effect of clay minerals on velocities may not adequately be explained if only the volume fraction of clay is taken into account. The insignificant correlation between clay content and velocity, at elevated effective stresses, in the Cooper Basin sandstones is preliminary related to the textural characteristics and the type of clay distribution within the studied samples.

The saturation heterogeneity at pore-scale, which is shown in capillary pressure data, controls the velocity-saturation in partially water-saturated samples. The steady decrease of V_p as saturation decreases from the high saturation range to near irreducible conditions suggests a simultaneous drainage of water from pores with a variety of high to moderate aspect ratios, while microcracks (low aspect ratio pores) retain water. Closure and degree of saturation of the low aspect ratio pores control the velocity-effective stress and velocity-saturation relationships at low saturation and stress conditions.

Comparison of measured velocities with theoretical low frequency predictions by the Biot-Gassmann equation suggests that velocity dispersion is negligible in the studied samples. Thus laboratory-measured velocities may actually be compared with sonic log and seismic data in the Cooper Basin.

The velocity-effective stress relationship obtained from laboratory data is consistent with the sonic log anomaly observed in partially pressure-depleted reservoirs in the Cooper Basin. Neglecting the pressure effect on velocity results in the overestimation of rock porosity by the sonic log in overpressured formations, and underestimation of porosity in pressure depleted zones. A calibration function ($dV/dP = 79.35e^{-0.05P}$, V in m/s and P in MPa) is proposed to correct the sonic log reading for pressure variation in the study area.

At in-situ reservoir effective stresses, V_s and V_p are strongly correlated and dry and water-saturated samples show significantly different velocity ratios (V_p/V_s). The V_p/V_s ratio is not affected by porosity and clay content and therefore has potential as a gas indicator in the study area. The strong stress sensitivity and the distinct V_p/V_s values for dry and water

saturated Cooper Basin cores suggest that the dynamic changes in pressure and saturation of the reservoir rocks may also be detectable from acoustic impedance or travel time at seismic and sonic log frequencies.

Future studies should focus on the velocity-stress relationships for different rock types under different saturation conditions. A quantitative approach is needed to link the acoustic and petrographical properties in partially saturated rocks. The use of capillary pressure curves and wettability data in describing the scale of saturation heterogeneity and their relationship to acoustic velocities may provide useful information on the saturation status of reservoir rocks from seismically derived interval velocities.

Table of Contents

List of Figures

List of Tables

Declaration

This thesis contains no material which has been accepted for the award of any other degree or diploma in any university and, to the best of the my knowledge and belief, the thesis contains no material previously published or written by any other person except where due reference is made in the text of the thesis. The author consents to the thesis being made available for photocopying and loan if accepted for the award of the degree.

Abbas Khaksar

Acknowledgment

I could not have completed this thesis without support from many people and institutes.

The Ministry of Culture and Higher Education of Iran provided a postgraduate scholarship and made this PhD study possible. The National Centre for Petroleum Geology and Geophysics (NCPGG) of the University of Adelaide provided supplementary studentship during the final stage of this research. Santos Ltd., the industrial sponsor of the project, generously contributed to the study by financial and logistical supports. The Research Foundation of the Australian Society of Exploration Geophysicists (ASEG) supported the project by awarding a 3-year research grant for the experimental and infrastructure costs.

I would like to express my appreciation to Professor Cedric Griffiths, my supervisor, for his advice, assistance, support, encouragement and friendship throughout the course of this study. I wish to thank to the academic staff at the NCPGG, especially, Drs Nick Lemon, Peter Tingate, the late Bill Stuart, John Kaldi, Ian Dyson, and Mr. Andy Mitchell for their assistance throughout the project. I acknowledge Ms. Maureen Sutton, Mrs. Barbara Wallis and Mr. Nick Mann for their untiring logistical support.

I indebted to Professor Clive McCann from the Postgraduate Research Institute for Sedimentology (PRIS) of the University of Reading, UK, who made available his geophysics laboratory, and for his supervision on my experiments in Reading. A special thank to Mr. Jeremy Sothcott at the PRIS for his outstanding technical support during my work in Reading. Drs Jalal Khazanehdari and Solomon Assefa from the PRIS are acknowledged for sharing their understanding of rock physics and fruitful discussion on acoustic properties of reservoir rocks.

I wish to thank following people for their assistance and support during the project. Richard Penny and Lachlan Finlayson from the Santos Ltd., Dough Robert from the ASEGRF, Dr. David Gravestock, Todd McKenzie and Brain Logan from the Primary Industries and Resources SA, David Thornley and Phil Isles from the PRIS and John Stanley from the Department of Geology and Geophysics of the University of Adelaide.

I would like to thank my fellow students at the NCPGG and PRIS, my Iranian friends in Adelaide, Graham and Vonni Blanchard and the Australasian friends for their precious friendship and moral support during the past few years. I am always indebted to my family in Iran for their support and encouragement. Finally, and most importantly, I thank my wife, Adeleh, for her love, patience and strength throughout the course of this study and to our children, Sina and Neeka whom I love so much.

Chapter 1

Introduction

1.1. Background

Understanding factors affecting elastic wave propagation in sedimentary rocks is essential to the establishment of relationships between the seismic signature and other properties of reservoir rocks. It is known that the measured velocity for a sedimentary rock is related to a number of factors, such as porosity, effective stress, clay content, pore geometry, fluid saturation, and nature of the pore fluid. These, sometimes interdependent, factors may have significant effects on the measured velocity and therefore on rock properties predicted from acoustic velocity measurements. Hydrocarbon production causes changes in dynamic reservoir properties such as effective stress and fluid saturation. The investigation of the variations in acoustic velocities due to change of the dynamic reservoir properties requires controlled experiments in which accurate acoustic data are complemented by detailed mineralogical and petrophysical analysis of the rock. This can only be done in a systematic way using laboratory measurements on a number of representative samples simulating, as much as possible, the in situ reservoir pressure and saturation condition. These so called 'petro-acoustic studies' (eg. Watts et al. (1996)), have become increasingly an important part of the rock physics literature. Petro-acoustic studies are used to establish models to relate elastic properties (velocities and attenuations) to reservoir properties (porosity, permeability, clay content, saturation, fluid type) and measurement conditions including frequency and effective stress (Jizba and Marion, 1994).

The stress and saturation dependence of compressional and shear velocities in rocks have been investigated by Wyllie et al. (1958), King (1966), Nur and Simmons (1969), Domenico (1974), Murphy (1982 and 1984), Han et al, (1986), Knight and Nolen-Hoeksema (1990), Enders and Knight (1989), Cadoret et al. (1993) Best and McCann

(1995), Jones (1996), Best (1997) and others. There are, however, few published acoustic data for low to medium porosity shaly sandstones measured under varying saturation and stress condition. The results of previous studies, e.g. Han et al. (1986) on a large set of sandstones (including both low and high porosity-permeability samples), gave insignificant correlation in tight sandstones (Tutuncu et al. (1994), Khaksar and Griffiths (1998a)). Further, there are very limited sets of data worldwide in which ultrasonic laboratory measurements have been combined with adequate petrological information of rock samples. McCann et al. (1997) comment that the lack of good sedimentological and mineralogical control in many of the older sets of measurements means that many of the associated acoustic measurements are of limited value and cannot be extrapolated to other rocks.

1.1. Study Objectives

The main aims of the study described in this thesis are:

1. To investigate systematically the effect of effective stress, type and degree of pore fluid saturation, porosity and mineralogy on the acoustic velocities in sandstone cores from the Cooper Basin, South Australia, identified as medium to low porosity gas-bearing shaly sandstones.

2. To investigate the role of fluid saturation, porosity and clay content on the stress sensitivity of acoustic velocities for the studied samples.

3. To investigate the application of ultrasonic laboratory measurements on cores for more accurate interpretation of acoustic data obtained from sonic log and surface seismic in exploration and development of hydrocarbon bearing reservoirs in general and in the Cooper Basin in particular.

1.3. Study Area

The study area encompasses the Cooper Basin in South Australia (Figure 2.1). The hydrocarbon reservoirs of the Cooper Basin represent one of Australia's major petroleum provinces. At present South Australia, New South Wales, and parts of Queensland depend on gas supplies from the study area. The gas-producing intervals in the Cooper Basin are multi-reservoir upper Permian sandstones. The Cooper Basin reservoir rocks represent

well-consolidated low to moderate porosity shaly sandstones. To date more than half of the initially estimated conventionally recoverable gas has been produced from the sandstone reservoirs in the Cooper Basin. Several of the producing fields are now heavily pressure depleted and many challenges exist to extract the remaining recoverable reserves in the region. One of the major challenges is to accurately map these remaining reserves in partially depleted fields. The Cooper Basin reservoir rocks provide a good range of useful examples for the project purposes in terms of rock type, porosity range and hydrocarbon production induced variations in pressure and fluid saturation.

1.4. Method Used

A multi-disciplinary approach was needed to achieve the above mentioned objectives. In this study field data and petrography have been integrated with laboratory measurements of acoustic properties of representative rock samples. An extensive review of field data available from the Cooper Basin fields was carried out, focussing on the Toolachee Formation (see Chapter 2), a major gas producing formation in the study area. Thirty three core samples were collected from three wells for which a range of wireline data were available including porosity logs and formation pressure information from an RFT tool. Petrographical studies were carried out on all samples in the form of whole-rock X-Ray diffraction, microscopic thin section, Scanning Electron Microscopy (SEM) and petrographic image analysis to determine mineralogy, the amount of individual minerals and other routine sedimentological analysis.

The necessary experimental equipment for acoustic measurements was not available in Australia during the course of this study. Professor Clive McCann from the Geophysics Group of the Postgraduate Research Institute for sedimentology (PRIS), The University of Reading, UK, kindly made available his laboratory to implement the experimental part of the project. As a result the author was a visiting PhD student at The University of Reading for a period of 11 months from October 1996 to August 1997 where he carried out the acoustic and petrophysical measurements required for the study. Systematic laboratory measurements of velocities and attenuations of compressional and shear elastic waves were undertaken on 22 Cooper Basin core samples. Acoustic measurements were made on dry, water-saturated core plugs at ultrasonic frequency under controlled pore pressure and confining stress conditions using the pulse-echo technique implemented by McCann and

Sothcott (1992). Acoustic measurements were made under partial saturation on a subset of samples for which capillary pressure data were also acquired.

Petrographic information and rock properties including porosity, permeability and capillary pressure curves were incorporated to interpret the experimental results on acoustic velocities on cores. The velocity-effective stress and velocity-saturation relationships for the studied samples were investigated. The role of other rock properties on these relationships was investigated and the results were compared with other studies. The implication of the experimental results for hydrocarbon exploration and development were highlighted with examples from the Cooper Basin using existing wireline log data.

1.5. Thesis Plan

Chapter 2 briefly describes the petroleum geology and hydrocarbon exploration history of the Cooper Basin. Chapter 3 is a literature review of theoretical and experimental studies on acoustic velocities in reservoir rocks. In this chapter the most important theoretical models and equations describing wave propagation in porous rocks are reviewed. Then a summary of the present state of knowledge of acoustic velocities in sandstones is presented with particular attention to the effect of porosity, clay content, effective stress and pore fluid saturation. Chapter 4 describes sampling procedure, petrography and petrophysical properties of samples used in the study. Chapter 5 shows the experimental techniques used for measuring the acoustic properties of the samples. The techniques described include the ultrasonic system for acoustic measurement, the sample preparation procedure and data processing.

Chapter 6 describes the results of a systematic laboratory study of the stress dependency of compressional and shear velocities for 22 Cooper Basin samples measured under dry conditions. An empirical velocity-stress relationship is presented and the role of porosity, permeability and clay content on the stress sensitivity of acoustic velocities are investigated. Chapter 7 presents data on the pore pressure dependencies of acoustic velocities and quality factors under a range of pore pressures and stress conditions for a Cooper Basin sample. The effective stress coefficients for compressional and shear velocities and quality factors for the sample are determined from the experimental results and the potential of these measurements for seismic interpretation is highlighted. Chapter 8 deals with the effect of pore fluid on the stress sensitivity of velocities in 21 water-

saturated Cooper Basin samples. The results are compared with data under dry conditions. In this chapter the effect of porosity and clay content on compressional and shear velocities are also examined at elevated effective stresses and the observed relationships are compared with previous research. Chapter 9 presents and examines the relationship between acoustic velocities and partial fluid saturation in sandstones under varying effective stress conditions. Petrographic information, capillary pressure curves, and acoustic data were incorporated into a simple pore geometry model to interpret the velocity-saturation relationship and stress sensitivity under partially saturated conditions for the studied samples. Chapter 10 elaborates on some of implications of the experimental results for hydrocarbon exploration and development with examples from the Cooper Basin. The main conclusions together with suggestions for future works are provided in Chapter 11.

Chapter 2

Petroleum Geology of the Cooper Basin

2.1. Basin Setting

The Cooper Basin is a northeast trending structural depression in the north-east corner of South Australia and south-west Queensland (Figure 2.1). The basin contains Permo-Triassic strata of glacial, fluvial and lacustrine origin and consists of shales, siltstones, sandstones and coals (Kapel (1972), Thornton (1979), Apak (1994)). These strata cover nearly 130,000 km^2, of which about 50,000 km^2 are located in South Australia. The Cooper Basin strata unconformably overlie the early Paleozoic beds of the Warburton Basin, and Carboniferous igneous rocks (Battersby (1976), Sun (1997)). The Permo-Triassic strata are unconformably overlain by Early Jurassic to Late Cretaceous sediments of the central Eromanga Basin (Figure 2.2).

The southern Cooper Basin contains major hydrocarbon producing fields with a thick Permian section. In contrast, the northern Cooper Basin has a relatively thin Permian section. In the southern part there are three major depocentres, the Patchawarra, Nappamerri and Tennapera Troughs. These troughs are separated by the structurally high Gidgealpa-Merrimelia-Innamincka (GMI) and Nappacoongee-Murteree (MN) Trends (Stuart 1976). The troughs contain up to 2500 m of sediments (Gidgealpa Group) laid down during three non-marine megacycles which occurred between the Late Carboniferous and the Early Triassic (Thornton, 1979). Since the study area of this thesis only includes the southern Cooper Basin, this chapter overviews the stratigraphy, major structural features and hydrocarbon occurrences of the southern part of the basin.

2.2. Stratigraphy

Since the pioneer work of Kapel (1966) the knowledge of stratigraphy of the Cooper Basin has been developed by many workers (for example, Martin (1967), Gatehouse (1972),

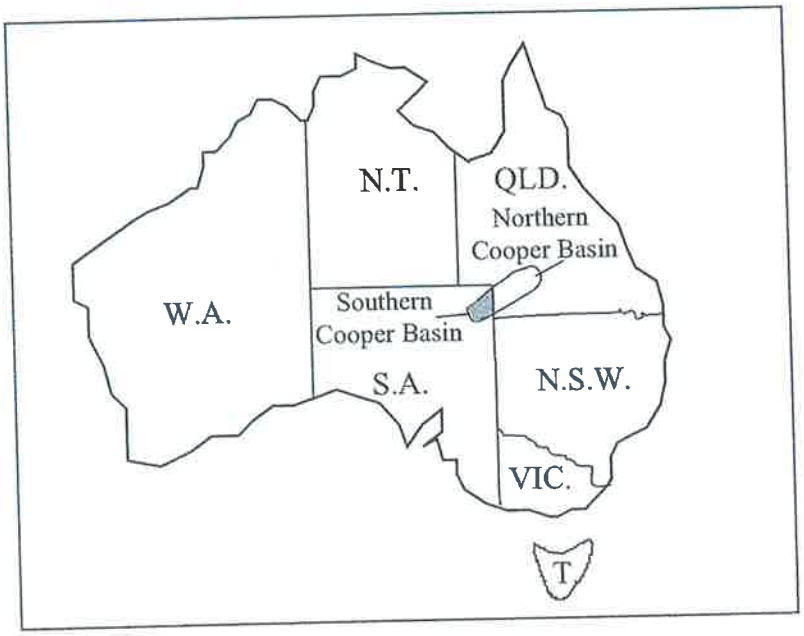

Figure 2.1. Location map of the Cooper Basin.

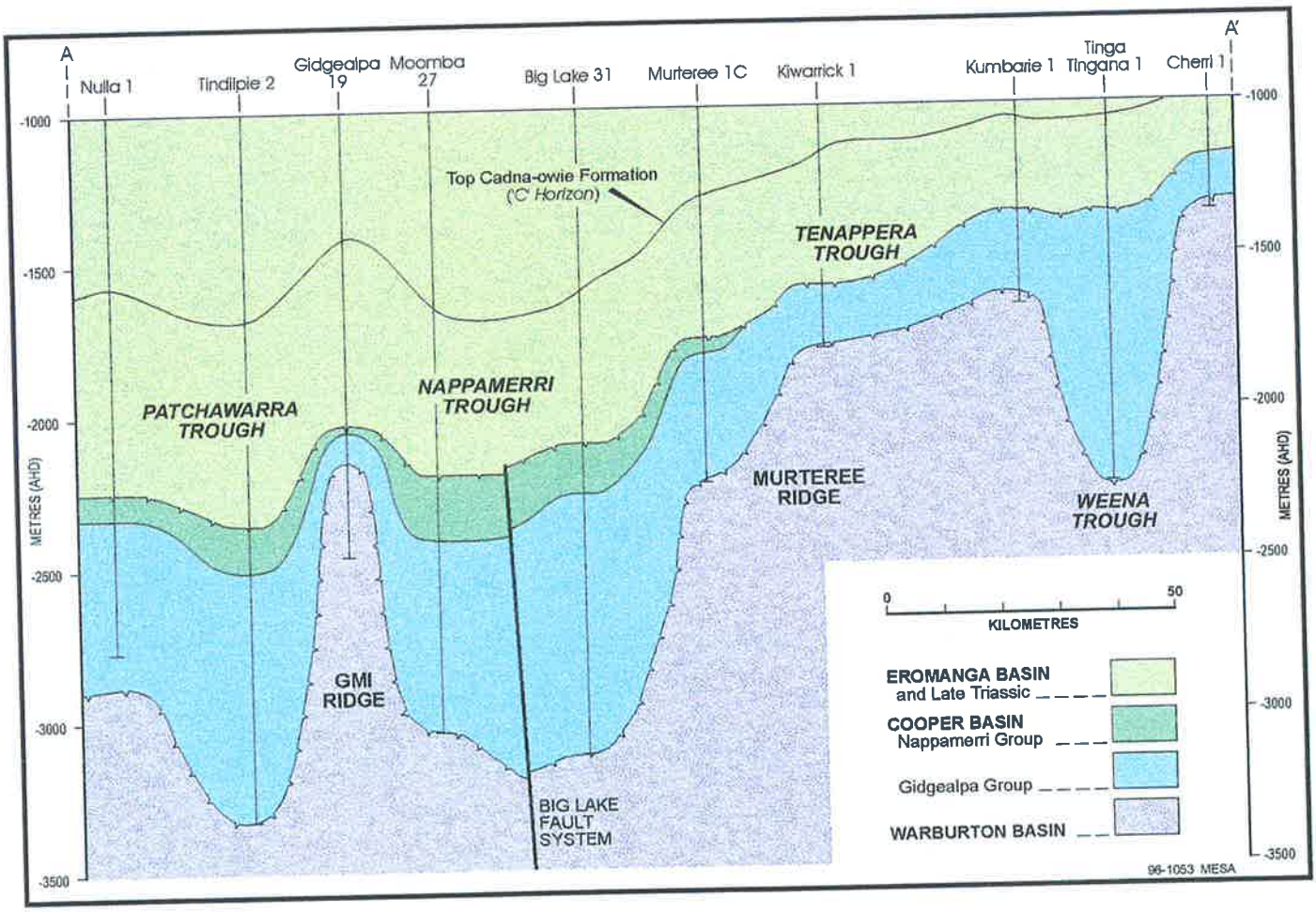

Figure 2.2. Schematic section across the Cooper Basin (From MESA, 1997). See Figure 2.3 for the location of section.

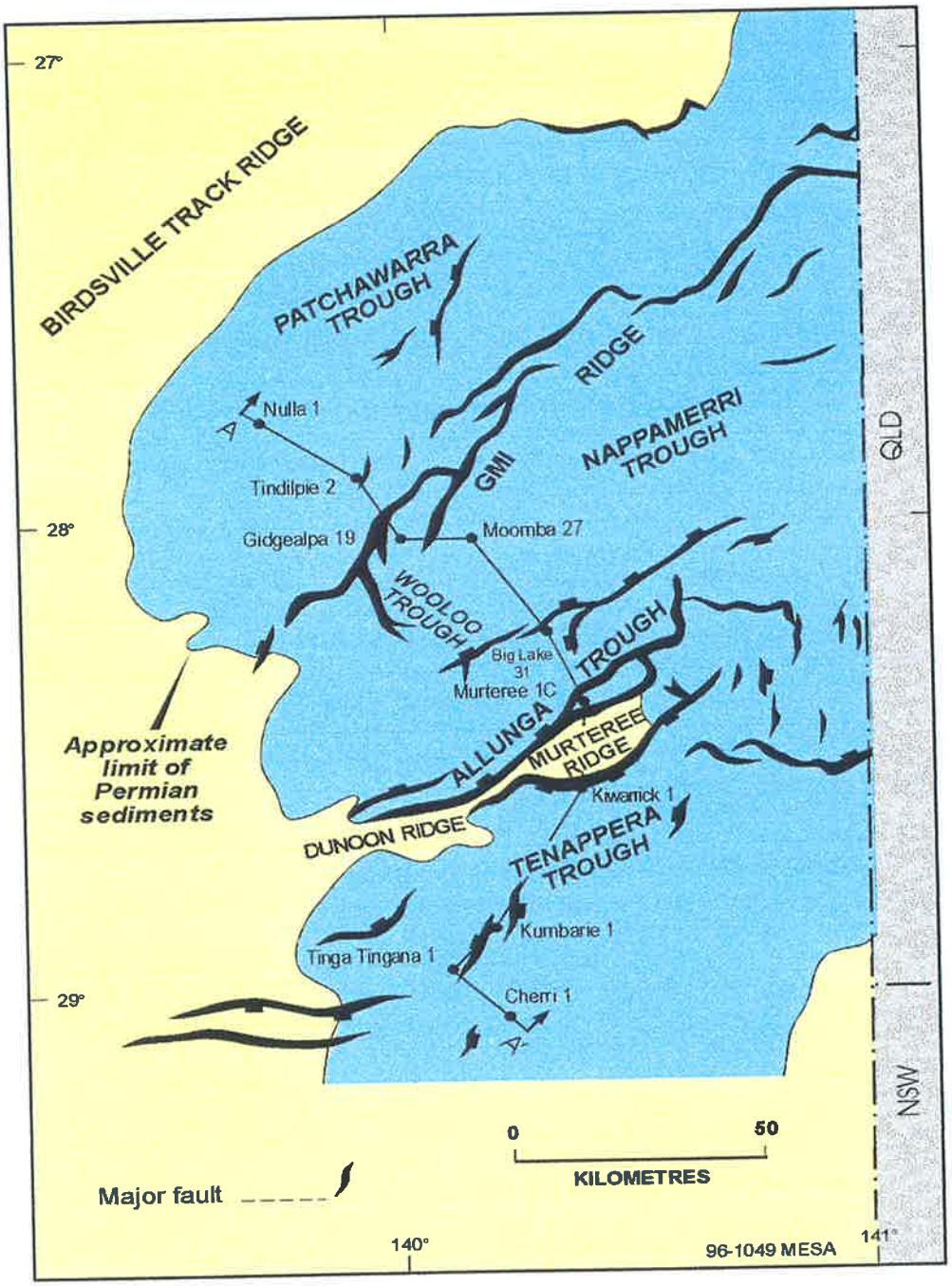

Figure 2.3. Major structural elements in southern Cooper Basin (from MESA, 1997).

Battersby (1976), Stuart (1976), Thornton (1979), Williams et al. (1985), Heath (1989), Apak (1994), Chaney et al. (1997) among others). Figure 2.4 shows the stratigraphic column of the Cooper Basin as published by Mines and Energy of South Australia (MESA) now Primary Industries and Resources South Australia (PIRSA). The Cooper Basin sequences range in age from the Late Carboniferous to Middle Triassic. They were deposited mostly in flood plain and lacustrine environments (Battersby, 1976). The Pre-Permian metasediments of the Warburton Basin underlie the Cooper Basin (Figure 2.2), and have been considered as economic basement (Battersby, 1976).

The Merrimelia Formation of Late Carboniferous age unconformably overlies the basement sediments (Figure 2.4). It consists of glacial, periglacial and glacial-aeolian (Williams et al., 1985), glacio-lacustrine, deltaic and fluvial sediments revealing a complex glacigenic environment (Chaney et al., 1997). The Merrimelia Formation comprises mainly a succession of conglomeratic sandstones and some siltstones and shales.

The Tirrawarra Sandstone of Early Permian age (Figure 2.4) is thought to conformably overlie the Merrimelia Formation (Battersby, 1976) but Chaney et al. (1997) considered it to be the fluvial part of the Merrimelia Formation. The Tirrawarra Sandstone comprises quartz sandstone with minor intercalations of thin siltstone, shale and coal (Thornton, 1979), indicating different sedimentary environments including braid-delta, marsh, beach barrier, lacustrine, meandering fluvial and aeolian (Rezaee, 1996). The Tirrawarra Sandstone is restricted to the south and southwestern parts of basin. Its absence in other parts of the basin is interpreted as being due to non-deposition over a pre-existing structure (Apak, 1994).

The Patchawarra Formation interfingers with sediments of the Tirrawarra Sandstone (Figure 2.4). It is composed of rhythmic successions of sandstone, siltstone, shale and coal indicating meandering stream, deltaic and lacustrine environments (Thornton, 1979). Three basic units were identified by Gatehouse (1972) in the Patchawarra Formation but Apak (1994) recognised five chronostratigraphic units within this formation. The Patchawarra Formation is the thickest (up to 677 m in Nappamerri Trough) and most productive formation in the basin. It is present in most of the basin.

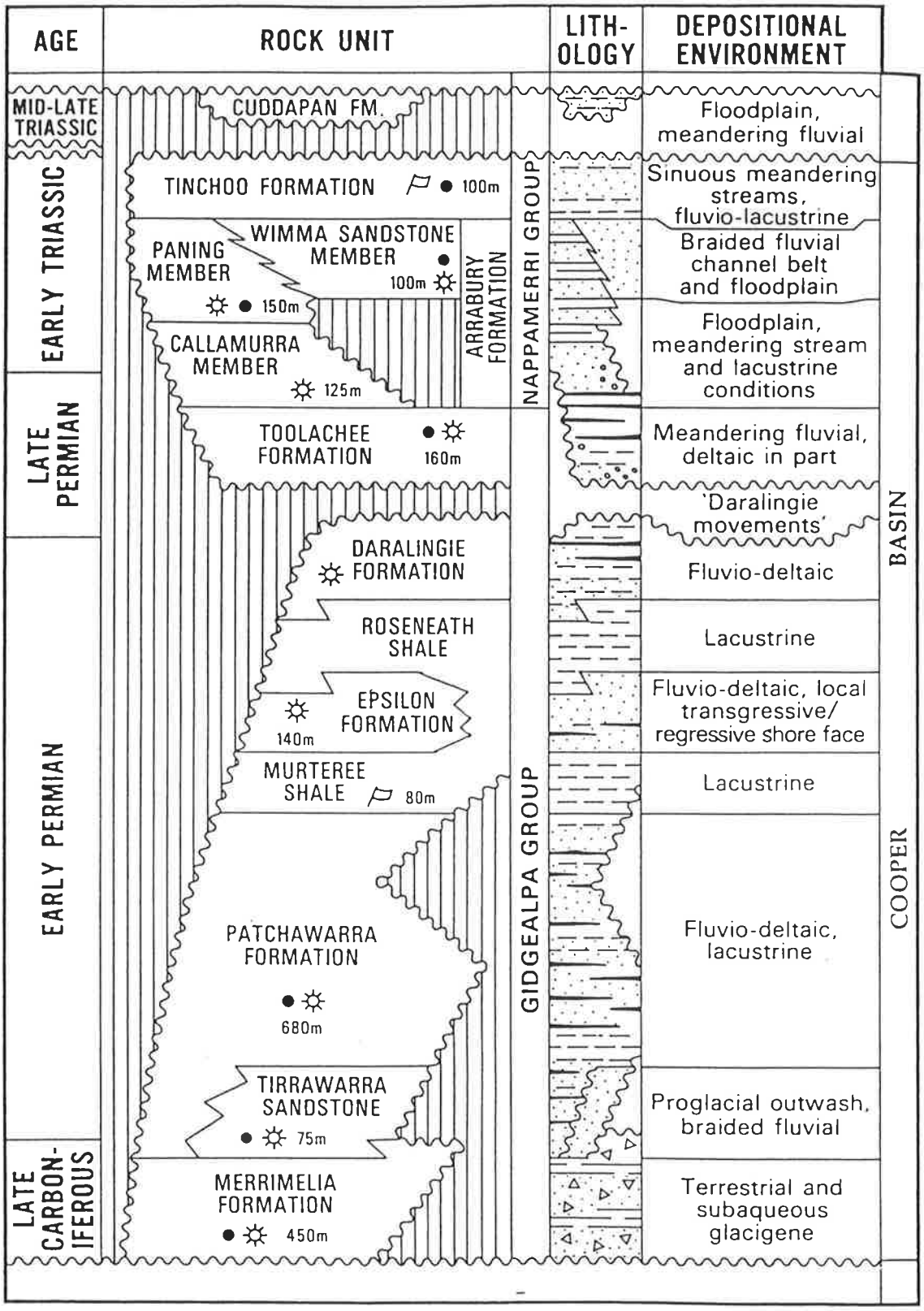

Figure 2.4. Cooper Basin stratigraphic nomenclature (from MESA, 1997).

The Cooper Basin was drowned by an extensive lake, which transgressed from the East during deposition of the Patchawarra Formation, leading the deposition of the Murteree Shale (Stuart, 1976). The Murteree Shale is a thick lacustrine unit, which conformably overlies the Patchawarra Formation (Figure 2.4) and comprises light to dark shales with interbedded micaceous siltstones (Thornton, 1979).

The Epsilon Formation conformably overlies the Murteree Shale (Figure 2.4) and is overlain by the Roseneath Shale (Thornton, 1979). The Epsilon Formation consists mainly of siltstone to fine sandstone with thin intercalations of sandstone and coal deposited in flood plain to shoreline environments (Battersby, 1976). The Roseneath Shale has essentially the same lithological and paleo-environmental characteristics as the Murteree Shale but the depositional basin was probably smaller than during deposition of the Murteree shale (Battersby, 1976 and Thornton, 1979).

Conformably overlying the Roseneath Shale is the Daralingie Formation (Figure 2.4). It comprises a succession of thin sandstones, siltstones, shales and coals which reflect a regressive environment similar to the lower part of the Epsilon Formation (Thornton, 1979). The upper part of the Daralingie Formation contains thicker sandstones and coals which were deposited in lower deltaic and flood plain environments (Battersby, 1976).

The Toolachee Formation unconformably overlies the Daralingie Formation (Figure 2.4). It consists of fresh water sandstones, siltstones, shales and coals (Battersby, 1976), deposited in fluviatile, point bar, overbank and backswamp environments (Stuart (1976), Thornton (1979)). The unconformity at the base of the Toolachee Formation is substantial as it was associated with a tectonic event (Apak, 1994). Although the Toolachee Formation is absent over the intra-basin highs, it is widespread throughout the basin including the northern portion. The Toolachee Formation exhibits two lithological units. The lower unit (Unit C) is dominated by point-bars and channel sandstones which are considered to be the main reservoir rocks within the formation (Stuart, 1976). The upper unit (Unit B) consists mainly of shales and coals indicating lacustrine and swamp conditions. The core plugs used in the current study were sampled from the Unit C of the Toolachee Formation (Chapter 4).

The final phase of sedimentation within the Cooper Basin resulted in the deposition of the Nappamerri Group, which consists of sandstones, siltstones and shales and red beds. The Nappamerri Group is considered to have been formed during a hot, humid and oxidising conditions typical of the Early to Mid Triassic (Paplia, 1969). The rocks of the Nappamerri Group generally do not show reservoir development and are considered to form a good seal for the Permian reservoirs. The depositional episode of the Cooper Basin was terminated by a major uplift in the Late Triassic-Early Jurassic which resulted in a rejuvenation of a pre-existing structures (Thornton, 1979) and basin-wide unconformity (Apak, 1994). Following the Late Triassic deformation and erosional period, deposition of the Eromanga basin sequence commenced during the Early Jurassic.

2.3. Structure

In the southern part of the Cooper Basin the major structural elements are oriented northeast-southwest (Battersby, 1976). Based on geophysical studies six major structural zones have been recognised (Figure 2.3). These are the Gidgealpa-Merrimelia-Innamincka (GMI) and Murteree-Nappacoongee (MN) Anticlinal Trends, the Patchawarra, Nappamerri and Tennapera Troughs, and the Karmona Anticlinal Trend in the north east corner (Kapel (1966), Stuart (1976), Thornton (1979), Apak (1994)).

The GMI Anticlinal Trend is the most prominent positive feature in the basin, and comprises several structural culminations. It is steep-sided, largely fault controlled and has a maximum relief of over 1000 m. The MN Anticlinal Trend is S-shaped, plunging northeast and southwest from the Murteree Ridge (Figure 2.2). Along its southern flank it is partly defined by a fault with a maximum throw of more than 450 m at the level of the 'P' Horizon (near Top Permian). This fault forms part of a major lineament that transects the Australian continent (Thornton, 1979). Figure 2.5 shows a depth structure map of the Top Permian 'P' Horizon.

The Nappamerri Syncline is nearly 300 km long and up to 100 km wide. The maximum proven thickness of Permian sediments in the Cooper Basin occurs in this structural province (Thornton, 1979). The Patchawarra Syncline runs sub-parallel to the GMI Anticlinal Trend (Figure 2.3) and attains a maximum depth of 3200 m below sea level at its northeastern extremity (Figure 2.5). Secondary asymmetrical fold structures such as that hosting the Tirrawarra Field occur near the axis of the trough (Stuart, 1976 and Thornton,

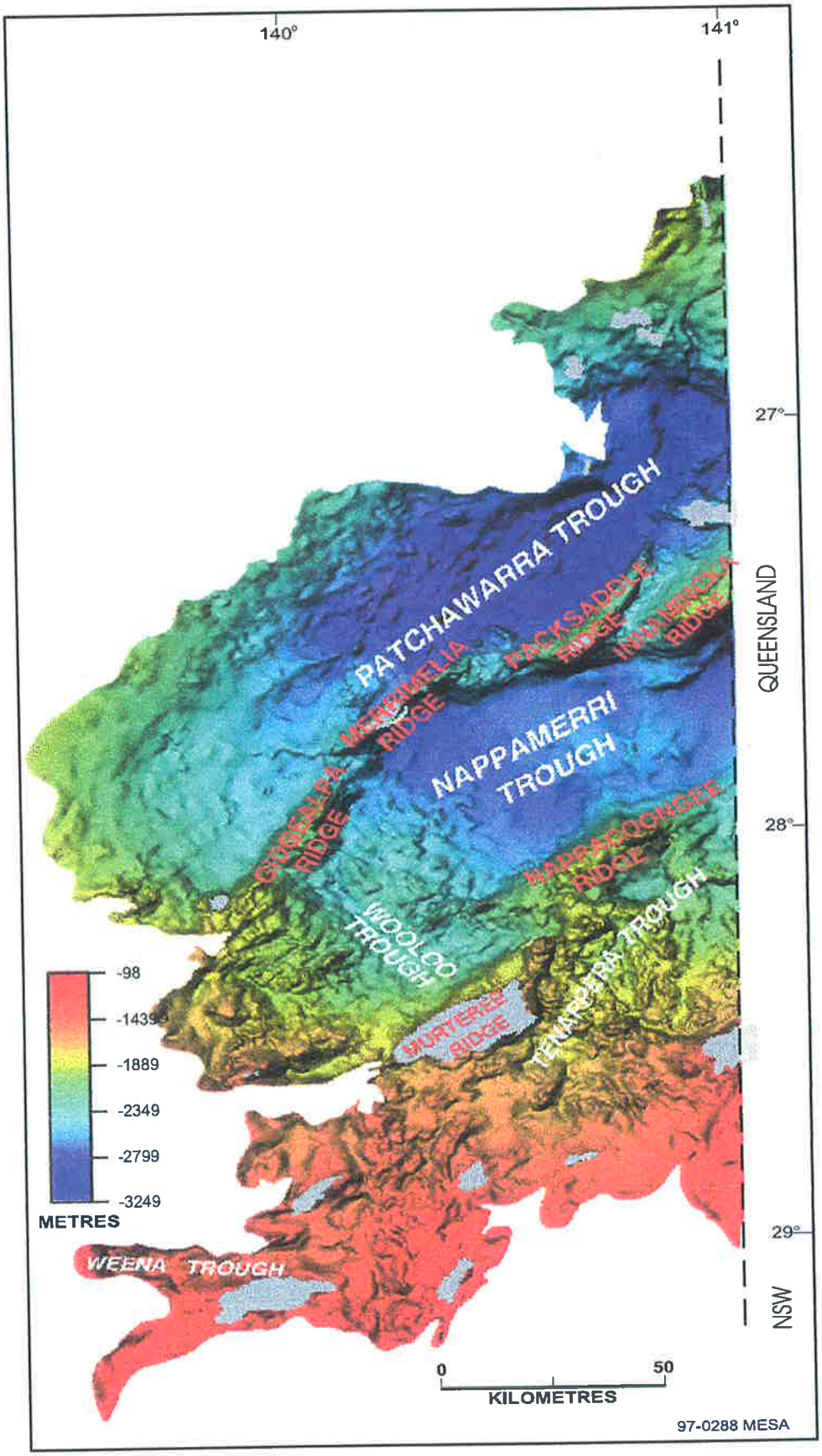

Figure 2.5. Depth structure map of the Top Permian "P" Horizon in the southern Cooper Basin (from MESA, 1997).

1979). The Tennapera Trough is the main synclinal feature along the southern flank of the Cooper Basin with a maximum depth of about 2200 m below sea level (Thornton, 1979).

The major anticlinal zones are faults-controlled basement features (Thornton, 1979), and were active during Permian (Stuart et al. 1988). Rejuvenation of pre-existing basement structures is a pervasive characteristic of the Cooper Basin (Battersby (1976), Stuart (1976)). There were several phases of mild deformation prior to and during Permian times (Stuart, 1976). Klemme (1980) and Stanmore (1989) have described the Cooper Basin as a complex intracratonic basin. Veevers et al. (1984) considered the Cooper Basin as a pericratonic basin, whereas Middleton and Hunt (1988) described the Cooper Basin as an interior sag basin. Yew and Mills (1989) suggested that it was a rift basin. In general, structures within the basin show evidence of fold interference patterns, thrusting and compressional wrench tectonics, indicating that the structural style within the Cooper Basin is complicated and can not be explained by a single tectonic regime (Apak, 1994).

2.4. Exploration History

Systematic exploration in the Cooper Basin was commenced in 1958 by Santos Ltd. and has continued to the present. The first exploration well, Innamincka 1, was drilled in 1959 and the first commercial gas discovery, Gidgealpa 2, was made in 1963. Following the large gas discoveries at Moomba (1966), Daralingie (1967) and Toolachee (1969) two pipelines were constructed to provide natural gas for industrial and domestic use in South Australia and New South Wales. Since then the Cooper Basin has become the major source of gas supplies in South Australia. In recent years natural gas from the basin has supplied over 75% of the state's primary energy needs and is used to generate about 50% of the state's electricity requirements (McDonough, 1998).

The discovery of oil at Tirrawarra in 1970 was a major boost to exploration in the Cooper Basin. However, despite further oil and condensate discoveries at Moorari and Fly Lake, natural gas is still the main product from the Cooper Basin. One hundred and nineteen gas fields have been identified in the South Australian sector of the Cooper Basin up to 1996. To date 1100 wells have been drilled and 66500 km seismic have been acquired in the Cooper Basin (MESA, 1997). Figure 2.6 shows oil and gas fields in the Cooper and Eromanga Basins.

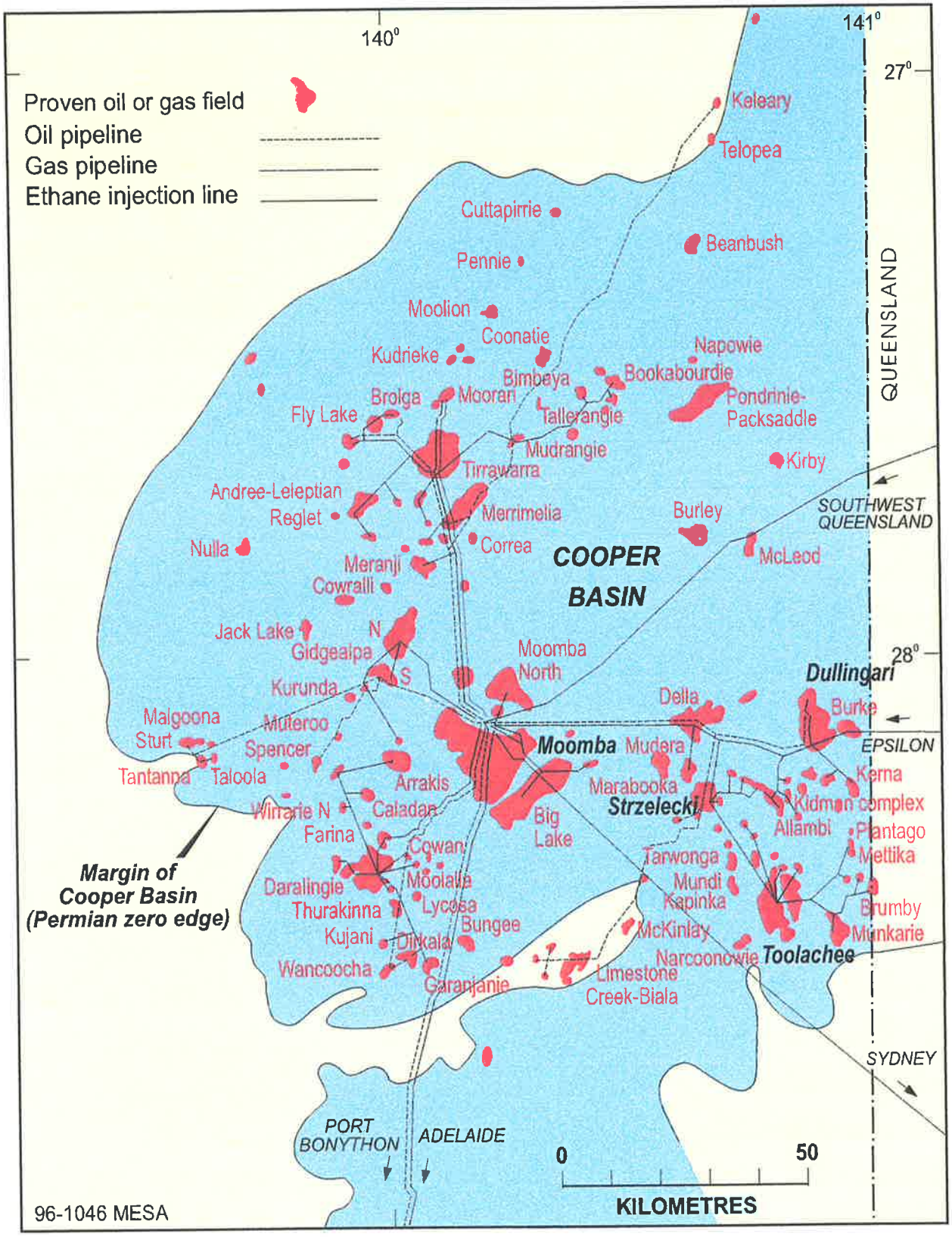

Figure 2.6. Oil and gas fields of the Cooper and Eromanga Basins in South Australia and the location of gas fields (in ***Italic***) addressed in the current study (from MESA, 1997).

The present, discovered, recoverable raw gas reserves (at 1.1.98) of the Cooper basin are 229×10^9 m^3 (8.2 tcf) comprising 129×10^9 m^3 (4.6 tcf) of produced gas and 101×10^9 m^3 (3.6 tcf) of gas yet to be produced from known discoveries. The average recovery factor for gas fields is 64%. The present discovered recoverable oil reserves (at 1.1.98) of the basin are 6.9×10^6 kL (43.9 mmstb) comprising 4.6×10^6 kL (29.1 mmstb) of produced oil and 2.3×10^6 kL (14.8 mmstb) of oil yet to be produced from known discoveries. The combined average primary and secondary recovery factors for oil fields is 21% (Morton, 1998).

2.5. Reservoirs

Fluvial sandstones in the Tirrawarra, Patchawarra and Toolachee formations provide the main reservoir rocks within the Cooper Basin. The Tirrawarra sandstone holds 95 per cent of oil reserves while the Toolachee-Daralingie and Patchawarra Formations hold 40 and 30 per cent of the gas reserves in the Cooper Basin respectively (Heath, 1989).

Most of the commercial petroleum discoveries occur in channel and point bar sandstones (Stuart (1976), Battersby (1976)). The other important reservoirs are deltaic sequences comprising shoreface sandstones and distributary and delta mouth bar deposits, which occur mainly within the Epsilon, the Daralingie and the upper part of the Patchawarra Formations (Stuart (1976), Stuart et al. (1992), MESA (1993)).

The reservoir quality of Cooper Basin sandstones is controlled by a complex interaction of sedimentary factors, diagenesis and structural development (Stuart et al., 1992). Primary (original intergranular) porosity, dissolution porosity, and microporosity within clay minerals are the main porosity types recognised within Cooper Basin sandstones. Reservoir rocks in the Cooper Basin are predominantly low-porosity, low-permeability sandstones. Ambient core porosity averages 10.7 per cent and permeability 30 mD, with over 75 per cent of sandstones having permeabilities of less than 5 mD. Despite the overall poor reservoir characteristics, the Cooper Basin is one of Australia's most important gas provinces (Stuart et al., 1992).

2.6. Sources, Traps and Seals

Hydrocarbons in the Cooper Basin are generally thought to have been sourced from the abundant dispersed organic matter in intraformational fluvial and deltaic shales and from

the coals of the Toolachee and Patchawarra formations (Hunt et al., 1989). The amount of total organic carbon (TOC), varies between 1 and 5 per cent (Jenkins, 1989) and the kerogens are mainly of type III (Hunt et al., 1989). Volumetrically significant generation of oil from this organic matter type occurs over a maturity range indicated by a vitrinite reflectance of 0.7 and 1.0 per cent (Jenkins, 1989). The hot Nappamerri Trough (40-50° C/km) underlain in part by granite, and the cooler Patchawarra and Tenappera Troughs, with thick infill of Permian strata, constitute the principal "kitchens" for source rock maturation (MESA, 1997).

Anticlinal and faulted anticlinal traps form most of the hydrocarbon targets explored to date in the Cooper Basin. Potential remains high for discoveries in stratigraphic and unconformity-related traps (Stuart (1976), Heath (1989)), especially where the Permian sediments pinch out against the overlying Eromanga Basin succession (MESA, 1997). Intraformational shales and coals form local seals in the major reservoir units (MESA, 1992). The Murteree and the Roseneath Shales and the Arrabury Formation in the Nappamerri Group form regional seals for the Patchawarra, Epsilon and Toolachee Formations respectively (Heath, 1989).

Chapter 3

Literature Review

3.1. Introduction

A knowledge of the elastic wave velocities in porous media is of considerable interest in the field of mechanical engineering, rock mechanics, geological engineering, seismology and mineral and hydrocarbon exploration. In hydrocarbon exploration this concept mainly concerns the elastic properties of rocks and their relationships with the reservoir rock properties. Both theoretical and experimental studies of the physical rock properties and their relationships are required to assess the influence of these factors upon wave velocities in reservoir rocks. To have the widest practical application, velocity measurements at laboratory scales on rock samples should simulate the in situ conditions. Then theories and models are needed to explain the experimental results. In this way experimental results provide the basis for the evaluation of theories and models and their application in practice.

Numerous theories and models along with many published experimental works exist in the literature on elastic properties of porous media in general and in reservoir rocks in particular. Watt et al. (1976) presented a review paper and outlined some of the most important theories and models. Wang and Nur (1992) summarised the commonly used theories and models in hydrocarbon exploration related rock physics and discussed the range of applications and limitations of these theories. This chapter firstly reviews theories and models commonly used in interpreting the laboratory measurements of elastic wave velocities in fluid-saturated rocks, namely the Gassmann equation, the Biot theory and the Kuster-Toksoz model. Then it presents an update review of the published experimental studies on the major factors affecting velocities, including porosity; clay content, effective stress and pore fluid saturation, in reservoir rocks.

It is worth noting that in the rock physics literature normally there are three types of velocity in terms of frequency range. These are seismic, sonic and ultrasonic velocities. Seismic velocity usually implies that the velocities are for frequencies between 10 to 100 Hz. Sonic velocity often refers to the velocities for frequencies ranging between 1 and 20 kHz, whereas ultrasonic are wave velocities that are measured at frequencies greater than 0.1 MHz. Throughout this thesis velocities refer to the entire frequency range, unless specified.

3.2. Theories and Models

3.2.1. Basic Relationships and Definitions

The velocity of propagation of elastic waves naturally depends upon the physical characteristics of the medium. The velocity of the compressional or pressure waves (P-waves), V_p, in a porous medium is determined by (White, 1983):

$$V_p = [(k + 4\mu/3)/\rho]^{1/2} \qquad (3.1)$$

where k is bulk modulus (incompressibility), μ is shear modulus and ρ is bulk density of the medium. The bulk modulus k is a measure of the degree to which the medium is able to resist a change in its volume upon application of a compressive force and it is expressed in GPa. The shear modulus is a measure of resistance of the medium to change in its shape upon application of a shearing force. The bulk density ρ of a rock is simply the volumetric sum of the medium constituents:

$$\rho = \phi\rho_f + (1 - \phi)\,\rho_m \qquad (3.2)$$

where ϕ is fractional porosity, ρ_f is density of pore fluid and ρ_m is density of grains. P-waves also are induced in a fluid (liquid, gas, or liquid-gas mixture) by sudden application of pressure at a point in the fluid. Since fluids generally have negligible resistance to shear forces, S-waves are not generated in fluids. The velocity of the shear waves (S-waves), V_s, in rocks is given by (White, 1983):

$$V_s = (\mu/\rho)^{1/2} \qquad (3.3)$$

Hence the V_s depends only upon the shear modulus and is inversely proportional to density. Equations (3.1) and (3.3) simply imply that when the elastic moduli and density of the rock and its constituents are known, one could calculate V_p and V_s in such a rock. However, the relationship between the elastic moduli of rock components, and k and μ for the whole rock on one hand and the factors affecting these parameters and their relationships on the other hand, is complex, and it is the main task of the most of the theories and models on elastic wave velocities in porous media to determine these relationships. This issue is discussed in the following section.

3.2.2. The Gassmann Equation

The components which characterise the composition of rocks are: (1) the matrix of which the skeleton or frame is built (index $_m$), (2) the frame, i.e. the dry or empty rock (index $_d$) and (3) fluid occupying the pore space of frame (index $_f$). With the use of elementary elastic theory Gassmann (1951) showed that when a fluid saturated rock is a closed system, macroscopically homogeneous and isotropic, and there is no relative motion between fluid and the frame, it is possible to calculate its bulk and shear moduli if the elastic properties of its components are known:

$$K = k_d + \{[(1 - k_d/k_m)^2] / (\phi/k_f) + [(1-\phi)/k_m] - k_d/k_m^2\} \qquad (3.4)$$

where k is the bulk modulus, k_d , k_m and k_f are the bulk moduli of the dry, matrix and pore fluid respectively, and ϕ is the fractional porosity. Since Gassmann assumed the fluid does not interact with the solid in any way that would change the shear modulus of the frame, then:

$$\mu = \mu_d \qquad (3.5)$$

where μ_d is the frame (dry) shear modulus of the rock. Equation (3.4) can be used to obtain the bulk modulus of a porous rock. Parameters k_d , μ_d and ϕ can be obtained from laboratory measurements or formation evaluation. When the mineralogy of the rock is known, k_m can be calculated from the other equations such as Hashin-Shtrikman (1963), or will have to be assumed. Many investigators (e.g. White (1983), Han et al. (1986), Wang

and Nur (1992)) showed how the Gassmann calculated velocities fit the measured velocities in sandstones. In general, a Gassmann calculated V_p is lower than the measured V_p (Figure 3.1a) while calculated V_s statistically fits the measured Vs, with significant error (Figure 3.1b). Figure 3.1b implies the assumption made by Gassmann in equation (3.5) does not happen in reality. Wang et al. (1991) suggested that introduction of water to some clay rich sandstones may soften the matrix. Uncertainty concerning input parameters to the Gassmann equation could be another reason for the lack of fit in Figures 3.1a and 3.1b. Wang and Nur, (1992) suggested that a 2% difference between velocities calculated from the Gassmann equation and the measured velocities could be considered as an adequate fit for practical purposes.

The Gassmann equation assumes that relative motion between fluid and frame has negligible influence on wave propagation in fluid-saturated rocks. This assumption requires that the wave frequency be low. The relative motion would result in loss of energy, through the fluid viscosity, and the Gassmann equation does not consider any attenuation effect on wave propagation in this equation. At high frequencies (MHz or possibly to KHz), relative motion between the solid matrix and pore fluid will occur and there would be a velocity dispersion. This relative motion is described by a local flow mechanism introduced by O'Connell and Budiansky (1977). In the local flow (or squirt flow) mechanism, some parts of the pore space such as cracks are assumed to be more compressible than others e.g. round pores. A passing wave deforms the pore space and causes the pore fluid in the compressible (soft) part of the pore space to flow to a less compressible (stiff) part. At high wave frequencies, during a half period of the wave the pore fluid does not have enough time to relax or equilibrate, so that the rock seems to be less compressible and velocity dispersion occurs. It has been shown that at low effective pressures the magnitude of velocity dispersion is large because the cracks are still open (Winkler (1986), Wang and Nur (1990)). The local flow mechanism for velocity dispersion is also addressed in relation to the Biot theory.

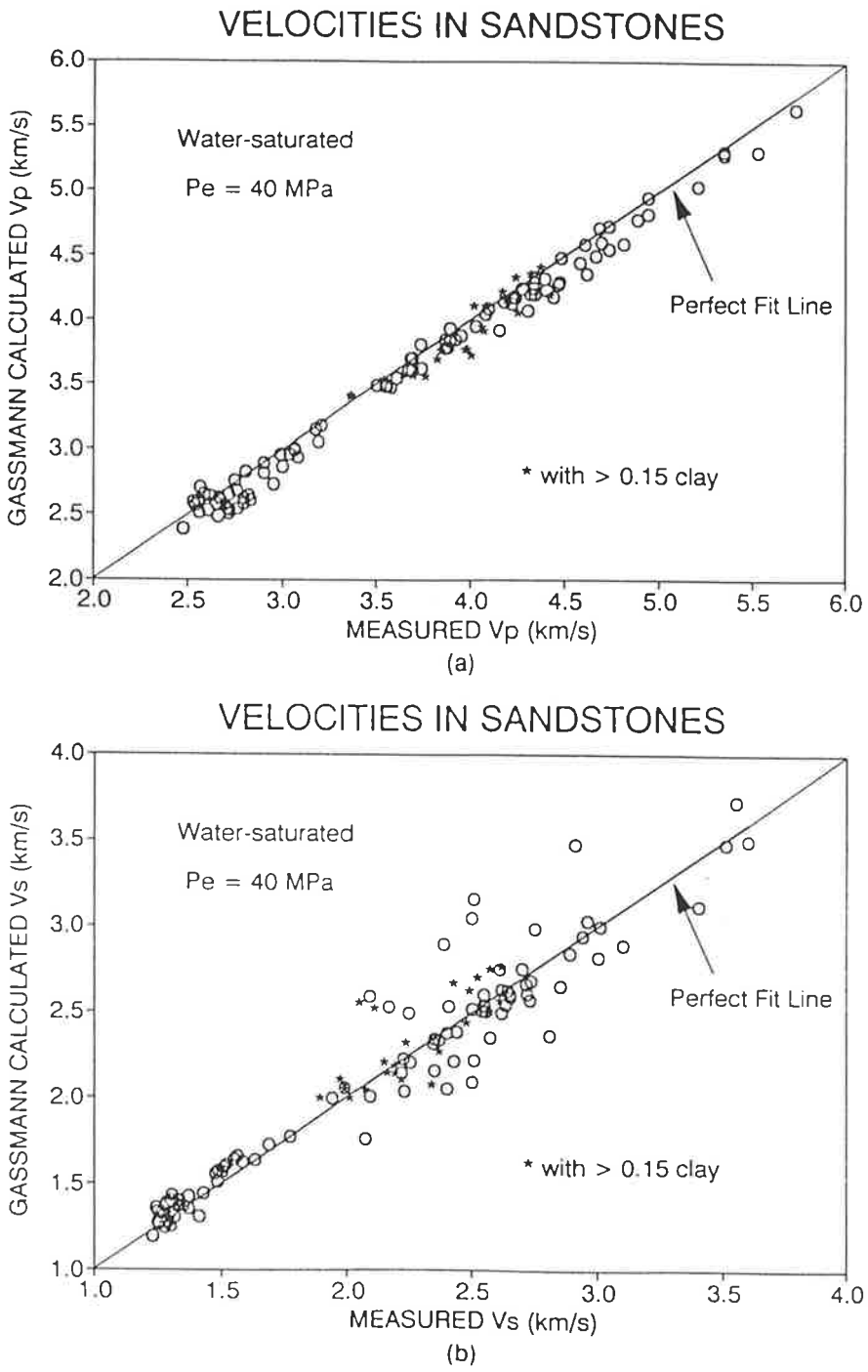

Figure 3.1. Comparison of laboratory measured V_p (a) and V_s (b) with those calculated using the Gassmann equation in 122 water-saturated sandstone and sand samples (from Wang and Nur, 1992).

3.2.3. The Biot Theory

As mentioned above, the Gassmann equation is a low frequency approach to elastic wave propagation in porous media. Biot (1956a, b and 1962) developed a theory covering the whole frequency range. The Biot theory predicts that both the compressional and shear velocities can be very dependent on wave frequency in the high frequency range and both are dispersive and dissipative. This theory is one of the few fundamental theories of wave propagation in fluid saturated porous media. Since publication there has been much further development and application of the theory. Except for the following, the basic assumptions in the Biot theory are same as in the Gassmann equation. The Biot theory assumes that: (1) the wavelength is appreciably larger than the largest dimension of the rock's grains and (2) relative motion between the rock matrix and pore fluid exists and follows Darcy's law of fluid flow through porous media. In addition to the rock constituent constants considered in the Gassmann equation the Biot theory requires more parameters to describe the rock fluid system. These are: η and K, fluid viscosity and frame permeability, respectively.

Based on the strain-stress relationship in a fluid saturated rock, Biot derived a pair of vector differential equations describing the coupled motion in terms of average displacements in the fluid and solid. The theory predicts the existence of two coupled compressional waves; the normal seismic or fast wave coupled to a slow wave, and one shear wave. The slow wave attenuates exponentially as the wave travels. At low frequencies the coupling between matrix and fluid is perfect and both shear and fast compressional waves are nondispersive. As the frequency approaches zero, the slow wave disappears and the Biot theory gives the same V_p and V_s as that in the Gassmann equation. White (1983) defined a characteristic frequency, f_c, for the low frequency limit in the Biot theory:

$$f_c = \eta\phi / 2\pi K\rho_f \qquad (3.6)$$

where η, ρ_f are the viscosity and density of pore fluid and K, ϕ are the hydraulic permeability and porosity of the rock, receptively. The range of characteristic frequency for low permeability rocks saturated with high viscous fluid is large. For example for a tight sandstone with 10% porosity and 1 mD hydraulic permeability, $f_c \sim 16$ MHz when the rock is saturated with water and $f_c \sim 1.8$ GHz if saturated with oil (viscosity of 100 cP and density of 0.9 g/cm^3) whereas for a sand pack of 30% porosity and with 1 D permeability f_c equals to 47 kHz and 5.3MHz, respectively. In practice where the wave frequency $f \leq 0.1f_{c,}$, the wave propagation is considered to be low frequency (White, 1983). As the frequency goes to infinity, the pore fluid in the Biot theory becomes effectively non-viscous, the coupling between fluid and rock is at a minimum and the relative motion is at a maximum. Under these circumstances V_p and V_s are calculated from the "high frequency" equations in the Biot theory. Mathematical explanation and details of the Biot theory can be found in original papers by Biot (1956a and 1956b).

Experimental studies (for example, Domenico (1977) and Plona (1980)) show that the Biot theory is widely applicable to unconsolidated materials and fully saturated rocks without micro-cracks or fractures and isolated pores. Biot assumed that velocity dispersion is caused by imperfect coupling between rock matrix and fluid. This assumption may be true for highly permeable rocks whose pores are well connected but is not true for many low porosity rocks whose pores are mainly in the form of micro-cracks (Wang and Nur, 1992). Winkler (1985) experimentally showed that the total velocity dispersion in saturated rocks is often larger than the Biot dispersion, and ultrasonic velocities are higher than those predicted by the Biot equations. Works by Mavko and Nur (1979) have shown that "squirt flow mechanism" results in much higher, realistic, attenuation values in partially saturated rocks than with the complete saturation discussed by Biot. This mechanism has been investigated by many authors (e.g. O'Connell and Budiansky (1977), Murphy et al. (1986), Wang and Nur (1990)).

Recently, in a series of papers by Dvorkin and Nur (1993) and Dvorkin et al. (1994 and 1995), a new dynamic poroelasticity model has been introduced which combines both Biot and squirt flow mechanisms (BISQ) to describe the propagation of P-waves in a porous

elastic solid containing a compressible viscous fluid. In this model, pore fluid is squeezed from thin soft cracks into the surrounding large pores. The frequency dependence of squirt-induced pressure in the soft cracks is linked with the porosity and permeability of the soft pore space, and the characteristic squirt flow length, R. These unknown parameters are combined into one expression R^2/κ where κ is the diffusivity of the soft pore space. This expression is assumed to be a fundamental rock property that does not depend on frequency. Dvorkin et al. (1995) showed that the BISQ model realistically predicts the observed velocity dispersion and attenuation on different fully saturated rocks. The applicability of this model to prediction of V_p and V_s and their dispersion at low and high frequency ranges for partially saturated rocks under different pressure conditions has yet to be reported.

3.2.4. The Kuster-Toksoz Model

Kuster and Toksoz (1974a and 1974b), and Toksoz et al. (1976) following previous approaches such as Ament (1953) developed theories for both velocity and attenuation of elastic waves in two phase-media. In this model it is assumed that pore spaces in rocks can be represented by spheres and oblate spheroids with different aspect ratios in various concentrations. The aspect ratio of an inclusion and the pore type concentration spectrum are defined as:

$$\text{Aspect ratio} = \alpha = b/a \tag{3-7}$$

$$\phi = \sum_{n=1}^{N} c(\alpha_n) \tag{3-8}$$

where a and b are the length of the major semi-axis and the length of the minor semi-axis, respectively in an ellipsoidal inclusion (Figure 3.2). The magnitude of α is unity for spherical pore and very small for crack-like pores. In equation (3-8), N is the total number of pore types, α_n is the *n*th aspect ratio of the inclusion, $c(\alpha_n)$ is the fractional concentration of α_n and ϕ is porosity. The Kuster-Toksoz model assumes that the distribution of pores and cracks are random and the whole medium is isotropic. The inclusions (or pores) are so dilute that they do not interact or overlap with each other. The wavelength is much larger than the size of the inclusions. Kuster and Toksoz (1974a and

b) and Toksoz et al. (1976) offer equation details and further explanation for calculation of the elastic moduli of spheroidal inclusions and a fluid saturated rock of this model.

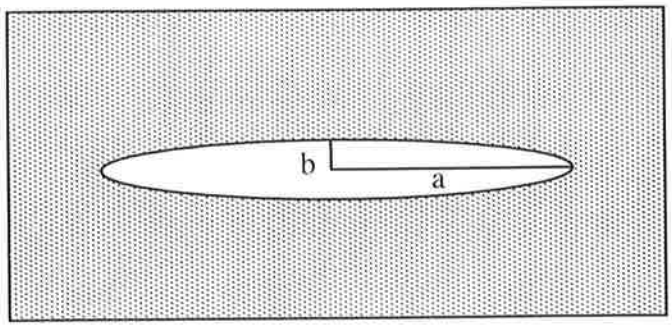

Figure 3.2. Ellipsoidal inclusion and parameters of the pore aspect ratio $\alpha = b/a$.

The most important difference between the Kuster-Toksoz model and both the Gassmann model and the Biot theory is the consideration of pore shape in changing elastic waves in porous rocks. For rocks containing only spherical pores the Kuster-Toksoz model gives the same results as the Gassmann equation. The Kuster-Toksoz model shows that the effective elastic moduli of a two-phase medium depend not only on the intrinsic moduli and the concentration but also on the shape of the inclusions. For a given porosity, flatter pores have a relatively greater effect on velocities than rounder or spherical pores. The role of low aspect ratio pores on velocity in partially saturated rocks and the relationship of velocity and effective stress in porous rocks has been emphasized by many authors (e.g. King (1966), Nur and Simmons (1969), Enders and Knight (1989), Xu and White (1995)).

To predict V_p and V_s using the Kuster-Toksoz model, the pore geometry of the rock, that is α and $c(\alpha)$, need to be known. In reality, rocks tend to contain pores of every possible shape and aspect ratio and it is very difficult to obtain an accurate pore spectrum for a rock. It is however possible to generalize the spectrum. Toksoz et al. (1976) used a trial and error method to determine input parameters in their model. Cheng and Toksoz (1979) presented an inverse method to resolve the pore aspect ratio spectra for a number of rocks using the velocities obtained in the laboratory. Zimmerman (1991) developed a methodology for extracting aspect ratio distributions from stress-strain curves. Based on the Kuster-Toksoz model, Tao and King (1993) used an equivalent spectrum

approximation to predict rock porosity from velocity data. Tao et al. (1995) have modelled the pore aspect spectrum from the measured velocities of sandstones using an iterative inversion algorithm based on the scheme developed by Cheng and Toksoz (1979). However, the real aspect ratio spectrum for a rock is still far from determination, and one can easily assume and adjust spectrum parameters so that one set fits any laboratory data. This results in the Kuster-Toksoz model being non-unique (Wang and Nur, 1992).

3.3. Experimental Studies

3.3.1. General

Wave velocities in reservoir rocks depend on many factors including porosity, pore fluid type and degree of fluid saturation, confining stress and pore pressures, pore geometry, temperature, lithology and clay content. These interdependent factors may have significant influence on measured wave velocities and thus on rock properties predicted from velocity data. With the rapid development in seismic and well logging technologies, detailed studies of hydrocarbon reservoirs are receiving more attention. An understanding of the seismic and acoustic properties of both fluids and rocks is essential to use these new technologies and interpret their results. This section reviews the most important published experimental studies on wave velocities in porous rocks addressing the effects of porosity, clay content, saturation pore fluid, and effective stress.

3.3.2. Porosity Effect

In general, in porous rocks, as porosity increases both compressional and shear velocities decrease, despite the decrease of bulk density with the porosity increase. Acoustic velocity data are often used to estimate porosity in hydrocarbon wells. A simple relationship between V_p and porosity was proposed by Wyllie et al. (1956, 1958). They assumed that the travel time of P-waves in the fluid saturated porous formation is a weighted average of the travel time in the matrix material and in the pore fluid (Figure 3.3). A porous rock of unit length is assumed to consist of a solid and pore fluid where the thickness of each is $1-\phi$ and ϕ, respectively. The total P-wave travel time, D_t, across the length is

$$D_t = D_{tf} + D_{tm} \qquad (3.9)$$

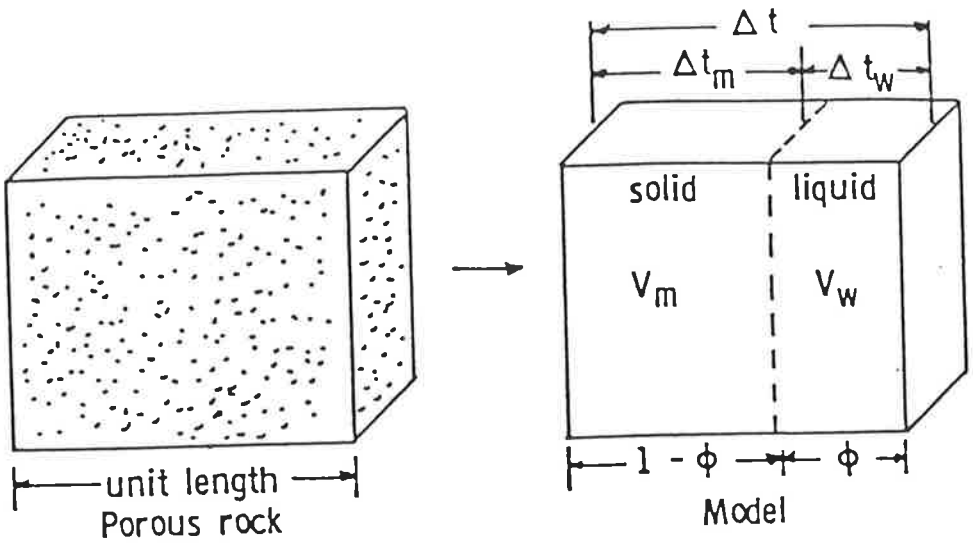

$$\Delta t = \Delta t_m + \Delta t_w$$

$$\frac{1}{V} = \frac{1-\phi}{V_m} + \frac{\phi}{V_w}$$

Figure 3.3. A porous rock model showing the basis of the time average formula.

where D_{tm} and D_{tf} are travel times across to solid and fluid portions respectively. Equation 3.9 is often called the time average or the Wyllie et al. equation. In terms of velocity and porosity, the equation (3.9) is written as:

$$1/V_p = \phi/V_f + (1-\phi)/V_m \qquad (3.10)$$

where V_m is velocity in the solid (matrix) and V_f is velocity in the fluid. Because of its simplicity, the time average formula has been one of the primary transforms used for porosity determination from velocity data. As a first-order approximation this equation is adequate for water-saturated clean sandstones with porosities ranging between 15% and 30% (Raymer et al., 1980).

However, several investigators (eg, Geertsma and Smith (1961), Raymer et al. (1980), Domenico (1984), Han et al. (1986)) have pointed out shortcomings to the time average equation. Generally, two problems exist in the application of this equation, namely estimation of D_{tm} and D_{tf}, and range of applicability (Wang and Nur, 1992). Velocity of the rock matrix and pore fluid are normally assumed rather than measured. The time average formula does not account for the effects of compressibility of pores and pore filling materials on wave velocity in porous rocks, and is not applicable in gas-bearing formations and carbonate rocks (Wang and Nur, 1992). Hence various pragmatic modifications, such as shale correction, lack of compaction factor and hydrocarbon effect, have been made to the time average formula to overcome its deficiencies.

Based on log and core data Raymer et al. (1980) proposed an empirical transform for V_p to porosity for porosities less than 37%:

$$V_p = (1-\phi)^2 V_m + \phi V_f \qquad (3.11)$$

This transform can be applied to saturating fluids other than water, provided fluid density is known. Equation (3.11) is thought of as an alternative to the time average formula, particularly for higher porosity sandstones, and is commonly used in formation evaluation. However, since the parameters used in equation (3.11) are similar to those in the time

average formula, this equation has many of the same problems as the time average approach, particularly within the porosity range from 10% to 30%. Xu and White (1995) showed that both the time average and Raymer et al. equations are valid only for clay-free sandstones containing pores with a mean aspect ratio almost equal to 0.07 and misrepresent porosity in rocks with different pore geometry.

3.3.3. Clay Effect

As there are exceptionally few hydrocarbon-producing sandstone formations that are free of clay minerals (Ruhouvest and Fertl, 1982), shaly sandstones predominate in hydrocarbon reservoirs. It is worth noting that the terms "clay", "shale" and "shaly sandstones" in the rock physics literature often differ from their usual meaning in petrology. Throughout this thesis the unqualified term "clay" is considered mainly a particle size rather than a mineralogy term, while shaly sandstone is referred to clay rich sandstone regardless of mineralogy and location of clay particles in the rock.

The influence of clay content on V_p in sandstones has been studied in several investigations (for example, Minear (1982), Tosaya and Nur (1982), Castagna et al. (1985), Wilkens et al. (1986), Han et al. (1986) Klimentos (1991), Freund (1992), Tutunco et al. (1994), Vernik (1994), Xu and White (1995)). Laboratory studies indicate that the presence of clay particles significantly influences acoustic wave velocities in sandstones. For unconsolidated sands, Marion and Nur (1991), and Yin and Nur (1993), showed that as the number of clay particles mixed with sand grains increases the velocity increases due to porosity decrease.

In contrast, it has been shown that, in consolidated sandstones, V_p is a linear function of porosity and clay content in which V_p decreases (D_t increases) with increasing porosity or clay content (Han et al. (1986), Klimentos (1991)). However, the mechanism of such influence has not been adequately addressed. Some investigators attributed the velocity reduction in clay-bearing sandstone to the matrix-softening by clay particles especially those situated between sand grain boundaries (Han et al. (1986), Klimentos (1991)). Conversely, Anstey (1991) attributed the velocity reduction to the effect of loose clay particles on the bulk density of the rock.

Wilkens et al. (1986) considered clay particles in sandstone to be pore filling material or the solid part of the non-framework component of the rock, and assumed that the framework (sand grains) transmit most of the compressional energy. Wilkens et al. (1986) suggest that because of microporosity in clay particles, particularly in gas saturated (dry) rocks, the solid part of the non-framework probably does not act as a good transmitter for P-waves. Rocks containing equal porosity but varying clay content have varying framework volumes and rocks with equal framework volumes will have roughly equal velocities if their pore geometries are similar. Accordingly, as the clay content of rocks with equal porosity increases, the matrix (framework) decreases. Hence it is the framework decrease which lowers velocity, not some intrinsic effect of the clay itself on the framework moduli of the sandstone. Although the model suggested by Wilkens et al. (1986) explains the reduction of velocity with clay content in sandstones with pore filling clay minerals, it may not be valid for other types of clay distribution, including laminated and structural clays, in shaly sandstones.

Pore geometry has also been cited by Xu and White (1995) as a mechanism for the effect of clay on P-wave velocity. The pore space in a clay-sand mixture can be considered to consist of two major components, volume and pore aspect ratio. They showed that pore geometry could explain most of the scatter in the relationship between velocity and porosity. Flaky clay particles create pores with very small aspect ratio compared to pores associated with sand grains. The mean aspect ratios in clay-related pores range between 0.02 and 0.05 compared to around 0.12 for sand related pores. As a result, shaly sandstones may present different mean aspect ratios according to their clay content. As the mean pore aspect ratio of a shaly sandstone decreases and the concentration of low aspect ratio pores increases, the P-wave velocity decreases (Xu and White, 1995).

3.3.4. Empirical Velocity-Porosity-Clay Content Equations

Over the past few years, several papers (including some of those mentioned above) have presented experimental results on factors affecting elastic wave velocities in sandstones, and a number of empirical relationships between velocity, porosity and clay content have been proposed. Most of these equations are in the form of velocity as a multivariable linear function of porosity and clay content. Han et al. (1986) showed that V_p in 75 water-saturated sandstones at 40 MPa effective stress was linearly related to both porosity and the volume fraction of clay (v_{cl}) with a correlation coefficient of 0.985 (r^2 equal to 0.97):

$$V_p = 5.59 - 6.93\phi - 2.18v_{cl} \qquad (3.12)$$

Others (for example, Tosaya and Nur (1982), Castanga et al. (1985)) proposed similar equations for their data set. In the experimental work mentioned above, point counting of thin sections was used for the clay content determination. It is known (eg, Nadeau and Hurst, 1991) that porosity within clay particles can constitute up to 50% for kaolinite and up to 75% for illite. Since porosity in clay minerals is hard to distinguish in thin section, equations of the form of equation (3.12) probably overestimate clay content and may therefore misinterpret the effect of clay on P-wave velocity.

Empirical equations in the form of equation (3.12) are independent of the mineralogy and distribution of clays in sandstones. However work by Tosaya and Nur (1982) and Minear (1982) indicate that the laminated clays and clays along structural grain boundaries may have significant effects on velocities, whereas dispersed clays make only a small contribution to velocity reduction due to clay content. Vernik and Nur (1992) used a petrophysical classification of siliciclastics for porosity prediction from velocity. Sandstones with less than 15% (by volume) of structural and/or dispersed clays are referred to as arenites. Further subdivision according to grain mineralogy included clean arenites with less than 2% clay. Sandstones with 15% or more clay are classified as wackes, with further transition at 35% clay to shales. Vernik (1994) proposed a velocity-porosity transform in the form of:

$$V_p = A - B\phi \qquad (3.13)$$

for each rock type, with r^2 values better than 0.92. The effect of clay content on V_p in Vernik's equations results in different coefficients for each equation. Unlike equation (3.12), where V_p is a linear function of porosity and clay content, in Vernik's equations V_p is a linear function of porosity and a step function of clay content (Figure 3.4). Despite the excellent correlation coefficients for Vernik's equations, sufficient physical causality has not been provided to explain the sudden change in V_p as the clay volume changes in the vicinity of rock type boundaries nor why there is an apparent lack of clay effect on V_p within a given rock group.

Assuming that the parameter used by Xu and White (1995) for the Kuster-Toksoz model is valid for the samples studied by Vernik (1994), one could distinguish four mean pore aspect ratios roughly equal to 0.16, 0.12, 0.08 and 0.04, respectively, for the four rock types proposed by Vernik. These equations should thus be more effective than the time average and Raymer et al. (1980) equations, which assume a single mean pore aspect ratio. However, applying Vernik's proposed equations in practice to wireline logs may sometimes be difficult especially where clay minerals such as kaolinite and illite, with varying radioactive response, exist in shaly sandstone formations. For a rock with a measured V_p of 3.5 km/s only one unit clay content miscount may lead to 3, 5.3 and 8 porosity units variation as the rock is misclassified as arenite, wacke or shale, respectively (Khaksar and Griffiths, 1998a).

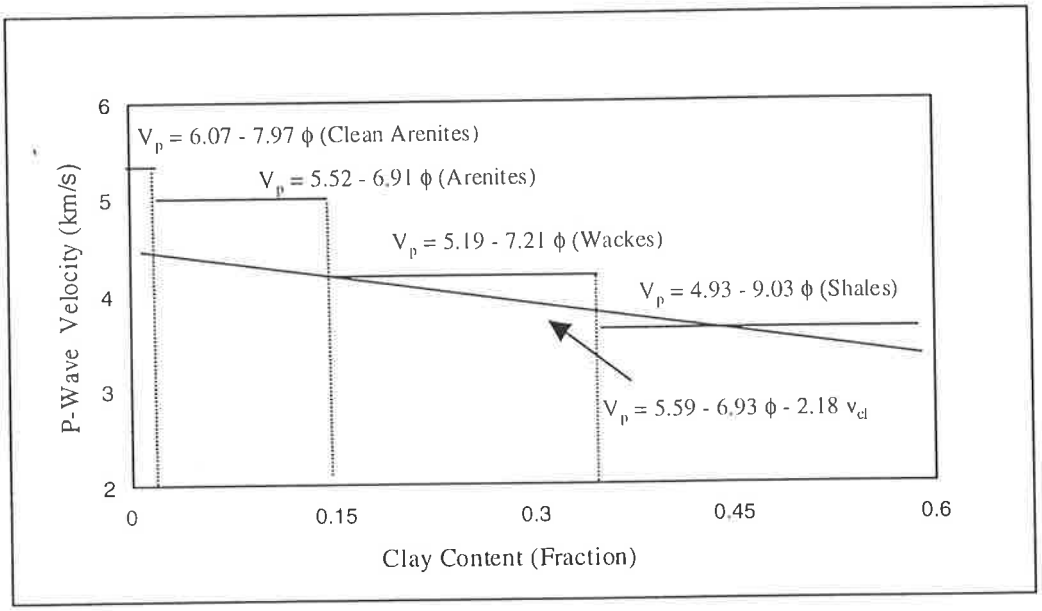

Figure 3.4. Comparison between the effect of clay content on P-wave velocity from empirical equations proposed by Han et al. (1986) and Vernik (1994) in a water-saturated sandstone with 15% porosity and various clay contents at 40 MPa effective stress (from Khaksar and Griffiths, 1998a).

3.3.4.1 Comparison with Field Data

Experimental studies mentioned above provide a better understanding of the complex nature of elastic wave velocities in reservoir rocks. However, the practical aspects of applying the empirical equations derived from these studies have not previously been examined. Log and core data from two hydrocarbon wells were thus used to examine the applicability of laboratory-derived empirical velocity-porosity equations.

Core data were derived from sandstone reservoirs of the Early Permian Patchawarra Formation in the Toolachee 3 and Toolachee 6 wells drilled in the Toolachee Field, a large gas field located in the southeastern Cooper Basin in South Australia (Chapter 2, Figure 2.6). Core porosities in the data set range from 3% to 22% with an average of 14%, whilst the clay content calculated from gamma varies from 3% to 56% with average of 20%. Although, there are some problems with using the gamma ray as a clay content indicator (for example Stuart et al. (1992)), it is the only commonly available log for lithology determination and clay content volume calculation in Cooper Basin wells (Khaksar (1994), Khaksar and Mitchell (1995)). Appendix B lists core and log data used for this comparison.

To compare core data with sonic log readings the following steps were taken. Ambient core porosity data were corrected for in situ pressure conditions using a relationship proposed by Morton (1989). Sonic log values over the Patchawarra Formation interval were blocked using a blocking method introduced by Griffiths (1982). A combination of all available wireline log data were used with core logs to obtain the best possible depth matching of core and log data. Clay content was determined from the gamma ray log using the general index formula of:

$$v_{cl} = (Gr_{log} - Gr_{sand}) / (Gr_{shale} - Gr_{sand}) \qquad (3.14)$$

where Gr_{log}, Gr_{shale} and Gr_{sand} are gamma ray log readings for each interval, pure shale and clean sandstone respectively. The frequency discrepancy between sonic log and ultrasonic lab velocity measurement was neglected and it was assumed that sonic log response in a perfect bore-hole corresponded to the measured velocity in the laboratory environment.

Figure (3.5a) shows significant scatter in the plot of core porosity versus D_t obtained from the Toolachee 3 and Toolachee 6 wells. Apart from the general difference between resolution and error in core and log data, other possible reasons for the scatter are variations in clay content, pore geometry and water saturation in intervals represented by the data set. Although the cross-plot of v_{cl} and core porosity (Figure 3.5b) is also widely scattered, it shows that high clay content sandstones tend to have lower porosities and vice versa.

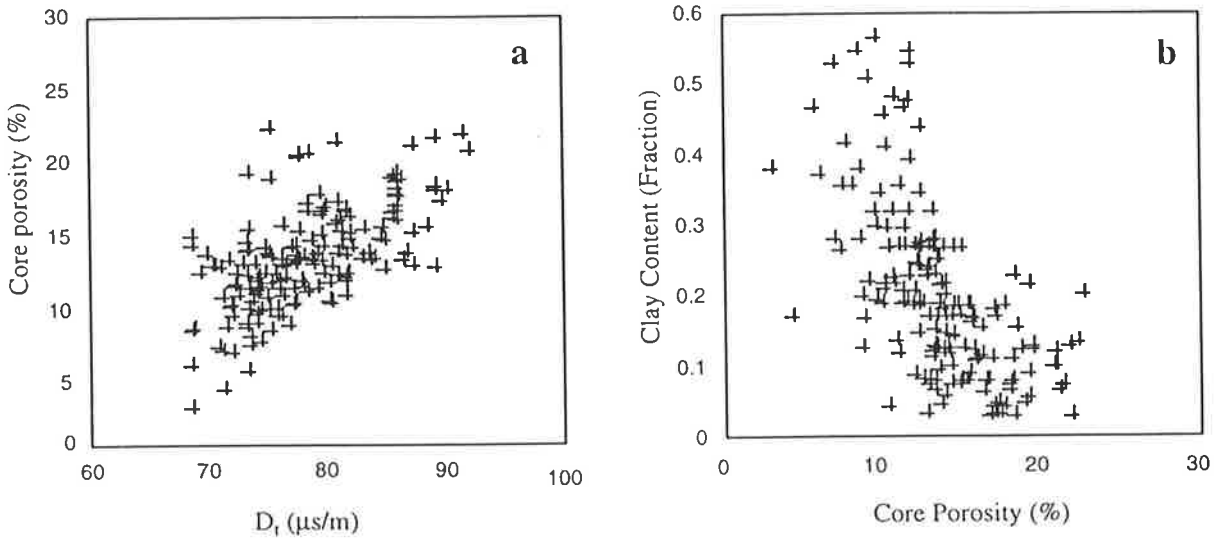

Figure 3.5. Porosity data for Toolachee 3 and 6 wells. (a) Core porosity versus sonic transit time. (b) Clay content versus core porosity.

3.3.4.2. Porosity from Empirical Equations

Five empirical velocity-porosity equations were used to determine porosity from sonic transit time, and the results were compared with actual porosity from core data. The matrix and fluid transit times in the time average formula are considered to be 182 μs/m (zero porosity) and 620 μs/m (D_t for water), respectively. D_{tm} in the Raymer et al. equation is assumed to be 183.7 μs/m whereas 620 μs/m and 1640 μs/m (D_t for gas) were used for D_{tfl} for water saturation greater than 0.75 and less than 0.75, respectively. The corresponding constant values at a confining stress of 24 MPa (the in situ stress condition in the Toolachee Field), were used in equation (3.12) for Freund's (1992) equation. Two locally developed sonic porosity methods, Overton and Hamilton (1986) and Morton (1989), for the Cooper Basin were also used. These two equations, which are based on the time average formula, are routinely used in formation evaluation in the region. The Overton and Hamilton equation considers the fluid sonic transit time as a linear function of gamma ray response. The Morton equation uses the following empirical modifications for matrix and fluid transit time in the time average formula:

$$D_{tm} = 183.7 + 9v_{cl} \qquad (3.15)$$

$$D_{tfl} = 787.5 - 167.4S_W; \qquad (3.16)$$

where S_W is water saturation. Figure (3.6) shows cross plots of the calculated porosity and actual core porosity for the above-mentioned equations. Table 3.1 summarises error distribution for each equation. The following is a brief discussion on the applicability of these equations to the data set considered in this study.

The Time Average and Raymer et al. Equation

The time average equation overestimates the actual porosity of the samples with mean absolute error (MAE) of 4.4 porosity units. This is mainly because the assumed D_{tfl} (620 μs/m) corresponds to transit time for water while sandstone reservoirs in Toolachee 3 and Toolachee 6 wells are gas-saturated. Changing D_{tfl} to 754 μs/m results in a bulk shift in calculated porosities and reduces the error indicators, but makes no difference to the correlation coefficient. Moreover, assigning 754 μs/m to D_{tfl} in the time average formula is purely empirical and has no physical justification.

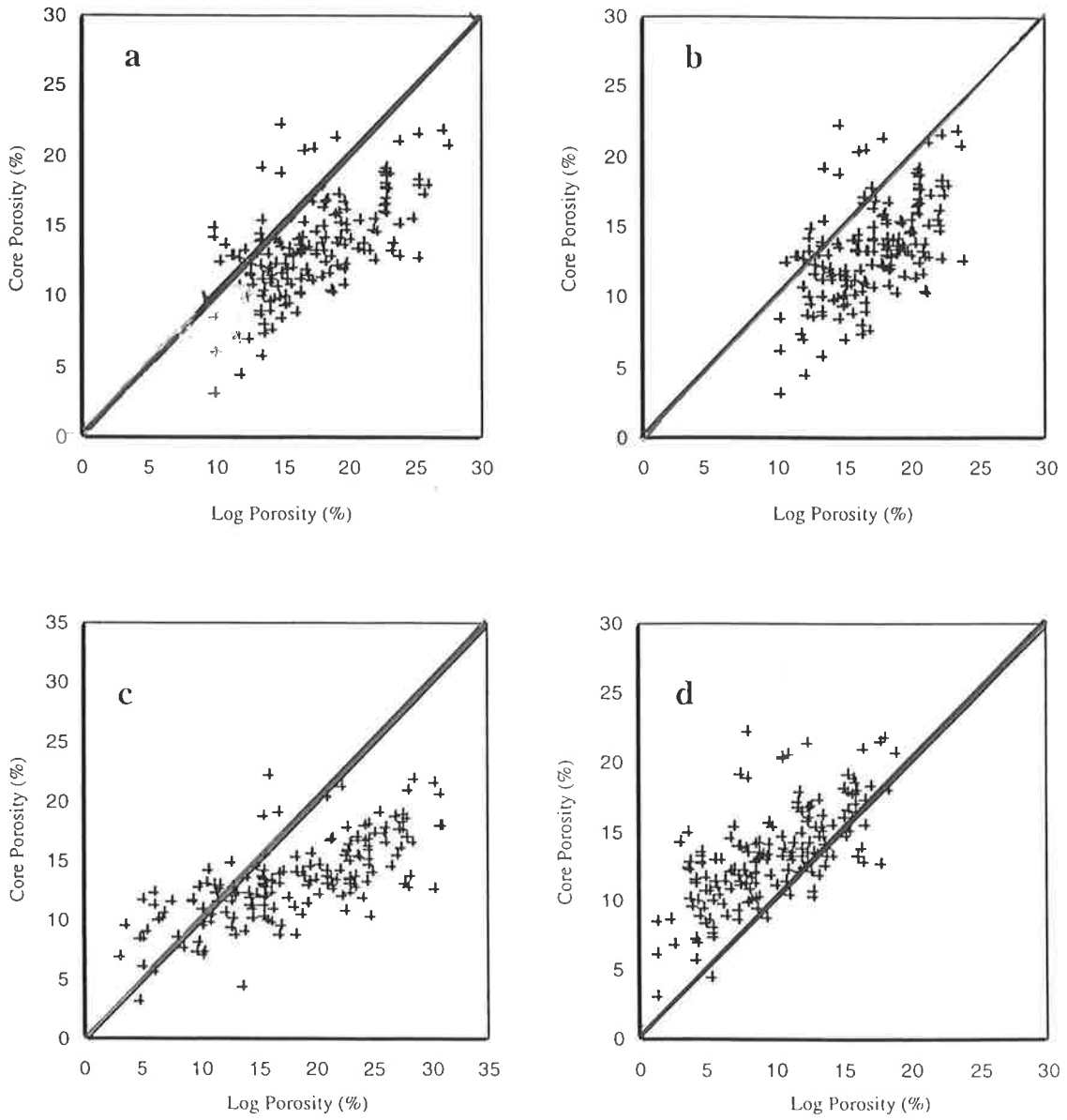

Figure 3.6. Core porosity (%) versus sonic log-derived porosity (%). Line shows a perfect correlation. The plots are for seven equations. (a) Time average formula (Wyllie et al. 1956), (b) Raymer et al. (1980), (c) Han et al. (1986), (d) Freund (1992), (e) Vernik (1994), (f) Overton and Hamilton (1986), (g) Morton (1989).

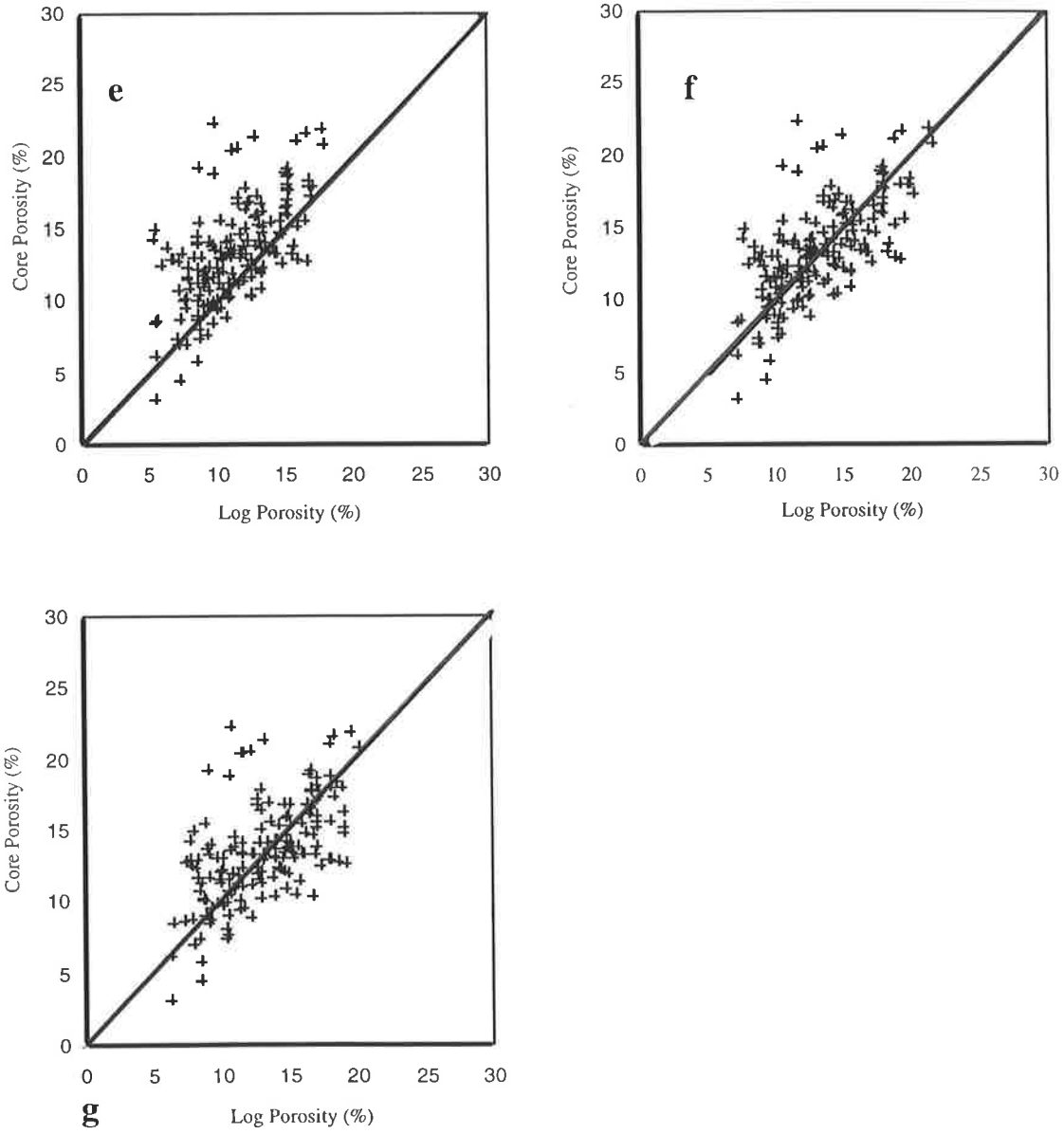

Figure 3.6. Cont.

Equation	Squared correlation coefficient (R^2)	Mean absolute error in porosity (porosity unit)	Median error (porosity unit)
Time Average (D_{tfl} = 620 µs/m)	0.398	4.36	3.97
Time Average (D_{tfl} = 754 µs/m)	0.398	2.20	-0.12
Raymer et al.	0.297	4.37	4.25
Han et al.	0.506	5.72	4.82
Freund	0.471	3.80	-3.46
Vernik	0.395	2.67	-1.91
Overton	0.429	2.18	-0.01
Morton	0.353	2.31	0.08

Table 3.1. Squared correlation coefficients and error indicators discussed in the text and shown in Figure 3.6. This table provides a comparison between core porosity and porosity calculated using empirical velocity-porosity equations.

Around 85% of core data show porosities between 10% and 20%. In this porosity range it is expected that the Raymer et al. equation would give very similar results to those obtained from the time average formula. This similarity has also been shown by the Toolachee data set. It is worth noting that the fluid sonic transit time in the Raymer et al. equation has been adjusted for the calculated water saturation for each interval. Raymer et al. porosities in gas saturated interval (S_W < 0.75, and D_{tfl} = 1640 µs/m) are similar to the porosity assigned by the time average formula with an assumed D_{tfl} of 620 µs/m, whereas assuming D_{tfl} = 620 µs/m results in higher Raymer et al. porosities (almost 2.5 porosity units).

Han et al. Equation

The Han et al. equation significantly overestimates high porosities (ϕ>14%) and underestimates low porosities (ϕ <10%). As the data set indicates that low core porosities coexist with high calculated clay contents, this equation overestimates the porosity for low clay content sandstones and underestimates porosity in high clay content sandstones. The Han et al. equation has originally been proposed for water-saturated sandstones but the wells studied here are gas wells. This might provide another explanation for the significant overestimation by the Han et al. equation in the high porosity range.

Freund's Equation

Freund's equation generally underestimates the actual porosity with MAE of 3.8 with underestimation at low porosities greater than at middle to high porosity. It should be

noted that the Freund equation was developed for dry rocks to simulate purely gas-saturated sandstones. Compared with other equations, the equations proposed by Han et al. and Freund show improved correlation coefficients (less scatter). This means that considering a clay content term in sonic porosity methods in general should reduce the scatter in velocity-porosity relationships.

Vernik Equations

In terms of error distribution, the Vernik equations gave better results for the Toolachee data compared to the other laboratory derived equations, even though the correlation coefficient has not improved dramatically. The Vernik equations generally underestimate porosity with an MAE of 2.7 porosity units.

Locally Modified Equations

Both the Overton and Hamilton, and Morton equations give a reduced MAE compared with the other equations examined above. Although there is no theoretical explanation for the relationship between gamma ray reading and fluid transit time as used in the Overton and Hamilton equation, this equation presents an improved correlation coefficient compared to the Morton equation for the data used in this study.

3.3.4.3. Conclusions Concerning the Empirical Equations

Field data from the Toolachee Field compared to published experimental data confirm that as well as porosity, other factors such as clay and fluid content are also important (and should be considered) when sonic logs are used for porosity determination. However, information on the clay content, fluid type and fluid saturation cannot be directly determined from the sonic log, and other information is required. None of the experimentally derived velocity-porosity equations examined in this section provide a globally applicable method for porosity calculation from sonic logs. The shortcomings of these equations are more pronounced when applied to gas-bearing shaly sandstone formations. Combined petrographic analyses and laboratory velocity measurements are required to improve the calibration between core porosity and sonic log readings (Khaksar and Griffiths, 1998a).

3.3.5. Influence of Effective Stress

Experimental results indicate that confining stress and pore pressures have almost equal but opposite effects on wave velocity in consolidated reservoir rocks. Confining stress has an effect on the wave velocities because it deforms most of the compliant parts of the pore space, such as microcracks and loose grain contacts. Closure of microcracks increases the stiffness of the rock and increases bulk and shear moduli. Increase in pore pressure mechanically opposes the closing of cracks and grain contacts, resulting in low effective moduli and velocities.

Wyllie et al. (1958) measured P-wave velocity as a function of pore and confining stress on water-saturated Berea sandstone. They showed that at constant confining stresses V_p increases with decreasing pore pressure, and for constant differential pressure, the V_p remains constant (Figure 3.7). Hence, when both confining stress and pore pressure are varied, only the difference between the two has a significant influence on velocity (Hicks and Berry, 1956) that is:

$$P_d = P_c - P_p \tag{3.17}$$

where P_d is differential pressure. The more accurate relationship may be of the form of

$$P_e = P_c - nP_p \tag{3.18}$$

where P_e is effective stress and n is the effective stress coefficient (**Terzaghi, 1943**) Equation 3.18 indicates that for n values not equal to unity, changes in a physical property caused by changes in confining stress may not be exactly cancelled by equivalent changes in pore pressure. Experimentally derived n values for the water-saturated Berea sandstone by Christensen and Wang (1985) show values less than 1 for properties that involve bulk compression (V_p).

A comparison of published experimental studies on the influence of effective stress on wave velocities, reveals that (1) the rock type and (2) the fluid saturate are both influential. The rate of increase in velocity as effective stress increases is controlled by the aspect ratio of the pore space and the contribution of crack-like pores to the total porosity of the rock. Rocks with microcrack porosity show a more marked variation in V_p versus effective stress

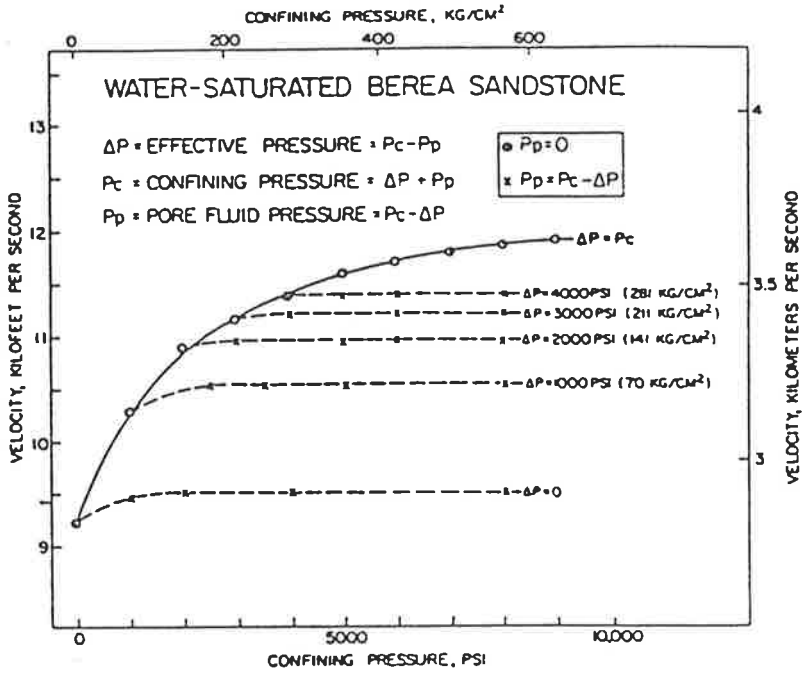

Figure 3.7. V_p as a function of differential pressure in Berea sandstone (from Wyllie et al. 1958).

compared to rocks with high aspect ratio pores ($\alpha \sim 1$) or spherical pores. That is, the greater the number of low aspect ratio pores ($\alpha << 1$), the more the velocity varies with pressure.

Examples of different stress sensitivity of velocities for rocks with microcrack porosity, and rocks consisting of pores with aspect ratios close to 1 have been shown in Figure 3.8. For Westerly granites and Bedford limestone, which are well known for their microcrack porosity (Bourbie et al. 1987), velocities are highly stress sensitive. Whilst wave velocities in Solenhofen limestone which consists of pores with aspect ratios close to 1 (Bourbie et al. 1987) exhibit no variation with effective stress increase. Considering the role of microstructure helps to understand the different velocity behavior between dry and saturated rocks under increasing effective stress. Since for a saturated sample the finite compressibility of water resists deformation and increases the elastic moduli of the rock, at low effective stresses a dry sample is less rigid than a saturated one. At high effective stresses, velocity becomes a quasi-linear function of effective stress for both water and air saturated samples (Bourbie, et al. (1987) and Vernik, (1997)). However, as Figure 3.8 demonstrates, the critical effective stress at which velocity-effective stress curve levels off is not the same for water and air saturated samples, and may differ from one rock type to another.

3.3.5.1. Log-Derived Porosities and Effective Stress

The sensitivity of the acoustic velocity to effective stress can be used to identify overpressure from the sonic log. Other things remaining constant, an increase in pore pressure is indicated by an increase in the sonic transit time (Rider, 1986). It is possible to calculate the amount of overpressure from the deviation of the sonic travel time from the normal compaction trend (Hottman and Johnson, 1965), when the shale transit time is plotted on a logarithmic scale versus the burial depth (Figure 3.9). In most cases the anomalously high porosity (under-compacted) rock present in a overpressure zone will amplify the sonic log deviation. However, there are some examples of overpressured shales which also demonstrate low porosities and high densities similar to rocks in normal pressure zones (Yassir and Bell, 1994). Therefore, to avoid the misinterpretation of velocity data in overpressured zones, the mechanism involved in the process of overpressure should also be taken into account.

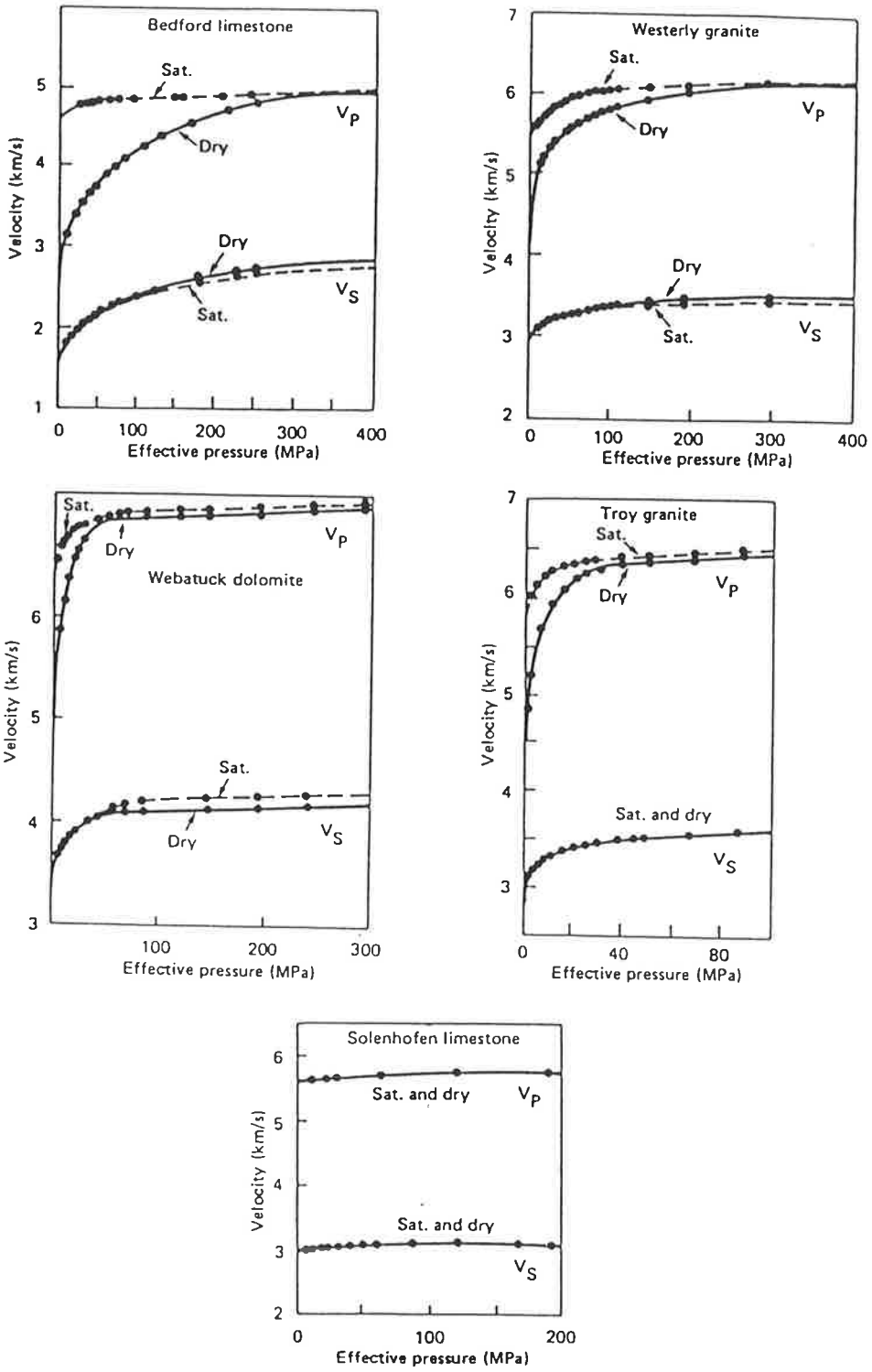

Figure 3.8. Relationships between velocity and effective stress in various rocks (from Bourbie et al. (1987).

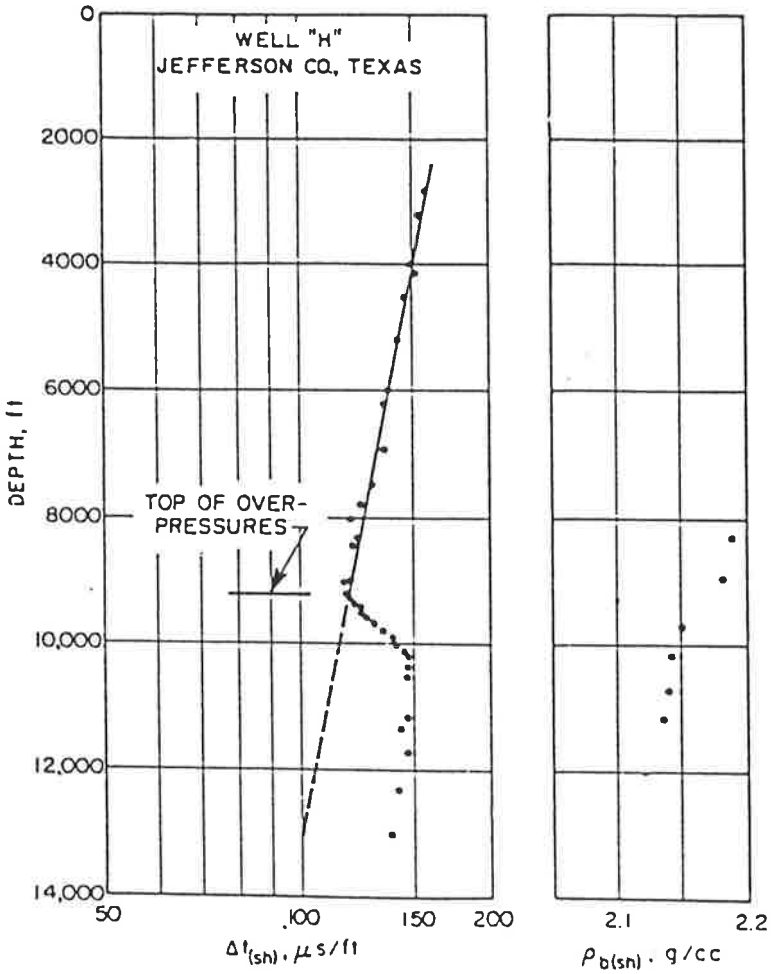

Figure 3.9. Application of the sonic log to identify of overpressuring (from Hottman and Johnson, 1965).

The stress sensitivity of velocities in rocks may also influence the porosity values assigned by sonic transit times in reservoir rocks in hydrocarbon producing fields. In other words the reservoir pressure reduction due to hydrocarbon production may cause the sonic log to be influenced by the changing effective stress in the formation. However, is the sonic porosity underestimation in partially pressure-depleted reservoirs of practical significance? Using published experimental data the following section illustrates the range of porosity underestimation due to changes in effective stress for both water saturated and dry sandstones.

Three sandstones have been modeled with assumed porosities of 5, 10 and 15 percent, and zero clay content. The sandstones are considered to be well consolidated so that the porosity reduction due to the applied pressure is negligible. Two effective stress levels, 30 MPa and 50 MPa, simulate normal pressure and partial pressure depletion conditions at 2500 m depth, respectively. Empirical equation of Eberhart-Phillilps et al. (1989) is used to calculate V_p under water-saturated condition.

$$V_p = 5.77 - 6.94\phi - 1.73\,(v_{cl})^{0.5} + 0.446\,(P_e - e^{-16.7\,P_e}) \qquad (3.19)$$

where V_p is in km/s and P_e is in kbar. Velocity-effective stress relationship derived from laboratory measurements by Freund (1992) is used for the velocity calculation under dry (gas-saturated) condition (Table 3.2). Again it is assumed that the sonic log response in an ideal bore hole condition corresponds to the calculated V_p. The time average formula (equation 3.9) and the Overton-Hamilton equation (this chapter, section 3.3.4.2) are used to determine the porosity of the sandstones under the water-saturated and dry (gas-saturated) conditions respectively.

Porosity (%)	A (km/s)	B (10^{-4} km/s MPa)	C (km/s)	D (MPa^{-1})
5	5.1	8.54	1.90	0.040
10	4.6	9.32	1.71	0.044
15	4.11	9.62	1.53	0.047

Table 3.2. Empirical constants in the velocity-effective stress relationship proposed by Freund (1992): $V_p = A + BP - Ce^{-DP}$ where V_p is P-wave velocity in km/s and P effective stress in MPa.

Table 3.3 summarises the above calculation for three assumed sandstones under both water-saturated and dry conditions. Apart from the difference between porosities assigned by the time average formula and the originally assumed porosities, the calculated values for water-saturated rocks show almost a 3.5 μs/m reduction in D_t for the 20 MPa increase in the effective stress. A 3.5 μs/m reduction in sonic log could be converted to a porosity underestimation ranging from 0.9 to 1.4 porosity units. The porosity values assigned by the Overton-Hamilton equation are very close to the assumed original porosities at normal pressure condition (30 MPa). On the other hand, this equation underestimates the corresponding porosities under pressure depleted conditions (50 MPa) by between 2.6 to 2.9 porosity units for the three dry sandstones. It is worth noting that while none of the most common sonic porosity methods consider the effective stress effect, using alternative equations to the time average formula such as Raymer et al. (1980) make no significant difference to the range of porosity underestimation presented in Table 3.3.

The implication for porosity calculations at the two pressure levels shown in Table 3.3 is that when the sonic log is used to determine porosity, the pressure condition in the reservoir needs to be taken into account. In general the common sonic porosity methods do not account for the variation of V_p due to reservoir pressure changes between partially pressure depleted and non-depleted reservoirs. The range of such underestimation for water (and probably for oil) saturated rocks appears not to be significant. However, since the influence of effective stress on V_p increases as the fluid saturation changes to gas, porosity underestimation by conventional velocity-porosity transforms for gas bearing rocks may increase (Khaksar and Griffiths, 1996a and b).

Effective Stress MPa	Rock I (ϕ =5%)		Rock II (ϕ =10%)		Rock III (ϕ =15%)	
	D_t (μs/m)	ϕ_{sonic}	D_t (μs/m)	ϕ_{sonic}	D_t (μs/m)	ϕ_{sonic}
Water-Saturated						
30	180.1	1.4%	192.2	6.3%	205.7	6.5%
50	176.7	0.1%	188.6	2.6%	202.1	5.6%
Dry						
30	219.5	6.6%	239.8	10.1%	265.7	14.7%
50	204.7	4.0%	224.4	7.4%	249.0	11.8%

Table 3.3. The approximate range of porosity underestimation due to increase of effective stress by conventional velocity-porosity equations for three sandstones at water-saturated and dry conditions.

3.3.6. Fluid Saturation and Velocity

Numerous published experimental investigations have shown that elastic wave velocities in fluid saturated rocks are related to pore fluid and level of saturation (for example, Wyllie et al. (1958), King (1966), Nur and Simmons (1969)). Theoretically, the influence of pore fluid on wave velocities in rocks is due to its effect on both bulk density and bulk modulus (equation 3.1). The role of compressibility dependence of V_p in fluid saturated rocks have been addressed in several experimental investigations (for example Fatt, 1958). For instance, Hicks and Berry (1956) showed that the velocity variation in a given formation due to change in compressibility of the pore fluid can exceed 20 percent. Figure (3.10) shows the variation of V_p and V_s with Sw modeled by Domenico (1976) using Biot theory. The gradual reduction V_p at low saturation (Sw < 0.80) is attributed to the increased bulk density as Sw increases. At high water saturation levels the effect of low pore fluid compressibility dominates the density effect and V_p increases sharply as pore space approaches full saturation. The decrease in V_s with increasing Sw results from the increase of bulk density (Domenico, 1976) , as discussed on page 16.

Laboratory studies, however have shown that apart from density and compressibility other factors such as pore structure, saturation history and fluid distribution should also be considered for wave velocities in partially saturated rocks (Domenico (1977), Knight and Nolen-Hoeksema, (1990) and Knight et al. (1998)). It has been found that the velocity is determined by the compliance and saturation state of the various region of the pore spaces. Domenico (1977) showed that discrepancies between experimental data and theory are related, at least in part, to the response of fluid distributed in microscopic pores to the different saturation techniques employed during velocity measurements. Two commonly used saturation techniques, drainage (flow) and imbibition result in different velocity-saturation relationships in rocks (Figure 3.11). The drainage technique involves decreasing saturation through capillary force or evaporative drying whereas the imbibition technique involves increasing saturation through the spontaneous uptake of water followed by depressurization of a saturated sample (Knight et al. 1998). During the imbibition process air is trapped in all pores resulting in a more even fluid distribution, whilst with the drainage technique the water tends to occupy the low aspect ratio pores and the gas tends to occupy the large pores (Figure 3.12). The key difference between these two processes is the saturation state of crack like regions of the pore space.

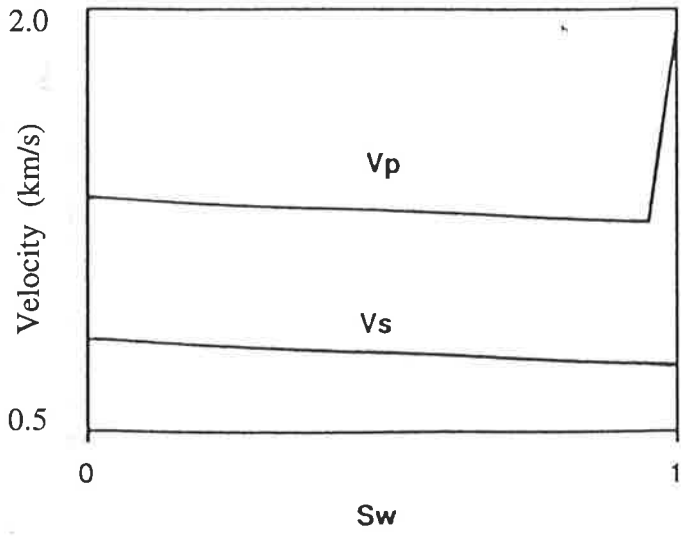

Figure 3.10. Variation of V_p and V_s with water saturation modeled by Domenico (1976).

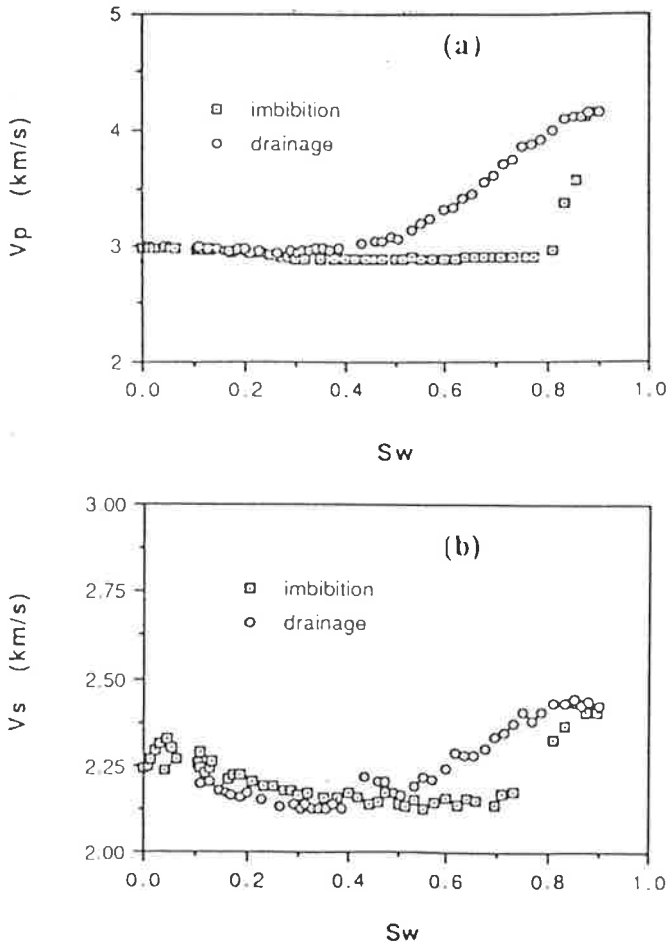

Figure 3.11. Velocity versus water saturation measured during continuing imbibition and drainage experiments. (a) V_p versus SW, (b) V_s versus SW (from Knight and Nolen-Hoeksema. 1990).

During imbibition the velocity is almost constant with increasing saturation and only at saturation close to full saturation velocity shows a dramatic change. The sharp increase in velocity at Sw = 0.8 shown in Figure (3.11) is attributed to the filling of low aspect ratio pores by the water resulting in a stiffening of the frame modulus, while air becomes discontinuous and segregated into a collection of isolated inclusions in stiff high aspect ratio pores (Knight and Nolen-Hoeksema, 1990). In the drainage process velocity gradually decreases with decreasing saturation where water remains longer in low-aspect ratio pores and air is initially placed in high aspect ratio pores. The practical point in the interpretation of velocity-saturation relationships is that if the laboratory data are a basis for field interpretation, the saturation technique used should simulate the in situ saturation process.

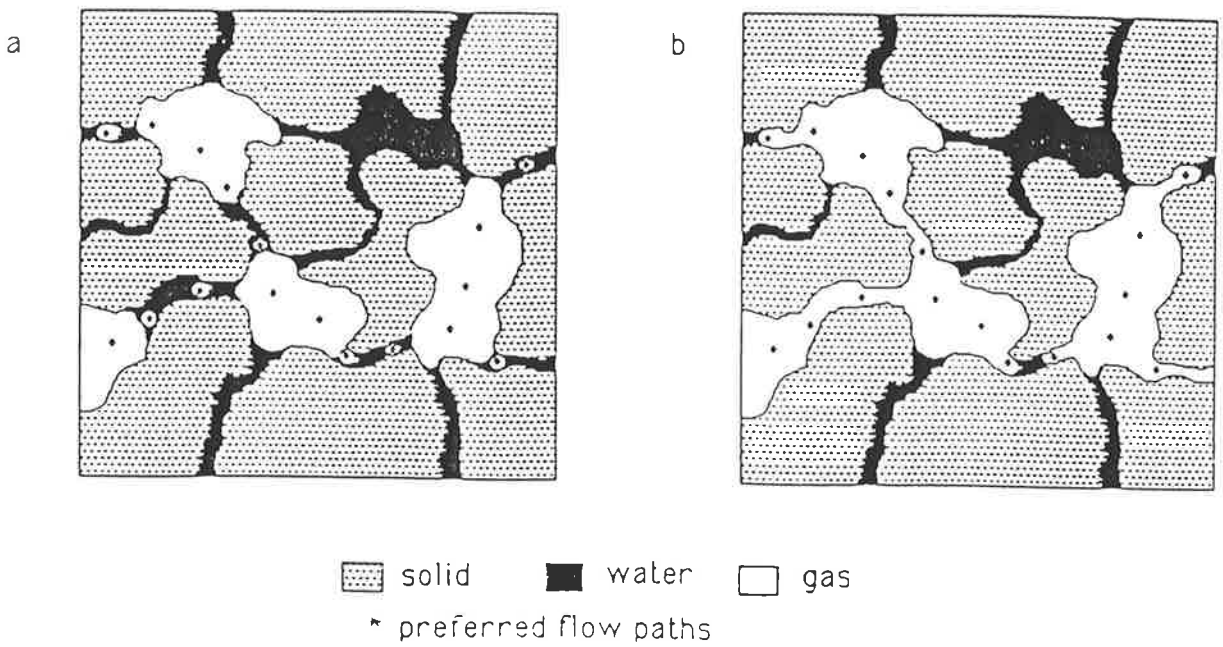

Figure 3.12. Fluid distribution model in partially saturated rocks during a drainage process. (a) Gas filling equi-dimensional pores at higher SW values, b) gas entering pores throats at lower SW values (from Enders and Knight, 1989).

Chapter 4

Samples

4.1. Introduction

Accurate and detailed petrographic and petrophysical analysis of rock samples are required to establish meaningful relationships between rock properties and acoustic measurements. This chapter addresses sampling procedure, and describes the petrographic and petrophysical properties of the rock samples used in this study.

4.2. Sampling

A total of 33 sandstone samples were collected from drill cores from depth between 1917 m and 2564 m three hydrocarbon producing wells in gas fields of the southern Cooper Basin (Figure 2.6). Samples are from the Unit C of the Late Permian Toolachee Formation intersected in Moomba-73, Dullingari-44 and Strzelecki-15 wells (Table 4.1). Depositional environment and stratigraphy of the Toolachee Formation in southern Cooper Basin was described Chapter 2. Compared with other Cooper Basin wells the above mentioned wells have a relatively complete well log suite including porosity logs and pore pressure data from Repeat Formation Tester (RFT). Sampling points were chosen on the basis of petrographic and sedimentological hand specimen characteristics. The samples represent a typical range of porosity and permeability of Cooper Basin sandstones within the study area.

Procedure for core plug preparation is described in Chapter 5. Specimens of each sample were prepared for thin section analysis, bulk-sample X-ray diffraction and scanning electron microscopy. After careful examination of core plugs and thin sections, 22 samples suitable for acoustic measurements were selected. These 22 samples had sufficiently low average grain size to avoid wave scattering and were relatively homogeneous and isotropic

Figure 4.1. (a) and (b) Photographs fine to medium grain size, unfractured and relatively homogenous core samples ***suitable*** for acoustic measurements.

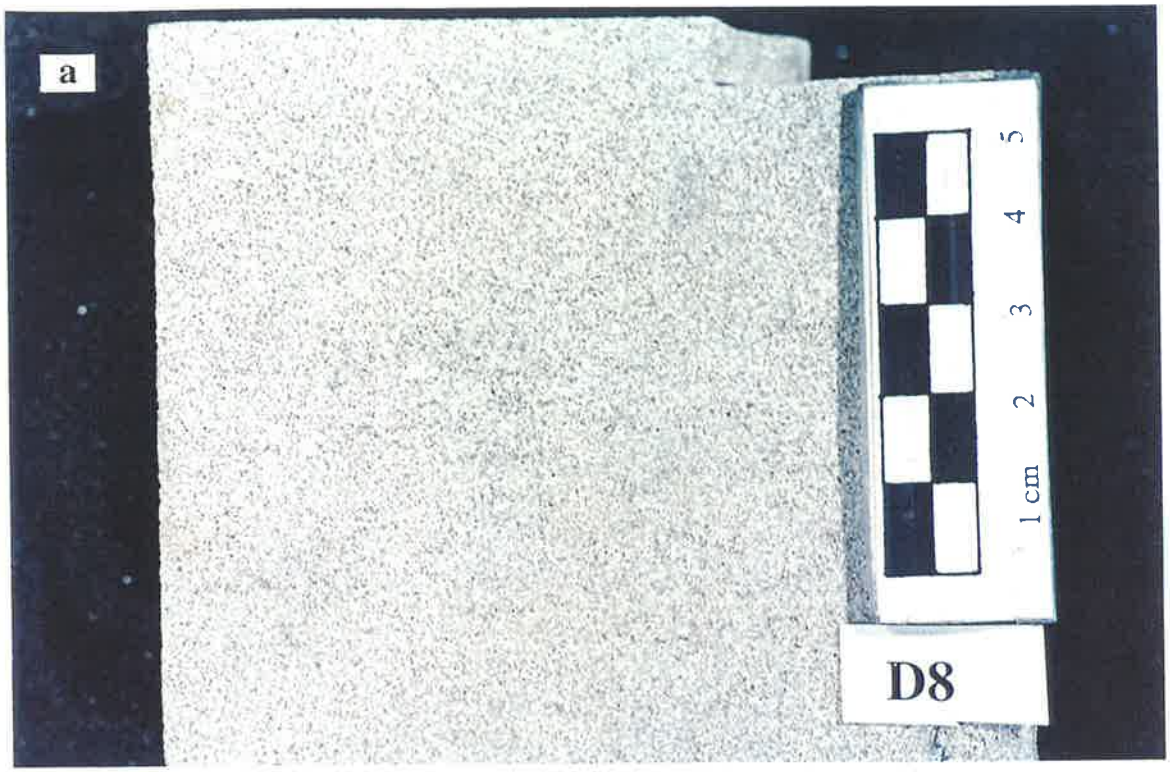
a
1 cm
2
3
4
5
D8

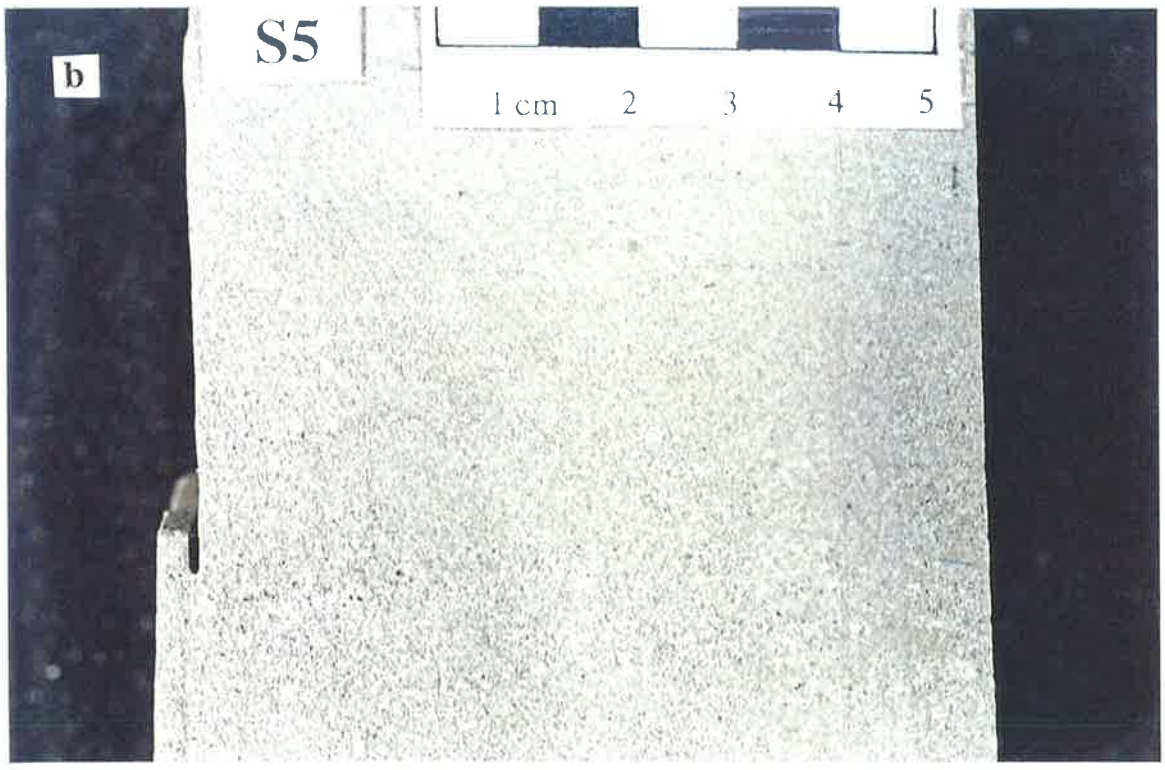
b
S5
1 cm
2
3
4
5

Figure 4.1. (c) and (d) Photographs of coarse to very coarse grain size, fractured and heterogeneous core samples ***unsuitable*** for acoustic measurements.


c
1 cm 2 3 4 5
M4

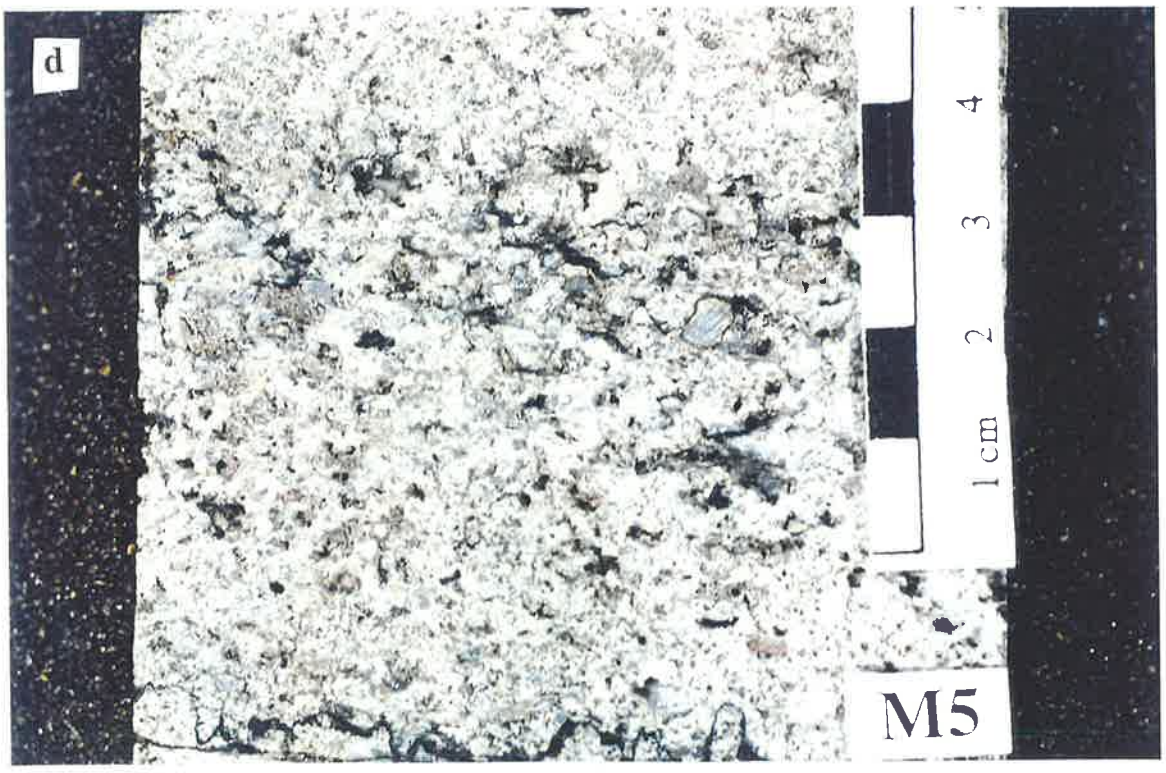
d
1 cm 2 3 4
M5

(Figure 4.1a and b). Unsuitable samples for acoustic measurements were rejected because of presence of micro-fractures and gravel in the plugs (Figure 4.1c and d).

Sample	*Well Name*	*Depth (m)*
D1	Dullingari-44	2211.8
D2	Dullingari-44	2213.1
D3	Dullingari-44	2214.1
D4	Dullingari-44	2215.4
D5	Dullingari-44	2216.3
D6	Dullingari-44	2217.5
D7	Dullingari-44	2220.3
D8	Dullingari-44	2221.1
D9	Dullingari-44	2221.5
D10	Dullingari-44	2221.8
D11	Dullingari-44	2222.3
M1	Moomba-73	2550.8
M2	Moomba-73	2551.4
M3	Moomba-73	2552.2
M4	Moomba-73	2552.9
M5	Moomba-73	2553.4
M6	Moomba-73	2554.1
M7	Moomba-73	2554.8
M8	Moomba-73	2556.6
M9	Moomba-73	2557.4
M10	Moomba-73	2558.7
M11	Moomba-73	2563.0
M12	Moomba-73	2563.3
M13	Moomba-73	2564.0
M14	Moomba-73	2564.5
S1	Strzelecki-15	1917.7
S2	Strzelecki-15	1918.5
S3	Strzelecki-15	1919.2
S4	Strzelecki-15	1919.8
S5	Strzelecki-15	1920.7
S6	Strzelecki-15	1921.4
S7	Strzelecki-15	1922.0
S8	Strzelecki-15	1922.6

Table 4.1. List of all core samples collected for the current study. Samples used for the acoustic measurements are written in ***bold*** font styles.

4.3. Bulk-Rock X-Ray Diffraction

Bulk-rock XRD analysis was carried out on all samples using X-ray diffractometer at the Department of Geology and Geophysics of the University of Adelaide. The small pieces of rock were ground into a fine powder using an agate mortar and pestle. The unorientated

powder sample was then placed in an aluminum cavity mount. The prepared samples were run in a Philips type PW 1050 X-ray diffractometer at 50 kV and 35 mA, using Co Kα radiation, at a speed scan at 2°/minute. Mineral identification was checked by comparison with Joint Committee on Powder Diffraction Standards (JCPDS) files using the CSIRO software Xplot™.

The bulk-rock X-ray diffraction results of the samples indicate that all samples have very similar mineralogy with quartz, kaolinite and illite as major minerals. Siderite occurs as a minor to trace mineral in some samples. Figure 4.2 shows typical bulk-rock X-ray diffractogram of samples used in this study.

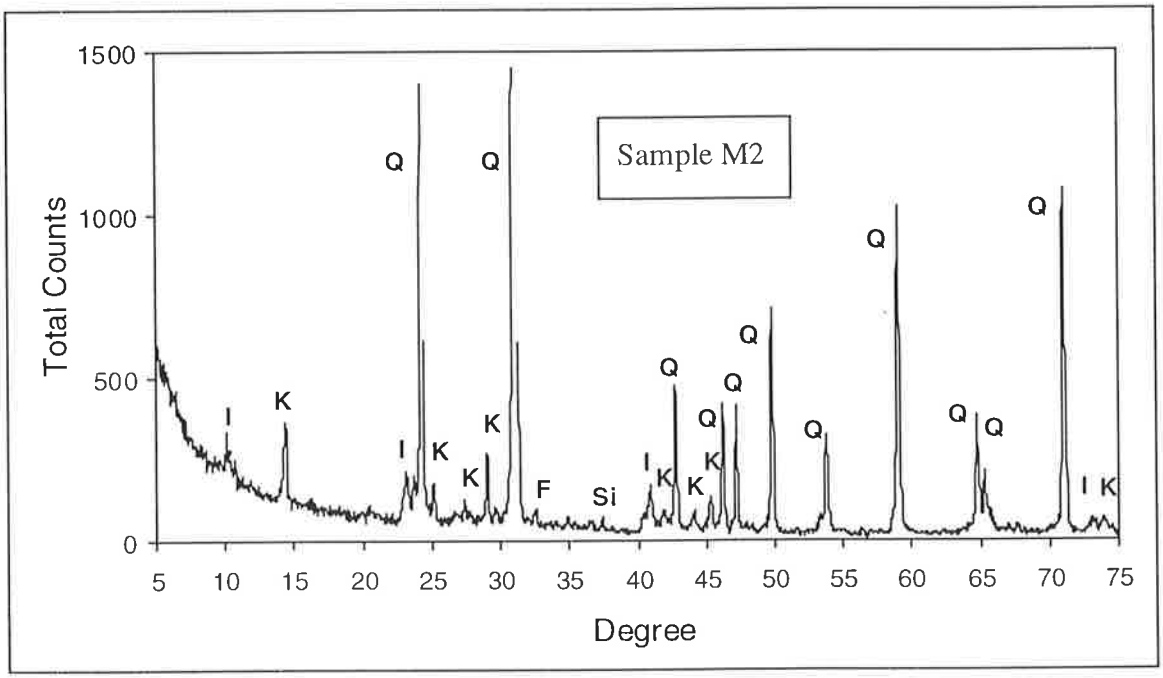

Figure 4.2. Representative XRD peak patterns for the samples used in the current study. Q = quartz, K = kaolinite, I = illite (mica), Si = siderite and F = feldspar.

The relative abundance of each mineral was assessed by comparison of the main peak heights using the relative intensity method described by Hardy and Tucker (1991). In this method the height of the principle peak, I, for each mineral component is multiplied by an H factor, which corrects for the relative "diffracting ability" of the mineral. The weight fraction, W, of the *i*th components is given by (Hardy and Tucker, 1991):

$$W_i = H_i I_i / (\sum_{n=1}^{N} H_i I_i) \qquad (4.1)$$

Quartz was used as an internal standard, and is therefore associated with an H factor of unity. The H factors for other minerals were determined empirically using a chart developed by the X-ray unit of the PRIS, the University of Reading. This method is semi-quantitative and only gives the relative percentage of minerals which could be helpful for compositional petrography. Table 4.2 shows the estimated volume percentages of minerals identified from the whole-rock XRD analysis.

Sample	Quartz	Kaolin	Illite/Mica	Siderite	Feldspar
D1	88	8	2	1	1
D2	79	13	5	2	1
D3	86	10	2	2	0
D4	89	8	1	1	1
D6	90	8	1	1	-
D7	85	11	3	1	-
D8	94	5	1	-	-
D10	81	17	2	-	-
M1	93	5	2	-	-
M2	93	6	1	-	-
M7	89	8	2	1	-
M8	86	9	3	2	-
M10	89	7	3	1	-
M11	93	5	2	-	-
M13	84	9	5	1	1
S1	85	11	3	1	-
S2	81	14	4	1	-
S3	87	12	-	1	-
S4	86	12	2	-	-
S5	94	5	1	-	-
S6	89	9	2	-	-
S7	78	17	3	1	1

Table 4.2. Semi-quantitative mineral compositions (%) of the samples from the bulk-rock XRD analysis.

4.4. Optical Petrography

4.4.1. Techniques

Thin sections were prepared for all samples. Rocks were cut perpendicular to the bedding plane and blue-dye epoxy resin was used during impregnation of the samples to assist the recognition of porosity. Photomicrographs were taken of representative features. Scanning electron microscopic (SEM) studies were carried out on all samples using a JEOL type JSM 5300 at the PRIS. SEM observations were used to study the texture, pore types, authigenic minerals and to obtain additional petrographic information. Freshly fractured

chips of rock samples were mounted on an aluminum stub and then were coated with gold according to methods described by Trewin (1991). A linked Energy dispersive X-ray analyser of Oxford Instrument type Link AN 10000 was also used to help in identification of individual minerals. Photomicrographs were obtained to illustrate features of interest in the rock samples.

4.4.2. Image Analysis

Computer-assisted analysis of microscopic images provides a means of making rapid, quantitative measurements of features observed in rock thin sections. In the current study Petrographic Image Analysis (PIA) of thin sections was used as an automated version of point counting. Ehrlich et al. (1984), and Ehrlich and Davis (1989) have described the principle of PIA. The PIA facilities used were consist of an IBM compatible personal computer, software (Video Pro 32™), a color video camera and an OLYMPUS ™ BH-2 type transmitted light microscope allowing real-time computer screen display of video images of thin sections. The software allows extraction and measurement of image features and provides a quantitative description of an image as numerical data. Images were acquired with the color video camera mounted on the microscope.

Transmitted-light images of thin sections were used permitting routine petrographic observations to be made during acquisition of individual images. For each sample between 5 to 10 field of views were collected at a magnification of 40×. At this magnification the resolution of an individual pixel is 2.1 microns and the true size of each field view is 350 by 512 pixels. Acquisition of 5 to 10 fields of view for each sample provides coverage of approximately 10% to 15% of the total area of a 5×2.5 cm thin section.

Identifying the pixels associated with a particular rock component (mineral, rock fragment, porosity, etc.) permits the creation of a binary image wherein intensities of the component pixels are discriminated from the rest of the image using a thresholding colour code (red for instance). The fraction of each component in each view was then determined from the ratio of the number of component pixels to the total number of pixels in the field of view. The fraction values for each component were averaged over all fields of view for each sample. The long dimension of quartz grains was also measured to estimate the mean grain size of the sample. In total between 100 to 200 grains were measured for each thin section.

4.4.3. Textural and Compositional Petrography

The grain size of the samples range from fine (84 μm) to medium (304 μm) with an average of 200 μm. The roundness of the samples ranges from subangular to well-rounded and sorting varies from well-sorted to poorly-sorted. In general, all samples are well consolidated and were classified as sublitharenite sandstones using the classification suggested by Folk (1974).

The main component of the studied samples is quartz, mainly single crystal without undulose extinction indicting igneous sources (Figure 4.3a and b). Quartz grains which are the main framework mineral show abundant overgrowths in most of the studied samples. The proportion of quartz grains within the samples ranges between 58% and 78%with an average of 68%.

Rock fragments including metamorphic, sedimentary and volcanic grains are the next most significant component of the studied samples. The proportion of rock fragments ranges between 2% and 19%, with an average of 9%. Muddy and silty rock fragments are abundant and appears in two forms. These two forms area: (1) very fine to medium grain size stable grains (Figure 4.4a and b) and, (2) pore filling pseudomatrix (squashed mud particles) between durable quartz grains (Figure 4.4c-f).

The proportion of clay minerals in the samples ranges from 7% to 19%. Clay minerals are authigenic kaolinite and illite with dominant kaolinite. Minor components of the studied samples (less than 2%) consist of heavy minerals (Zircon), organic matter, mica, opaque (pyrite?) carbonate (siderite) and few traces of feldspars. Table 4.3 shows the mineralogy and petrophysical properties of the samples.

Figure 4.3. Micrographs showing subangular to rounded and well-cemented quartz grains that form the main framework mineral in the studied Cooper Basin samples. Development of silica cement can be recognised by the presence of dust rims (white arrow) on the edge of detrital grains. Blue areas in (a) show porosity. (b) Crossed-nichols view of (a). Sample D8, Scale bar = 200 μm.

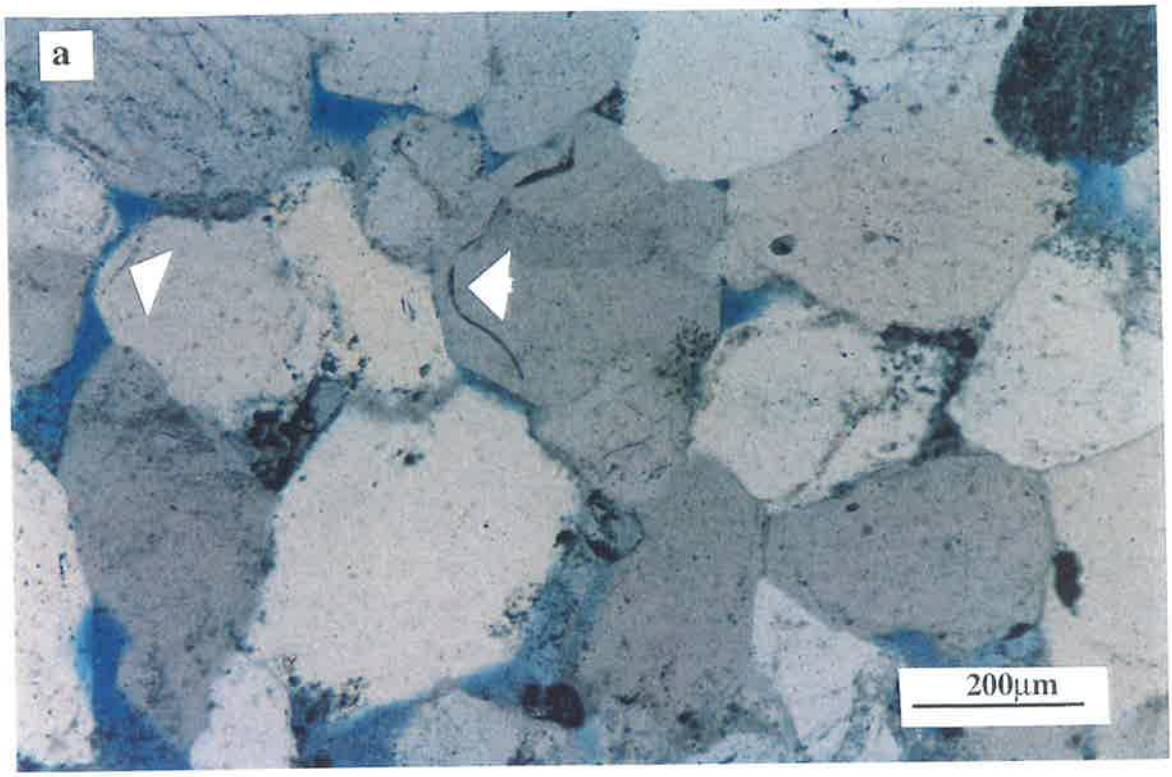
a
200μm

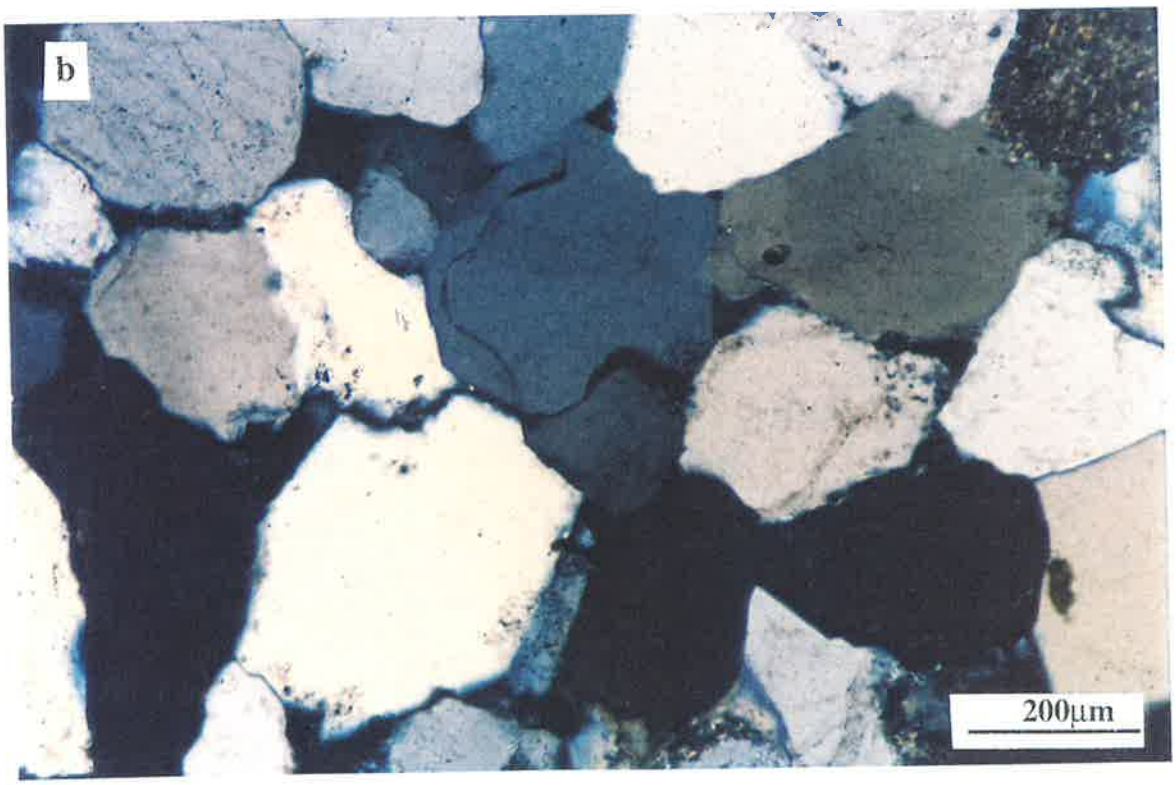
b
200μm

Figure 4.4. Micrographs of Rock Fragments.

a) Fine to medium grain-size stable sedimentary rock fragments (arrows). Sample D4, scale bar = 400 μm.

b) Crossed-nichols view of (a).

c) Ductile , altered and pore-filling rock fragments. These types of rock fragments are muddy in origin and act as psedumatrix between durable quartz grains reducing primary intergranular porosity and change it into microporosity. Sample S1, scale bar = 200μm

d) Crossed nichols view of (c).

e) SEM view showing abundant clay particles, originated from the alteration of muddy rock fragments, filling pore spaces between quartz grains. Sample S6. Scale bar 100 μm.

f) Close up view of (e). Scale bar = 50 μm.

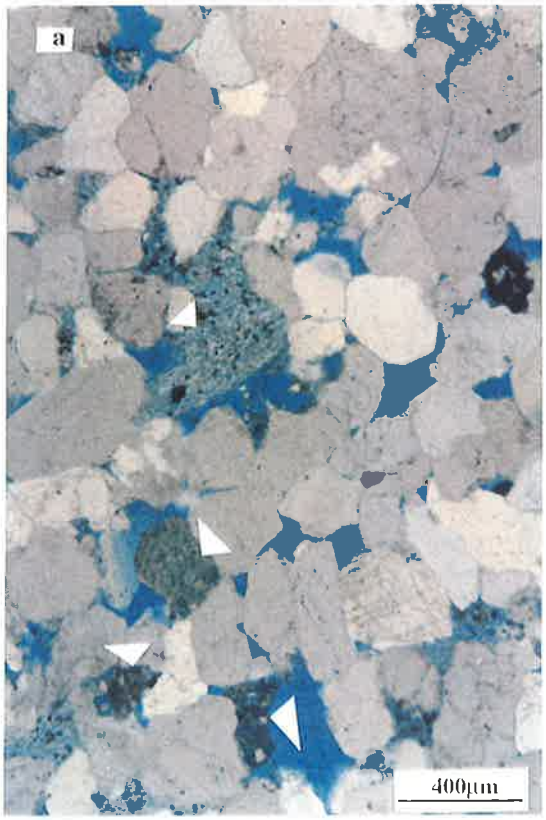
a
400µm


b
400µm

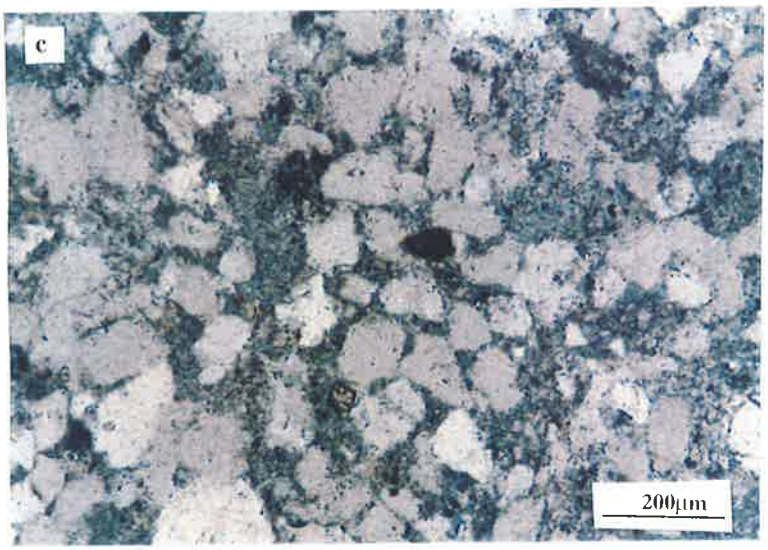
c
200µm


e
20kV X200
100µm 018233

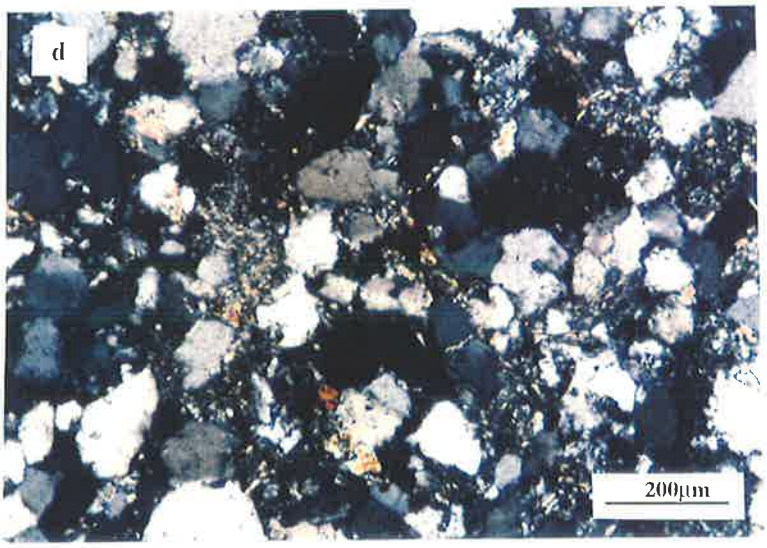
d
200µm


f
20kV X350
50µm 018234

Sample	Porosity (%)	Permeability (mD)	Bulk density (g/cm^3)	Grain size (μm)	Quartz (%)	Clay (%)	Rock fragment (%)	Minor components* (%)
D1	7.3	0.04	2.43	84	60.3	10.1	19.2	3.1
D2	8.5	0.28	2.39	157	65.0	17.4	5.7	3.4
D3	12.5	3.42	2.29	219	68.8	12.0	3.0	3.7
D4	13.0	33.70	2.30	297	70.4	8.7	6.4	1.5
D6	11.2	30.50	2.31	298	69.4	9.5	7.9	2.0
D7	11.9	2.05	2.33	185	67.5	10.0	8.5	2.1
D8	11.2	36.27	2.29	218	75.8	7.0	6.0	0.0
D10	14.9	153.20	2.19	345	66.2	13.7	3.2	2.0
M1	5.0	0.04	2.48	158	77.9	8.0	8.0	1.1
M2	6.5	0.07	2.45	185	72.3	11.5	8.6	1.1
M7	2.6	0.01	2.56	197	68.9	12.0	13.0	3.5
M8	4.0	0.03	2.52	304	69.1	11.5	13.6	1.8
M10	4.1	0.02	2.51	197	72.0	9.6	13.3	1.0
M11	3.4	0.00	2.55	128	70.4	10.5	10.8	4.9
M13	5.1	0.04	2.48	131	70.0	13.3	10.6	1.0
S1	10.5	0.20	2.34	97	58.9	12.5	15.6	2.5
S2	8.9	0.15	2.37	112	58.1	17.0	13.0	3.0
S3	15.6	186.20	2.17	276	69.3	10.1	2.4	2.6
S4	16.6	70.94	2.13	215	61.0	14.4	7.0	1.0
S5	13.9	17.60	2.21	163	68.1	9.0	7.0	2.0
S6	13.6	14.33	2.27	186	67.0	12.0	6.4	1.0
S7	12.6	4.03	2.31	241	65.8	18.9	1.7	1.0

Table 4.3. Petrographical and petrophysical properties of samples used in the study.

*Minor components include mica, carbonate, feldspar, opaque and organic matter.

4.4.4. Diagenesis

Several authors (for example: Schulz-Rojahn (1991), Stuart et al. (1992) and Rezaee (1996)) have studied, in some detail, the petrology and diagenesis of the southern Cooper Basin sandstones. These studies have shown that mechanical and chemical compaction, silicification, kaolinisation and dissolution are the major diagenetic features in Cooper Basin sandstones. These features can also be recognised in samples investigated in the present study. The following is a brief description of the diagenetic features observed in the samples.

Mechanical Compaction

Bent mica flakes and deformed ductile rock fragments indicate mechanical compaction in the samples. Mechanical compaction is more evident in less well-sorted, finer grained rocks particularly those with a high proportion of rock fragments.

Chemical Compaction

Chemical compaction is defined by Houseknecht (1987) as "the bulk volume reduction caused by the dissolution of framework grains at points of contacts". Sutured grain contacts, dissolution seams and stylolites (Figure 4.5a and b) observed in the samples indicate chemical compaction. In general, in southern Cooper Basin reservoir rocks chemical compaction is of lesser importance than mechanical compaction (Stuart et al. 1992).

Silicification

Authigenic quartz represents the most common cement type observed in Cooper Basin sandstones (Stuart et al. 1992). In the studied samples silica cement occurs as syntaxial overgrowths on detrital quartz grains, frequently with euhedral terminations. In thin section, overgrowth are distinguished by euhedral crystal faces (Figure 4.5c), and by dust lining over detrital grains (Figure 4.3a). In SEM, many of quartz grains with overgrowths show rhombohedral and prismatic terminations (Figure 4.5d). The development of quartz cement in same instances is in the form of druse, numerous crystal grown on the surface of a quartz grain (Figure 4.5d). Quartz cementation is more widespread in samples with coarser grains and less clay and rock fragment contents (for example: samples D4, D6, D8, S3, S4). Stuart et al. (1992) commented that the silica required for quartz cementation in the Cooper Basin sandstones was probably derived from framework grain dissolution, clay mineral transformation and chemical compaction.

Clay Authigenesis

Kaolin group clays are the dominant clay mineral in the Cooper Basin sandstones (Stuart et al. 1992). The euhedral habit of kaolinite is indicative of the authigenic origin of this clay type (Figure 4.6a). Two types of authigenic kaolinite exist in the studied samples. These are replacement kaolinite and pore filling kaolinite. Replacement kaolinite is thought to have formed by either complete or partly replacement (dissolution) of an original grain, mostly feldspars and rock fragments (Stuart et. al., (1992) and Rezaee (1996)). In the case

Figure 4.5. Micrographs of Compaction and Silicification

a) Micrograph showing sutured grain boundaries in a well-compacted and well-cemented sample. Sutures represent the combined effect of mechanical and chemical compaction. Sample M2, scale bar = 200 μm.

b) SEM view of sutured grain contacts due to chemical compaction (white arrow). Sample D4, scale bar = 50 μm

c) Micrograph of silica cement showing euhedral faces (arrows) of quarts overgrowth. Sample S3, scale bar = 200 μm.

d) SEM view of silica cement showing well-developed quartz overgrowth in the forms of single large quartz prisms (upper arrow) and druse, numerous crystal grown on the surface of a quartz grain (lower arrow). Sample D4, scale bar = 100 μm.

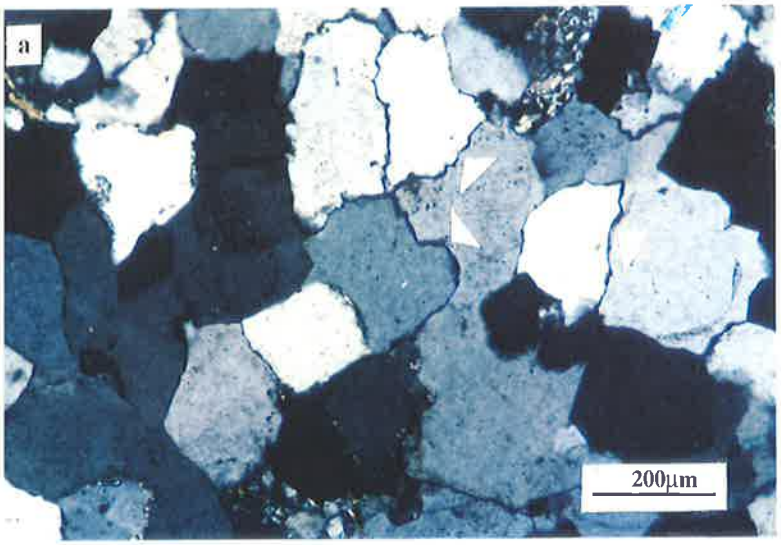
a
200μm

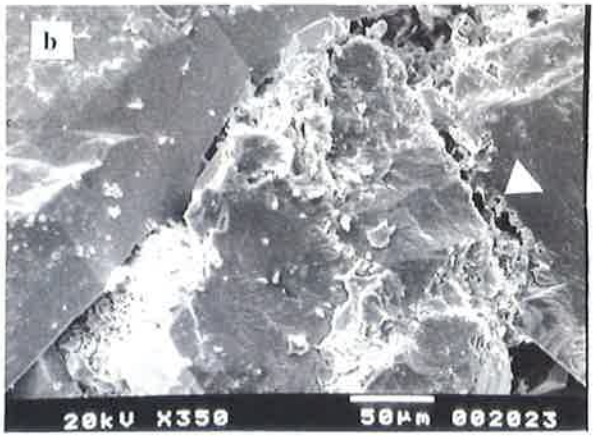
b
20kV X350
50μm 002023

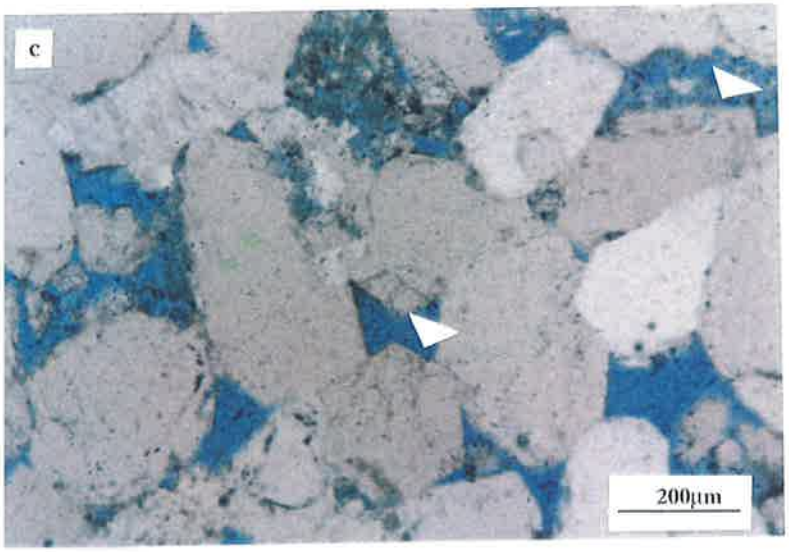
c
200μm

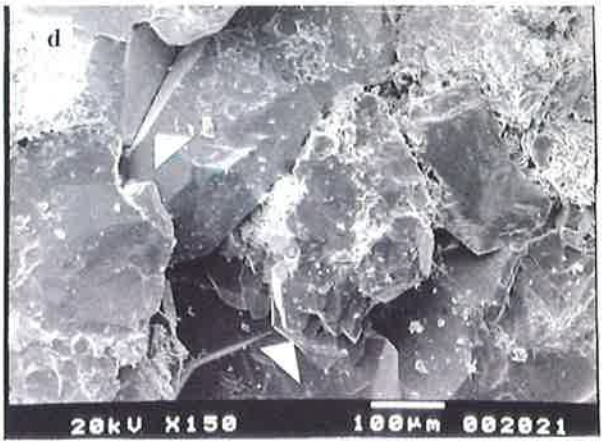
d
20kV X150
100μm 002021

of complete replacement, this kind of kaoloinite shows the exact margin of the original grains (Figure 4.6b). Pore filling and dispersive kaolinite is thought to have participated directly from the pore fluids (Wilson and Pittman, 1977). This type of kaolinite, which is coarser-grained, shows less packing and is intergrown with the quartz overgrowths (Figure 4.6.c and d). The occurrence kaolinite in the samples is mostly in the form of pore filling and dispersive type. The authigenic illite is thought to have largely formed from the alteration of unstable rock fragments (Rezaee, 1996).

4.5. Pore Types

4.5.1. Petrographic Classification

The classification of porosity type suggested by Pittman and Thomas (1979) is commonly used for describing pore types in reservoir sandstones. The Pittman classification is based on both the observed geometry and the origin of pores. Using Pittman's terminology, three types pores are recognised in Cooper Basin sandstones (Stuart et al. 1992). These include primary, secondary (dissolution) and micropores. Primary pores are dominant in moderate to well-sorted sandstones with no or minor amounts of ductile rock fragments (Figure 4.5a and 4.7a). In these rocks primary porosity is preserved due to early quartz cementation which provides a rigid framework that prevents mechanical compaction. Samples characterised by abundant primary pores have core porosities normally greater than 10% and permeability higher than 10 mD. This type of pore is easily recognisable and often there is a good agreement between total porosity estimated from thin section and core porosity in samples with abundant primary pores.

Secondary (dissolution) pores are distinguished by the presence of oversized pores, irregular or elongate pore spaces (Figure 4.7b). Secondary pores are the products of dissolution of unstable grains or the enlargement of the preexisting porosity by dissolution of the margin grains.

Microporosity is defined as including all pore spaces associated with clay minerals. These type of pores in the studied samples are mostly associated with authigenic kaolinite (Figure 4.7c). Individual kaolin pore diameter is less than 10 μm and therefore micropores are hardly distinguishable under the working magnification range of ordinary polarized microscopes (Figure 4.7d). This type of pore is abundant in samples with high clay content

Figure 4.6. Micrographs of Kaolinite

a) SEM view of pore-filling, euhedral kaolinite booklets suggesting an authigenic origin. Notice the well-developed micropores between the kaolinite booklets. Sample S3, scale bar = 10 μm.

b) Micrograph of the complete replacement of an original grains by kaolinite. Notice the original marginal of precursor grains. Sample D4, scale bar = 400 μm.

c) Pore filling kaolinite with a significant amount of microporosity (blue epoxy). Sample D4, scale bar = 200 μm.

d) Precipitation of kaolinite in pore spaces and adjacent pore throats, which reduces porosity and permeability. Intergrowth of kaolinite and quartz overgrowth is evident from jagged contacts. Sample D8, scale bar = 10μm.


a
20kV X750
10µm 002416

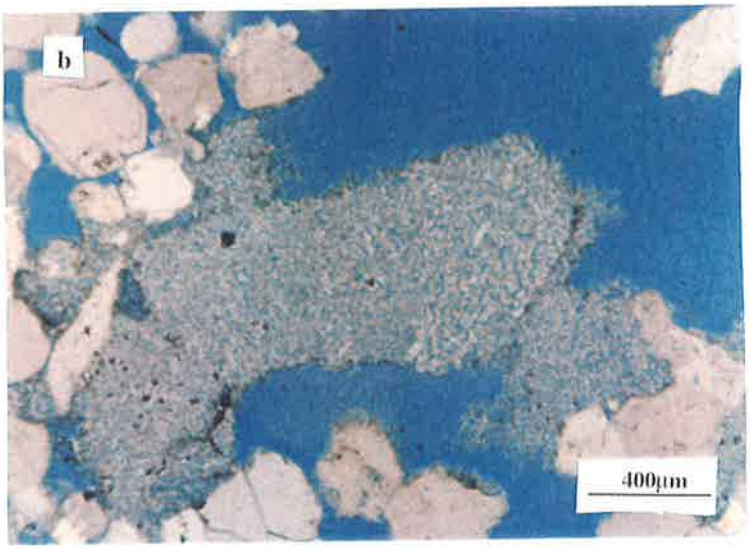
b
400µm

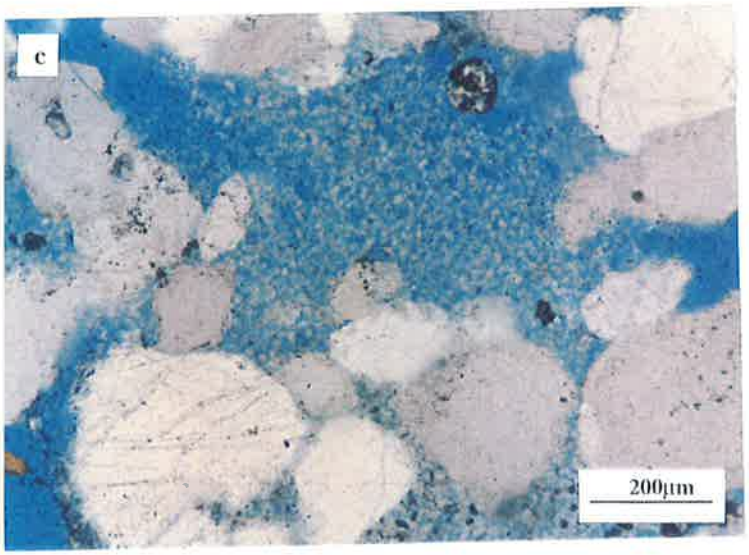
c
200µm


d
20kV X750
10µm 018229

Figure 4.7. Micrographs of Pore Types

a) SEM view of primary pores in a moderately sorted sample. Primary pores survive between the euhedral faces of quartz cement. Sample D8, scale bar = 100 μm.

b) Micrograph of secondary (dissolution) pores. Notice the irregular and oversized nature of the pore (arrow). The edges of original grains are still recognisable. Sample D8, scale bar = 400 μm.

c) Micrographs of clay associated pores (micropores). Sample D4, scale bar = 400μm.

d) SEM view showing abundant micropores in a kaolinite aggregate. Sample S3, scale bar = 1000 μm.


a
20kV X75
100µm 018228

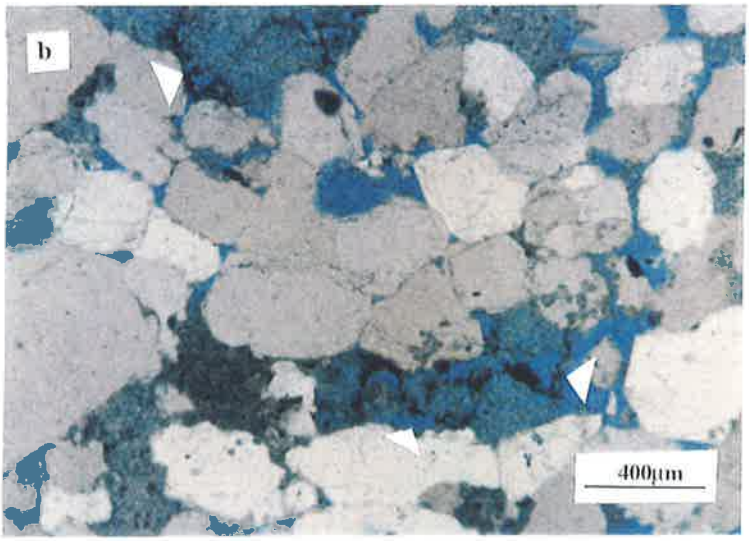
b
400µm

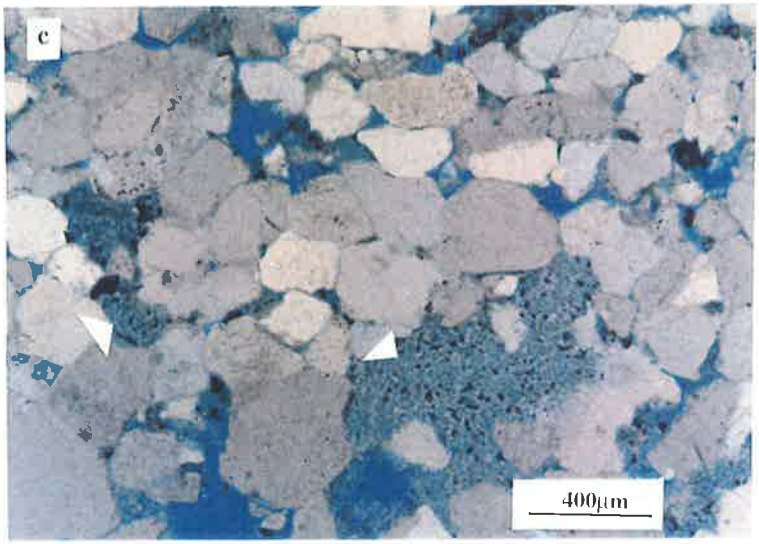
c
400µm

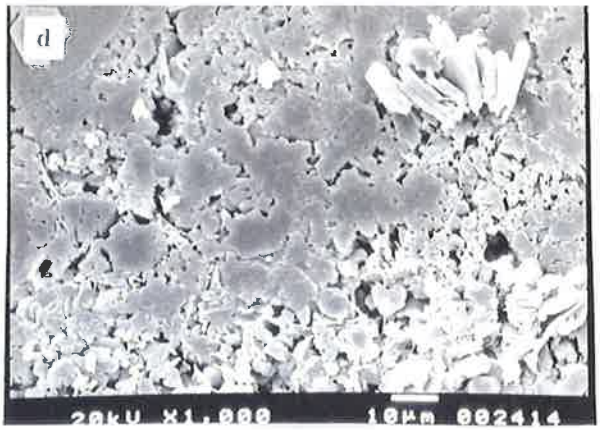
d
20kV X1,000
10µm 002414

with abundant ductile rock fragments. Samples dominated by microporosity have core porosities as high as 10% but core permeability is limited to less than few millidarcies.

4.5.2. Petrophysical Classification

The pore type classification presented above which is based on petrographical observation and the parageneses of pores, is aimed at describing the reservoir quality of samples. To develop a relationship between various physical properties (for example acoustic properties) and reservoir rock properties (for example porosity and permeability) it is necessary to consider a terminology and classification based on the petrophysical behaviour of the rock. For instance it is known that crack-like pores or low aspect ratio pores in sandstones significantly affect the propagation of elastic waves in rocks (see Chapter 3) and yet this type of pore is not adequately addressed by petrographical classification.

The terminology used in petrographical classification of pore types was found to be lacking for the purpose of the present study. Caruso et al. (1985) demonstrated a pore type classification in sandstones by considering crack-like pores as a separate pore class. Their pore type classification is based on observed features of pores alone, without considering the petrological origin of different pore types. Using the Caruso et al. (1985) terminology, three types of pores may be recognised by considering the size, shape and relation to others. There are macro pores (intergranular), micropores and connective pores. Figure 4.8 shows each pore type.

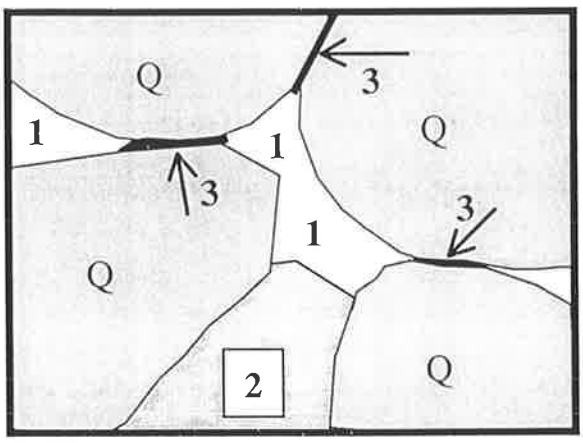

Figure 4.8. Schematic representation of petrophysical classification of the pore types in sandstone with dominant quartz (Q) grain; Macropores (1), Clay associated pores (2), Connective pores (3).

Figure 4.9. Micrographs of Connective Pores

a) Clay-free and straight-line connective pores. Notice the termination of all low aspect ratio pores to a pore with a relatively larger aspect ratio. Sample D6, scale bar = 50 μm.

b) Clay-free connective pores adjacent to a high aspect ratio pore (macropore). Sample D6, scale bar = 100 μm.

c) Clay-free and straight-line connective pore at the loose contact of euhedral faces of quartz overgrowths. Sample D4, scale bar = 50 μm.

d) Combination clay-free and clay-filled (arrows) connective pores. Sample D4, scale bar = 100 μm.

e) Clay-filled (illite) connective pores and macropores. Sample M10, scale bar = 50 μm.

f) Clay-filled (kaolinite) connective pore. Sample D4, scale bar = 50 μm.

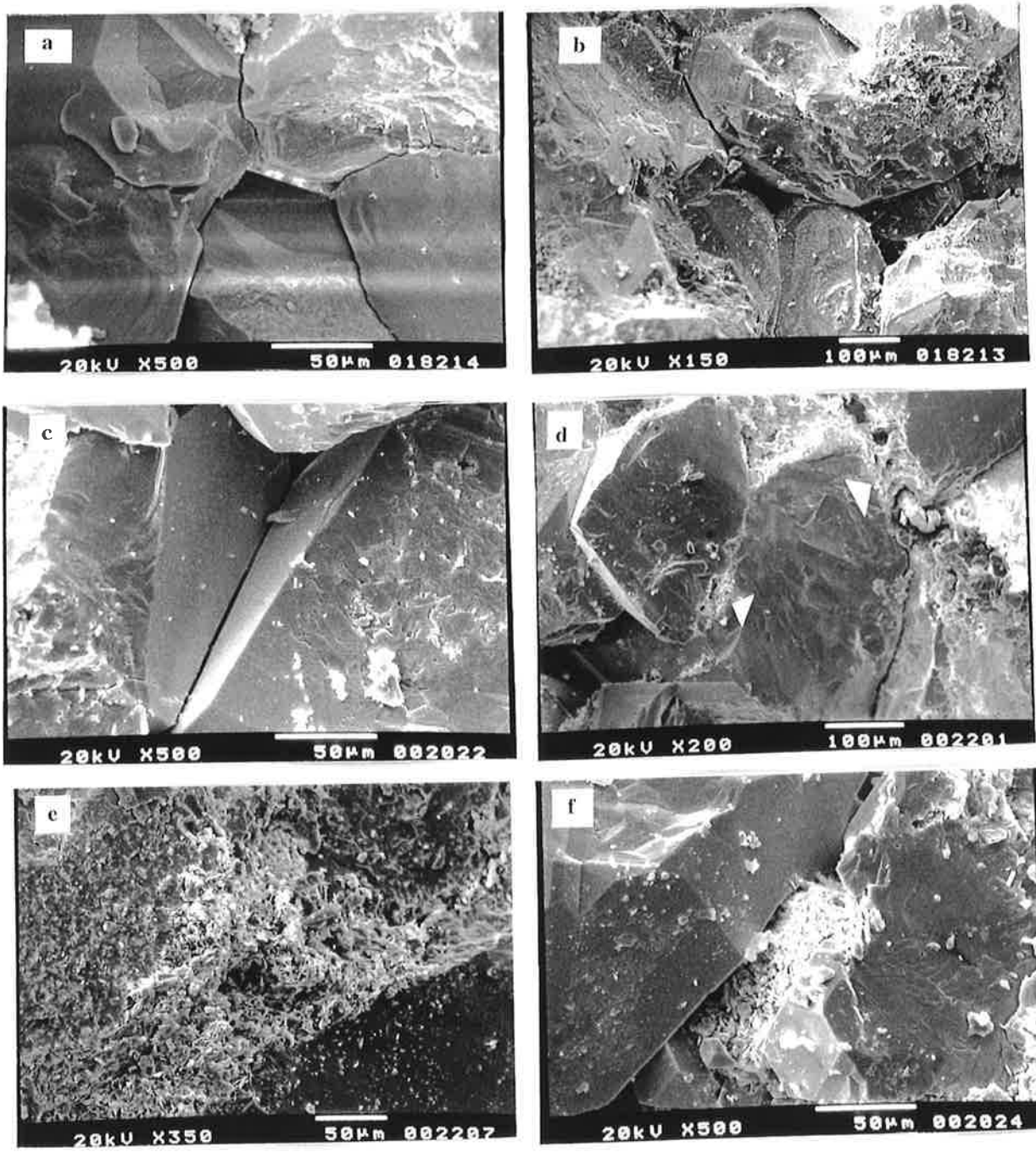
a
20kV X500 50µm 018214
b
20kV X150 100µm 018213
c
20kV X500 50µm 002022
d
20kV X200 100µm 002201
e
20kV X350 50µm 002207
f
20kV X500 50µm 002024

In the studied samples macropores are relatively large in size (greater than 50 μm), irregular shaped with aspect ratio between 1 and 0.1. This pore type includes both large primary pores and secondary pores in Pittman's classification. Macropores appear to be the dominant pore type in samples S3, S4, S6, D3, D4, D6, D8. Micropores are defined as pores with dimensions equal to or less than a few microns and basically are clay-associated pores as discussed in previous section. Micropore is the dominant pore type in samples S1, S2, S5, D1, D2, M1, M2, M7 M8, M10, M11, M13.

Connective pores often have one dimension much less than the other and can therefore be considered low aspect ratio or crack-like pores (in a two dimensional view) with aspect ratios between 0.1 and 0.001. Connective pores could either extend between macropores and act as pore throat (in a three dimensional view), or occur at the contact between quartz grains with connection to another other low aspect ratio pore. Samples with high silica cement appear to have a greater number of clay-free and straight-line connective pores (Figure 4.9a-c). In contrast, in samples with higher proportion of ductile rock fragments (pseudmatrix), connective pores are mostly filled by clay and squashed particles (Figure 4.9 d-f). Connective pores in the studied samples mainly occur at loose grain contacts and have a very small contribution to the total rock porosity.

4.6. Core Porosity

4.4.1. Helium Porosimetry

An Edinburgh Petroleum Equipment Ltd. Helium Gas Expansion Porosimeter, Mark II was used to measure the porosities of core plug samples. The principle of operation of the Porosimeter is based on Boyle's Law assuming that helium behaves as an ideal gas at room temperature. A reference chamber containing helium (volume v_r, pressure p_r) is allowed to expand into the sample chamber (volume v_s) causing the pressure to fall p'. According to Boyle's Law:

$$p_r v_r = p' (v_r + v_s - v_m) \qquad (4.2)$$

where v_m is the grain (solid) volume of the sample. By knowing the dry mass of the sample (m_d) and rearranging equation 4.2 for v_m, then the grain density (ρ_m) can be found from:

$$\rho_m = m_d/v_m \qquad (4.3)$$

The porosity $\phi$is given by:

$$\phi = (v_t - v_m)/v_t \qquad (4.4)$$

where v_t is the bulk volume of the sample, which can be calculated from measurements of its length of and radius. A digital top-pan balance with an accuracy of ±0.1 mg was used for the measurement of samples masses. The measured helium porosity of the samples ranges from 2.6% to 16.6%. The accuracy of porosity measurements using this apparatus is quoted as being ± 0.1 porosity unit (Jones, 1996).

4.6.2. Porosity versus Stress

The variation of core porosity with confining stress was investigated for a sub-set of samples. An experimental technique developed by the geophysical group of the PRIS was used to measure porosity as a function of confining stress. This technique, which was first used by Jones (1996), measures the quantity of water squeezed out of each water-saturated sample with the increase of confining stress. The apertures used for these experiments is basically an adaptation of the system used for ultrasonic measurements which will be described in more detail in Chapter 5.

The pore-fluid pipe on the lower transducer assembly (Figure 5.1) is connected to a T-junction, with one side connected to the pore fluid reservoir pump and other side connected to a pipe attatched to graduated dispensing-pipette gauge. The fluid flow to and from each side of the T-junction is controlled using separate screw valves. The rock sample is initially held at a confining stress of less than 1 MPa and the gauge valve is shut while the pore fluid is pumped into the rock to dissolve any trapped air. The pore-fluid pump valve is then closed and the gauge valve is opened to allowed the pore fluid through to the gauge pipe. The water level in the pipette is allowed to equilibrate and is monitored as the confining stress increases. The water level can be converted into porosity by assuming that the total volume of water injected from the rock under pressure in equivalent to the volume of pore closed. In general volume reduction under stress for the samples is not significant

compared with the core volume under ambient conditions. Table 4.4. lists the core porosities measured under a range of confining stress for the selected samples

4.7. Nitrogen Permeability

The permeabilities of the samples were measured using a nitrogen gas permeameter constructed at the PRIS. A gas permeameter measures the flow rate Q of nitrogen through a sample, caused by a known pressure fall Δp across the thickness L. The fluid-flow relationship is given by Darcy's law:

$$Q = (K.A\ \Delta p)/(\eta\ L) \tag{4.5}$$

where K is the permeability, A is the surface area of the sample, and η is the viscosity (0.0175 cP for nitrogen gas). The relationship between gas permeability (K_g) and liquid permeability (K_l) is investigated by Klinkenberg (1941), and is given by:

$$K_g = K_l\ (1 + b/p) \tag{4.6}$$

where p is the mean pressure, and b is a constant which is dependent on the pore size. Hence, it is possible to deduce the liquid permeability from the nitrogen gas permeameter. In practice, this is done by measuring the nitrogen permeability of a sample at several pressure fall points and then plotting these against the reciprocal of pressure. The equivalent liquid permeability is given where the graph intersects the ordinate axis.

The core plug samples were placed inside a Hassler cell, and a confining pressure of 2 MPa was exerted on the sleeve to prevent side leaks. The pressure gradient was adjusted by inlet-pressure and back-pressure regulators up to 0.65 MPa. Using this technique, permeabilities can be measured in the range of 0.01 mD to 10 D, with a precession of about 2% for samples having permeabilities of more than 0.05 mD (Assefa, 1994). The equivalent liquid permeability of the samples used in current study varies from 0.003 mD to 186.2 mD. Helium porosity and nitrogen permeability were measured on vacuumed dry core plugs. Helium porosity, grain density and equivalent liquid permeability of the samples are listed in Table 4.3.

Stress	D2	D4	D6	D10	M2	M8	S1	S3
5	7.93	12.35	10.76	14.47	6.39	3.94	10.22	15.26
10	7.52	12.02	10.61	14.24	6.27	3.86	9.69	15.04
20	7.09	11.84	10.39	13.95	6.10	3.78	9.48	14.72
30	6.93	11.73	10.29	13.82	6.06	3.74	9.35	14.60
40	6.83	11.64	10.23	13.71	6.01	3.69	9.24	14.49
50	6.70	11.52	10.17	13.59	5.97	3.66	9.17	14.38
60	6.61	11.43	10.09	13.49	5.92	3.62	9.11	14.29

Table 4.4. Core porosity (%) measured under elevated confining stress (MPa) for a subset of samples.

Chapter 5

Experimental Techniques

5.1. Introduction

This chapter describes the experimental techniques used for measuring the acoustic properties of the Cooper Basin core samples. The techniques described include the ultrasonic system for acoustic measurement, the sample preparation procedure, and data processing.

5.2. Measurement Technique and Equipment

5.2.1. Ultrasonic System

The velocity and attenuation of elastic waves were measured using an ultrasonic reflection technique devised by Winkler and Plona (1982) and implemented by McCann and Sothcott (1992). Figures 5.1 and 5.2 illustrate the reflection system. The rock sample is placed between two cylindrical perspex buffer rods. An ultrasonic transducer transmits a signal, which is partially reflected from the top and base of the sample and the arrivals are displayed on an oscilloscope. The length and the choice of material for the buffer rods are important in the reflection system. They are designed to produce a time window for arrival of the sample reflections so that no other reflections (for example, from the base of the lower buffer rod) interfere with the sample reflections. Perspex has a relatively low velocity and relatively high attenuation. The low velocity of perspex allows the required time window to be provided by a 5-cm length. The high attenuation of perspex reduces unwanted reverberation such as sidewall reflections (Section 5.4) so that the direct sample reflections may be clearly detected. A rubber jacket encloses the system and axial and radial hydraulic presses apply hydrostatic stress. Pore pressure is controlled separately via an inlet to one face of the rock.

For single frequency (f) measurements, velocities can be calculated from:

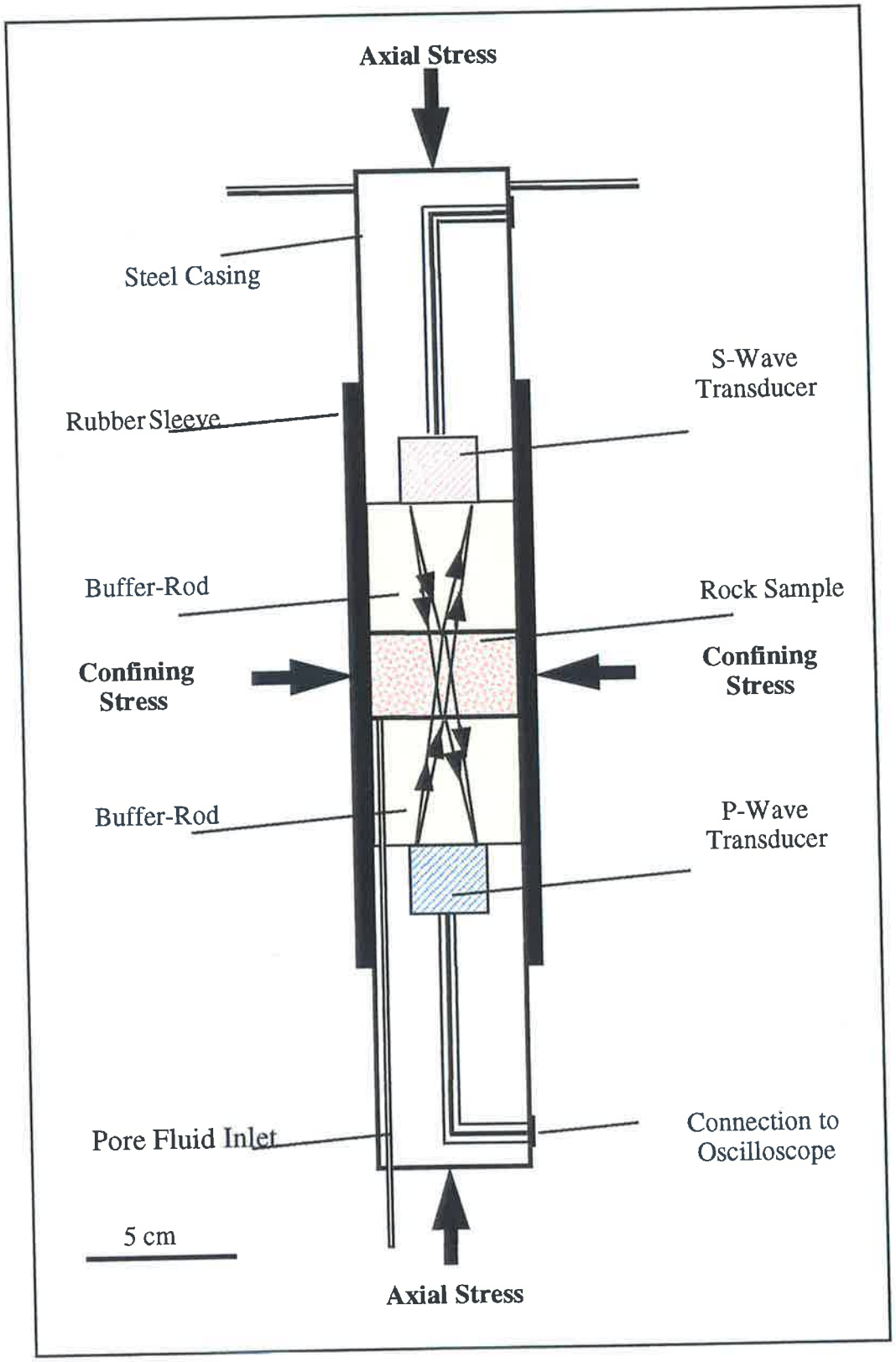

Figure 5.1. Schematic diagram of the reflection technique used for measuring acoustic velocity and attenuation in rocks.

$$V(f) = \Delta x/\Delta t \qquad (5.1)$$

where Δx and Δt are the differences between the path lengths and travel times between the two pulses. For broadband measurements, velocities are calculated from:

$$V(f) = 2\pi fL/\Delta\varphi \qquad (5.2)$$

where L is the sample length, and $\Delta\varphi$ is the phase difference between the two pulses (Winkler and Plona, 1982). In both cases the velocities must be corrected for the phase diffraction and effects of the transducer (section 5.4). The attenuation coefficient, a, is computed by the spectral ratio method and is given by:

$$a = (8.686/2L) \ln \{[1 - R^2(f)]\, A_1(f)/A_2(f)\} \qquad (5.3)$$

where $A_1(f)$ and $A_2(f)$ are the amplitude of the top and bottom reflections, respectively, and R(f) is the reflection coefficient of the rock and buffer rod interface. Equation 5.3 corrects for the effects of partial reflection at the rock/buffer-rod interfaces and the unit of a is given in dB/unit length. The attenuation coefficient must be corrected for the effects of wave diffraction. The dimensionless quality factor, Q, is derived from the relationship;

$$Q = 8.686\pi f/Va \qquad (5.4)$$

After correcting for diffraction effects (Section 5.4), velocities and attenuation measured by this reflection method are accurate to ± 0.3% and ± 0.1 dB/cm at 0.85 MHz.

5.2.2. Hydraulic Pressure Cell

An integrated Technology Resource Ltd, (ITR) Triaxial Hoek cell (serial no. 00050/901) (shown in Figure 5.3) was used to exert confining stress on the sample/transducer assembly. The Hoek cell consists of a hollow stainless steel cylinder 16 cm in diameter and 27 cm in length, with two stainless steel threaded annular end-caps. A hollow I-shaped rubber sleeve with an internal diameter of 5 cm is fitted inside the vessel. The space between the sleeve and the wall of the pressure vessel contains an oil reservoir, and is connected to an external hydraulic pump (Enerpac type P 80 D c9B) and Budenberg

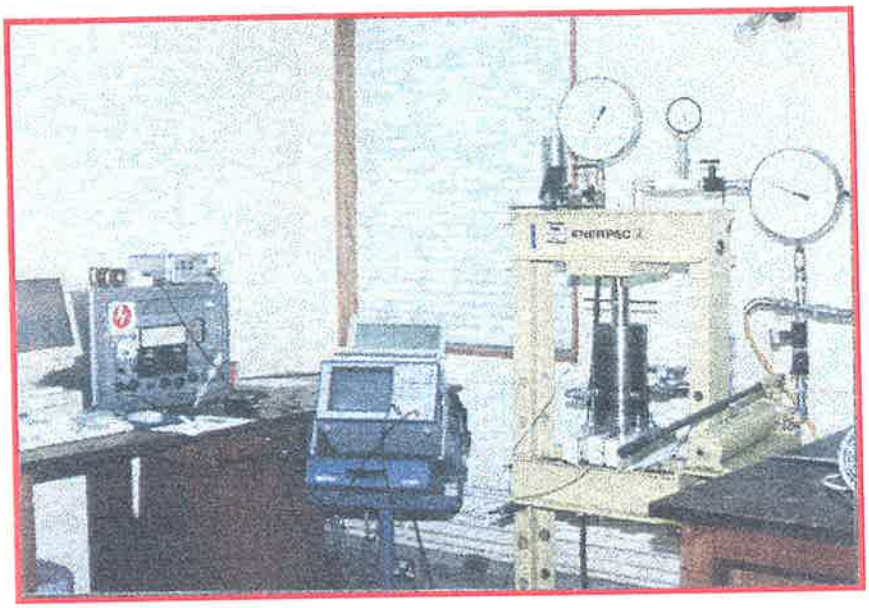

Figure 5.2. Photograph of the ultrasonic system and equipment in operation. From left to right: the Arenberg pulse generator (large grey box on bench); the Avtech pulse generator (small box to the left of the Arenberg); the LeCroy digital oscilloscope and the IBM laptop computer (on top of the oscilloscope); the ITR rig and Enerpac hydraulic press (yellow); the hand-pump for applying the pore pressure (on top of the press); the ITR high pressure Hoek cell and ultrasonic assembly (in middle of ITR rig) and the hand-pump for applying the confining pressure (yellow).

Figure 5.3. Dismantled ITR high-pressure Hoek cell.

pressure gauge. The pump provides confining stress to the assembly via the rubber sleeve, and also provides axial stress through an external ram attatched to an Enerpac pressure-rig. Thus a uniform hydrostatic stress can be maintained around the sample. The vessel has a maximum working pressure of 70 MPa. Fluid-saturated samples can be measured at any desired pore pressure as long as the pore pressure is less than confining stress.

5.2.3. Pulse Generators

Two pulse generators were used; one producing a single frequency and the other a broadband (transient) pulse. An Arenberg type PG-650C generator (serial no. 851) was used to generate single-frequency toneburst (flat-topped) sinusoidal pulses with variable signal lengths. Frequency ranges were varied by changing a tuner coil. The frequencies used in the experiments were from 0.8 MHz to 1 MHz for P-waves and from 0.55 MHz to 0.75 MHz for S-waves. For broadband signals, an Avtech type A VR-1-PW-C-P pulse generator (serial no. 5506) was used, which provides pulses with frequency spectra of 0.5 MHz to 1 MHz. The reflections from the top and the base of the sample were stored Figure 5.4 shows the typical oscilloscope traces for P-waves using the two pulse generators.

5.2.4. Transducers

The ultrasonic transducer used in all experiments were Panametrics type V102 for P-waves and Panametrics type V152 for S-waves with nominal frequency 1 MHz. Both consist of a cylindrical stainless steel casting with a wear plate on the front face. The casting encloses a buffered piezoelectric crystal element, which is electrically connected to an external fitting. Both transducers have broadband characteristics and are heavily damped. The P-wave transducer has a diameter of 20 mm and the S-wave transducer has one of 25.4 mm.

Two types of couplants were used to ensure a good contact between transducers and the buffer-rods. The P-wave couplant was a water based gel (Sonatrace, manufactured by Diagnostic Sonar Ltd.) which has useable temperature range of -2°C to 66°C. The S-wave couplant was a highly viscous honey-based compound (SWC 1, manufactured by Diagnostic Sonar Ltd.) with a maximum useable temperature of about 22°C. The laboratory was air-conditioned to ensure that temperature was held at about 20°C. the S-wave couplant also breaks down in the presence of water. Therefore a gasket sealer (Hermetite non-hardening fluid) was applied at the contact between the buffer-rod and S-

wave transducer housing assembly, to prevent water invasion during experiments on saturated samples.

5.2.5. Recording Equipment

The signal reflections were received by the transducer and displayed on a LeCroy type 9400A Digital Oscilloscope (serial no. 9339) with a vertical and horizontal resolution of 1024 pixel. For single-frequency pulses, the travel time, frequency and amplitude of the traces were measured by selecting the third peak from the first (top) reflection and the corresponding third trough from the second (bottom) reflection (in order to account for the phase reversal of the latter (Figure 5.4a). To maximise the accuracy of these measurements, the horizontal (time) axis was set on 50 ns/cm, and the vertical (amplitude) axis was expanded to between 5 mV/cm and 50 mV/cm. This allowed arrival times and amplitude to be measured with a precision of ±1 ns and ±0.01 mV, respectively. For each measurement signals were stacked 1000 times to improve the signal to noise ratio. This procedure was repeated twice for every measurement.

For broadband data, the amplitude of pulses from top and bottom reflections were optimised by adjusting the amplitude control on the Avtech signal generator. The pulse width of the top reflection was adjusted to minimise the pulse rise time. The amplitude of each pulse was maximised by adjusting the oscilloscope gain, and each trace was displayed in turn with the time base set to 1 μs/cm for P-waves and 2 μs/cm for S-waves. Each trace was then stacked 20 times and the stacked traces were stored on a floppy disk using an IBM PC Convertible type 5140-002.

5.3. Sample Preparation

5.3.1. Production of Core Plugs

Cylindrical core plugs of 4.7 cm diameter were drilled parallel to the bedding plane from semi-cylindrical core slabs (9 cm diameter), taken from the Cooper Basin wells, using a water-cooled diamond-tipped coring bit. Since only 4 cm-thick core slabs were available for the study all samples were cored only in one direction with respect to the bedding plane. The core plugs were then cut perpendicularly to their long axes using a Wolfgang Conrad 50/20 diamond circular saw, leaving a length approximately 21 mm on each core plug. The faces of core plugs were then ground flat and parallel to ±3 μm using a Jones and

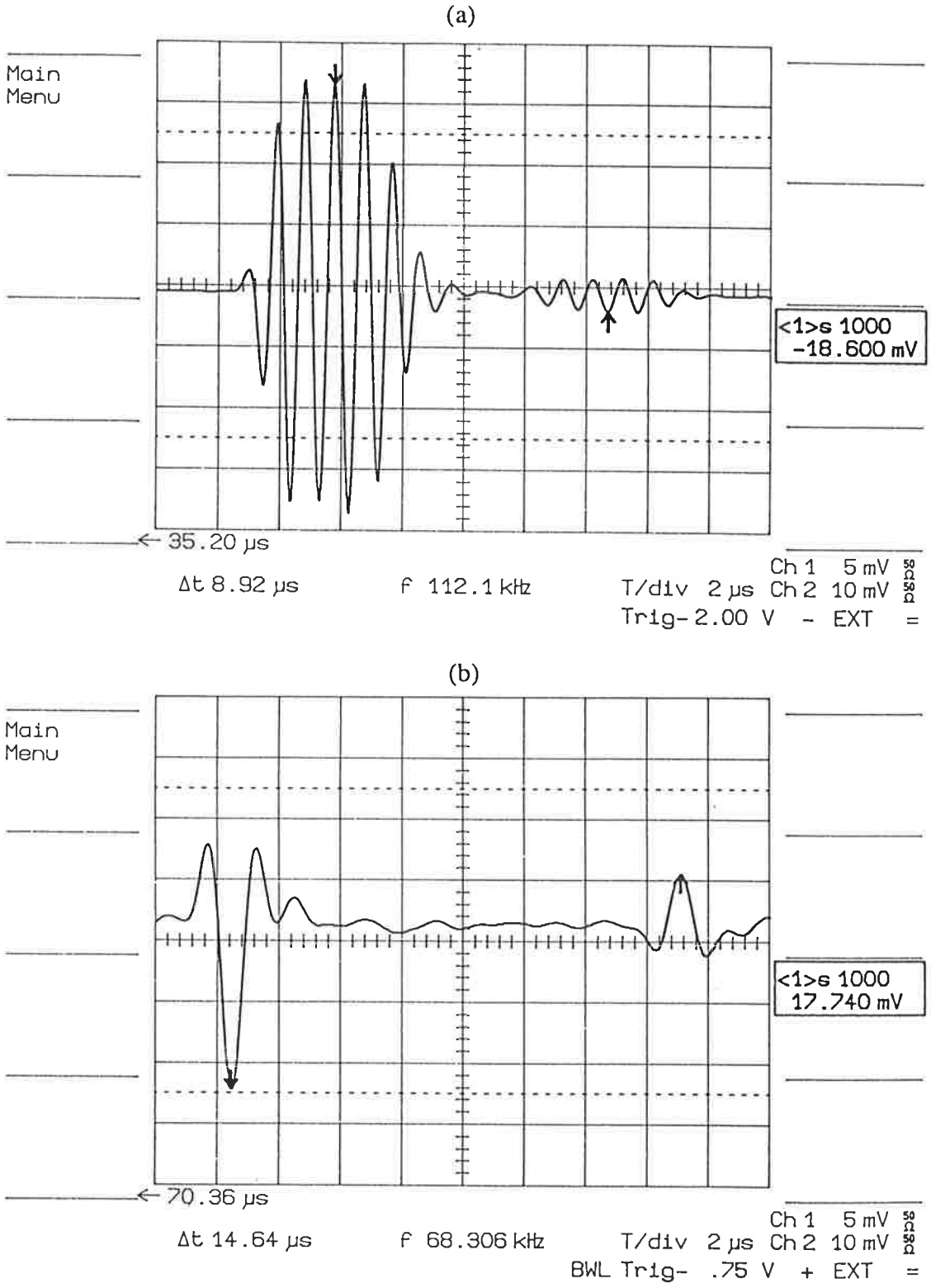

Figure 5.4. Typical oscilloscope traces. (a) Single frequency P-wave traces obtained from the Arenberg pulse generator. The first and second five reflections are the reflections from the top and base of the sample. The arrows show the third positive and corresponded negative peaks used for the measurement of travel time (Δt). (b) Broadband P-wave traces obtained from the Avtech pulse generator showing reflections from the top (negative peak) and the base (positive peak) of sample.

Shipman type 540 surface grinder. It is the high degree of parallelism of these samples that enables the velocity and attenuation to be measured with the degree of accuracy achieved here. All samples were oven-dried at 40°C for several days. Each final sample thickness at room temperature and pressure was determined by multiple measurements with micrometer (±1μm) and diameter was determined by caliper to ± 10μm.

5.3.2. Drying and Saturating Method

The oven-dried core plugs were transferred to a vacuum vessel and evacuated to about 10^{-4} Pa, for several days to boil out any residual volatile. The vacuumed samples were then saturated with dry air and stored at a constant temperature of 40°C until they were needed for the acoustic measurements. In order to produce fully water-saturated samples when vacuuming was completed, the cores were flooded with distilled, de-ionized and de-aired water. To ensure a uniform distribution of water in the pore spaces of the sample, the vacuum vessel was pressurized to 7 MPa and allowed to stand until no pressure drop was noticed. The water-saturated plugs were then stored in a closed jar of de-aired and distilled water.

5.3.3. Partial Saturation Technique

There are number of methods for producing partial saturation in rock samples. Each technique results in a different distribution of the pore fluid with the rock and some produce heterogeneous saturation. Heterogeneous saturation could result in differing relationships between acoustic properties and saturation (Bourbie et al. 1987). The porous plate technique was chosen to produce partially water-saturated samples in the present study. Details of the porous plate extraction technique can be found in the literature (for example, Maerefat et al. 1990). The following is a brief description of the technique.

5.3.3.1. Porous plate Extraction Technique

Porous plate extraction utilises a permeable ceramic membrane to produce a controlled desaturation of a rock sample. It is widely used in soil science research and on cores in the petroleum industry for capillary pressure studies. It is believed to produce a relatively homogeneous distribution of pore fluids within a sample between the dry and saturated states and simulates the conditions found in situ (Maerefat et al. 1990). Jones (1996) used a porous plate extraction technique to produce partially saturated samples in his PhD study on acoustic properties of sandstones. Figure 5.5 shows the apparatus used for the porous

Figure 5.5. Photograph of pressure vessels used for the porous plate extraction technique.

plate extraction. The two principal features of the system are a pressure vessel and an unglazed porous ceramic pressure plate, which is placed inside the vessel (Figure 5.6).

The pressure vessels and ceramic plates were manufactured by Soilmoisture Equipment Corp. The vessels used were models 1500 and 1600 for maximum working pressures of 1.5 MPa and 0.5 MPa, respectively. Attached to the underside of the ceramic plate is a double-mesh wire screen and a neoprene skirt sealed to the rim of the plate. The underside of the plate is held at atmospheric pressure through a small vent, which is connected to the drainage tube on the outside of the vessel. The plate itself contains cylindrical capillaries with radii characteristic of the maximum working pressure of the plate. Once saturated, the non-wetting fluid phase (nitrogen) can not enter the plate below this threshold pressure. Three types of plate were used, with maximum working pressures of 0.1 MPa, 0.5 MPa and 1.5 MPa. High pressure plates have capillaries of smaller diameters than low-pressure plates and hence draw the wetting fluid through them more slowly. In order to minimise the equilibration time for the rock samples, the plate with lowest pressure rating above the inlet pressure was used.

The samples were hydraulically coupled to the plate using a saturated kaolinite paste, which was prevented from invading the rock pores by placing wetted filter paper (Whatman No.1) between the sample and paste. Good coupling ensures that the non-wetting phase can not enter the contact region and inhibit the desaturation process. Moderate stress was applied to each sample by a lead weight placed on a wire gauze. The samples were in equilibrium with water vapor from several water dishes placed inside the pressure vessel. With the exception of the pore fluid within the samples, all water used in the porous plate extraction technique contained 1% methanal (formaldehyde) to inhibit bacterial grown inside the vessel.

In each experiment the pressure vessel was sealed and nitrogen gas admitted through the side inlet at a fixed pressure. This sets up a pressure gradient across the plate, which draws the wetting phase from rock samples and through the plate. The pressure front drives the wetting phase through pores with radii greater than a critical value (dependent on the capillary pressure), and after some time each sample reaches equilibrium with the plate and the desaturation process stops. The point of equilibrium can not be determined absolutely, but was assumed to have occurred when the mass of water collected from the drainage tube

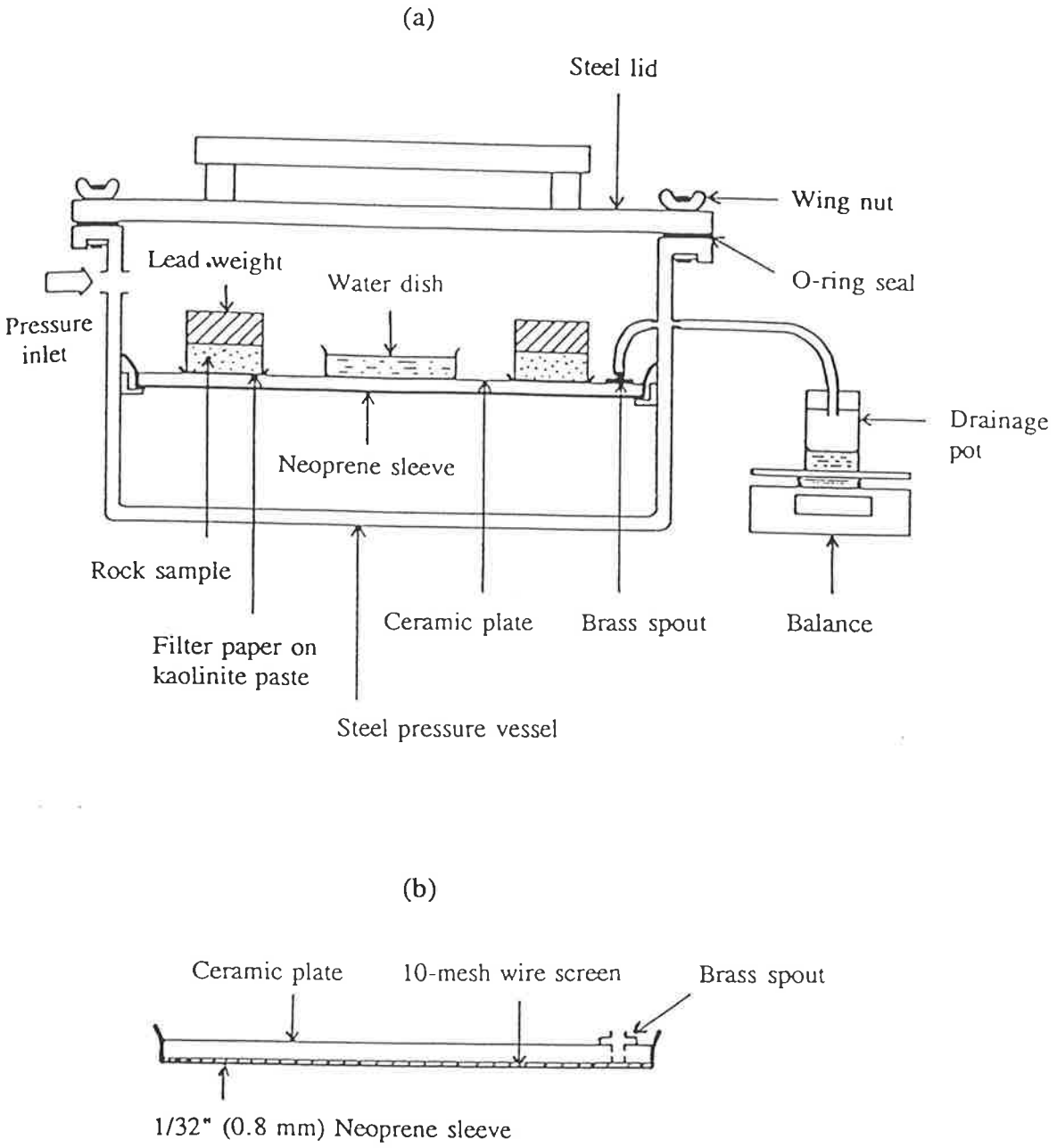

Figure 5.6. Schematic diagrams of equipment used in the porous plate extraction technique. (a) Pressure vessel, (b) Porous plate (after Jones, 1996).

remained unchanged for several days. Once equilibrium was established the pressure inside the vessel slowly returned to atmospheric, with the drainage tube sealed to prevent the sample imbibing water from the plate. Each sample in turn was removed from the vessel, weighed, and the acoustic properties measured over a range of effective stresses. The sample was then reweighed and returned to the pressure vessel. After all samples in the vessel have been measured in this way, the inlet pressure was increased to further the desaturation process. This procedure was repeated several times until the samples reached their irreducible saturation.

The principal advantage of the porous plate is that it can provide a macroscopically homogeneous distribution of the wetting phase throughout the rock (Maerefat et al., 1990). The main disadvantage of this technique is that it is a time consuming process particularly for low permeability rocks. Furthermore, if the pressure vessel contains more than one sample, the samples may have different capillary pressures and therefore show different saturation for a particular inlet pressure. In this case the samples must be removed from the vessel, more frequently, in order to calculate their saturation. To minimise the disruption to the desaturation processes in the present study, low porosity and low permeability samples were desaturated in a separate pressure vessel. It was necessary for the samples to be removed in order to perform the acoustic measurements. Regular handling and experimentation may result in sample grain loss, which can lead to errors in the calculation of the degree of saturation. This is less critical for the Cooper Basin samples used here since they are hard and well cemented rocks.

5.3.3.2. Saturating the Porous Plate

The ceramic plates used in the porous plate extraction technique are strongly hydrophilic, and may be saturated under relatively low inlet pressure. The plate was positioned inside the vessel and water containing 1% methanal was filled up to the level of the neoprene skirt. The pressure vessel was sealed and a low inlet pressure was applied in order to allow the water to invade the plate. The plate was initially flushed with water to remove any particulate debris in the capillaries.

5.3.3.3. Measuring Sample Saturation

Sample saturation was measured using a gravimetric technique, which has reasonable accuracy when grain loss is minimal. All samples were weighed to an accuracy of $\pm$ 0.01 g

in their vacuum-dried states (m_d) before the experiment began, and before and after each set of acoustic measurements. The mean value of the latter was taken to represent the partially saturated mass (m_{ps}), and the fractional water saturation Sw was calculated from:

$$Sw = (m_{ps} - m_d)/\rho_w v_{pore} \qquad (5.5)$$

where v_{pore} is the pore volume (cm^3) determined from the helium porosimetry (with an accuracy of $\pm$ 0.1 cm^3), and ρ_w is the density of water (1.00 g/cm^3). Assuming an accuracy of $\pm$ 0.1 cm^3 for v_{pore} values, the error involved in Sw values calculated from equation 5.5 may be as high as 2.6% in a sample with 10% porosity and 82.27g weight at dry condition.

5.4. Diffraction and Geometric Corrections

Extrinsic effects including geometrical spreading and diffraction losses in acoustic measurements using a reflection method must be corrected for if they are found to be significant. Both effects are inherent in a system using high frequencies and small samples and can lead to distortion of both the amplitude and phase of the signal. In this section these effects are examined and corrections are given for acoustic measurements carried out by the reflection technique. These corrections were tested by comparing the experimental results using the reflection technique with those from a bench-top experiment at a frequency of 5 MHz.

5.4.1. Diffraction Corrections

The finite diameter of the transducers causes acoustic diffraction (beam spreading) as the wave travels from its surface. This wave interference alters the travel time and attenuation coefficient measured using the reflection technique. There have been a number of studies into wave diffraction from a circular piston source, particularly for P-wave propagation through liquid media (for example, Papadakis (1972). The near field diffraction of radiation from a piston source is analogous to the Fresnel diffraction of light through a circular aperture (Kinsler and Frey, 1962). The near field is the region in which the distance from the source is small in comparison with the transducer radius a, and extends to a distance of $2a^2/\lambda$ (where λ is the wavelength) from the source (Figure 5.7). The axial intensity of the received stress I_0 in this region oscillates with increasing wavelength as the distance z from the transducer increases.

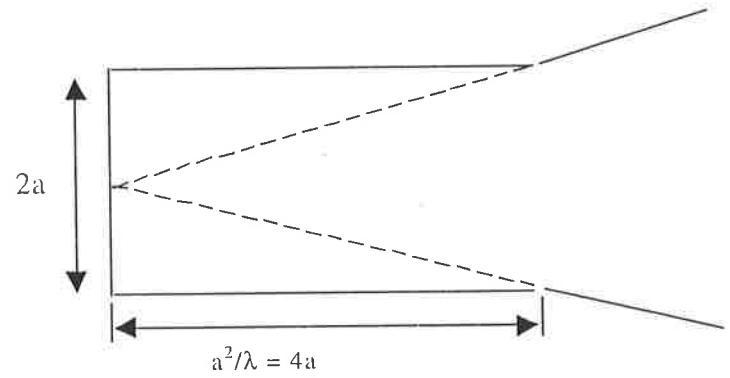

Figure 5.7. The Fresnel and Fraunhofer regions of a sound beam from a piston source (after Kinsler and Frey, 1962).

Papadakis (1972) showed that the average received stress (P) varies with the distance from the source z, the diameter of the transducer a, and the wavelength λ:

$$S = z\lambda/a^2 = zV/a^2f \qquad (5.6)$$

where S is the normalised distance, f is the frequency and v the velocity of the waves. The diffraction increments on the travel times and attenuation coefficients, Δt and Δa, are given by:

$$\Delta t = [\varphi(S_n) - \varphi(S_m)] / 2\pi f \qquad (5.7)$$

and,

$$\Delta a = [a(S_n) - a(S_m)] / [2L(n-m)] \qquad (5.8)$$

where a is given in units of inverse length, φ is the diffraction phase shift, L is sample length and S_n and S_m are the normalised distances for the nth and mth echoes, respectively. In the reflection system used in the present study S_n and S_m correspond to the top and bottom rock-to buffer-rod reflections, respectively. The travel times and attenuation coefficients corrected for diffraction effects are then;

$$t = t' + \Delta t \qquad (5.9)$$

and,

$$a = a' - \Delta a \qquad (5.10)$$

where t' and a' are the experimentally measured values of travel time and attenuation coefficient, respectively. Figure 5.8 shows the diffraction loss Δa (in dB) and diffraction phase shift φ plotted as functions of the normalised distance S. Benson and Kiyohara (1974) used the diffraction theory of Papadakis (1972) to produce tabulated values of φ and Δa. The tables were originally designed for P-waves only, however if they are applied as correction for S-wave McCann and Sothcott (1992) showed that they are only slightly less effective.

In the reflection technique used in the present study, the radii of the transducer was 1.27 cm and 1.00 cm for P- and S-wave respectively. Considering the average frequency used during the experiments and the velocities in the perspex buffer-rod (V_p = 2752 m/s and V_s = 1390 m/s) the Fresnel zone extends up to 10.4 cm for P-waves and 13.4 cm for S-waves. Since the buffer rods are 5 cm in length, the path length traveled by the top reflection is within the Fresnel zone. The greater path traveled by the bottom reflection ensures that it is within the far-field region (Fraunhofer zone). Interpolations of Benson and Kiyohara corrections were used for the diffraction corrections in all calculation in the present study.

5.4.2. Geometric Effects

Sidewall effects are inevitable in the measurement system due to the small size of the sample compared to the radius of the transducer. Figure 5.9 illustrates the far field (Fraunhofer) radiation pattern of a piston transducer. The energy within the central lobe decreases with increasing angle from the normal to the transducer face. At angles greater then θ, the energy contributed by the main lobe is zero. As frequency decreases, beam spreading (and therefore θ) increases, and interference from sidewall reflection is more likely to occur since the energy will not be sufficiently attenuated.

The lowest frequency at which there is no risk of interference from reflection off the sidewalls can be calculated. Figure 5.10a shows an arrangement of the transducer-receiver, the perspex buffers (V_p = 2752 m/s) and a high velocity (5000 m/s) sandstones. The rock sample has been replaced by a length of perspex (Figure 5.10b) corresponding to an equivalent travel time for the direct raypath (normal incidence). This direct arrival travels a distance of 17.27 cm, and therefore the sidewall reflection occurs at a distance of (17.27 – X) cm along the sample wall. From Figure 5.10c:

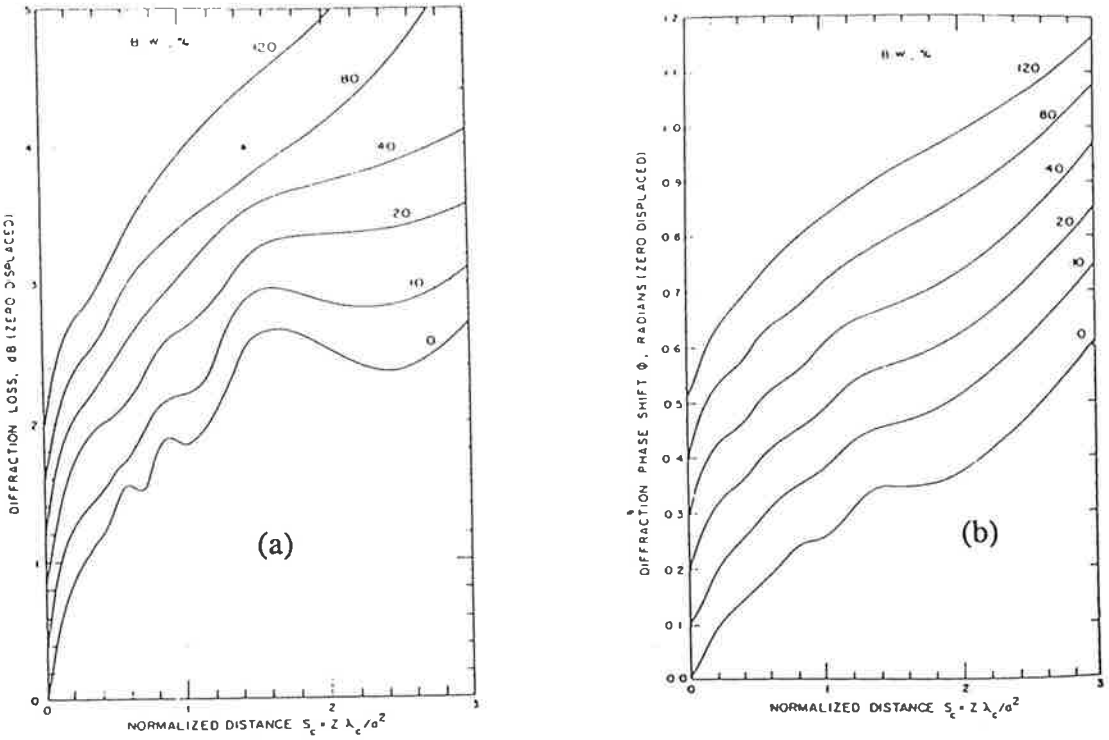

Figure 5.8. Diffraction corrections as a function of normalised distance S. (a) Diffraction loss, (b) diffraction phase shift (after Papadakis, 1972).

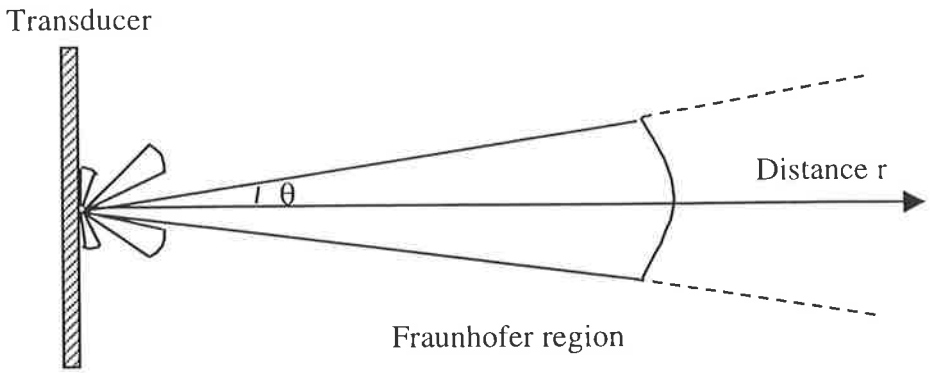

Figure 5.9. Radiation pattern from a circular piston transducer (after Kinsler and Frey, 1962).

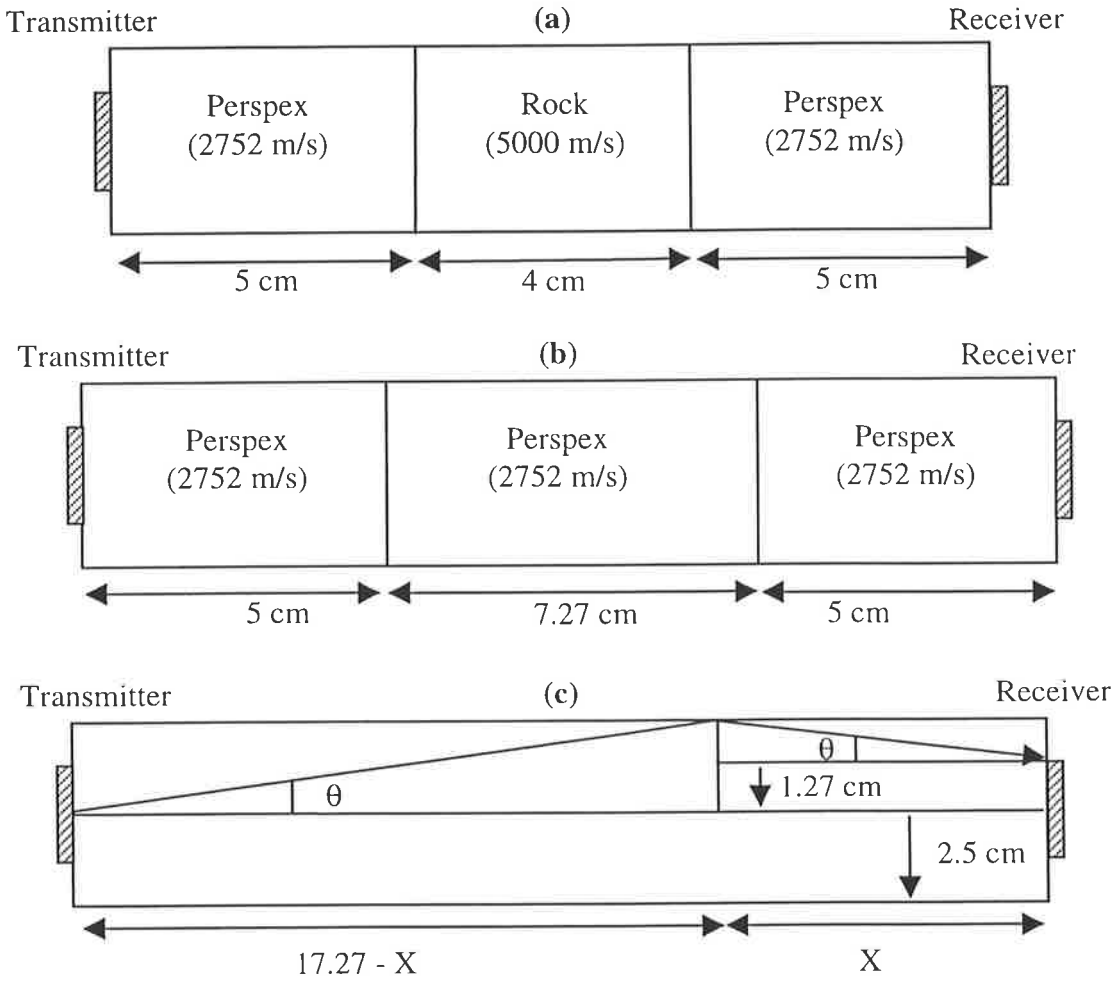

Figure 5.10. (a) Equivalent travel path of a pulse which has propagated through the reflection system. (b) Travel path after the rock sample in (a) is replaced by an equivalent length of perspex. (c) The geometry used to calculate the minimum frequency at which side wall reflection become significant.

$$X/1.27 = (17.27- X) / 2.54 \quad (5.11)$$

and therefore $\theta = 12.6°$. If the maximum intensity is reduced by one quarter (-12dB) for example and the length is 12.6°, the directivity function plotted in Kinsler and Frey (1962), gives X = 3. Therefore, for a radius a = 1.27, the minimum frequency for P-waves is 0.47 MHz. This value is lower than the frequencies used in experiments performed in the present study and therefore interference from sidewall reflections may be considered to be negligible.

5.4.3. Corrections for Stress Dependence

5.4.3.1 Acoustic Impedance of Buffer-Rod

The acoustic velocities of the perspex buffer-rod increase slightly as confining stress increases and this affects the calculated value of attenuation in rock samples. To correct the stress-dependence, regression equations for V_p and V_s for the buffer-rod were calculated using velocity and bulk modulus data for perspex from Hughes et al. (1950). These were combined with the experimental measurements of velocities, V(br), and density, ρ(br), in perspex at atmospheric pressure and room temperature to produce the equation:

$$V_p(br) = 2823 + 2.518P - 3.570T \quad (5.12)$$

$$V_s(br) = 1444 + 0.962P - 2.697T \quad (5.13)$$

$$\rho(br) = \rho_0 [1 + P_c/(5706 + 10.3P - 9.377T)] \quad (5.14)$$

where P_c is the confining stress in MPa, T is the temperature in degree Celsius, and ρ_0 is the density of perspex at atmospheric pressure (1186 kg/m^3). Between confining stresses of 5 MPa to 60 MPa, V_p(br) varies from 2764m/s to 2903 m/s, V_s(br) varies from 1395 m/s to 1448 m/s, ρ(br) varies from 1186 kg/m^3 to 1197 kg/m^3. Equations 3.12 to 5.14 were used to calculate the velocity and density of the buffer-rod during data processing.

5.4.3.2. Sample Thickness

A rock sample loaded under hydrostatic stress will undergo a small change in its volume depending on how soft it is. Jones (1996) showed that the maximum change in length between measurements made at 60 MPa and ambient stress for a 2 cm Berea sandstone

core plug is about 0.0038 cm, which leads to an error of 7 m/s for V_p and 5 m/s for V_s, under dry conditions. Hence the maximum velocity error due to sample shortening in dry condition is within the accuracy of the velocity measurements. In fully- and partially-saturated samples the effect of stress on sample lengths may be offset by sample swelling, particularly in clay-rich rocks. Since the suite of rocks used in the present study are well cemented and highly consolidated sandstones, it was assumed the total change in length between measurements at high effective stresses and ambient conditions would produce negligible effects in the measured velocity and attenuation.

5.5. System Calibration

Velocity and attenuation of P- and S-waves were measured on a 28.262 mm long aluminum alloy (~ zero attenuation and density = 2710 kg/m^3) cylinder in order to calibrate the measurement system. Table 5.1 shows the measured velocities and attenuations of aluminum alloy under confining stresses of 20 MPa to 60 MPa. At 0.915 MHz (P-wave) and 0.750 MHz (S-wave) frequency. The accuracy of diffraction corrections in the reflection system was examined by comparing data in Table 5.1 and 5 MHz bench-top experiments on the aluminum block. The high frequencies used in the bench-top experiment ensure that wave diffraction is negligible and therefore the velocities can be regarded as true values. The average velocities in the bench-top experiment were calculated from the travel of multiple arrivals. The true velocities from bench-top measurements were V_p = 6479 ± 1 m/s and V_s = 3112 ± 0 m/s. Zemanek and Rudnick (1961) quote values of 150.000 for Q for aluminum. The correspondent attenuation coefficient for aluminum is 0.0003 dB/cm which is very low and considered negligible.

Table 5.1 shows that the precision of velocity measurements in the reflection system is better than 0.1%. However, the diffraction corrections lower the overall accuracy of the results compared with velocity data obtained from bench-top measurements. The accuracy of velocities from the reflection system after diffraction corrections have been made is better than 0.3%. This is in agreement with the accuracy of the reflection system for velocities quoted by McCann and Sothcott (1992). The difference between the calculated attenuation coefficients and the true value (zero attenuation) indicates that attenuation can be measured to an accuracy of better than 0.16 dB/cm which is of the same order of magnitude as the 0.1 dB/cm suggested by McCann and Sothcott (1992).

P_c (MPa)	Vp (m/s)	Vs (m/s)	α_p (dB/cm)	α_s (dB/cm)
20	6470	3121	0.198	0.123
30	6469	3121	0.185	0.133
40	6467	3120	0.149	0.128
50	6465	3120	0.130	0.101
60	6470	3121	0.134	0.134
Average	**6469**	**3121**	**0.1595**	**0.123**

Table 5.1. Velocity and attenuation of aluminum alloy measured at ultrasonic frequency, 0.915 MHz and 0.75 MHz for P- and S-waves, respectively.

5.6. Data Processing

Data from the two pulse generators were processed separately using different methods. The single frequency data obtained from the Arenberg Pulse Generator were recorded during the experiments on a data sheet. The raw data were then transferred from this sheet to a spreadsheet program written in Microsoft Excel format. The single frequency travel times and amplitude were entered into the spreadsheet together with the bulk density, length and error in length of the sample and the transducer radius. The data are presented in columns corresponding to the effective stresses at which the experiments were performed. The spreadsheet included diffraction corrections from tables by Benson and Kiyohara (1974). The end results are P- and S-waves velocity in m/s and quality factors (Q) together with their 95% confidence levels. The results of the single frequency data were used in the broadband calculations.

For the broadband data computer processing of the traces was performed using series of programs written by Best (1992) and Jones (1996) from the PRIS. These programs reformat the raw data recorded from the oscilloscope, window and taper the signals, and then perform a fast Fourier transform on them. The end results are attenuation and velocity spectra for data collected at each effective stress level.

Chapter 6

Stress Sensitivity of Dry Sandstones

6.1. Introduction

While the increase of velocity with stress is well established, variations in the amount of this effect with petrophysical properties have rarely been examined. In particular the role of porosity in the velocity-stress relationship for consolidated sandstones has not clearly been addressed in the literature. This chapter describes the results of a systematic laboratory study of the stress dependency of V_p and V_s in 22 samples from the Cooper Basin measured under dry (Sw = 0) conditions. Acoustic measurements were made on the full suite of 22 dried samples whose petrography and petrophysical characteristics were discussed in Chapter 4. Sample preparation, ultrasonic measurements and data processing procedure have already been described in Chapter 5.

6.2. Results

6.2.1. General

V_p and V_s were measured during stress unloading at elevated confining stresses of 60, 50, 40, 30, 20, 15, 10 and 5 MPa while pore pressure was kept constant at atmospheric pressure. For a few samples, accurate measurements could not be performed at low confining stresses (<10 MPa) due to high wave attenuation. Total core volume reduction was also measured over the stress range for a sub-set of samples. The method of measurement and data on the variation of core porosity versus confining stress were demonstrated in Chapter 4. Measured volume reduction for the selected samples showed no significant changes compared with the core volume under ambient conditions. As shown in Figure 6.1 both V_p and V_s show similar non-linear increases with stress regardless of the porosity of the sample. Figure 6.2 shows measured core porosity at different confining stresses for a subset of samples.

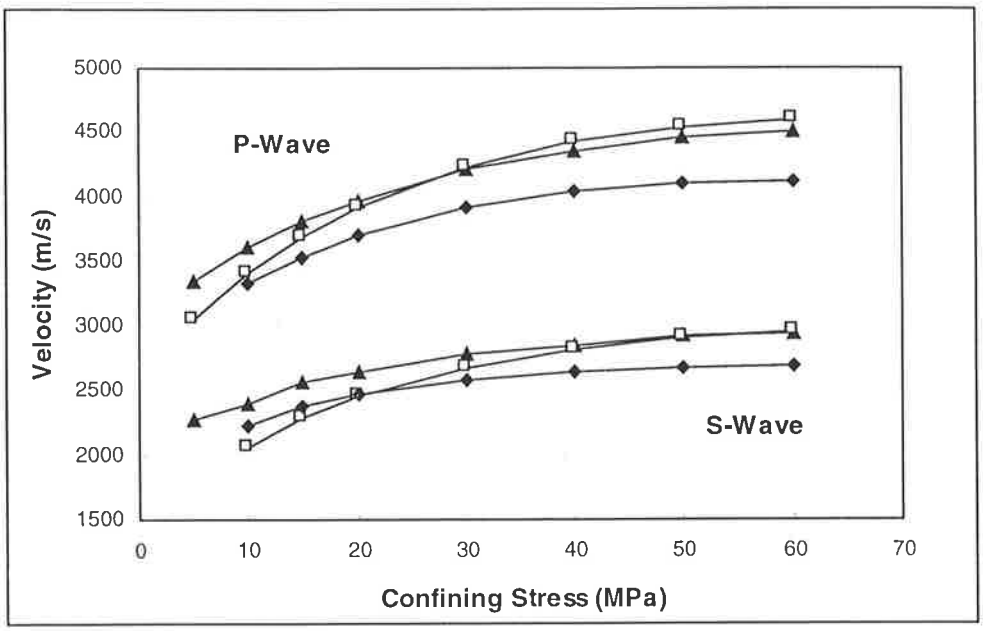

Figure 6.1. V_p and V_s as a function of confining stress in three Cooper Basin samples. Triangle, square and diamonds represent samples: S1 (ϕ = 10.5%), D4 ((ϕ = 13%), and S4 (ϕ = 16.6%), respectively.

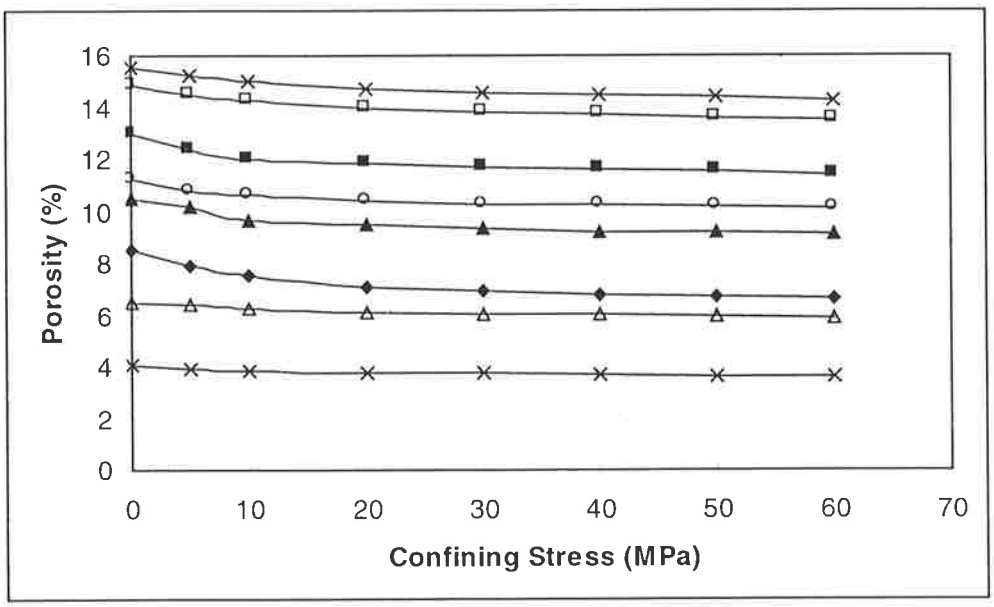

Figure 6.2. Measured core porosity at different confining stresses for a subset of samples

6.2.2. Statistical Analysis

Statistical analysis was performed on the measured data to generalise the observed velocity-stress relationship. The generalised relation then was used to predict wave velocities beyond the experimental data point. Several authors (eg Eberhart-Phillips et al.

(1989), Freund (1992), and Jones (1996)) demonstrated that the velocity-stress relationship could be expressed by an empirical equation with a constant value, an exponential part and a linear part:

$$V = A + KP - Be^{-DP} \qquad (6.1)$$

where V is velocity and P is confining stress for dry samples and effective stress (P_e) for saturated samples, and A, K, B and D are best-fit coefficients to be evaluated by statistical analysis. In this equation A is the crack free velocity and varies according to the porosity and clay content of the rock. K is the slope of the linear section of velocity-stress curve with a generally low gradient for consolidated sandstones, and D is related to the closure of cracks. The difference between A and B parameters indicates the velocity at zero stress.

Equation (6.1) was initially used to find the best fit for the 22 samples used for this part of the study. A least-squares method was used to derive the coefficients in the equation for the measured V_p and V_s for each sample. The standard error of the estimates was used to assess the evaluated coefficients. It was found that the variations of both V_p and V_s with stress are fitted well by values predicted from equation (6.1) over the measured confining stress range (< 60 MPa). However, for the majority of samples the calculated coefficient 'K' shows either negative or large positive values. A negative K means there is a maximum point in the velocity-stress curve (between 70 MPa and 100 MPa) beyond which velocity decreases with increasing confining stress. A large positive K value indicates that the velocity increases sharply and monotonically even at high confining stresses. Both of these cases are found to be unrealistic and inconsistent with the stress dependence of wave velocities in consolidated sandstones. Jones (1996) reported a similar problem in applying a similar equation to predict the quality factors of P and S waves in sandstones at high stresses and attributed the negative K values to experimental error in the measured quality factors. Since the velocity data are accurate to 0.3% this explanation can not account for negative K values in equation (6.1). It seems therefore that although equation (6.1) gives a good fit for interpolation between the measured data, it is not applicable for extrapolating beyond the experimental limit (P > 60 MPa).

The present study indicates that a new empirical equation is needed to explain the observed velocity-stress relationship in the Cooper Basin Samples. The general trend of

velocity as a function of confining stress can be seen in Figure 6.1, while Figure 6.2 shows that there is a small initial drop in porosity associated with the stress changes which stabilises after around 20 MPa. Figure 6.3 shows plots of 'velocity change' (defined as difference between velocities measured at two sequential confining stress levels, e.g. 50 MPa and 40 MPa, divided by the maximum velocity value) versus confining stress.

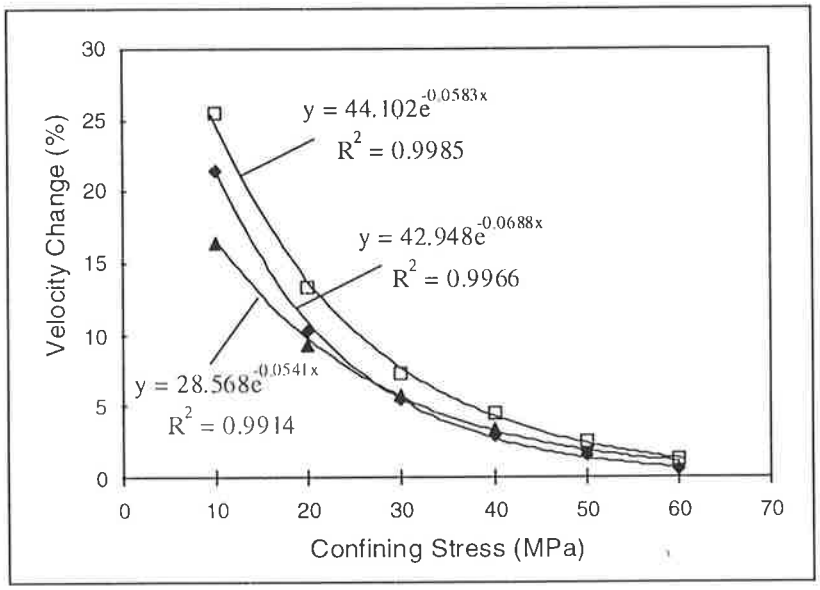

Figure 6.3. Velocity change (P-wave) versus confining stress for samples shown in Figure 6.1. Lines show regression curves.

The good fits of exponential trend lines to these data suggest the following relationship between velocity and confining stress for the samples.

$$dV/dP = a\, e^{-bP} \qquad (6.2)$$

By integration

$$V = A - Be^{-DP} \qquad (6.3)$$

Figure 6.4 shows the velocity of P-waves and S-waves for sample D4 with regression lines calculated both by equation (6.1) and equation (6.3). As it is shown equation (6.3) gives a realistic extrapolation to high confining stresses. The regression equations calculated for all samples fit well with observations and may enable predictions of both V_p and V_s at

high confining stresses. Mean standard errors of residuals of the estimated velocities are 3.0 ±1.5 m/s and 4.5 ± 2.3 m/s for V_p and V_s, respectively. The standard errors of residuals are not significant compared to the accuracy of the measured velocities.

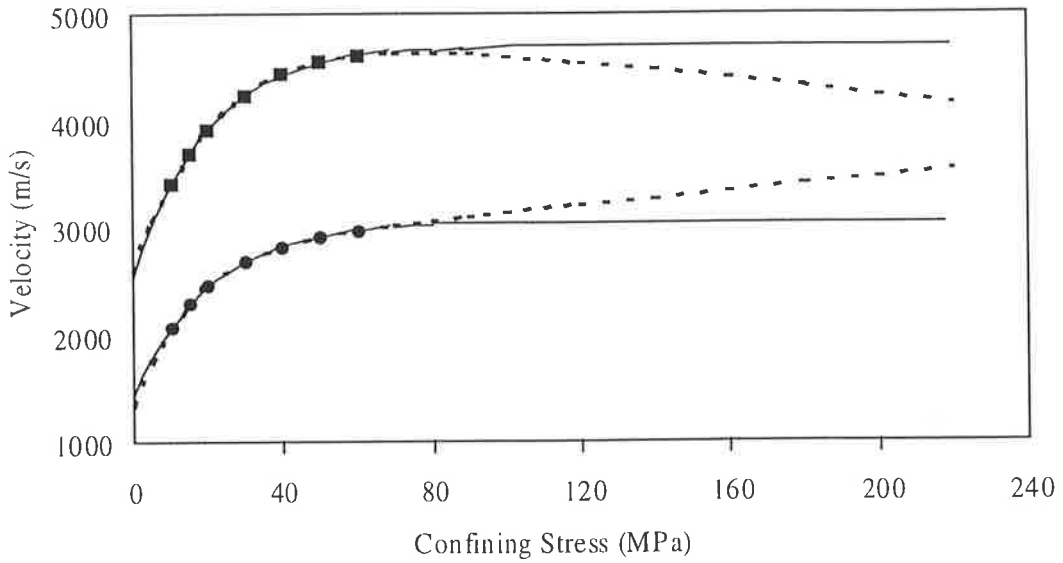

Figure 6.4. Experimental data and regression curves for sample D4. Squares; measured V_p, circles; measured V_s, solid curves; predicted velocity using equation (6.3), dashed curves; predicted velocities using equation (6.1).

Equation (6.3) also gives a good fit to the data reported by Freund, (1992) which contains velocity data for dry sandstones at confining stresses of up to 300 MPa. Figure 6.5 comparison between the measured velocities for samples 140 and 146 of Freund (1992), and regression curves using equation (6.3). Figure 6.6 presents a graphic description for equation (6.3). Table 1 lists the regression parameters in equation (6.1) and (6.3) for V_p and V_s for the Cooper Basin samples measured under dry conditions.

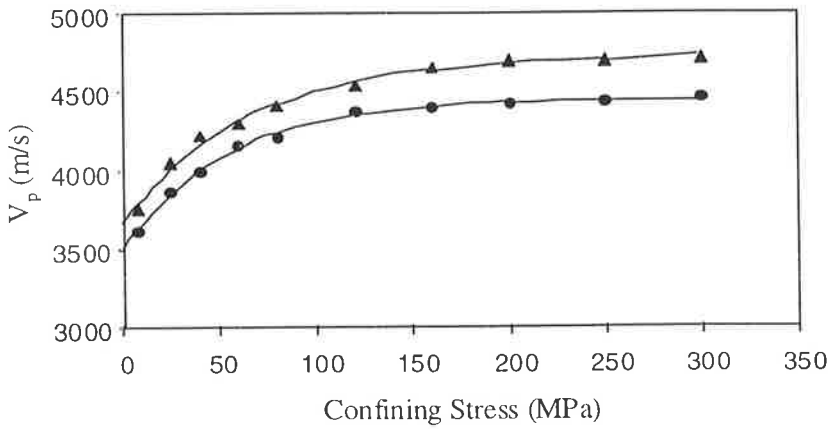

Figure 6.5. Regression curves and measured P-wave velocity. Experimental data are from Freund (1992); sample140 (diamonds) and 146 (triangles). Lines show regression curves using equation (6.3).

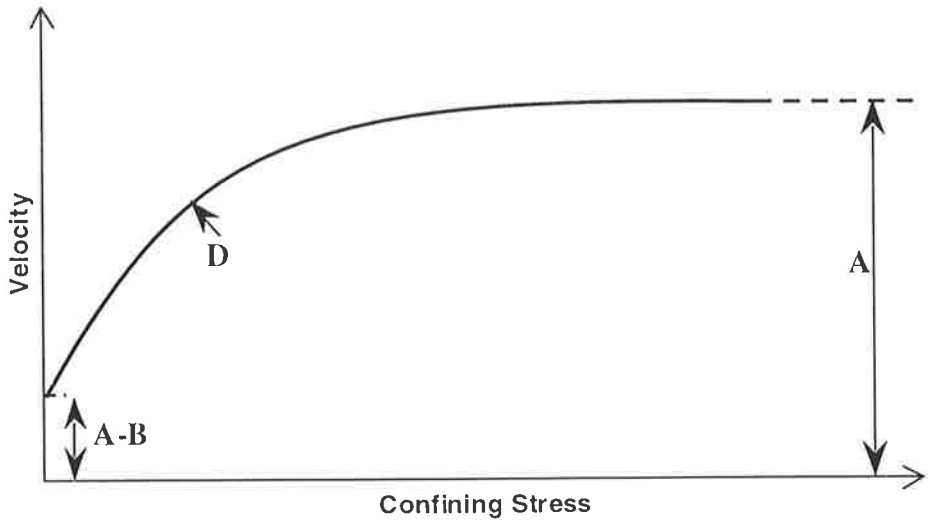

Figure 6.6. A graphical demonstration of the velocity-confining stress relationship defined by equation (6.3).

	Regression coefficients for equation (6.1)								Regression coefficients for equation (6.3)					
Sample	A_p	K_p	B_p	D_p	A_s	K_s	B_s	D_s	A_p	B_p	D_p	A_s	B_s	D_s
D1	4945	-2.64	1633	0.043	3631	-5.50	1436	0.029	4743	1442	0.050	3189	969	0.042
D10	6930	-21.97	4180	0.018	4840	-18.80	3120	0.019	4317	1827	0.045	2765	1399	0.058
D2	5048	-4.84	2310	0.039	3106	-0.67	1244	0.054	4660	1953	0.047	3056	1200	0.057
D3	4159	2.60	1532	0.064	2748	1.67	1061	0.061	4347	1642	0.053	2865	1133	0.052
D4	5020	-3.89	2422	0.043	2798	3.40	1466	0.064	4707	2173	0.051	3045	1619	0.045
D6	4456	0.91	2195	0.043	2966	0.61	1536	0.059	4543	2275	0.041	3013	1570	0.049
D7	4519	1.06	1738	0.058	3011	3.65	1161	0.055	4593	1798	0.055	3011	1159	0.055
D8	4887	-2.24	1993	0.042	2998	1.19	1221	0.055	4705	1844	0.047	3087	1284	0.049
M1	5388	-2.90	1549	0.039	8299	-29.21	5631	0.010	5154	1335	0.046	3523	954	0.034
M2	5067	-0.53	1188	0.042	3186	2.59	606	0.085	5021	1145	0.044	3352	716	0.057
M7	7298	-18.05	3080	0.017	5480	-18.32	2940	0.017	5404	1026	0.041	3394	900	0.045
M8	5379	-2.92	1566	0.042	3257	1.85	717	0.058	5156	1367	0.048	3388	830	0.048
M10	6072	-8.20	1831	0.027	5313	-16.90	2790	0.019	5314	1109	0.043	3484	1007	0.045
M11	5792	-4.27	1152	0.026	4750	-7.50	1699	0.012	5374	748	0.038	3589	546	0.026
M13	5219	-1.24	1244	0.041	3932	-6.45	1513	0.029	5114	1145	0.045	3351	960	0.045
S1	4524	0.54	1527	0.053	3831	-9.40	1746	0.028	4604	1595	0.046	2988	932	0.052
S2	6197	-15.28	3050	0.025	3363	-3.51	1194	0.038	4731	1640	0.044	3083	938	0.05
S3	4234	1.10	1772	0.070	2513	3.80	5544	0.020	4308	1836	0.065	2737	1337	0.079
S4	4380	-2.93	1698	0.050	2604	1.10	972	0.085	4163	1554	0.061	2700	967	0.072
S5	4225	1.50	1433	0.064	2699	1.81	996	0.084	4328	1575	0.058	2809	1058	0.07
S6	4655	-3.07	2018	0.058	2882	-0.28	1238	0.078	4442	1920	0.070	2863	1240	0.081
S7	4244	-2.73	1836	0.056	2791	1.10	1038	0.076	4064	1966	0.064	2885	1078	0.069

Table 6.1. Regression coefficients in equations (6.1) and (6.3) for P- and S-wave velocities for Cooper Basin samples.

6.2.3. Regression Coefficients and Petrophysical Properties

Figure 6.7 shows the relationships between porosity and the calculated regression coefficients in equation (6.3) for V_p and V_s. Parameters A_p and A_s (crack independent velocities) and A_p-B_p and A_s-B_s (velocity at zero confining stress) are related to the rock porosity. The weaker correlation in the plots of A_p-B_p and A_s-B_s versus porosity (Figure 6.7b) arises from variations in the number of open cracks (higher crack density) within the samples at zero confining stress.

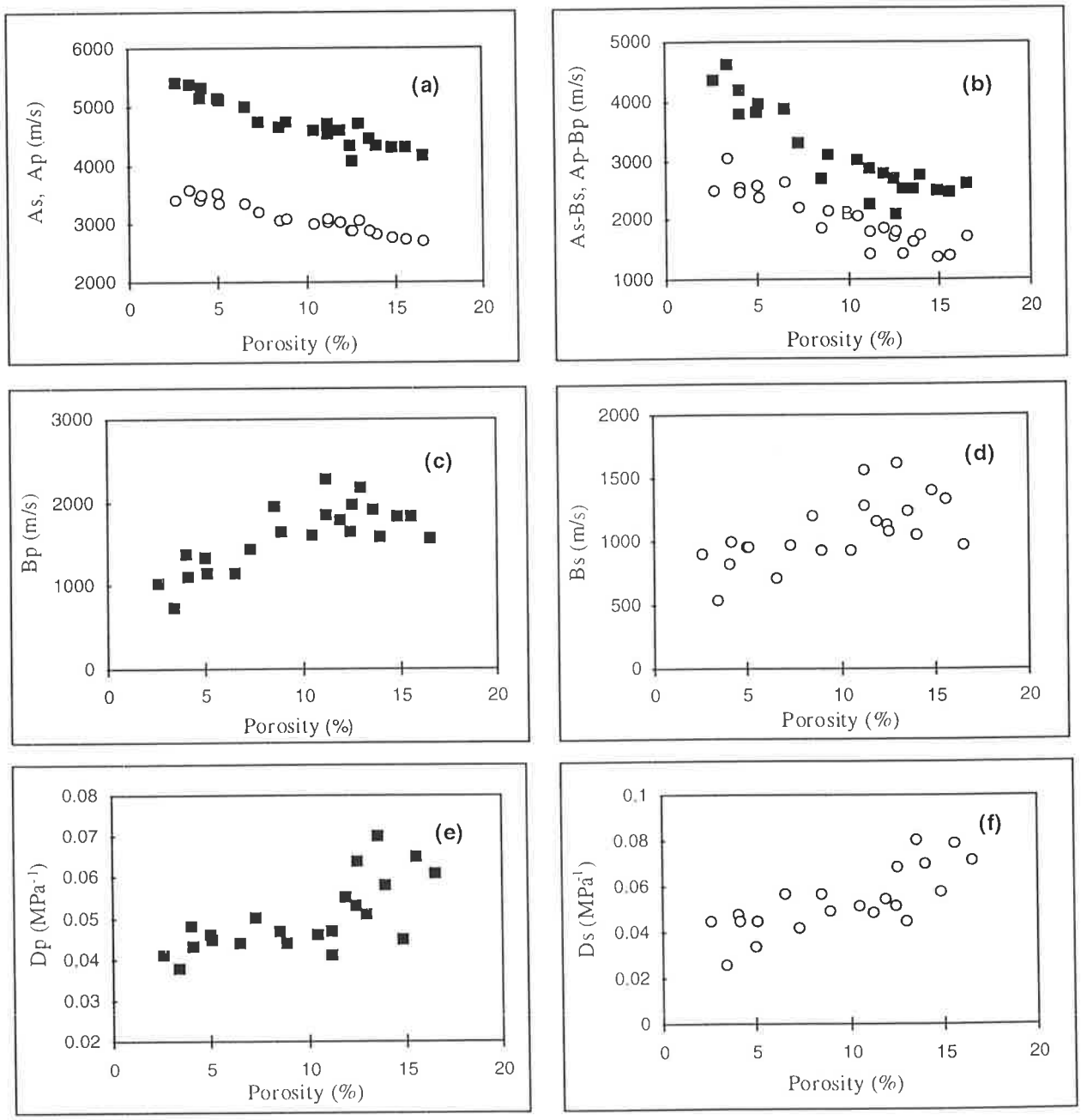

Figure 6.7. Calculated regression coefficients in equation (6.3) for V_p and V_s versus porosity. The subscripts "s" and "p" in vertical axes refer to V_p and V_s, respectively.

The parameter B shows positive correlation with porosity (Figure 6.7c-6.7d) and permeability (Figure 6.8c-6.8d) with a greater scatter at higher porosity and permeability values. The parameter D (crack closure rate) does not show a distinct correlation with core porosities for the entire porosity range in the data set. For instance the plot of the calculated parameter D versus porosity for V_p indicates that D is not related to porosity for samples with porosity less than 10%, but it is positively correlated to core porosity for samples with porosities greater than 10 %. In contrast, the parameter D for V_s shows positive relationships with porosity for both the low and high porosity samples while high porosity rocks show a steeper trend. None of the parameters A, B and D correlate with either volumetric clay content or average grain size as determined from the thin sections.

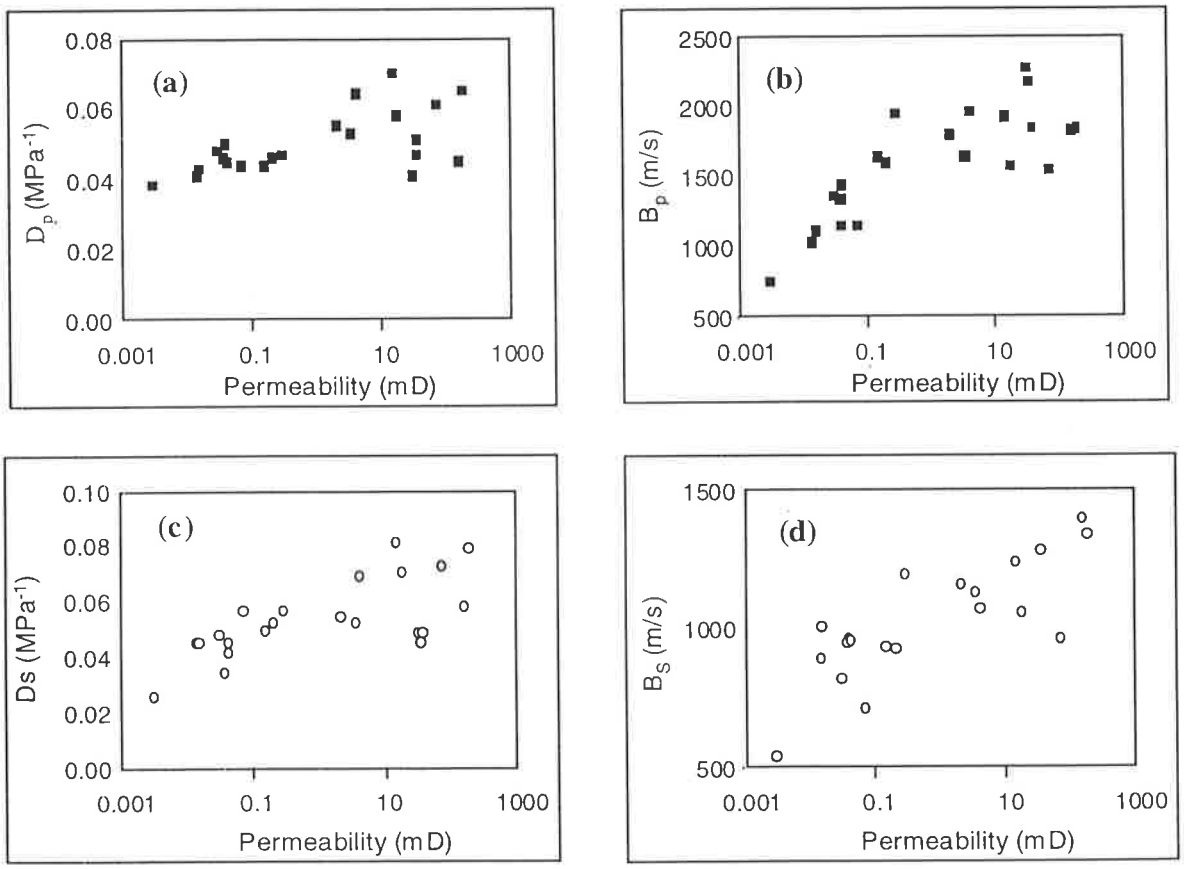

Figure 6.8. Calculated regression coefficients (B and D) in equation (6.3) for V_p and V_s versus permeability.

The parameter D has a relatively small range throughout the samples. The mean values of D for Vp and Vs with 95% confidence intervals are 0.050 ± 0.0038 MPa^{-1} and 0.054 ± 0.0059 MPa^{-1}, respectively. Eberhart-Phillips et al. (1989) and Jones (1996) also have shown similar D values for their samples. The small range of variation in parameter D

indicates that although the crack density under zero stress conditions may vary for different samples, the shape of the velocity-stress curve is similar for all samples and remains independent of porosity and permeability of the samples.

6.2.4. Prediction of Crack-Closure Stress

The pressure level at which the change of velocity with increasing confining stress decreases markedly is known as the 'crack closure stress' ($P_{Closure}$) and the corresponding velocity is defined as the 'crack free velocity' (Eberhart-Philips et al., 1989). $P_{Closure}$ is a useful parameter for comparing the velocities of different samples at high stress conditions. Knowing the $P_{Closure}$ of reservoir rocks in hydrocarbon-producing fields is helpful for monitoring the sensitivity of seismic waves to the variation of the in situ reservoir stress conditions.

In order to determine the $P_{Closure}$ of Cooper Basin samples equation (6.3) was used to extrapolate the velocity-confining stress curve to higher stress values. The stresses at the plateau in the velocity-confining stress curves were considered to be the $P_{Closure}$ of each sample. Figure 6.9 demonstrates an example of this technique. The $P_{Closure}$ determined from V_p and V_s show similar values for each sample. The mean value of $P_{Closure}$ for all 22 samples is 81 ±3 MPa with 70 MPa and 95 MPa as the minimum and maximum values.

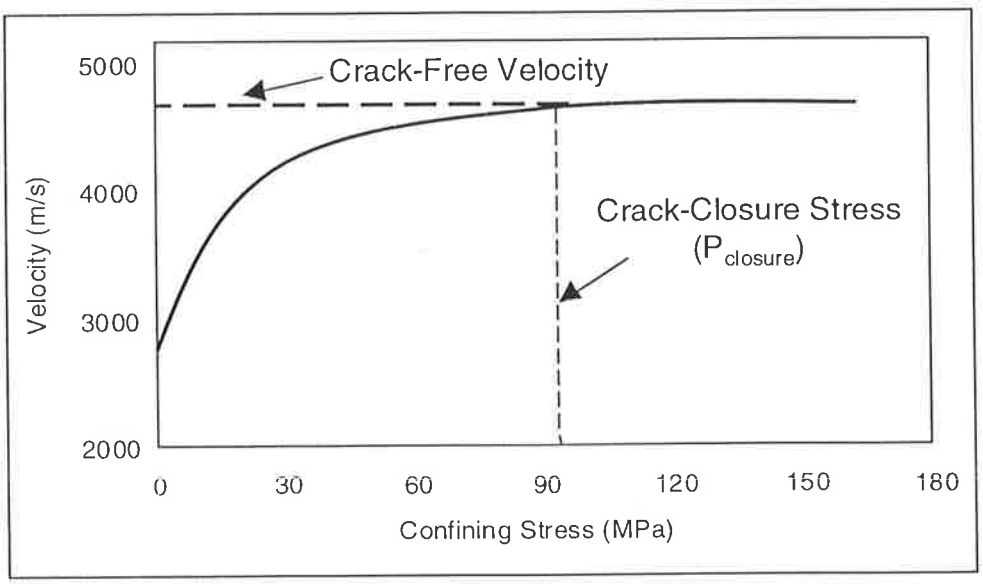

Figure 6.9. Graphical determination of $P_{closure}$ from extrapolation of velocity data using equation (6.3).

The $P_{Closure}$ of the Cooper Basin samples show insignificant correlation with porosity, permeability or clay content. This observation is consistent with that of Eberhart-Phillips et al. (1989); they emphasised that the crack-closure stress of their samples was not dependent on porosity or clay content. The $P_{Closure}$ of several consolidated sandstones measured by Freund (1992) were also were determined graphically from V_p and no significant association was found between the $P_{Closure}$ and porosity in that data set.

Vernik (1997) compared crack-closure stresses for different rocks and sediments, and concluded that $P_{Closure}$ may increase with decreasing porosity. For instance as is shown in Figure 6.10, for Westerly granite (0.7% porosity) the $P_{Closure}$ is 100 MPa, while for a tight gas sandstone (10% porosity) and Ottawa sand (38% porosity) this reduces to 60 MPa and 20 MPa, respectively.

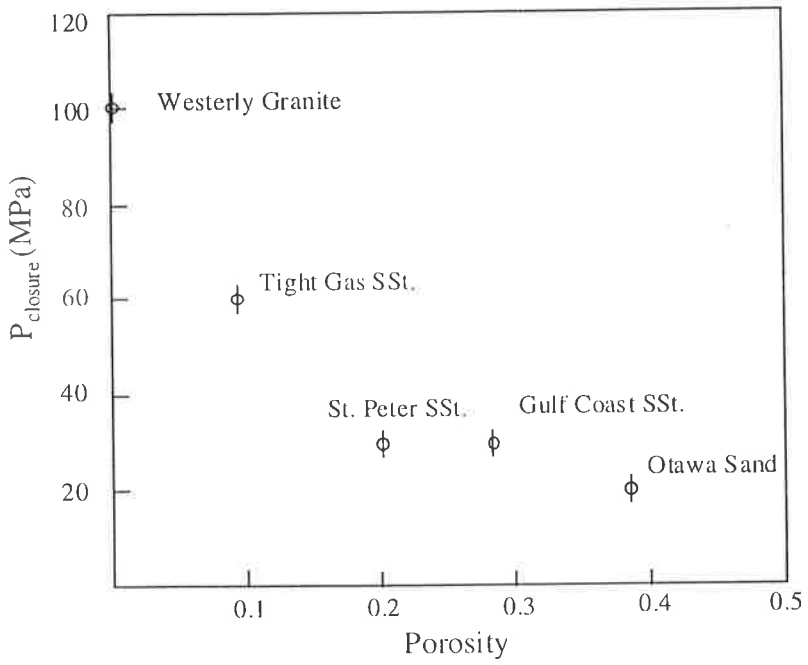

Figure 6.10. Crack-closure stress versus porosity for different rocks (from Vernik, 1997).

Figure 6.11 demonstrates the plot of the crack-closure stress versus core porosity for the Cooper Basin samples. There is no significant trend between the $P_{Closure}$ and core porosity as postulated by Vernik (1997) for the Cooper Basin sandstones. The small range of $P_{Closure}$ variations in these samples indicates that sandstones with similar diagenetic histories and (perhaps) relatively similar pore geometry may have similar crack-closure stress regardless of their porosities.

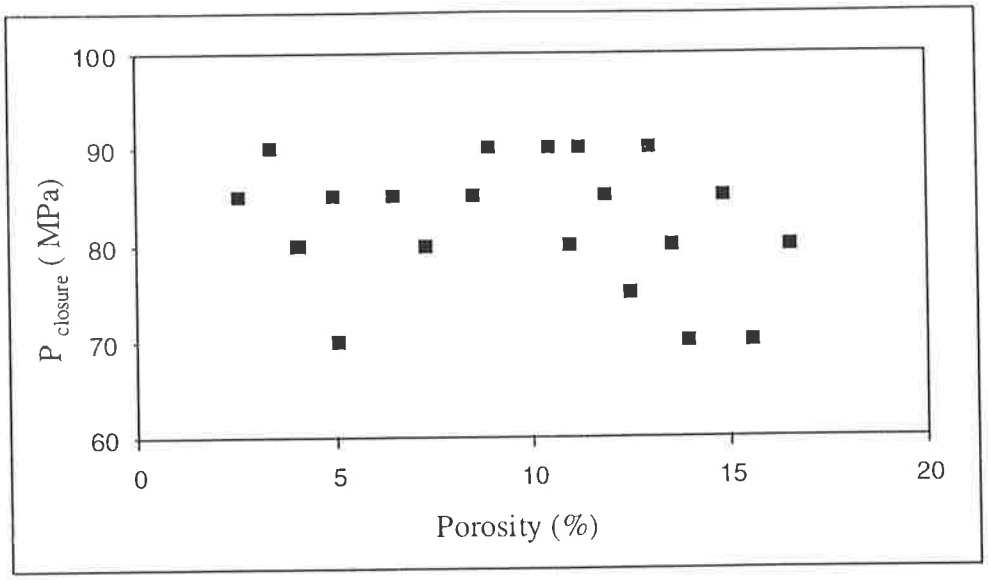

Figure 6.11. Crack-closure stress predicted from measured P-wave velocity versus porosity for Cooper Basin samples.

6.2.5. Velocity Gradient

Equation (6.2) was used to calculate the velocity gradient (dV/dP) at different confining stress levels. The velocity gradient was then used to examine the relation ship between the stress sensitivity of the samples and their petrophysical properties. Figures 6.12 and 6.13 show the wave velocity gradients versus porosity and permeability respectively. At low pressure, high porosity and high permeability samples show greater velocity gradients. For instance at 10 MPa pressure, a 15% porosity sample may show a velocity gradient twice as high as that in a sample with 4% porosity. The difference between the maximum and the minimum velocity gradient values decreases with the increase in pressure. In addition, the correlation of high velocity gradient and high porosity disappears as stress increases, so that at confining stresses greater than 40 MPa there is no distinguishable relationship between velocity gradient and porosity. The stress sensitivities of both V_p and V_s in the samples are not correlated with grain size.

The volume fraction clay content does not correlate with the velocity gradient of P-waves. The lack of significant correlation between clay content and stress sensitivity of P-waves in sandstones has also been demonstrated by Dvorkin et al (1996). Figure 6.14 shows the variation of S- wave velocity gradient with clay content. The relationship between clay content and shear wave velocity gradient of the samples varies across the range of confining stresses. At low stresses, clay content and shear wave velocity gradient are uncorrelated, whereas at high stresses (P > 40 MPa) samples with higher clay content show lower shear wave velocity gradient (albeit with a weak correlation).

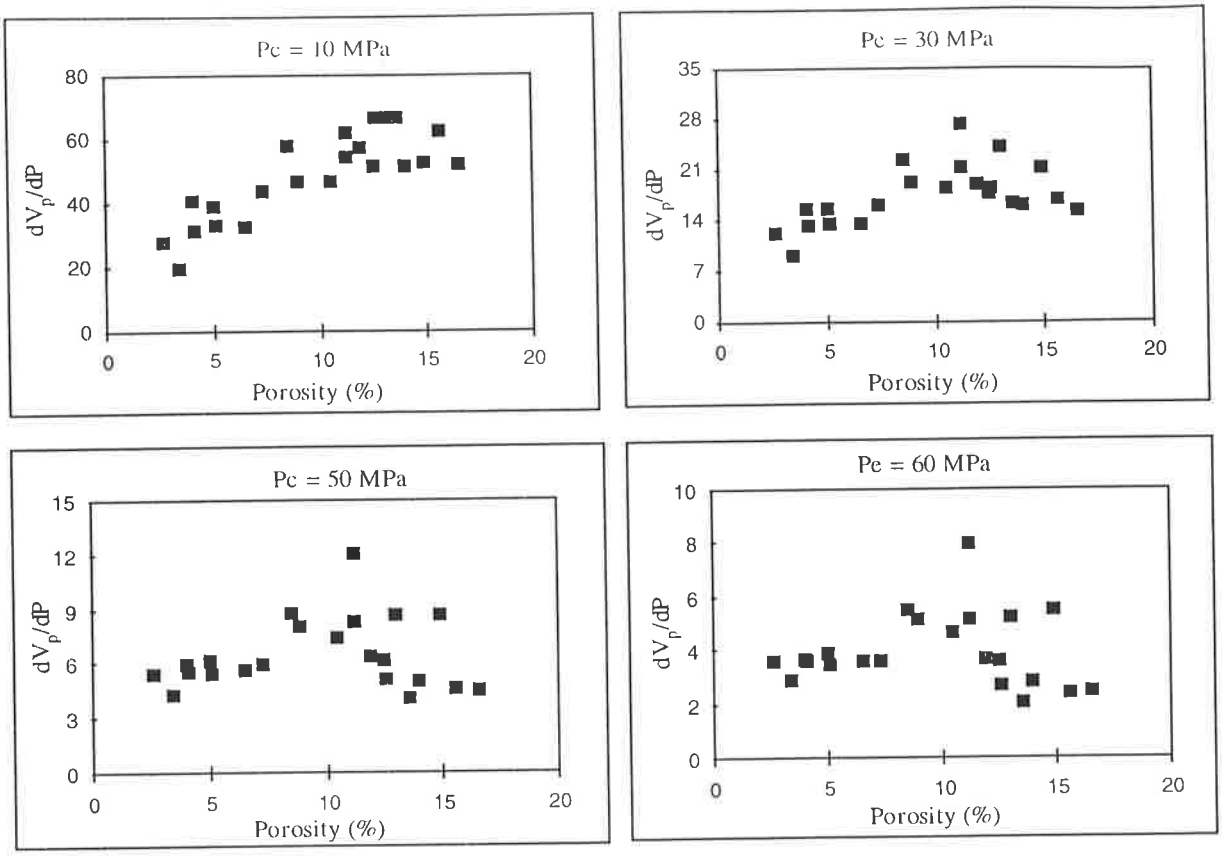

Figure 6.12. P-wave velocity gradient versus porosity at different confining stresses. Velocity gradients of S-waves also show similar trend with porosity.

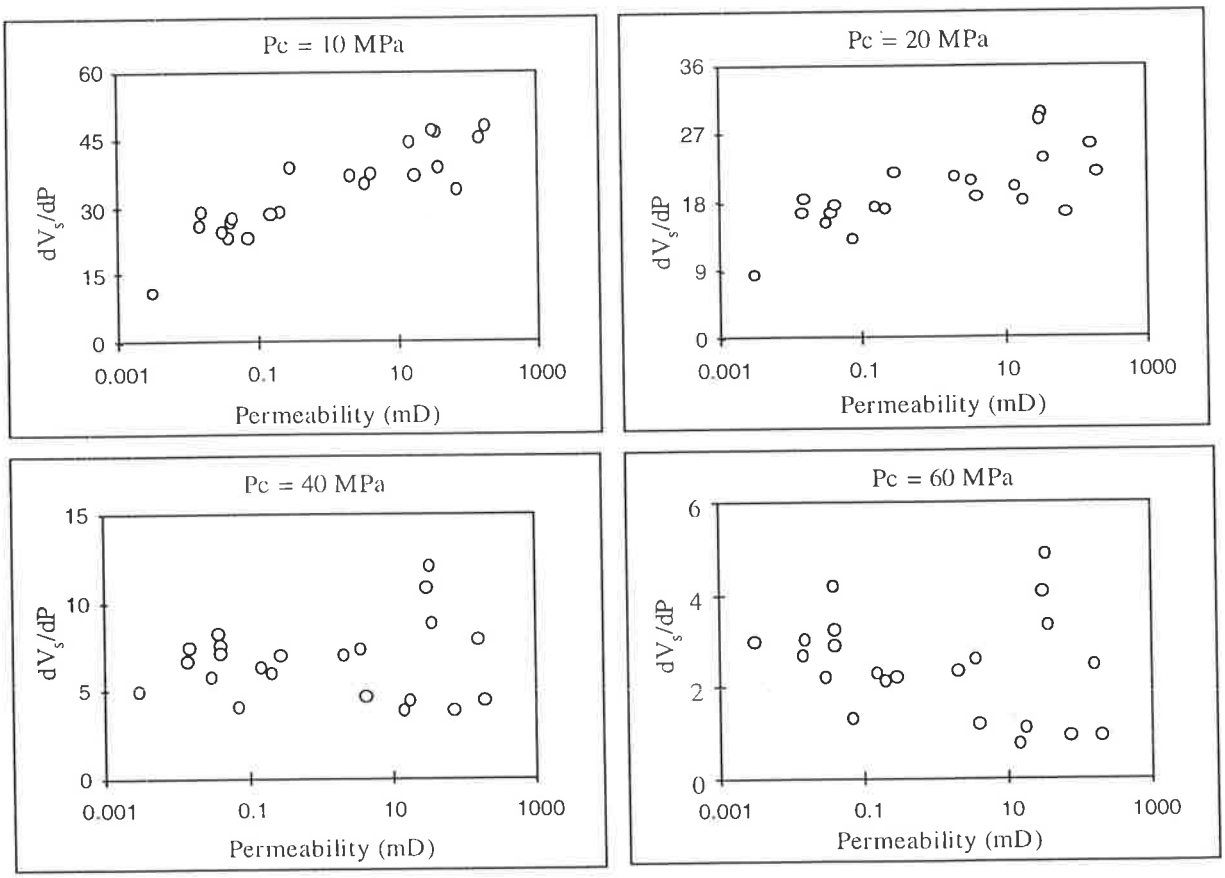

Figure 6.13. S-wave velocity gradient versus permeability at different confining stresses. Velocity gradients of P-waves also show similar trend with permeability.

Tosaya and Nur (1982) showed the importance of pore structure and the distribution of clay particles in reducing the P-wave velocities in shaly sandstones. Observations on the Cooper Basin samples also indicate that the position of the clay is probably more important than the volume fraction clay content in controlling the stress sensitivity of elastic waves. In Figure 6.12, the plot of P-wave velocity gradient versus porosity at 60 MPa confining stress, it is noticeable that samples with porosities greater than 8% fall in two groups, high stress-sensitive rocks ($dVp/P > 4$) and low stress sensitive rocks ($dVp/P < 4$). Thin section and SEM analyses, with the velocity data at 60 MPa, reveals that high stress-sensitive samples have a greater number of clay-free and straight-line connective pores (low aspect ratio pores at quartz to quartz contacts), while lower pressure-sensitive samples have a greater number of tangential and sutured grain contacts. Connective pores in low stress-sensitive samples are filled mainly by dispersed and pore-lining clay minerals and altered muddy rock fragments. Similarly in the plots of shear wave velocity gradient versus clay content at 50 MPa and 60 MPa (Figure 6.14) the low stress-sensitive samples show, under thin section and SEM, predominance of quartz-clay-quartz contacts, regardless of their total clay content.

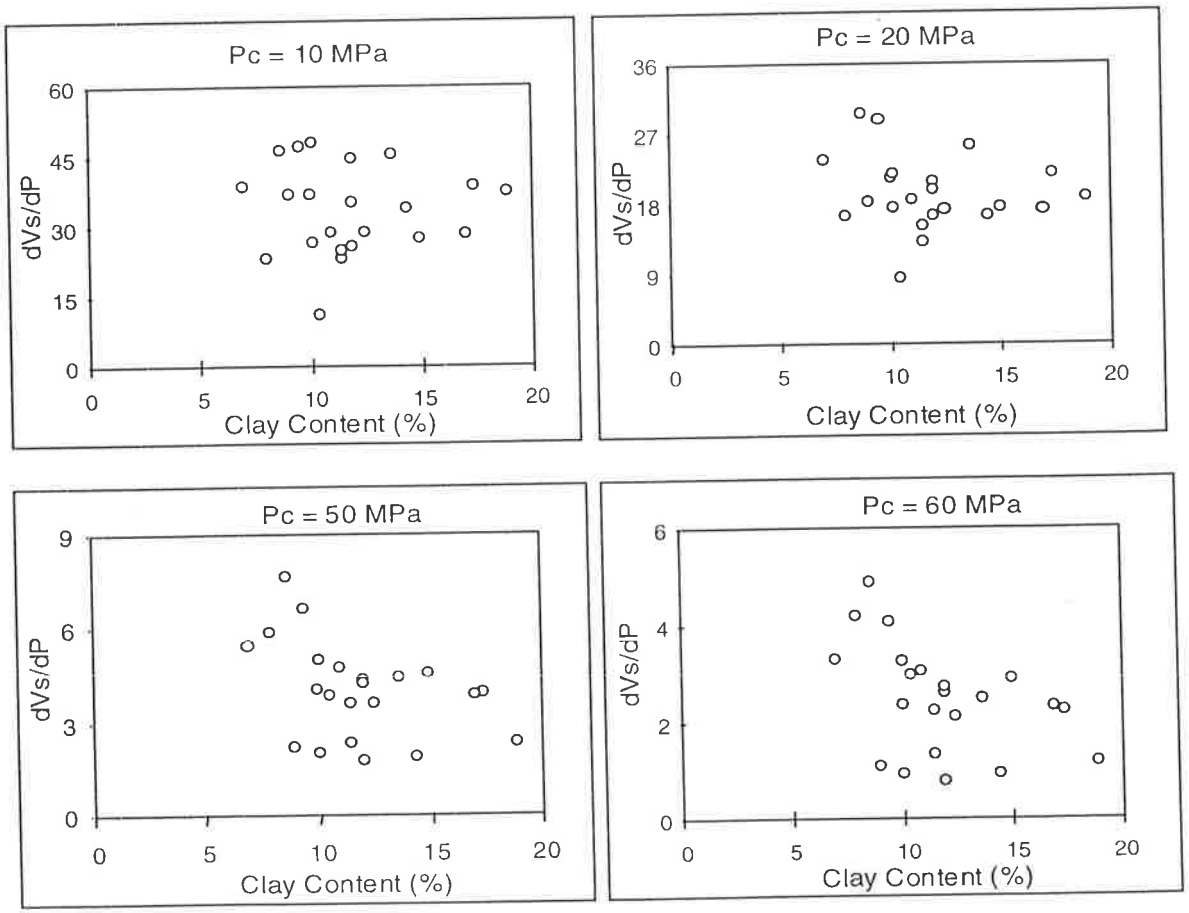

Figure 6.14. S-wave velocity gradient versus clay content at different confining stresses.

6.2.6. Comparison of the Stress Sensitivity of V_p and V_s

A parameter called velocity gradient ratio (VGR) is defined by the author as

$$VGR = (dV_p/dP)/(dV_s/dP) \qquad (6.4)$$

was used for comparison between the stress sensitivity of V_p and V_s. A VGR (equation 6.4) greater than one indicates a higher stress sensitivity for V_p whereas VGR less than one implies Vs is more stress sensitive. The stress sensitivity of V_p is higher than Vs (VGR > 1) in the majority of the studied samples over confining stress range between 10 MPa and 60 MPa. The only exceptions are samples M1 and M11 which show slightly higher stress sensitivity for V_s (VGR equal to 0.92 and 0.97 respectively) at 60 MPa confining stress.

With the stress increase both shear and bulk moduli increase. Since V_p is related to both shear and bulk modulus and V_s is related to shear modulus only, therefore V_s appears to be less stress sensitive than V_p. Apart from the samples D1, D3, D4, M1 and M11 for which the value of VGR decrease with stress in the rest of samples the VGR increase as stress increases. Figure 6.15 demonstrates the plot of the average of VGR values versus confining stress for the all samples. The VGR of the Cooper Basin samples are not significantly correlated with porosity, permeability and clay content.

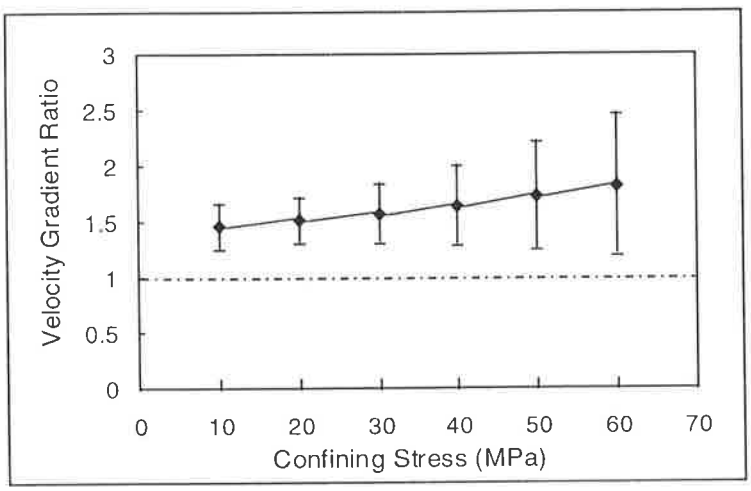

Figure 6.15. Plot of the mean velocity gradient ratios (VGR) versus confining stress. Error bars show standard deviations of VGR values at each stress level.

6.3. Differential-Stress Dynamic Elastic Moduli

Dvorkin et al. (1996) studied the changes of elastic moduli with confining stress on a wide range of dry sandstones using published ultrasonic data. They found that the plots of the

difference between the elastic moduli at two sequential stress levels versus porosity showed lower scatter at high porosity (38%) but increasing scatter with decreasing porosity. Figure 6.16 shows examples of differential-stress elastic moduli versus porosity for the data used by Dovrkin et. al. Based on this observation, Dvorkin et al. (1996) concluded "*low porosity sandstones may be more sensitive to effective stress than high porosity sandstones*". They had also observed a uniform scatter at all porosities in plot of relative elastic moduli difference, defined as $(M_{20} - M_{10})/M_{20}$, where M_{20} is the compressional modulus at 20 MPa, versus porosity. This is demonstrated in Figure 6.17. The latter plot shows that the stress dependency increases with increasing porosity. Dvorkin et al. (1996) analysed the stress sensitivity in absolute terms and used the concept of "critical porosity" to generalise observations and conclusions. They defined upper and lower limits for changes of the elastic moduli with confining stress at a given porosity. The following section is a comparison between the Cooper Basin data set with those of Dvorkin et al. (1996).

6.3.1. Comparison with Other Studies

The measured velocity values at various confining stresses are used in conjunction with density measurements to derive dynamic compressional (M) and shear moduli (G) of the Cooper Basin samples, (neglecting density changes).

$$M = \rho V_p^2 \, , \, G = \rho V_s^2 \qquad (6.5)$$

where ρ is the bulk density of the sample. Figures 6.19 and 6.20 show differential-stress and relative differential-stress elastic moduli respectively as a function of porosity for the Cooper Basin samples. The plots of absolute differential-stress for both M and G moduli versus porosity (Figure 6.18) do not show the association between porosity and stress sensitivity postulated by Dvorkin et al. (1996). In contrast the plots of relative differential-stress elastic moduli versus porosity show a steady increase in stress sensitivity with porosity for both M and G moduli (Figure 6.19). The association of high-stress sensitivity with high porosity is reduced at high confining stresses if the relative differential-stress elastic moduli are calculated at small stress intervals. This is in agreement with the relationship between velocity gradients and porosity shown earlier in section 6.4.4.

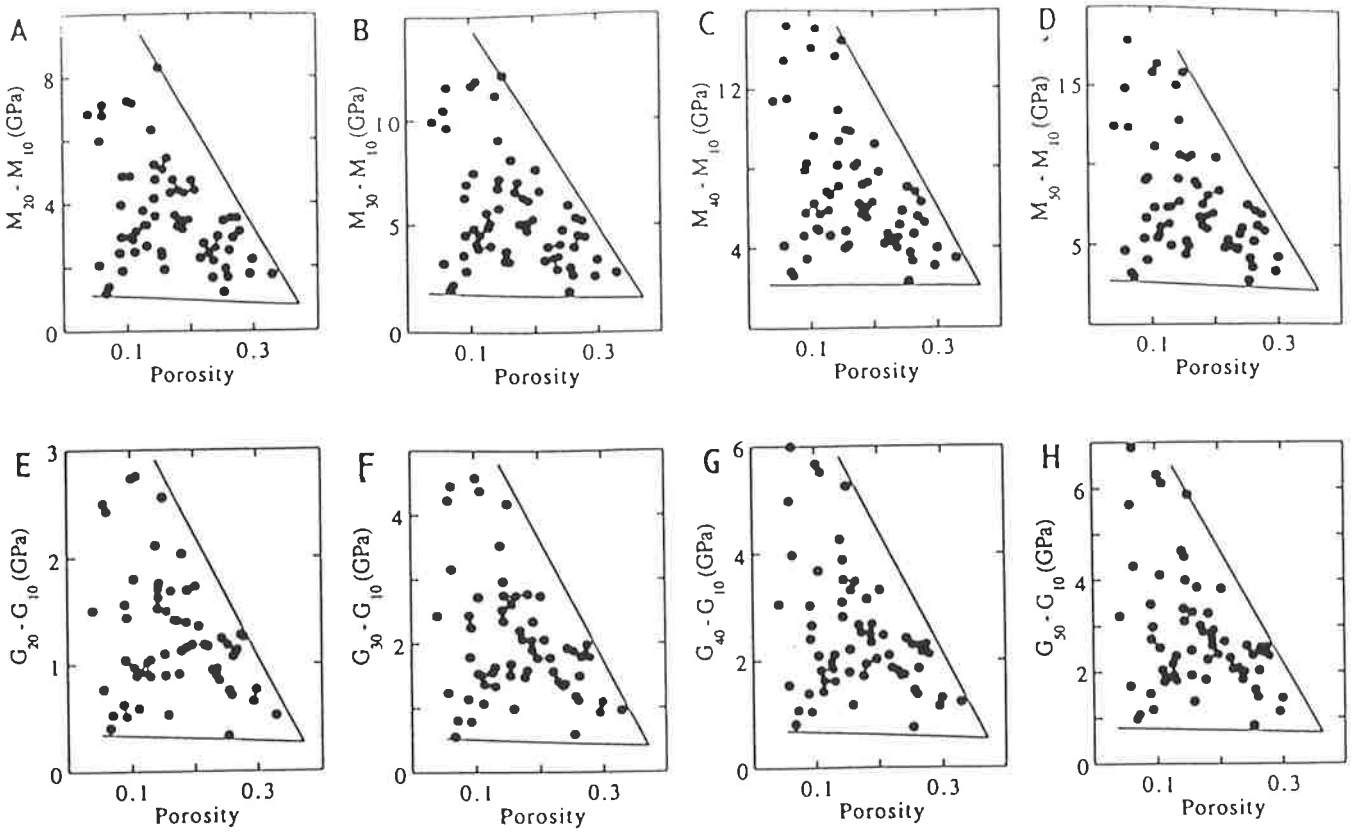

Figure 6.16. The difference between the elastic moduli measured at 20 MPa and 10 MPa (a) and (e), 30 MPa and 10 MPa (b) and (f), 40 MPa and 10 MPa (c) and (g), and 50 MPa and 10 MPa (d) and (h) (from Dvorkin et al.1996).

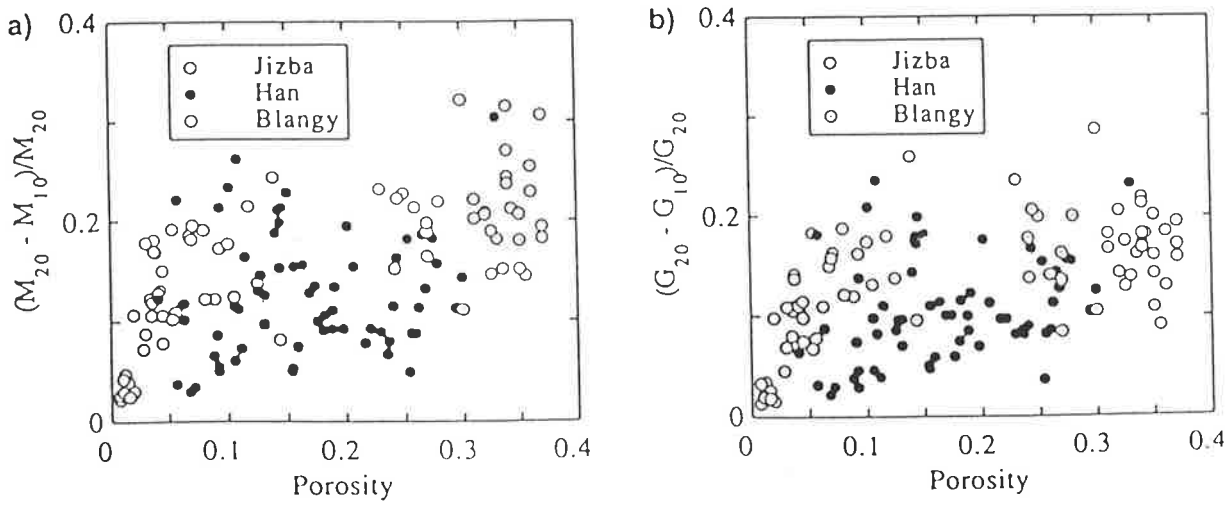

Figure 6.17. Relative moduli difference between 20 MPa and 10 MPa. (a) M-moduli, (b) G-moduli (from Dvorkin et al. 1996).

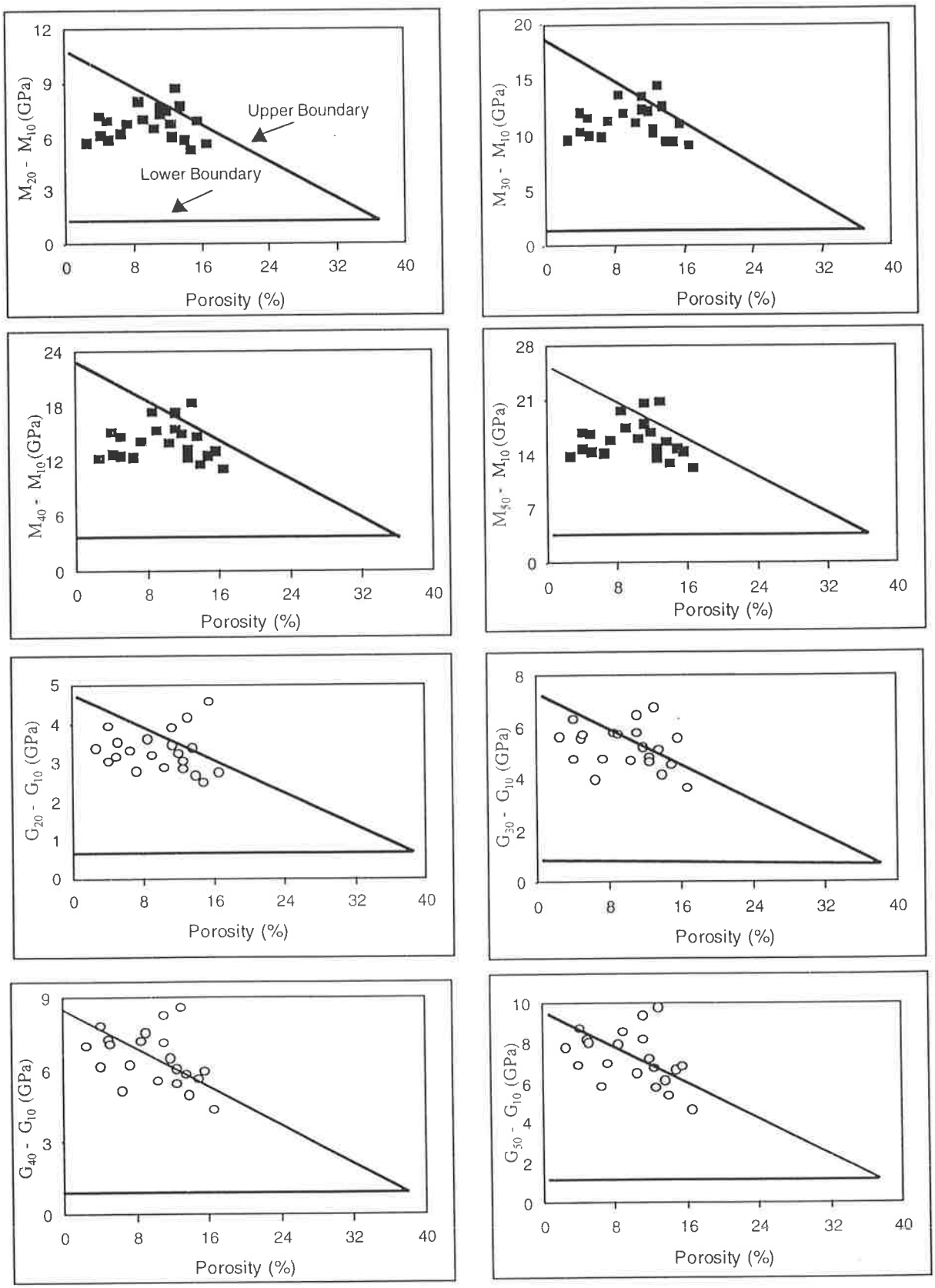

Figure 6.18. Plots of differential-stress elastic moduli as a function of porosity for the Cooper Basin samples. Triangles show the upper and lower bounds suggested by Dvorkin et al. (1996).

Despite the differences in the amount of scatter, which may be caused by similarity in petrology and pore types within the Cooper Basin samples, the observed trends in the plots shown in Figures 6.19a and 6.19b are consistent with the plots showed in Figure 6.17 showing the data used by Dvorkin et al. (1996).

Figure 6.19 also shows that the differential-stress elastic moduli for the Cooper Basin samples fall within the upper and lower boundaries of elastic moduli variation with confining stress proposed by Dvorkin et al. (1996). While the value of differential-stress compressional moduli for low porosity samples (porosity < 10%) falls between the upper and lower limits, samples with higher porosity show differential-stress M moduli close to, or even higher than, the upper boundary. The differential-stress G moduli of the Cooper Basin samples show a more uniform scatter with a greater number of samples showing values above the upper boundary. This indicates that the stress sensitivity of wave velocities in some of samples used in the current study is higher than some of those reported in the literature. Further, the recipe suggested by Dvorkin et al. (1996) for predicting the changes in velocities with confining stress, from a single measurement and at a given porosity, needs to be modified before it can be used for rocks with higher stress sensitivities.

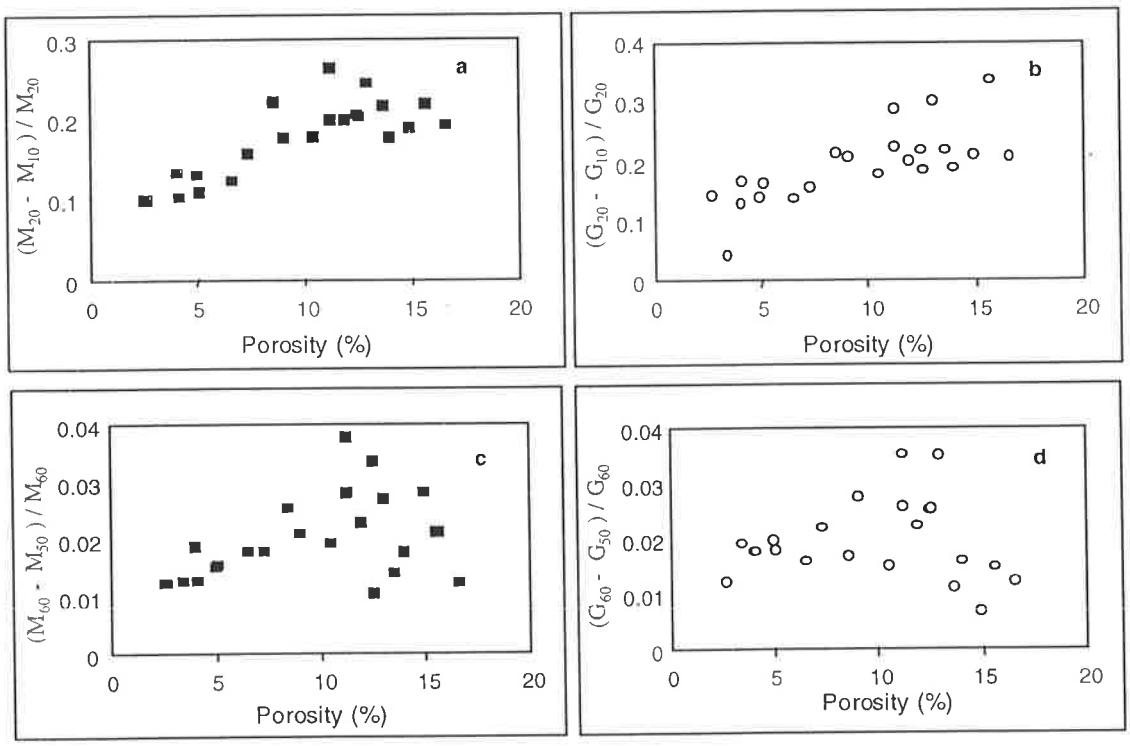

Figure 6.19. Relative differential-stress elastic moduli versus porosity for Cooper Basin samples.

6.4. Discussion and Conclusions

The rapid increase in velocity over the confining stress range of 5 MPa to 40 MPa results from the closure of the low aspect ratio pores (connective pores) which act as defects in the solid part of the rock. Nevertheless some of these micro-cracks are artefacts that could have been created by unloading and stress relief processes during drilling and coring at the well site. The closure of low aspect ratio pores, which Figure 6.2 demonstrates, hardly changes the rock porosity, improves the grain contact conditions in the rock skeleton and increases the rock's stiffness through an increase in elastic moduli. At stresses above 40 MPa velocity increases at a reduced rate,

It is found that the change of velocity with stress in the Cooper Basin sandstones may be defined by a non-linear function of the form of $V = A - Be^{-DP}$. In this equation V and P are velocity and confining stress and A, B, D are regression coefficients determined from the observations. This equation gives improved prediction of velocities at high stresses compared to an alternative equation (Figure 6.4) published by Eberhart-Phillips et al. (1989). The non-linear equation is also applicable to the velocity-stress data for dry sandstones published by Freund (1992).

The absence of a linear relationship in the velocity-confining stress curve within the measured stress ranges may indicate that the crack-closure stress in the samples studied may be beyond the experimental limits. The predicted crack-closure stress ($P_{closure}$) of the samples range from 70 MPa to 95 MPa with no significant correlation with porosity (Figure 6.11), permeability or clay content.

There is a positive correlation between change in velocity with confining stress (velocity gradient) and both core porosity and permeability, but this association becomes weaker with increasing stress (Figures 6.12 and 6.13). The increase of stress sensitivity with increasing porosity has also been demonstrated by the relationship between relative differential-stress elastic moduli and porosity in the Cooper Basin samples (Figure 6.19).

The plots of absolute differential-stress elastic moduli and porosity show insignificant correlation (Figure 6.18). Using the ratio of velocity gradient of V_p and V_s in comparing stress sensitivity of velocities it appears that the stress sensitivity of V_p is significantly higher than that for V_s at elevated confining stresses. Pore geometry and the nature of

grain-contact type may be more important than total porosity in describing the stress sensitivity of sandstones at in situ reservoir pressure conditions. No significant relationship was found between either clay content (Figure 6.14) or average grain size with the stress sensitivity of wave velocities. The distribution and location of clay particles within the rock framework (quartz grains) may be more important than the total volumetric clay content in determining the stress dependency of velocity in sandstones.

Chapter 7

Effective Stress Coefficient for Wave Velocities and Quality factors

7.1. Background and Introduction

Pore pressure (P_p) and confining stress (P_c) have opposing controls on many physical properties of porous rock such as bulk and pore volume compression, permeability, electrical resistivity and acoustic velocity. The different influences of pore pressure and confining stress on rock properties lead to the concept of effective stress, P_e. This defines pressure dependent physical properties in terms of effective stress, P_e, defined as (equation 3.18):

$$P_e = P_c - nP_p, \qquad (7.1)$$

where n is effective stress coefficient. Following Biot's theory, equation (7.2) has been used to empirically determine the effective stress coefficient for compressional velocity (Todd and Simmons, 1972) and other stress-dependent physical properties (Christensen and Wang (1985), Prasad and Manghnani (1997)).

$$n = 1 - [\partial A/\partial P_p]_{Pd} [\partial A/\partial P_d]_{Pp}^{-1} \qquad (7.2)$$

where A is the above mentioned physical property and P_d is differential pressure equal to the difference between confining stress and pore pressure (P_c - P_p). The stress dependent nature of n in equation (7.2) implies that it may vary from rock to rock depending on the particular pore structure and mineral composition of the rock. Although the effective stress relationship is valid for many physical quantities, different physical quantities in a particular rock type could show different effective stress coefficients (Nur and Byerlee, (1971), Zimmerman, (1991)).

This chapter presents data on the pore pressure dependencies of velocities and quality factors of compressional and shear waves under a range of pore pressures and confining stresses, in a water saturated Cooper Basin sandstone. The effective stress coefficients for wave velocities and quality factors for the sample are determined from experimental results and the potential of these measurements for seismic interpretation is highlighted.

7.2. Sample and Measurement Technique

Compressional and shear wave velocities (V_p and V_s) and quality factors (Q_p and Q_s) were measured under various differential pressures on sample D7 under fully water-saturated conditions. The sample D7 is a fine grain size, moderately well-sorted sublitharenite. Quartz grains are mono-crystalline, sub-rounded to rounded and show significant authigenic overgrowth. The rock is supported by quartz-quartz framework with abundant straight line and mostly clay-free contacts between the quartz grains (Figure 7.1). Clay minerals are authigenic kaolinite and illite. Rock fragments are muddy with few mica grains showing compaction features. The altered and squashed rock fragments fill spaces between adjacent quartz grains and resemble a pseudo-matrix in some parts of the sample. The physical and mineralogical characters of the sample D7 are listed in Table 7.1.

The technique of obtaining fully water-saturated samples and the procedure of ultrasonic measurements are described in Chapter 5. Velocity and attenuation were measured a) whilst increasing confining stress from 10 MPa to 65 MPa with the pore pressure kept constant at 5 MPa and b) at differential pressures of 10 MPa to 40 MPa achieved by changing both the pore pressure and confining stress simultaneously. The stress condition was maintained at each pressure level for one-hour prior to each acoustic measurement.

Depth (m)	Porosity (%)	Permeability (mD)	Bulk density (g/cm^3)	Grain size (μm)	Quartz (%)	Clay (%)	Rock fragment (%)	Other minerals (%)
2220.3	11.9	2.05	2.33	185	67.5	10.0	6.4	2.1

Table 7.1. Petrographical and petrophysical properties of sample D7. Other minerals include mica, carbonate, feldspar, opaque and organic matter.

Figure 7.1. Micrographs of sample D7 used for determination of the effective stress coefficient for wave velocities and quality factors. Scale bar = 200 μm.

A general view of the petrography and pore geometry of the sample. Quartz (q) is the main mineral which forms the framework of the rock. Rock fragments (r) are sedimentary in origin. Clay minerals are authigenic kaolinite (k) and illite with dominant kaolinite. Traces of mica (m) and carbonate (not shown here) are also present. Porosity is shown in blue. The three main pore types are: intergranular (macropores), clay associated (micropores) and low aspect ratio (connective) pores. Black arrows in the lower graph show connective pores at loos grain contacts. Micrograph (b) is the crossed-nichols view of micrograph (a).

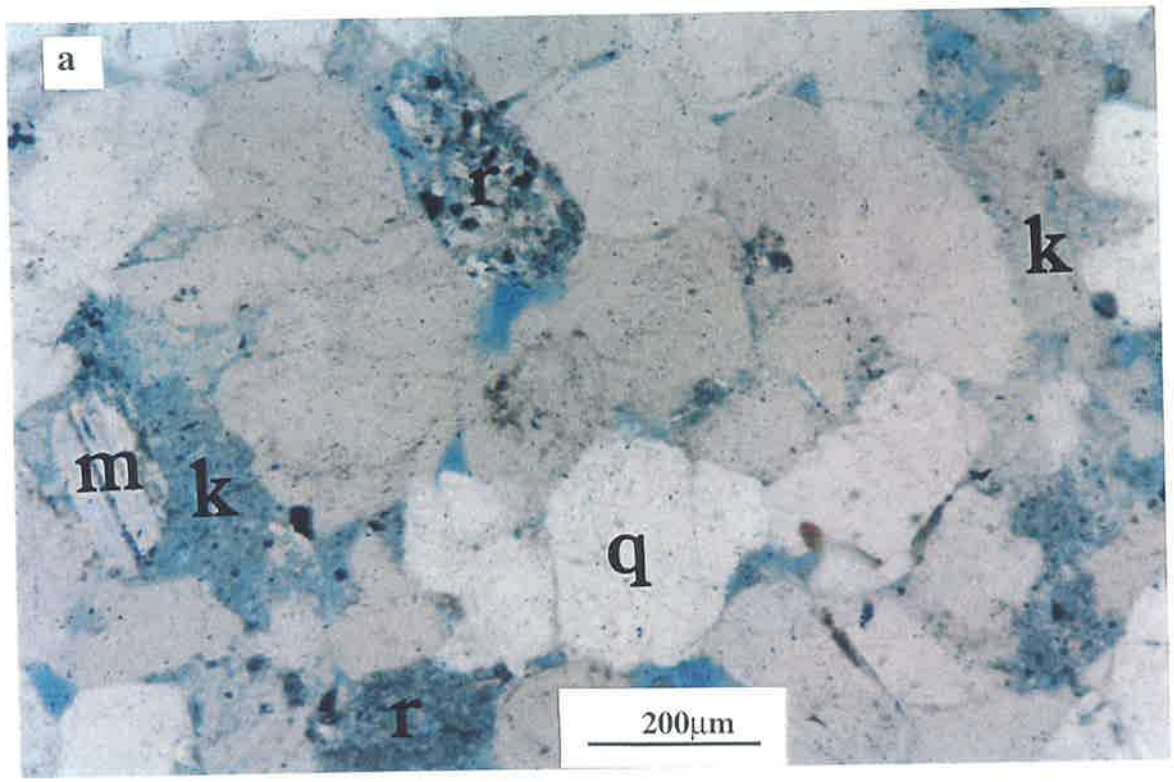
a
r
k
m
k
q
r
200μm

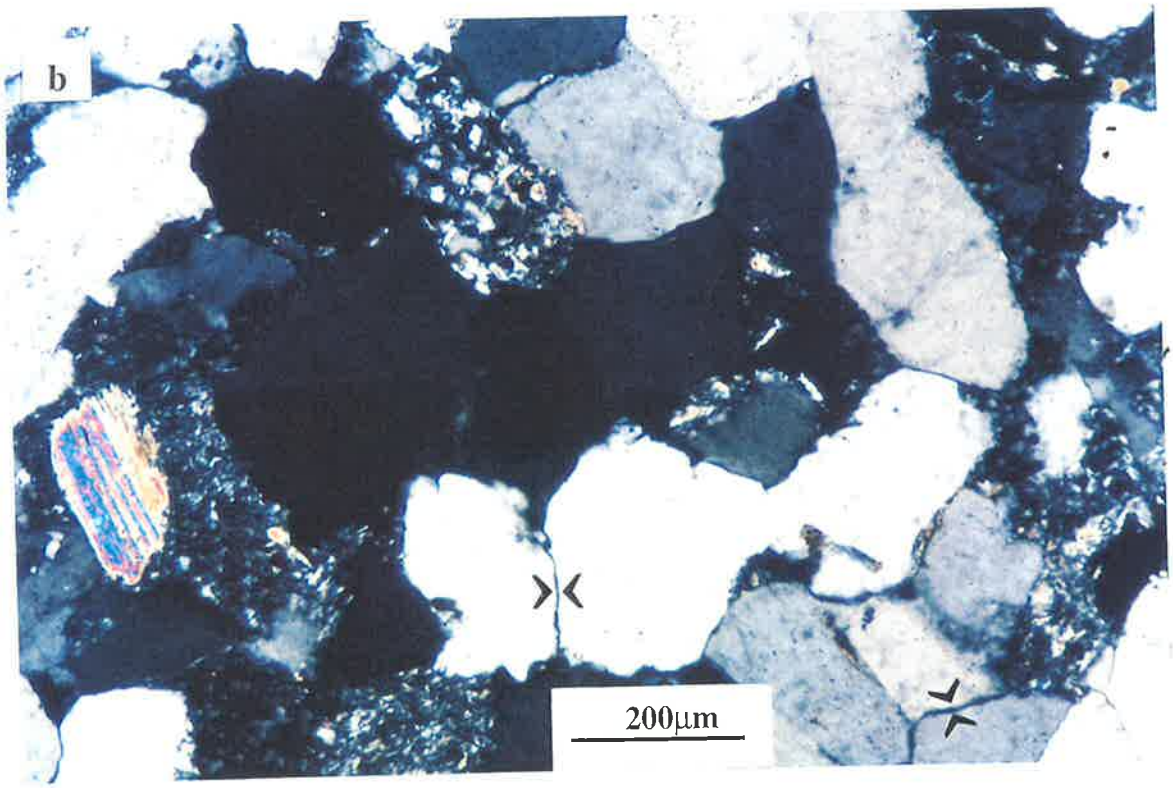
b
200μm

7.3. Results

Figure 7.2 shows the velocities and quality factors of sample D7 measured over differential pressures ranging between 5 and 60 MPa. The measured acoustic properties of the sample are listed in Table 7.2. The P- and S-wave velocities increase non-linearly with increasing confining stress. The rapid increase of velocities and quality factors at low pressures is generally attributed to the closure of low aspect-ratio pores such as microcracks and loose grain contacts within the framework of the rock (Nur and Simmons (1969) and Toksoz et al. (1976)). At differential pressures greater than 40 MPa the velocity-differential pressure gradient, although reduced, remains significant. The decreases in the slopes of the variation of Q_p and Q_s versus confining stress above 40 MPa also correspond to the influence of microcrack closure on wave attenuation.

Figure 7.3 shows velocities and quality factors plotted as a function of confining stress for a set of constant differential pressures with varying pore pressures. Figure 7.3 indicates that the measured velocities and quality factors at elevated differential pressures are not constant, showing a noticeable increase with increasing pore pressure. At constant P_d, the increase of both P- and S-wave velocities with increasing pore pressure, is greatest at low differential pressure (about 2%) decreasing with increasing P_d. At high P_d, the velocities increase systematically with pore pressure. The magnitude of increase in V_p and V_s with increasing pore pressure at high P_d is around 0.3%. Compared with the velocities, Q_p and Q_s show greater sensitivity (between 8% and 11%) to the pore pressure showing a steady increase as differential pressure increases. Investigation by Prasad and Manghnani (1997) demonstrated a similar trend for Q_p versus pore pressure at constant P_d for Berea and Michigan sandstones. The observation on the variation of Q_s with pore pressure at constant P_d is novel and has not been published elsewhere.

7.4. Empirical Determination of Effective Stress Coefficient

Comparison of Figures 7.2 and 7.3 reveals that the velocities and quality factors of compressional and shear waves in the sample are functions of both pore pressure and differential pressure, although the effect of P_p is smaller than that of differential pressure. The pore pressure dependence of velocity and quality factor implies that, for the sample D7, P_p does not exactly cancel the effect of P_c. Hence $P_d \neq P_e$ and therefore $n \neq 1$ for the measured acoustic properties.

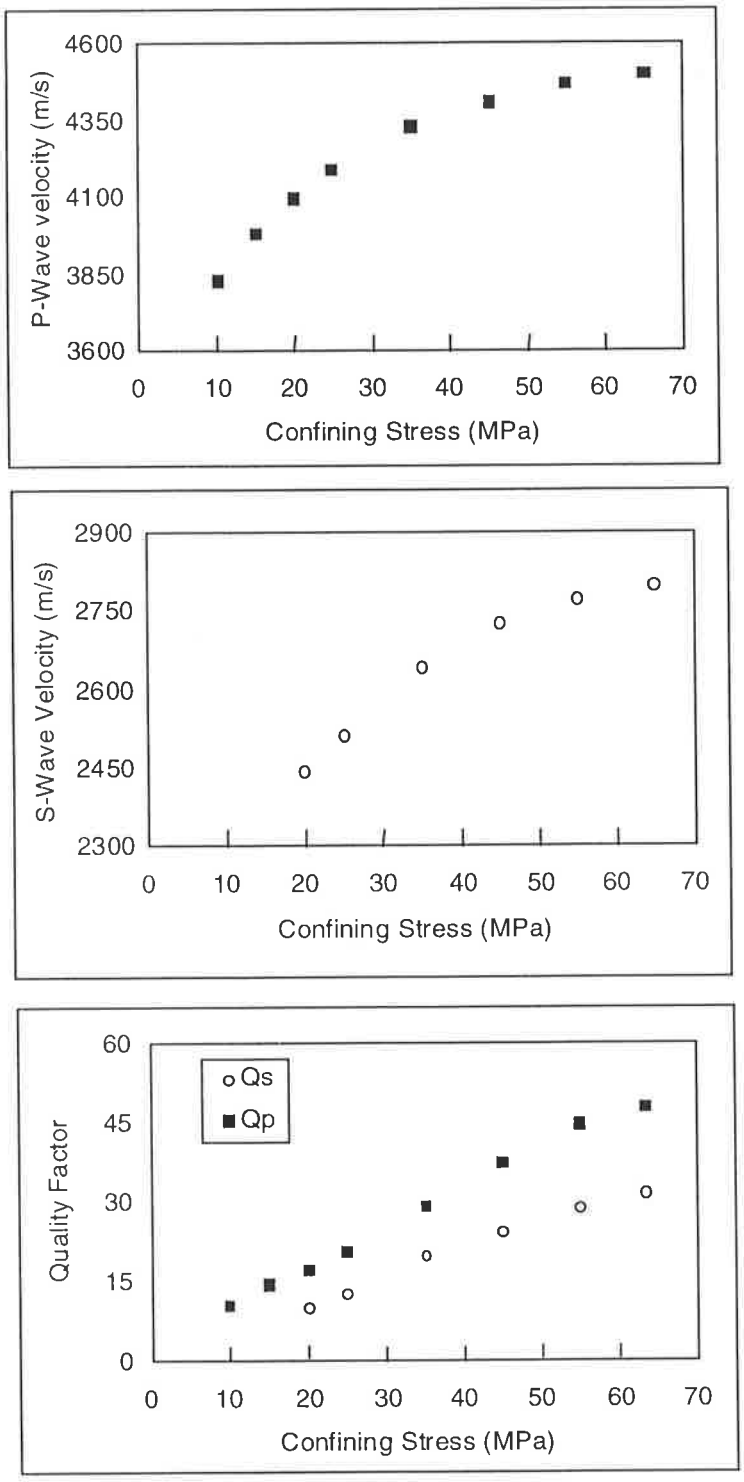

Figure 7.2. P- and S-wave velocities and quality factors versus confining stress for sample D7. Measurements were made at constant pore pressure of 5 MPa.

P_c (MPa)	P_p (MPa)	V_p (m/s)	V_s (m/s)	Q_p	Q_s
10.0	5.0	3831	-	10.1	-
10.5	0.5	3973	-	14.9	-
20.0	5.0	4093	2471	17.1	10.0
20.0	10.0	4004	-	15.6	-
21.5	1.5	-	2501	-	14.1
25.0	5.0	4190	2510	20.6	12.5
30.0	20.0	4031	-	15.7	-
30.0	10.0	4160	2512	18.2	14.1
31.0	1.0	4303	2630	25.3	16.5
35.0	5.0	4310	2632	26.1	17.8
40.0	30.0	4042	-	16.2	-
40.0	20.0	4163	2528	18.3	15.2
40.0	10.0	4317	2633	27.2	18.9
42.5	2.5	4402	2724	32.2	17.8
45.0	5.0	4404	2724	37.2	24.2
47.5	7.5	4403	2725	33.6	18.9
50.0	40.0	4061	-	16.2	-
50.0	30.0	4183	2554	18.4	15.5
50.0	20.0	4319	2639	28.2	19.3
52.5	12.5	4403	2726	35.2	21.1
55.0	5.0	4468	2771	44.5	28.7
55.0	35.0	4189	2551	19.9	15.6
55.0	25.0	-	2641	-	19.7
57.5	17.5	4403	2728	35.5	21.8
65.0	5.0	4499	2797	48.1	31.3

Table 7.2. Compressional and shear velocities and quality factors at various confining stress and pore pressure conditions for sample D7.

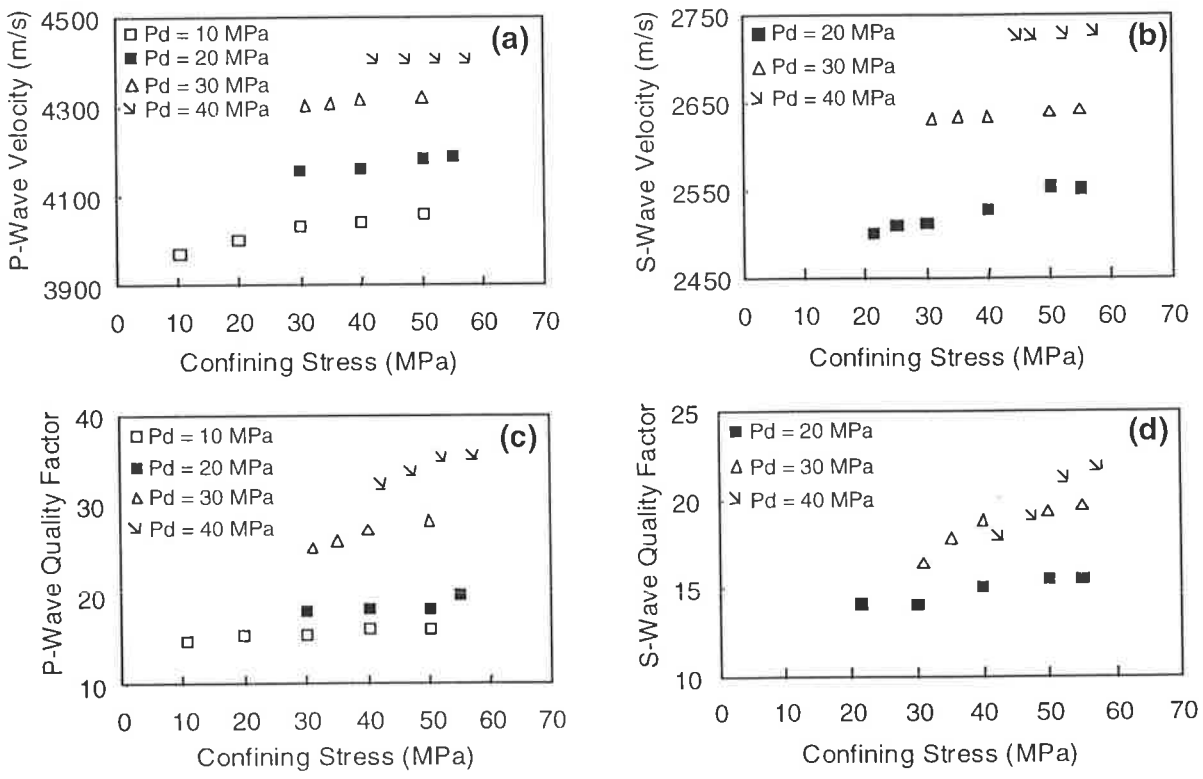

Figure 7.3. P- and S-wave velocities and quality factors as a function of confining stress (P_c) and differential pressure (P_d) in sample D7.

In order to determine the effective stress coefficients for V_p, V_s, Q_p and Q_s in the sample, equation (7.2) was solved for each parameter with the use of experimental data. As the changes in P_p and P_c were identical ($\partial P_p = \partial P_c$), the values of $[\partial A/\partial P_p]_{Pd}$ were determined from the slopes of graphs in Figure 7.3 for the corresponding parameter. Similarly values of $[\partial A/\partial P_d]_{Pp}$ were determined from Figure 7.2 for P_p equal to 5 MPa. Table 7.3 lists the calculated n factors for the velocities and quality factors of the sample D7. The effective stress coefficients of the dynamic elastic moduli of the sample can also be calculated in a similar way.

P_d (MPa)	$[\partial V_p/\partial P_p]_{Pd}$	n_p	$[\partial Q_p/\partial P_p]_{Pd}$	n_{Qp}	$[\partial V_s/\partial P_p]_{Pd}$	n_s	$[\partial Q_s/\partial P_p]_{Pd}$	n_{Qs}
10	2.15	0.91	0.03	0.95	-	-	-	-
20	1.22	0.94	0.05	0.93	1.61	0.87	0.05	0.89
30	0.83	0.95	0.10	0.86	0.38	0.96	0.85	0.74
40	0.06	0.99	0.23	0.69	0.16	0.97	0.21	0.51

Table 7.3. Empirical effective stress coefficients for V_p, V_s, Q_p and Q_s in the sample D7 at elevated differential pressures and varying P_p and P_c.

7.5. Discussion

Table 7.3 enables the following conclusions to be drawn:

a). n has different values for the velocities and the quality factors;

b). n is less than one for both velocities and quality factors, and

c). n increases for velocity and decreases for quality factor with the increase of P_d.

The increase in the effective stress coefficients for V_p and V_s with increase of P_d have also been reported for water saturated low porosity Chelmsford granite and Trigg limestone (Todd and Simmons, 1972), for coal (Yu et al., 1991) and for an outcrop carbonate (Ringstad and Fjaer, 1997). These experimental results are consistent with Biot's theory of the elastic wave propagation in fluid saturated porous rocks (Todd and Simmons, 1972). The closure of cracks in rocks is thought to be responsible for the increase of velocity with increasing P_d, whereas small changes in pore fluid compressibility (Prasad and Manghnani, 1997) may partly explain the slight increase of V_p with pore pressure increase at constant

P_d. Nevertheless the change of pore fluid properties with increase of pore pressure does not explain the increase of V_s with pore pressure increase at constant P_d.

Furthermore, the strong dependence of quality factor on pore pressure particularly at high P_d implies that the experimental data cannot be fully explained by crack closure. Squirt flow due to microcracks (eg Mavko and Nur, 1979) has been established to be an important mechanism causing wave attenuation in rocks. Klimentos and McCann (1990) and Best and McCann (1995) showed that clay minerals may also have strong influence on wave attenuation at ultrasonic frequencies in sandstones. These authors gave experimental evidence showing that, at high differential pressure, attenuation due to microcrack may become negligible and clay particles at grain contacts become a dominant cause of ultrasonic wave attenuation.

The grain contact model (for example, Zoback and Byerlee (1974) and Christensen and Wang (1985)) which considers the different reactions of quartz grains and clay particles to differential pressure may explain the increase of quality factors with increasing pore pressure at high P_d. Quartz grains in a low compressibility rock framework respond to differential pressure by changes in contact conditions (the microcrack effect). Due to their micro-porosity and high compressibility, pore-filling and grain-coating clay particles are more sensitive to the pore pressure change. Whilst the equivalent increase of pore pressure and confining stress (constant P_d) has little effect on crack density and the grain-grain contacts of quartz grains, the pore pressure increase may significantly change the clay-clay and clay-quartz contact conditions and change the pore geometry within the clay aggregates, may lead to slight increase in velocities and quality factors.

7.6. Practical Applications

The magnitudes of the effective stress coefficients of V_p and V_s for the sample D7, approach unity as the differential pressure increases (Table 7.3). Assuming the simple differential pressure dependence $n = 1$, at high differential pressures ($P_d > 30$ MPa), results in less than one-percent error in the V_p and V_s measurements obtained under varying pore pressure. The Cooper Basin sandstones have an in situ reservoir effective stress of between 25 MPa to 50 MPa. Consequently the error caused by assuming $P_e = P_d$ is practically insignificant. In contrast, the influence of pore pressure on the quality factors increases at high P_d, as indicated in Table 7.3. Assuming that the effective stress dependence is unity

may result in an 8% to 11% error in Q, as measured at varying pore pressures. It must be emphasized that the data presented here have been obtained at ultrasonic frequencies on a 2 cm thick core plug. For P-wave velocities there are increasing number of publications showing that the effects of changes in reservoir pressure conditions on seismic and sonic logs at field scales are comparable with ultrasonic results at laboratory scale (for example, Khaksar and Griffiths (1996a, 1998c), Watts et al. (1996), Best and Sams (1997) and Lumley et al, (1997)). Very limited data are available on the variation of Q with pore pressure changes, and therefore the trends presented in this chapter for sample D7 remain to be tested for Q data at seismic frequencies and on the reservoir scale. Further experiments relating quality factors to pore pressure are necessary to confirm these results at lower frequency ranges. Future studies should focus on sandstones with different mineralogies, different types and amount of clay and pore geometries.

7.7. Summary and Conclusions

Compressional- and shear-wave velocities and quality factors were measured as a function of confining stress and pore pressure on a fully water-saturated sandstone core from the Cooper Basin. The experimental results show that wave velocities and quality factors of the sample are sharply dependent on differential pressure and somewhat less dependent on pore pressure changes at constant P_d. Thus equal increments of pore pressure and confining stress, do not have a precisely zero effect on the measured acoustic properties. It has been shown that V_p, V_s, Q_p and Q_s in the Cooper Basin sandstone depend on effective stress, defined as $P_e = P_c - nP_p$, with $n \leq 1$. The value of the effective stress coefficients for V_p and V_s approaches unity at high differential pressures. This observation is consistent with data on low porosity granite and carbonate rock reported by Todd and Simmons (1972), and on coal by Yu et al. (1991). The pore pressure dependency of Q_p and Q_s for the Cooper Basin sandstone increases as the differential pressure increases. The strong effect of pore pressure on Q_p and Q_s at high P_d is attributed to the wave attenuation due to pore filling clay minerals. Assuming the simple differential pressure dependence ($n = 1$) results in 8 to 11 percent error in Q measurements under varying pore pressure while similar assumption for velocity causes negligible error. Prasad and Manghnani (1997) showed similar pore pressure dependency of Q_p for Berea and Michigan sandstones. Further measurements are needed to verify these observations at seismic and sonic log frequencies and on different rock types.

Chapter 8

Velocity in Water-Saturated Sandstones

8.1. Introduction

This chapter investigates the effect of pore fluid on the stress sensitivity of velocities in 21 water-saturated Cooper Basin sandstones. The experimental results are compared with velocities measured under dry conditions. The influence of porosity and clay content on V_p and V_s for water-saturated samples are examined under elevated effective stresses and the observed relationships are compared with other studies.

8.2. Samples and Measurement Techniques

V_p and V_s were measured at elevated effective stresses from 60 MPa to 5 MPa on 21 water-saturated Cooper Basin core samples. Samples are described in Chapter 4. The samples were fully saturated with distilled, de-ionized and de-aired water using the method described in Chapter 5. Sample S4 collapsed during measurement and no acoustic measurements were performed on this sample under water-saturated conditions. For sample D8 shear velocity could not be acquired due to a technical problem. For the remaining samples the acoustic measurements were undertaken under varying confining stresses while pore pressure was kept constant at 5 MPa. The effective stress at each confining stress level was calculated from equation 7.1 assuming effective stress coefficient, n, equal to one. Pore pressure and confining stress were maintained at each pressure level for 30 minutes prior to each acoustic measurement and throughout the experiment.

8.3. Results

Both compressional and shear velocities increase non-linearly over an effective stress range of 5 to 60 MPa. All experimental data on Vp and Vs in water-saturated samples are tabulated in Appendix D. Equation 6.3 was used to generalise change of velocity with

effective stress in the water-saturated samples. Table 8.1 shows the regression parameters in equation 6.3 for the velocities of the water-saturated samples.

Figure 8.1 shows the relationship between porosity and the calculated regression coefficients in equation 6.3 for the studied samples. For samples with core porosity less than 10% the value of D decreases as porosity increases whereas for other samples it shows a positive trend with porosity. In general, trends between the petrophysical properties and the calculated regression coefficients for water-saturated samples are similar to those showed in Chapter 6 for dry samples.

Sample	A_p	B_p	D_p	A_s	B_s	D_s
D1	4744	851	0.052	2984	785	0.041
D2	4658	1145	0.048	2954	867	0.040
D3	4346	791	0.039	2735	652	0.038
D4	4655	1059	0.052	2895	991	0.056
D6	4493	1087	0.043	2932	912	0.035
D7	4559	907	0.045	2828	761	0.039
D8	4706	1024	0.044	-	-	-
D10	4664	1004	0.013	2681	867	0.048
M1	5274	637	0.020	3401	723	0.030
M2	5024	598	0.040	3278	549	0.046
M7	5104	1196	0.095	317	802	0.071
M8	5160	878	0.057	3239	915	0.057
M10	5211	778	0.044	3265	1239	0.064
M11	5369	612	0.026	3340	857	0.050
M13	5855	1461	0.01	3169	648	0.039
S1	4600	942	0.031	2843	813	0.037
S2	4638	912	0.041	2911	665	0.042
S3	4263	835	0.051	2582	811	0.067
S4	-	-	-	-	-	-
S5	4273	849	0.047	2641	742	0.054
S6	4318	1103	0.063	2676	846	0.061
S7	3982	1159	0.052	2750	711	0.041

Table 8.1. Regression coefficients in equation (6.3) for V_p and V_s measured at water-saturated condition for the studied samples.

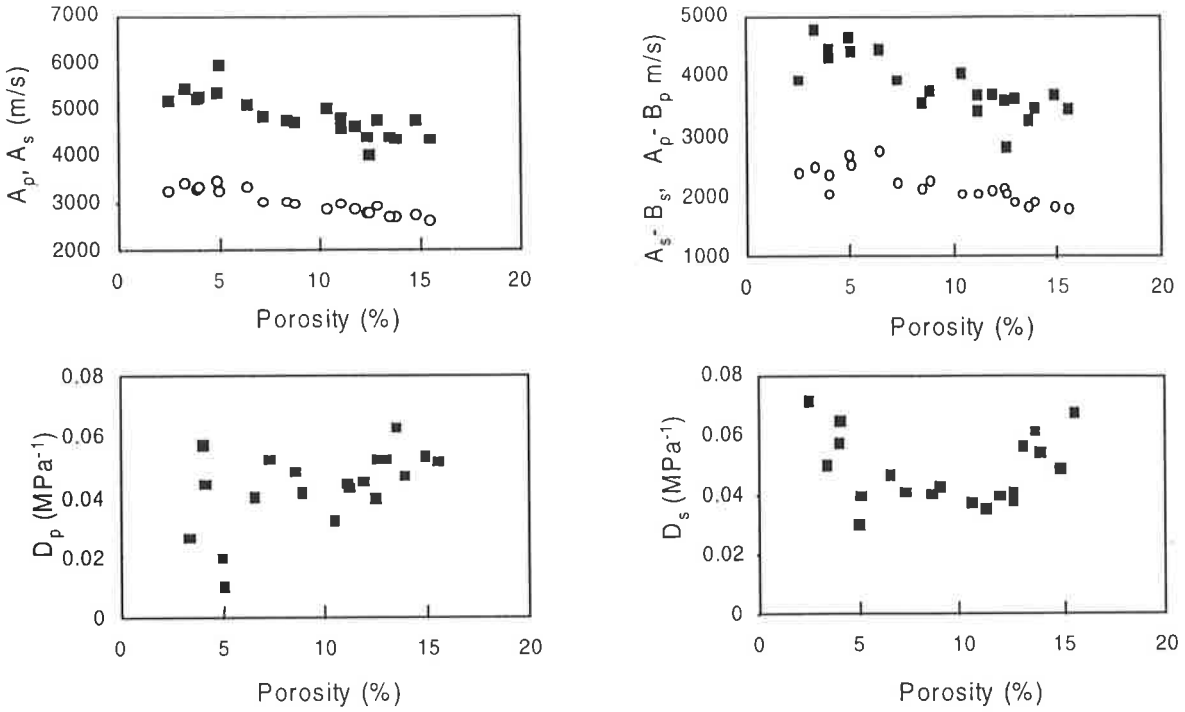

Figure 8.1. Calculated regression coefficients in equation (6.3) for V_p and V_s in water saturated samples versus porosity. The subscripts "p" and "s" in vertical axes refer to compressional and shear waves respectively.

Figure 8.2 indicates that a similar trend also exists between core porosity and clay content versus the velocity gradient under both dry and water-saturated conditions for the studied samples. This trend is weak and diminishes at high effective stresses. However a negative correlation exists between porosity and the velocity gradients for both V_p and V_s for water-saturated samples with core porosity greater than 10%, at high effective stresses (P_e > 30 MPa). This is consistent with the relationship between core porosity and parameter D in equation (6.3) as illustrated in Figure 8.2.

The correlation between velocity gradient and porosity for high porosity (ϕ> 10%) samples becomes stronger as effective stress increases, particularly for V_s. The absence of a single trend between the velocity gradient and core porosity in the data set implies that the total porosity may not reasonably describe the stress sensitivity of the studied samples.

In Chapter 6 it was demonstrated that at high confining stresses (P_c > 50 MPa) the velocity gradient of the dry samples may be related to the position of the clay particles in regard to connective pores within the rock skeleton. For the water-saturated samples, however such a relationship between stress sensitivity and the position of clay minerals is not apparent.

The effect of water on pore compressibility may explain why the clay position and its relation to the microstructure are not so important for stress sensitivity of velocities under water saturated conditions. The presence of water filling the pore spaces, particularly the micropores (pores within clay aggregates) and low aspect ratio pores, may cause a more uniform pore compressibility within the sample. Consequently, under water saturated conditions, samples with clay-free connective pores do not show significantly different stress sensitivity compared to the samples with a greater amount of clay-filled connective pores (Khaksar and Griffiths 1998b).

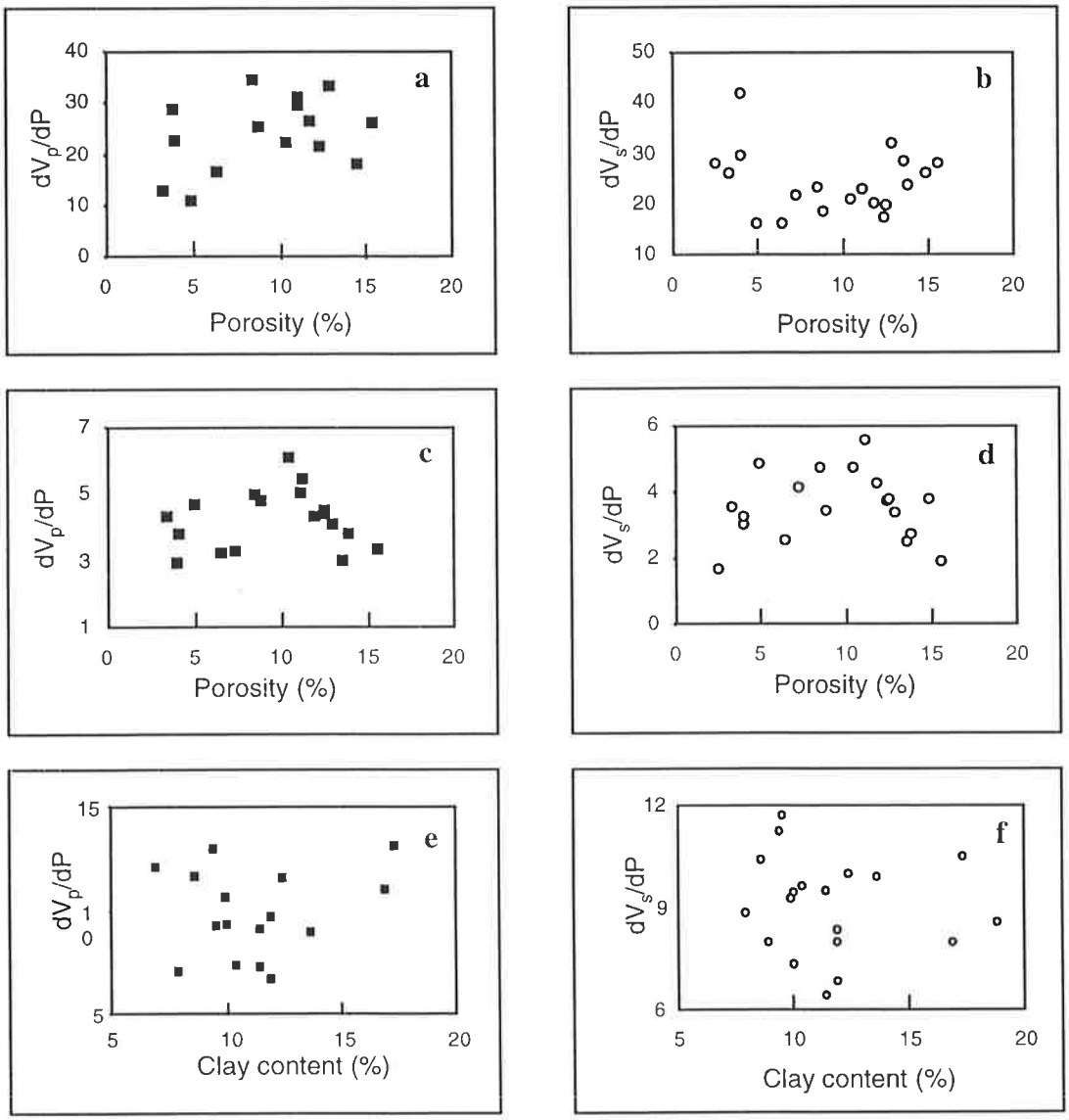

Figure 8.2. Relationship between velocity gradient (dV/dP) and porosity (a-d) and clay content (e and f) for water-saturated samples at various effective stresses; 10 MPa (a and b), 30 MPa (e and f) and 50 MPa (c and d).

Figure 8.3 plots the calculated VGR (the ratio of the of P-wave velocity gradient to the S-wave velocity gradient, equation 6.4) versus porosity for water-saturated samples at various effective stresses. In general at elevated effective stresses the overall stress sensitivity of V_p is slightly higher than V_s's with VGR showing an average value between 1.1 and 1.2 within the studied samples. At effective stresses below 40 MPa the VGR increases as core porosity increases with a very low gradient (Figure 8.3a and 8.3b). However, at higher effective stresses the value of VGR is independent of core porosity (Figure 8.3c).

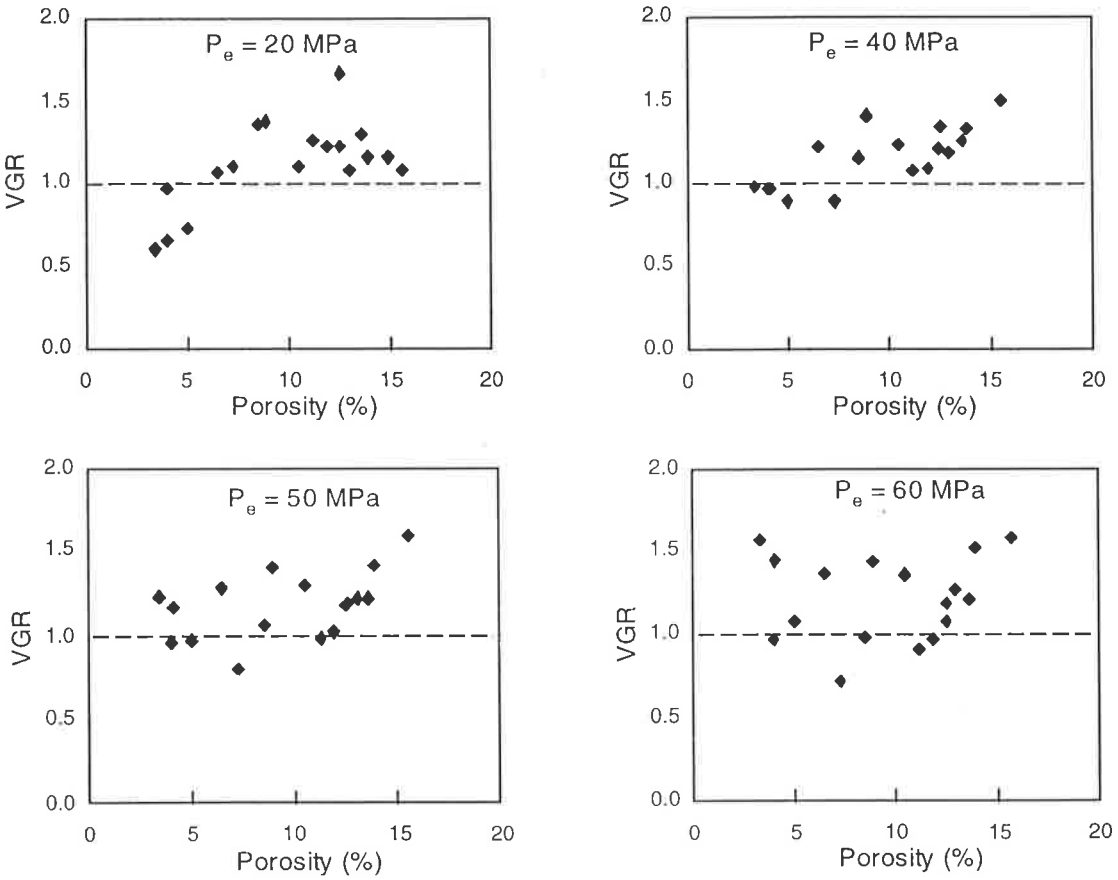

Figure 8.3. Plots of ratio of the P-wave velocity gradients to the S-wave velocity gradient versus core porosity for water-saturated samples at various effective stresses.

8.3. Comparison of Stress Sensitivity in Dry and Water-Saturated Samples

Figure 8.4 shows the variation of V_p and V_s with effective stress for two Cooper Basin sandstones under both dry and water saturated conditions. Experimental results reported by King (1966) showed a similar relationship between velocities measured under dry and water saturated conditions for Berea and Torpedo sandstones. For a water-saturated rock the finite modulus of the water increases the bulk modulus of the rock and resists the

closure of cracks. At low effective stresses (P_e < 30 MPa), a sample is stiffer (higher bulk modulus) when it is saturated with water, so the compressional waves propagate faster in a water-saturated sample. With the increase of effective stress and as a result of closure of crack-like pores the moduli of dry samples increase at a faster rate compared with water saturated condition. So at high effective stresses (P_e ~ 40 MPa) the V_p-effective stress curve of the dry and water-saturated samples cross over. At higher effective stresses the influence of the compressibility difference between water and air on both the magnitude and stress sensitivity of velocities become less important, even though the magnitude of V_p for the dry samples slightly exceed the value of V_p at water-saturated condition. The lower values of S-wave velocities in water saturated samples shown in Figure 8.4 simply results from the higher value of bulk density compared with that under dry conditions.

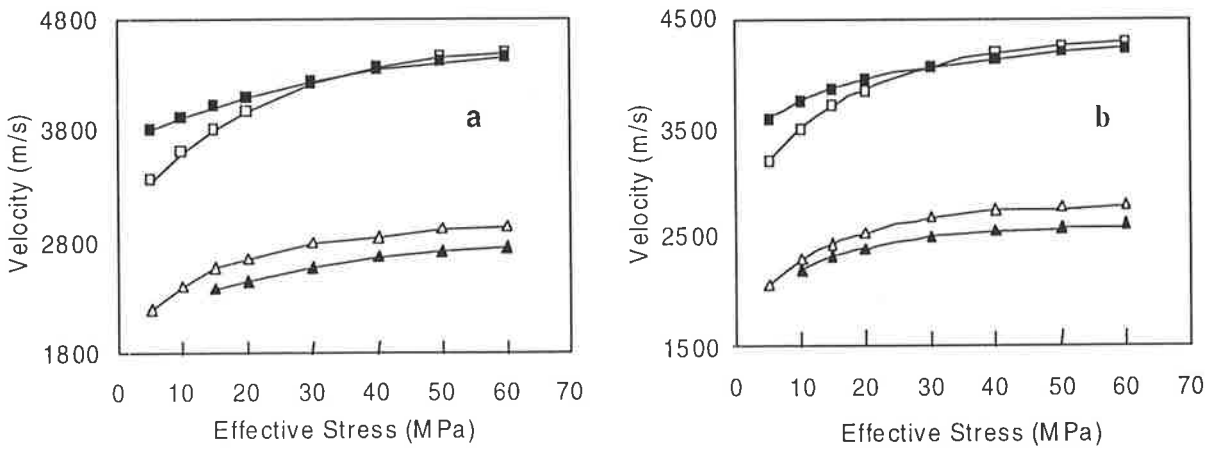

Figure 8.4. V_p and V_s a function of effective stress for two Cooper Basin sandstones. (a) sample D2 with ambient core porosity of 8.5%, (b) sample S5 with ambient core porosity of 13.9%. Triangles for V_s and squares for V_p , open and solid symbols show wave velocities measured under dry and water-saturated conditions, respectively.

The above observations on the stress sensitivity of velocities in dry and water-saturated samples are consistent for all the studied samples. Similar relationships can also be derived from the comparison between the velocity gradients at dry and water-saturated conditions. Figure 8.5 demonstrates plot of the mean of the ratio of velocity gradients defined as $[(dV/dP)_{dry}/(dV/dP)_{water\ saturated}]$ for all samples versus effective stress for both compressional and shear velocities. At elevated effective stresses the ratio of velocity gradients under dry and water-saturated conditions show insignificant correlation with core porosity, permeability and clay content. The economic significance of the observations on

the strong stress sensitivity of velocities for dry samples and the different values for V_p and V_s in dry and water-saturated Cooper Basin cores is addressed in Chapter 9.

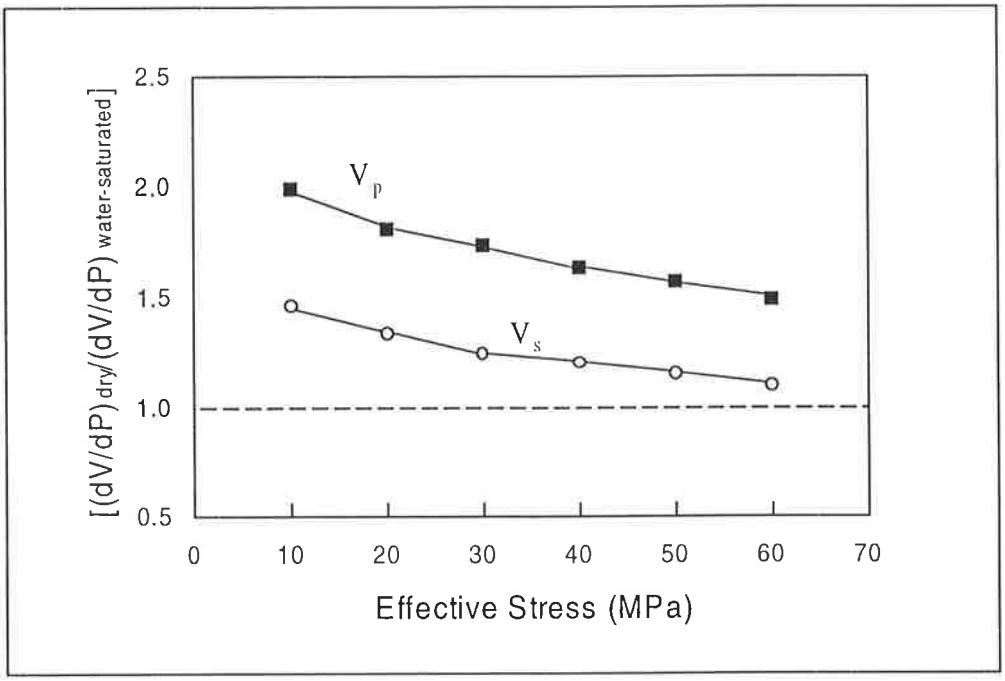

Figure 8.5. Plot of the average [$(dV/dP_{dry}$ / $(dV/dP_{water\text{-}saturated}$] versus effective stress for both compressional and shear velocities for Cooper Basin samples.

8.5. The Effect of Porosity and Clay Content on Velocities

Experimental results on velocity measurements along with petrographic and core porosity data are used to investigate the effect of porosity and pore filling material including clay content on wave velocities in the Cooper Basin samples. Empirical equations are determined for V_p and V_s as a function of porosity and clay content for dry and water-saturated samples under elevated effective stresses, and results are compared with other studies.

8.5.1. General Trends and Regression Models

Figures 8.6a and 8.6b demonstrate the plots of V_p and V_s measured under 40 MPa effective stress versus porosity for all samples at both dry and water-saturated conditions. The plots show a clear trend indicating that velocities decrease with increasing porosity. In contrast the plots of velocities versus clay content (Figures 8.6c and 8.6d) are highly scattered and do not show significant correlations. The trend between velocities and porosity and clay

content at other effective stress levels are similar to those shown in Figure 8.6. A least-square regression technique was used to find the best fit for the velocity-porosity data. Several regression models were examined. Models with the best fit and correlation coefficients were selected with the criterion of 0.05 for F value (95% confidence interval). It is found that the following simple linear model fit the data reasonably well with a correlation coefficient around 0.9 ($R^2 = 0.81$).

$$V = a - b\phi \qquad (8.1)$$

In this model, a and b are constant, ϕ is fractional porosity and V is velocity in m/s. The relative deviations of the data from the values predicted by the equation 8.1 although are small (standard deviation = 0.036), show wide scattering when they are plotted versus porosity (Figure 8.7a). In addition, the relative deviations are weakly correlated with the clay content (Figure 8.7b). Comparison of Figures 8.6 and 8.7b reveals that although the variation of the clay content is not significantly correlated with the velocities, it could influence the velocity-porosity relationship in the studied samples. A multivariate linear regression similar to the equation proposed by other researchers (eg. Tosaya and Nur (1982) and Han et al. (1986)) in the form of

$$V = a_1 - b_1\phi - c_1C \qquad (8.2)$$

was then performed on the data set. In equation 8.2, a_1, b_1 and c_1 are constant and the capital C is fractional clay content.

The correlation coefficients for both dry and water-saturated samples using equation 8.2 are slightly stronger (around 0.93) than those calculated using equation 8.1. Furthermore, as it is shown in Figures 8.8a and 8.8b, the relative deviation of the data from the values predicted by the multivariable linear equation are less scattered versus porosity (standard deviation = 0.026) and show an even distribution versus clay content. The regression and correlation coefficients of the simple and multivariable models for the studied samples at effective stress levels between 20 MPa and 60 MPa are shown in Table 8.2.

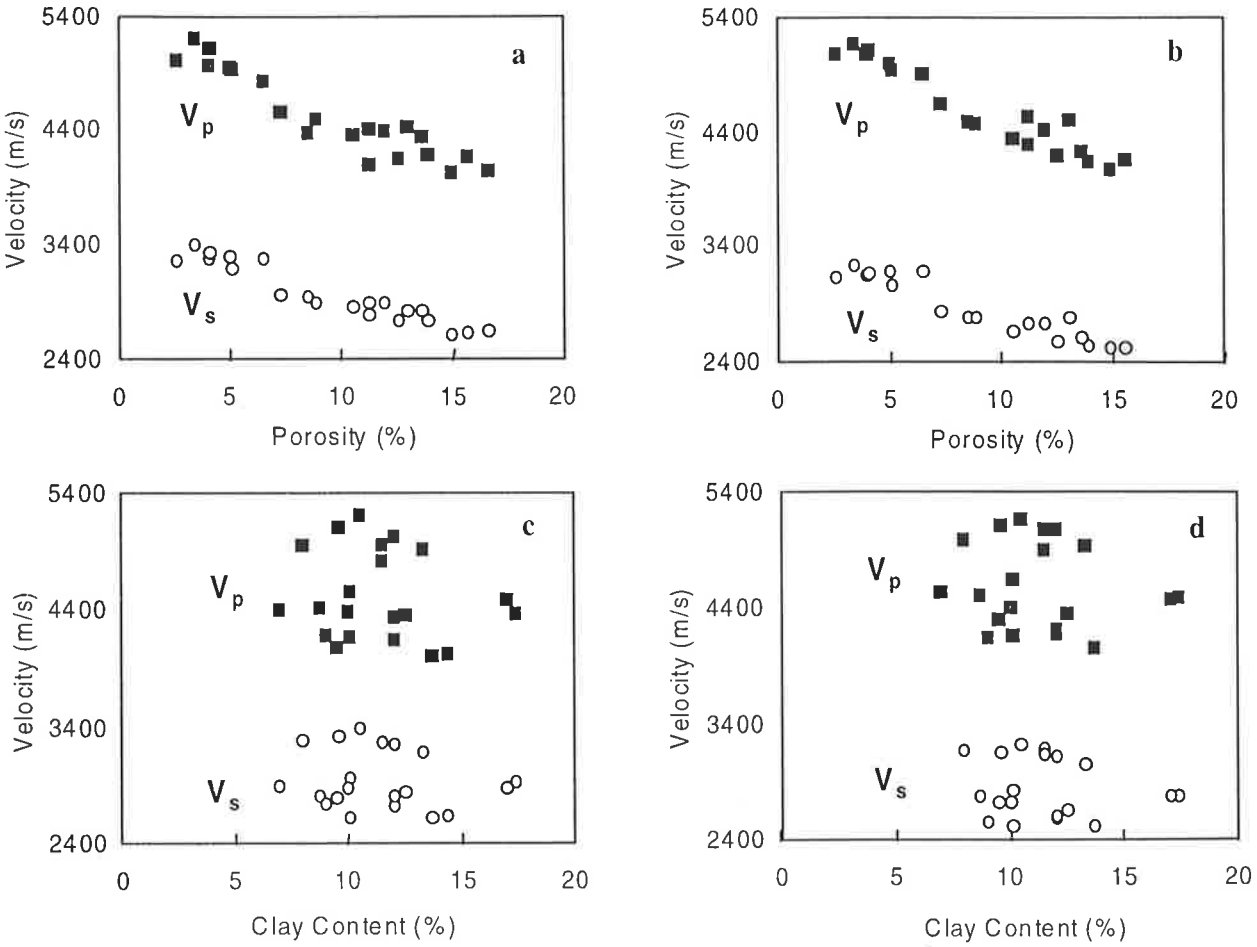

Figure 8.6. Plots of Vp and Vs measured under 40 MPa effective stress versus porosity and clay content for all studied samples. (a) and (c) dry samples, (b) and (d) water-saturated samples.

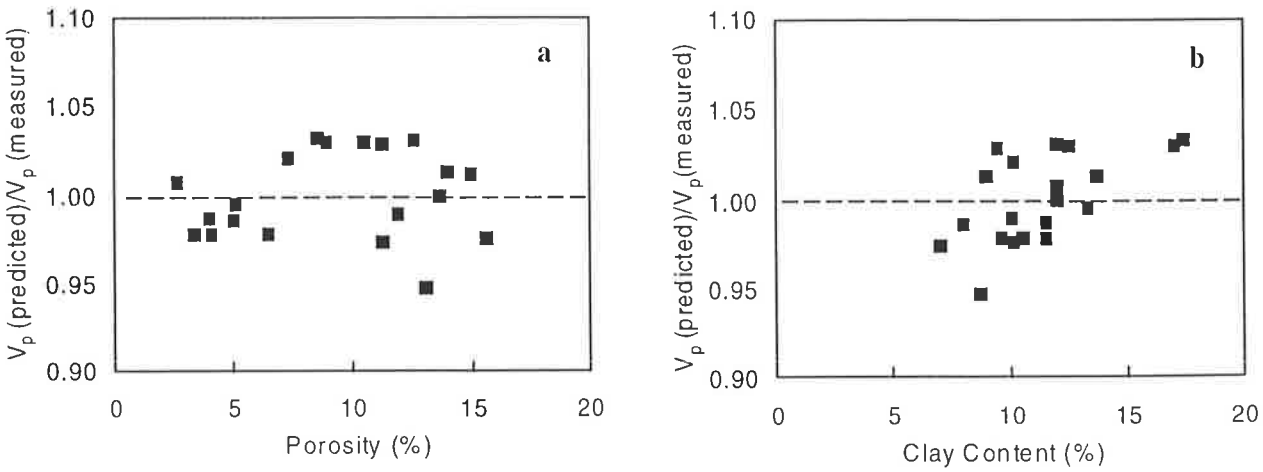

Figure 8.7. V_p fitted by a linear model (equation8.1). (a) Relative deviations of V_p versus porosity. (b) Relative deviations of V_p versus clay content. Velocities are for water-saturated samples measured at 40 MPa effective stress.

The magnitude of coefficient a_1 in the multivariable model increases and b_1 decreases with effective stress whereas there is no clear trend versus pressure for the coefficient c_1. The coefficients in the multivariate model indicate that the influence of clay content (by volume) is about 2.25 time less than that of the influence of porosity for V_p and between 3.5 and 4 for V_s. These ratios also remain relatively constant over the measured pressure range.

It should be mentioned that similar results will be obtained if instead of the clay content the fractional volume of pore filling fines, defined as sum of the non-quartz minerals and particles including clay, altered and ductile sedimentary rock fragments and organic matter in the sample, to be used for the term C in equation 8.2.

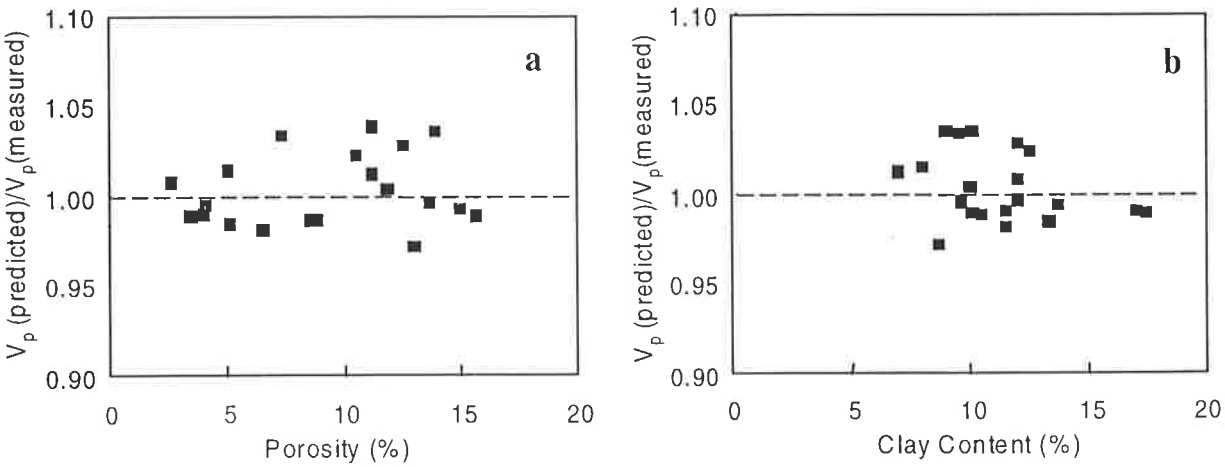

Figure 8.8. V_p fitted by a multivariate linear model (equation 8.2). (a) Relative deviations of V_p versus porosity. (b) Relative deviations of V_p versus clay content. Velocities are for water-saturated samples measured at 40 MPa effective stress.

Water-saturated condition

	$V_p = a_p + b_p\,\phi$			$V_p = a_{1p} - b_{1p}\,\phi - c_{1p}C$				$V_s = a_s + b_s\,\phi$			$V_s = a_{1s} - b_{1s}\,\phi - c_{1s}C$			
P_e (MPa)	**a_p**	**b_p**	**R_p**	**a_{1p}**	**b_{1p}**	**c_{1p}**	**R_{1p}**	**a_s**	**b_s**	**R_s**	**a_{1s}**	**b_{1s}**	**c_{1s}**	**R_{1s}**
20	5135	8336	0.883	5657	8477	4322	0.942	3143	5144	0.909	3307	5159	1356	0.923
30	5249	8156	0.901	5688	8274	3633	0.945	3263	5319	0.907	3440	5335	1462	0.922
40	5326	8163	0.897	5772	8283	3687	0.943	3328	5162	0.914	3492	5177	1355	0.928
50	5378	8093	0.887	5808	8210	3557	0.935	3400	5350	0.913	3588	5371	1548	0.932
60	5393	7922	0.873	5845	7852	3963	0.936	3433	5334	0.899	3641	5302	1819	0.930

Dry condition

	$V_p = a_p + b_p\,\phi$			$V_p = a_{1p} - b_{1p}\,\phi - c_{1p}C$				$V_s = a_s + b_s\,\phi$			$V_s = a_{1s} - b_{1s}\,\phi - c_{1s}C$			
P_e (MPa)	**a_p**	**b_p**	**R_p**	**a_{1p}**	**b_{1p}**	**c_{1p}**	**R_{1p}**	**a_s**	**b_s**	**R_s**	**a_{1s}**	**b_{1s}**	**c_{1s}**	**R_{1s}**
20	4989	8558	0.873	5315	8526	2768	0.894	3248	5194	0.886	3305*	5184*	487*	0.888*
30	5126	7871	0.852	5546	7829	3561	0.891	3361	5005	0.893	3494	4992	1136	0.904
40	5260	7745	0.895	5575	7714	2675	0.920	3461	5141	0.925	3590	5128	1095	0.934
50	5328	7600	0.900	5666	7567	2865	0.929	3511	5069	0.930	3662	5055	1273	0.944
60	5367	7524	0.899	5723	7489	3019	0.932	3545	5103	0.929	3704	5088	1352	0.944

Table 8.2. Regression (m/s) and correlation coefficients of the simple linear (equation 8.1) and multivariate linear (equation 8.2) velocity-porosity-clay models for the studied samples at various effective stresses (P_e). * Values are statistically insignificant.

8.5.2. Comparison with Previous Studies

The observation that considering a clay content term will improve the velocity-porosity transforms in the Cooper Basin sandstones is consistent with previous studies including Tosaya and Nur (1982), Castagna et al. (1985), Han et al (1986), Klimentos (1991), Freund (1992) and Vernik (1994). However the influence of clay content or pore filling fines on velocities in Cooper Basin samples appears to be weaker than has been reported in the literature for other sandstones.

For example, Han et al. (1986) showed that, for their water-saturated velocity data at 40 MPa effective stress, there is a significant difference between the correlation coefficient of the multivariate linear model and the simple linear model indicating a high dependency on clay content ($\Delta R = 0.145$ and 0.255 for V_p and V_s, respectively). Under similar effective stress conditions the corresponding ΔR for the Cooper Basin sandstones are 0.046 and 0.014, for V_p and V_s, respectively. The relative deviation of V_p versus clay content reported by Han et al. (1986) show a much stronger positive correlation (Figures 8.9b) than those in the Cooper Basin samples (Figures 8.8b). Another example of discrepancy

between the Cooper Basin sandstones and other data set in regard to the influence of clay content on velocity can be seen in the velocity data reported by Klimentos (1991). Figure 8.10 shows the variation of V_p with clay content in sandstones with core porosities between 6% and 36% studied by Klimentos (1991) indicating a clear negative correlation between V_p and clay content. In contrast, as it is demonstrated in Figure 8.6d for the Cooper Basin samples the measured P-wave velocities do not show a significant correlation with clay content.

8.6. Discussion

Several investigators commented that considering the effect of clay and fines on velocities and velocity-porosity transforms in shaly sandstones could be necessary but this effect may not adequately be explained if only the volume fraction of clay is being taking into account. Other factors including pore geometry (Xu and White (1995), textural pattern and microstructure of the rock such as grain or matrix supported (Wilkens et al. (1986), Vernik and Nur (1992)), type and the position of clay particles within the rock skeleton which may be conveniently characterised by the volume fractions (Tosaya and Nur,1982) could also have considerable influence on velocities.

The range of clay content and pore filing materials in the Cooper Basin samples studied here is relatively small compared with those cited in the literature (eg. Han et al. (1986) and Klimentos (1991)). There is no significant difference in the mineralogy of Cooper Basin sandstones in general and in the studied samples in particular. Although the Cooper Basin sandstones show a rather complex pore geometry, if one considers sedimentological and petrographic criteria, their measured acoustic properties such as velocity-pressure relation and $P_{closure}$ demonstrate similar characters indicating perhaps a rather similar microstructure in regard to wave propagation. Using the siliciclastics classification of proposed by Vernik and Nur (1992) for the velocity-porosity relationship, the samples may be classified as wackes (sandstones with $15\% < C < 35\%$ where C is the clay content plus altered grains). As discussed in Chapter 3, according to this classification there is no clay effect on both the velocity and the velocity-porosity transform for those rocks which fall in a particular class (arenites, wackes and shales) regardless of their degree of shaliness. Figure 8.11a and 8.11b demonstrate the plots of predicted V_p using Vernik's (1994) equations for arenites and wackes respectively versus measured V_p at 40 MPa effective stress for water-saturated Cooper Basin samples. Vernik's velocity-porosity equation for wackes gives a better

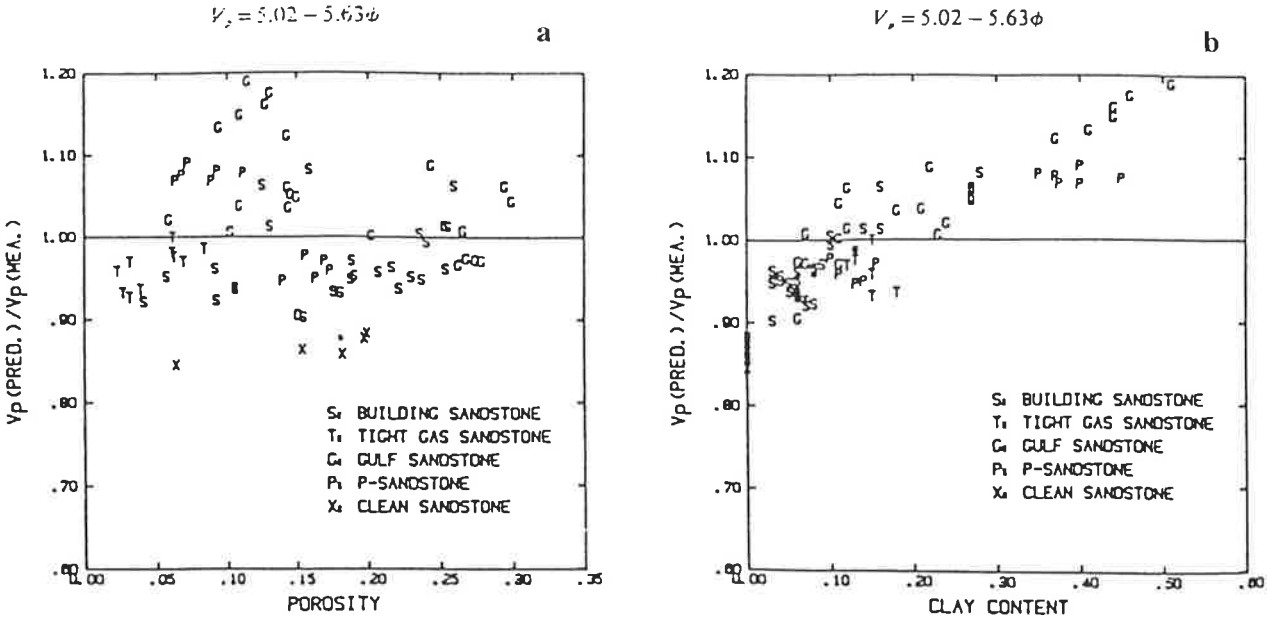

Figure 8.9. V_p fitted by simple linear model (equation 8.1). (a) Relative deviations of V_p versus porosity. (b) relative deviation of V_p versus clay content. (from Han et al. , 1986).

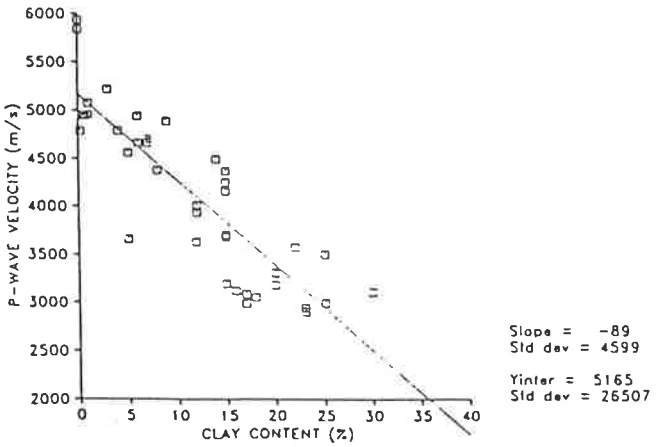

Figure 8.10. V_p versus clay content in water-saturated sandstones with porosities between 6% and 36% (from Klimentos, 1991).

prediction whereas the equation for arenites (C < 15%) significantly overestimates V_p in Cooper Basin samples.

The lack of relationship between velocities and clay content may also be related to the type of clay distribution within the studied samples. Minear (1982) modelled the effect of clay on velocity in shaly sandstones considering the clay distribution and showed that suspended (dispersed) clays have only small effects on velocities whereas laminated and structural clays have significant effects on velocities. Suspended clay which is assumed to occur dispersed in the pores or lining the surfaces of pores affects only the elastic properties of pore space. The density of dispersed clay determines its effect on velocity. The closer the density of dispersed clay is to the pore fluid the less will be its effect on velocity. For instance, dispersed clay of density of 1.6 g/cm^3 in a sandstone with any porosity produces negligible effect on V_p (Figure 8.12). The dominant clay type within the Cooper Basin samples is the dispersed authigenic kaolinite. The relationship between velocity and clay content for the Cooper Basin samples may be compared with the dispersed model of Minear (1982). SEM and thin section observation of Cooper Basin samples confirm this analogy. Similarly the strong clay effect on velocity reported by Han et al. (1986) and Klimentos (1991) may be compared with the laminated or structural clay models of Minear (1982), although the exact arrangement of clays within sandstones studied by these authors is unknown.

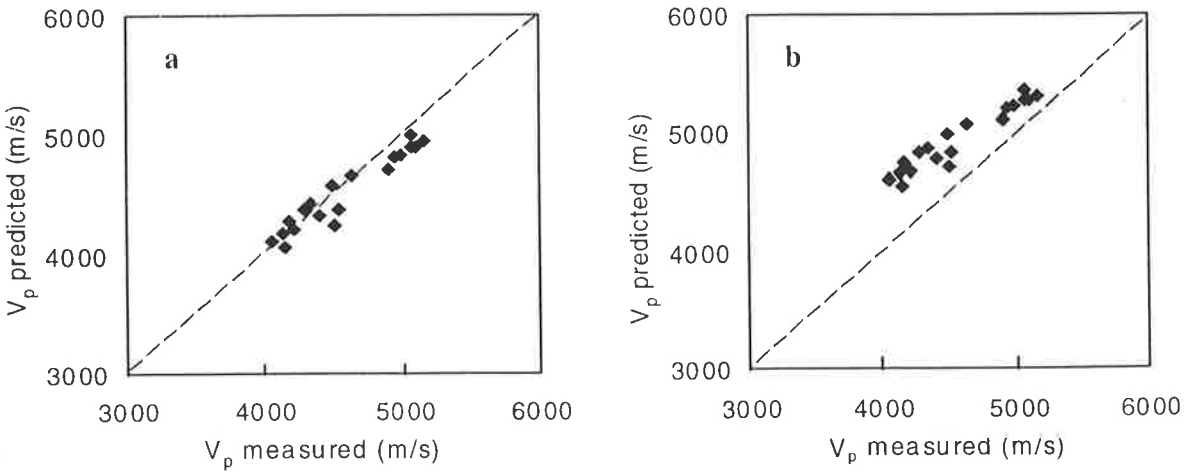

Figure 8.11. Predicted V_p using Vernik's (1994) equations versus measured V_p for water-saturated Cooper Basin samples measured at 40 MPa effective stress. Line shows a perfect correlation. (a) predicted by velocity-porosity transform for wackes: $V_p = 5190 - 7.21\phi$. (b) predicted by velocity-porosity transform for arenites: $V_p = 5520 - 6.91\phi$.

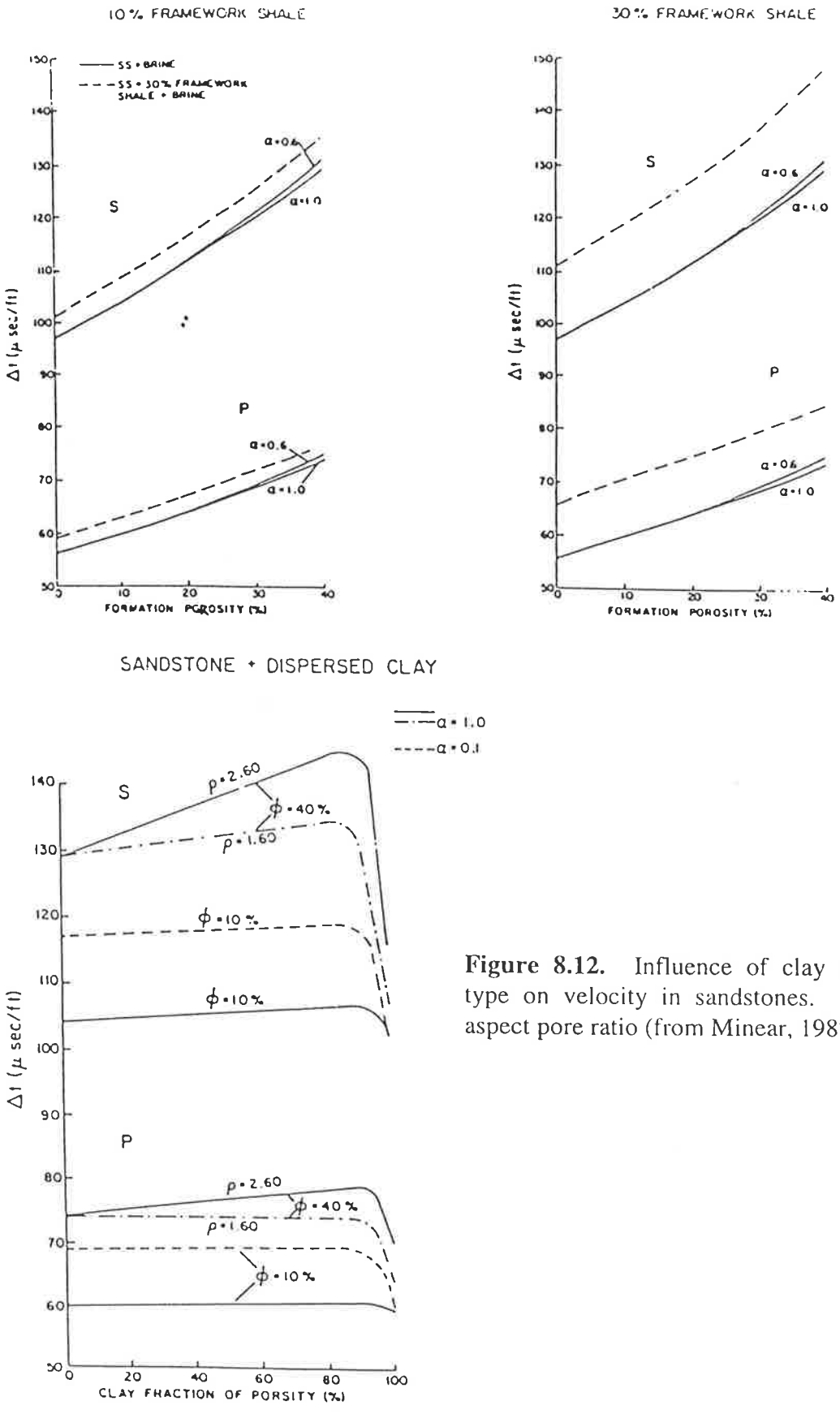

Figure 8.12. Influence of clay distribution type on velocity in sandstones. α is mean aspect pore ratio (from Minear, 1982).

8.7. Summary and Conclusions

Systematic laboratory measurements were carried out to investigate the stress sensitivity of velocities in 21 fully water-saturated Cooper Basin core plugs. Both V_p and V_s increase non-linearly over an effective stress range of 5 to 60 MPa and that the change of velocity with effective stress can be generalised according to equation 6.3. Comparison of the velocity gradients (VGR) at elevated effective stresses for water-saturated samples shows that the overall stress sensitivity of V_p is slightly higher than V_s's. However water-saturated samples show smaller VGR values (between 1.1 and 1.2) when compared with VGR for dry samples (between 1.4 and 1.8) at corresponding pressures. In general the stress sensitivity of water-saturated samples is less than that for dry rocks particularly at low effective stress ranges. For a saturated rock, the finite modulus of the water increases the bulk modulus of the rock and resists the closure of cracks. At effective stress below 40 MPa, V_p shows smaller stress dependence when the rock is saturated with water. At pressure above 40 MPa the influence of pore fluid on the stress sensitivity of V_p is less significant due to the closure of crack-like pores and increase of elastic moduli in dry rocks. The observation on the difference between stress sensitivity of dry and water-saturated Cooper Basin sandstones is in consistent with those reported by King (1966) for Berea and Torpedo sandstones.

Statistical analysis of experimental data shows that considering a clay content term would improve the velocity-porosity transform for the Cooper Basin sandstones. This observation is in consistent with works by Tosaya and Nur (1982), Castagna et al. (1985) and Han et al. (1986) and Klimentos (1991). However the plot of volume fraction clay content versus both V_p and V_s for the studied samples shows no correlation. This is in disagreement with the experimental studies mentioned above. The lack of correlation between clay content and velocity in the Cooper Basin sandstones is attributed to the textural characters and the type of clay distribution within the studied samples. The clay models of Minear (1982) and the velocity-porosity model of Vernik (1994) for "wackes" provide an explanation for the observed velocity-porosity-clay content relationship in the Cooper Basin samples.

Chapter 9

Velocity in Partially Saturated Samples

9.1. Introduction

The influence of saturation by water, gas and mixtures of them on acoustic velocities and elastic moduli of reservoir rocks is of considerable interest in exploration seismology. However, very few studies have investigated the relationship between acoustic velocities and partial fluid saturation in sandstones under varying stress conditions. This chapter presents and examines compressional and shear velocity data obtained from laboratory measurements on a sub-set of Cooper Basin core samples as a function of water saturation (Sw) under varying confining stresses. The suit of samples consisted of 6 selected core plugs of the total 22 samples studied in previous chapters. Two samples from each well were selected on the basis of their petrophysical character. Table 9.1 shows the physical properties of these samples. The porous plate extraction technique was used to induce partial saturation in the samples. The desaturation technique has been described in Chapter 5.

Sample	Depth (m)	Porosity (%)	Permeability (mD)	Bulk density (g/cm^3)	Grain size (μm)	Quartz (%)	Clay (%)	Rock fragment (%)	Other minerals (%)
D4	2215.4	13.0	33.7	2.30	297	70.4	8.7	6.4	1.5
D6	2217.5	11.2	30.5	2.31	298	69.4	9.5	7.9	2.0
M2	2551.4	6.5	0.1	2.45	185	72.3	11.5	8.6	1.1
M8	2556.6	4.0	0.0	2.52	304	69.1	11.5	13.6	1.8
S1	1917.7	10.5	0.2	2.34	97	58.9	12.5	15.6	2.5
S3	1919.2	15.6	186.2	2.17	276	69.3	10.1	2.4	2.6

Table 9.1. Petrographical and petrophysical properties of samples used for partial saturation measurements. Other minerals include mica, carbonate, feldspar, opaque and organic matter.

Capillary pressure curves and effective pore throats were also determined from inlet pressure and water saturation data obtained from the porous plate extraction technique for each sample. Capillary pressure information was integrated with the interpretation of acoustic velocity of partially saturated samples.

9.2. Capillary Pressure Data

Capillary pressure information may be of use in visualising relatively simple models of pore structure within the complex pore system of rocks. Capillary pressure results from the interaction of forces acting within and between liquids and their bounding solids. In the two-phase system normally encountered in partially saturated rocks, one phase may be defined as the wetting fluid which has the greatest affinity to the solid surface, and the other phase is defined as the non-wetting fluid (Figure 9.1a).

Within a single capillary, capillary pressure (P_{cap}) is the amount of extra pressure required to force the non-wetting phase to displace the wetting phase (Figure 9.1b). Capillary pressure can be calculated by:

$$P_{cap} = 2\tau \cos\theta / r_c \qquad (9.1)$$

where τ is interfacial tension, θ is the contact angle between the fluid and capillary tube, and r_c is the radius of the capillary (Vavra, et al. 1992). The pressure at which the non-wetting phase first enters the sample is termed the entry or displacement pressure. The irreducible saturation is that percent of the pore space that the non-wetting phase cannot penetrate (Figure 9.2). In reservoir rocks the wetting fluid is usually water or brine and the non-wetting fluid is usually hydrocarbon. In the porous plate extraction technique used in the current study the wetting phase is water and non-wetting phase is nitrogen.

Capillary pressure curves were generated from the data gathered during the desaturation process from the inlet pressure values of nitrogen gas and the degree of water saturation for each sample. Data from the capillary pressure curve were used to approximate the distribution of pore volume accessible by pore throats of a given effective size (r_c) using equation 9.1. Tabulated values of interfacial tension τ = 72 (dyne/cm) and the contact angel $\theta = 0°$ (Vavra et al. 1992) were used for the effective pore throat estimation of the studied samples. The plot of estimated effective pore throats versus water saturation

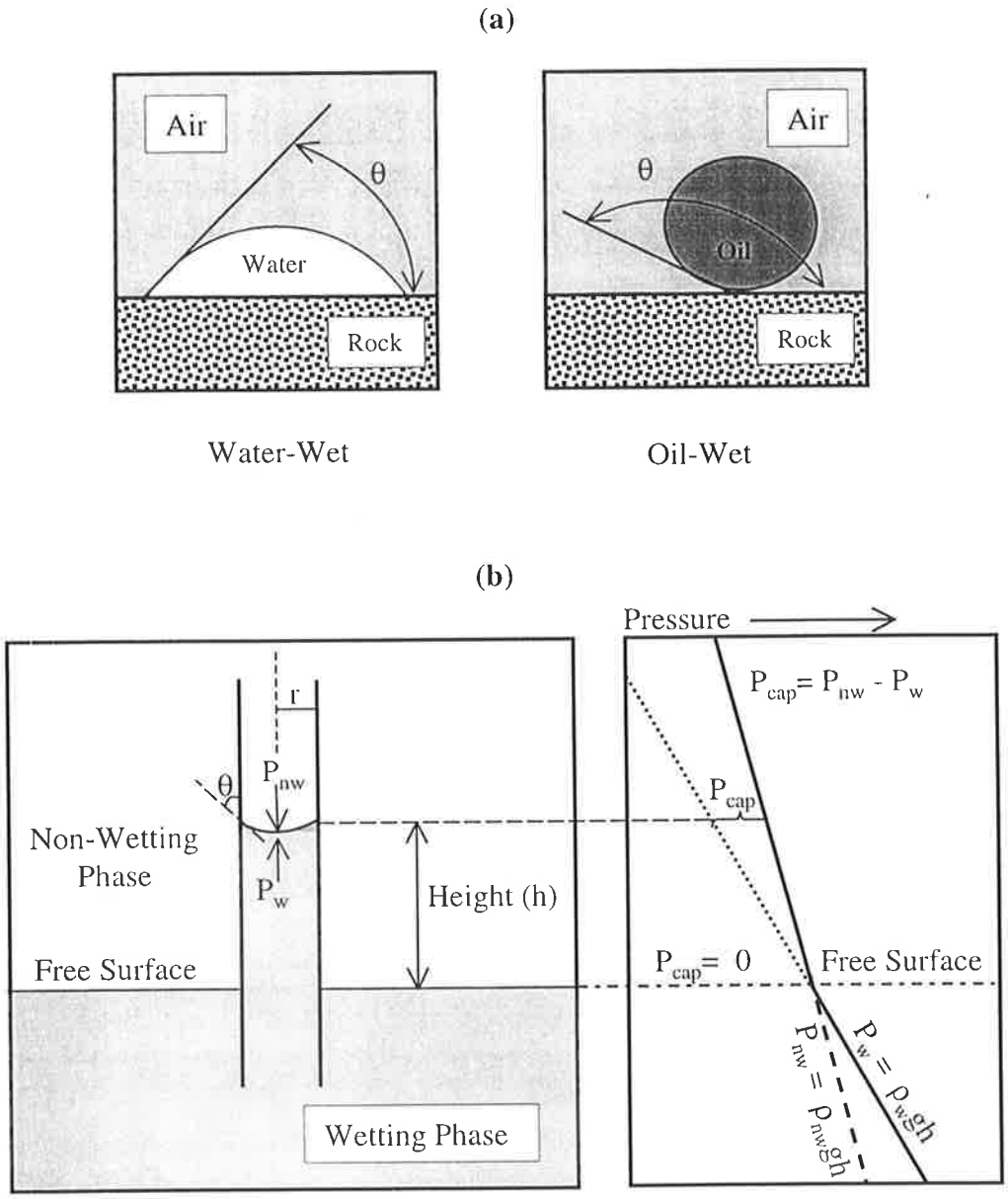

Figure 9.1. Schematic representation of the principle of capillary pressure effects in reservoir rocks. (a) rock–fluid wettability and contact angle, (b) capillary tube in a wetting fluid; Capillary pressure (P_{cap}) is defined as the different in pressure measured across the interface in the capillary (P_{cap}= P_{nw}-P_w), resulting from the contrast in pressure gradients caused by the difference densities of the nonwetting (ρ_{nw}) and wetting (ρ_w) phases. g is the gravitational constant (modified from Vavra et al., 1992).

reflects the largest throat through which the pore volume can be accessed by nitrogen gas at a given saturation condition. Figures 9.3 and 9.4 plot capillary pressure and effective pore throat versus water saturation for the studied samples. The following are general remarks concerning capillary pressure curves for the samples.

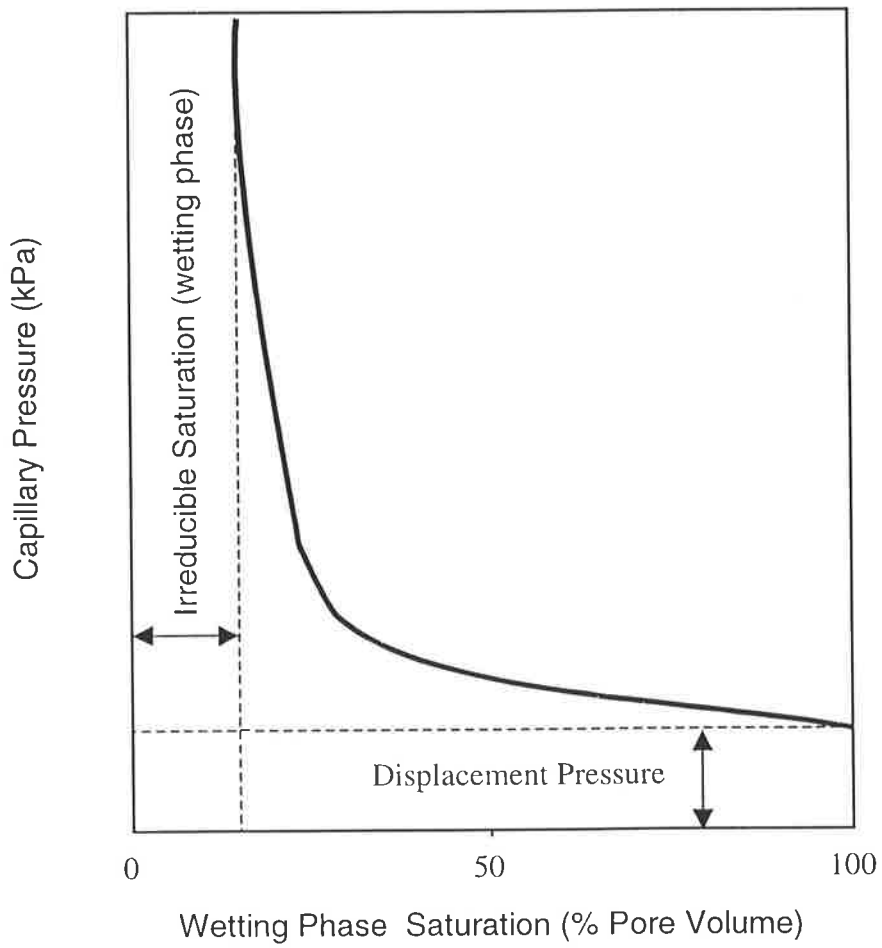

Figure 9.2. Typical capillary pressure curve for a porous rock.

Samples S3, D4 and D6 have a low displacement pressure (2.5 kPa) and a relatively low irreducible water saturation of less than 20%. The effective pore throat size varies from 60 microns to less than 1 micron and nearly 50% of pore volume in these samples is associated with effective pore throats of greater then 10 microns radius. Pores associated with large throat size appear to be accessible by gas at very low capillary pressures, whereas the small effective pore throats (< 10 microns) will be gas saturated only at high capillary pressures (low water saturation). One could distinguish basically two zones within the capillary pressure curves for samples S3, D4 and D6. Zone I which is

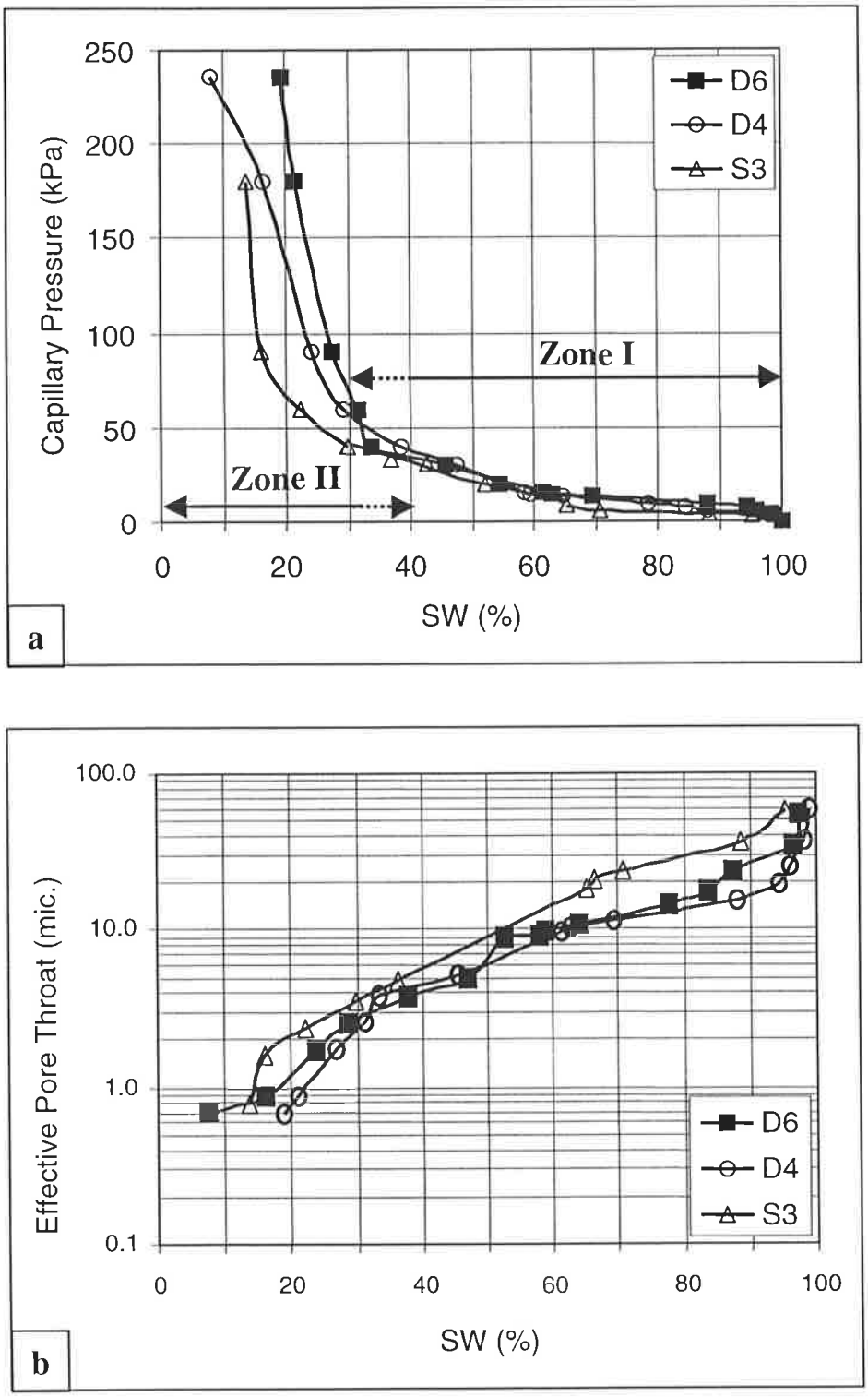

Figure 9.3. (a) Capillary pressure curves, (b) estimated effective pore throats for samples D6, D4, and S3.

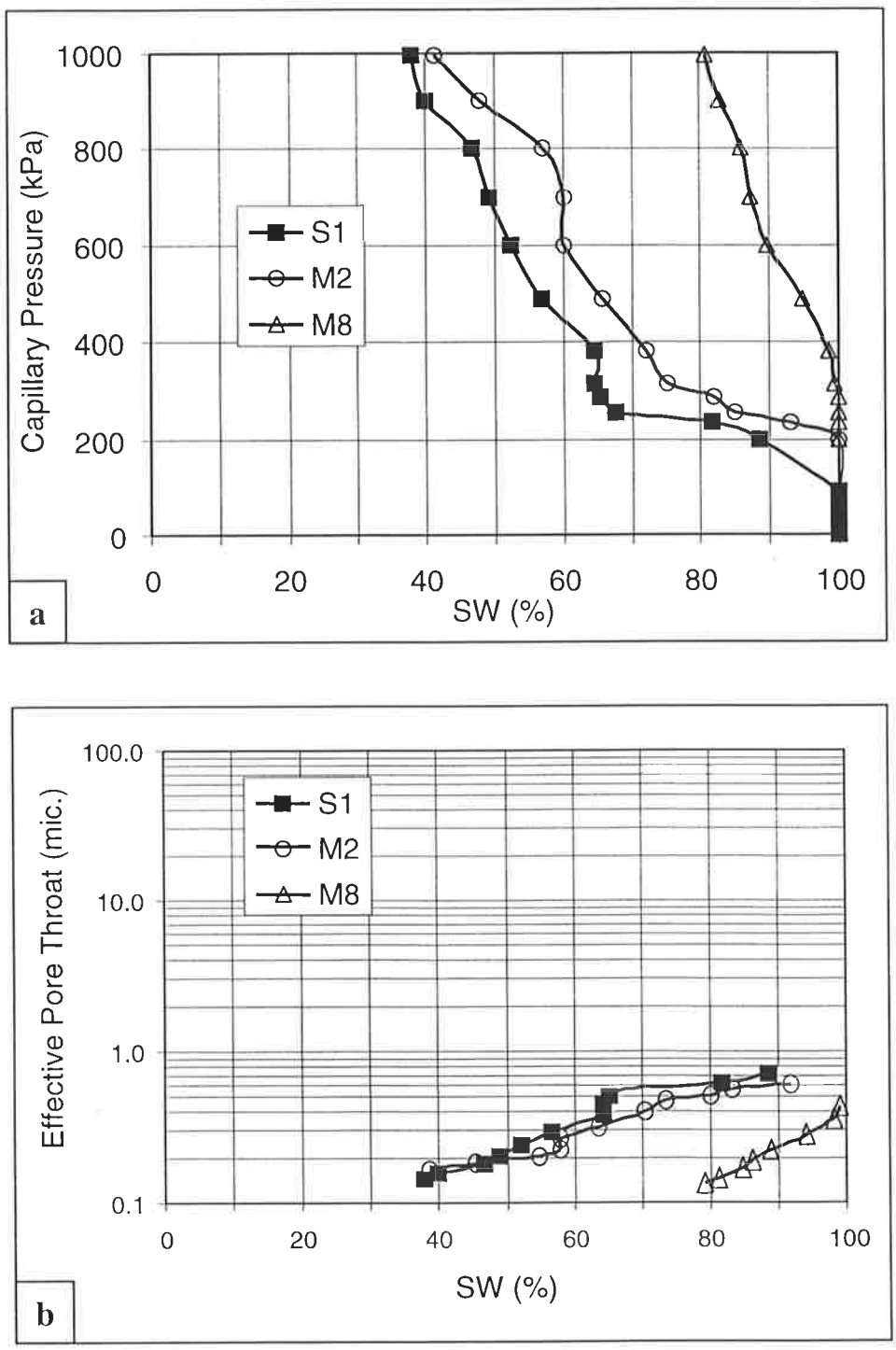

Figure 9.4. (a) Capillary pressure curves, (b) estimated effective pore throats for samples S1, M2, and M8.

characterised by large to medium pore throats expands over a large saturation range between Sw =100% and Sw = 30% to 40%. The rate of desaturation at Zone I is rapid, and relatively low capillary pressure (less than 50 kPa) is required for the replacement of water with gas within the pore spaces. Zone II corresponds to the higher capillary pressure region characterised by small pore throats and slow desaturation. In zone II samples approach their irreducible water saturation.

Samples S1, M2 and M8 have high displacement pressure (greater than 200 kPa). Capillary pressure curves for these samples indicate that none of them has reached irreducible water saturation at the maximum pressure (1 MPa) of the pressure vessel used in the desaturation process. Estimated effective pore throats for these samples range between 0.6 and 0.14 microns and show less variation compared with other samples.

In general, capillary pressure curves and estimated effective pore throats indicate heterogeneous distribution of gas and water within the pore space under partial saturation conditions for all samples.

9.3. Velocity versus Fluid Saturation - Results

Acoustic velocities were measured under conditions of varying confining stress and atmospheric pore pressure (i.e. $P_e = P_c$) and a series of partial saturation levels. Samples S3, D4 and D6, with relatively high permeabilities, showed lower irreducible water saturation and hence, acoustic data were acquired at a wider range of Sw for these samples. For these samples acoustic measurements could not be performed at low effective stresses due to either high wave attenuation or poor coupling between rock sample and buffer-rods. In contrast for the samples S1, M2 and M8 capillary pressures beyond the working limit of the porous plate extraction vessel (1 MPa) were needed to reach the irreducible water saturation level. Hence only a short range of Sw levels over a more complete effective stress range were obtained for these low permeability samples. Acoustic data obtained from measurements under fully water-saturated and dry conditions (described in Chapters 6 and 8) were used to compare the velocities of partially saturated samples with those measured under Sw = 100% and Sw = 0% conditions, respectively. All experimental data on V_p and V_s in partially water-saturated samples are tabulated in Appendix E. The following is a brief description of experimental data for each sample.

9.3.1. Sample S3

High permeability (186.2 mD) allowed this sample to reach equilibrium at each capillary pressure over a relatively short period of time. Nine different stages of partial saturation were analysed on the sample S3. A water saturation of 8% was reached at a maximum applied capillary pressure of 180 kPa, with the sample approaching its irreducible saturation. Figures 9.5a and b show the plots of V_p and V_s versus effective stress for the sample S3 at various saturation levels. The general shape of the V_p-effective stress curve (Figure 9.5a) is consistent over the entire saturation range except for the dry condition (Sw = 0%) which shows a higher velocity gradient over the effective stress range. Stress sensitivity of shear velocity for entire saturation level remains similar over the measured effective stress range (Figure 9.5b).

Figure 9.6 shows the variation of V_p, V_s and their ratio (V_p/V_s) with saturation at an effective stress of 40 MPa. The change of velocities and their ratio with saturation is not consistent over the entire saturation range. V_p slightly increases with saturation decrease between 100% and 88% (Figure 9.6a). Over the saturation range between 88% and 38% V_p decreases continually by 100 m/s but remain almost constant from Sw = 38% to Sw = 17%, and then again increases by 24 m/s as saturation approaches dry condition. V_s rises with decreasing saturation over the saturation range between 100% and 38% by 92 m/s, but it remains almost constant over saturation between 38% and 8%. V_s increase rapidly at low saturations (8% < Sw < 0%). The value of V_p/V_s falls sharply from 1.65 to 1.57 as Sw decreases from 100% to 38% and remains nearly the same over the saturation range between 38% and 8% with further decrease to 1.55 at saturations between 8% and 0% (Figure 9.6c).

9.3.2. Sample D4

The sample D4 has a moderate permeability (33.7 mD), and, like sample S3 it equilibrated rapidly in the porous plate extraction vessel. The sample reached Sw = 19% at a maximum applied capillary pressure of 235 kPa and was approaching its irreducible saturation. Measurements were made at seven partial saturation levels between 19% and 88%. Figures 9.7a and b show the experimental results of velocities versus effective stress for different saturation stages. The stress sensitivity of V_p at partial and fully saturation conditions are similar for the entire measured effective stress range, and only the dry sample V_p shows a higher velocity gradient particularly at low effective stress ranges. Variation of V_s with

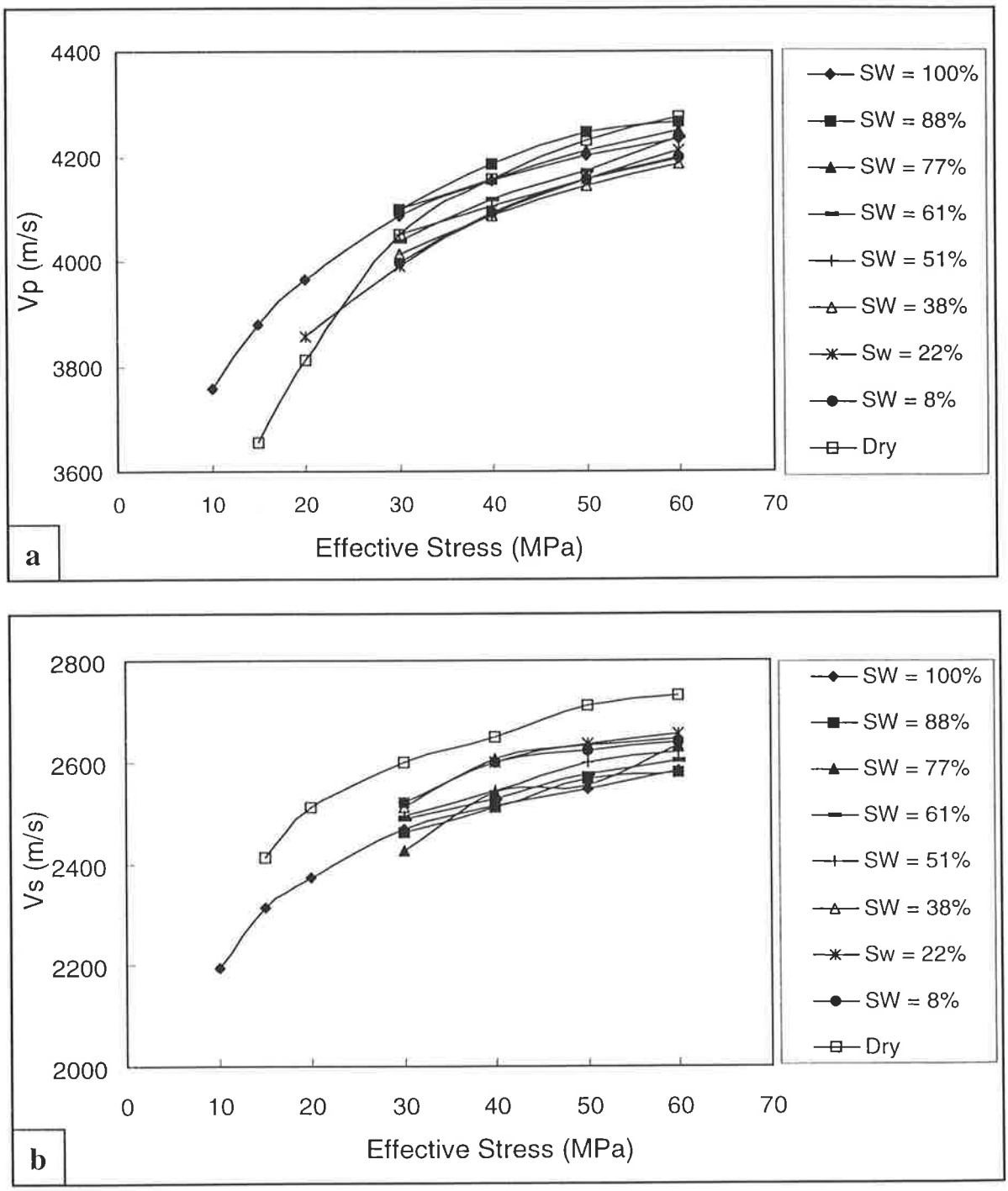

Figure 9.5. Variation of V_p (a) and V_s (b) with effective stress in sample S3 at different water saturation conditions.

effective stress varies over the measured saturation levels and does not follow a consistent pattern (Figure 9.7b).

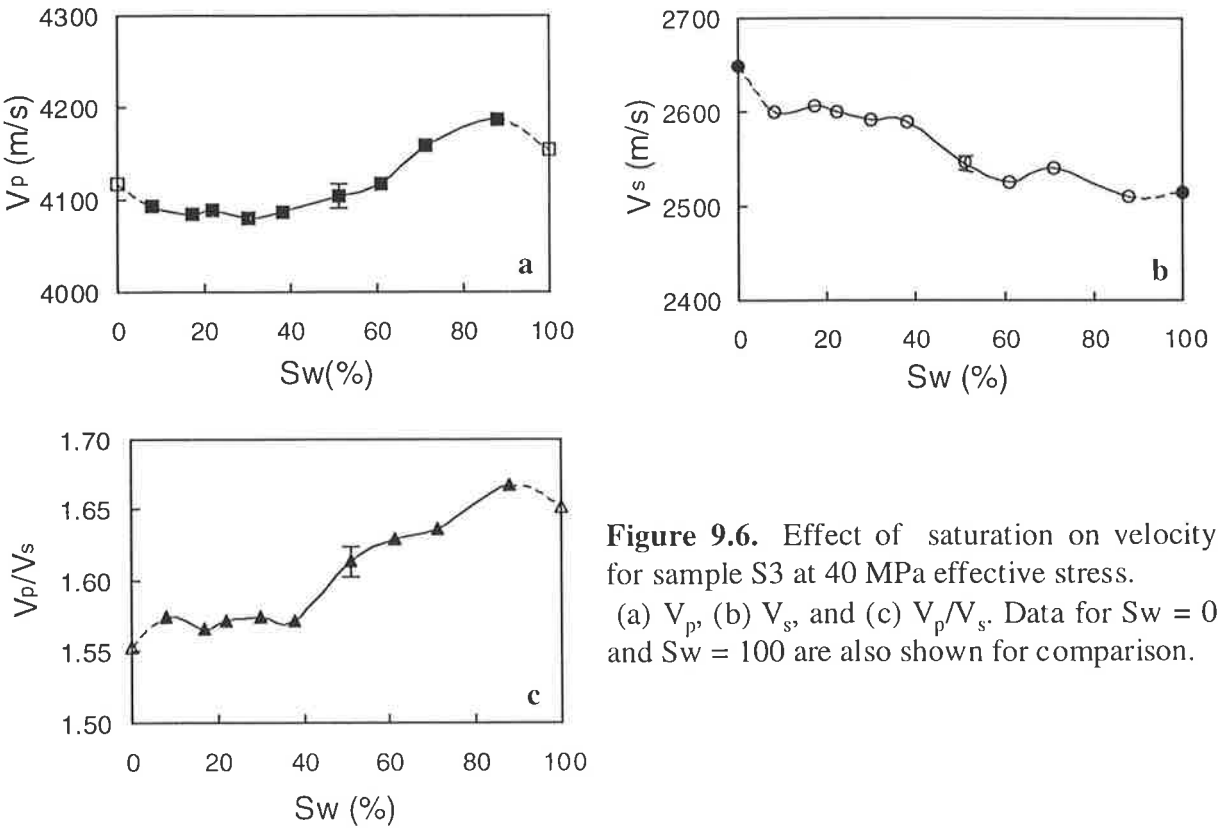

Figure 9.6. Effect of saturation on velocity for sample S3 at 40 MPa effective stress. (a) V_p, (b) V_s, and (c) V_p/V_s. Data for Sw = 0 and Sw = 100 are also shown for comparison.

Figure 9.8 shows the changes in V_p, V_s and V_p/V_s with saturation at 40 MPa for the sample D4. The magnitude and pattern of the variation of V_p with saturation for sample D4 vary over the entire saturation range. At high saturation levels (67% < Sw <100%) V_p shows no significant changes. V_p decreases by 81 m/s at medium saturation stages (31% < Sw < 67%), whereas at low saturation stages (0% < Sw <31%) it decreases by 25 m/s (Figure 9.8a). V_s steadily increases with saturation decrease over the entire saturation range except at saturation level higher than 88% (Figure 9.8b). Similar to sample S3, the value of V_p/V_s decreases sharply from 1.64 to 1.57 with the decrease of saturation from 88% to 40% while at saturations less than 40% the velocity ratio does not show significant variation (Figure 9.8c). Apart from small differences under dry and fully water saturation conditions, the variations in velocities with saturation at partial saturation condition in this sample at other effective stresses are generally consistent with the trends shown in Figure 9.8.

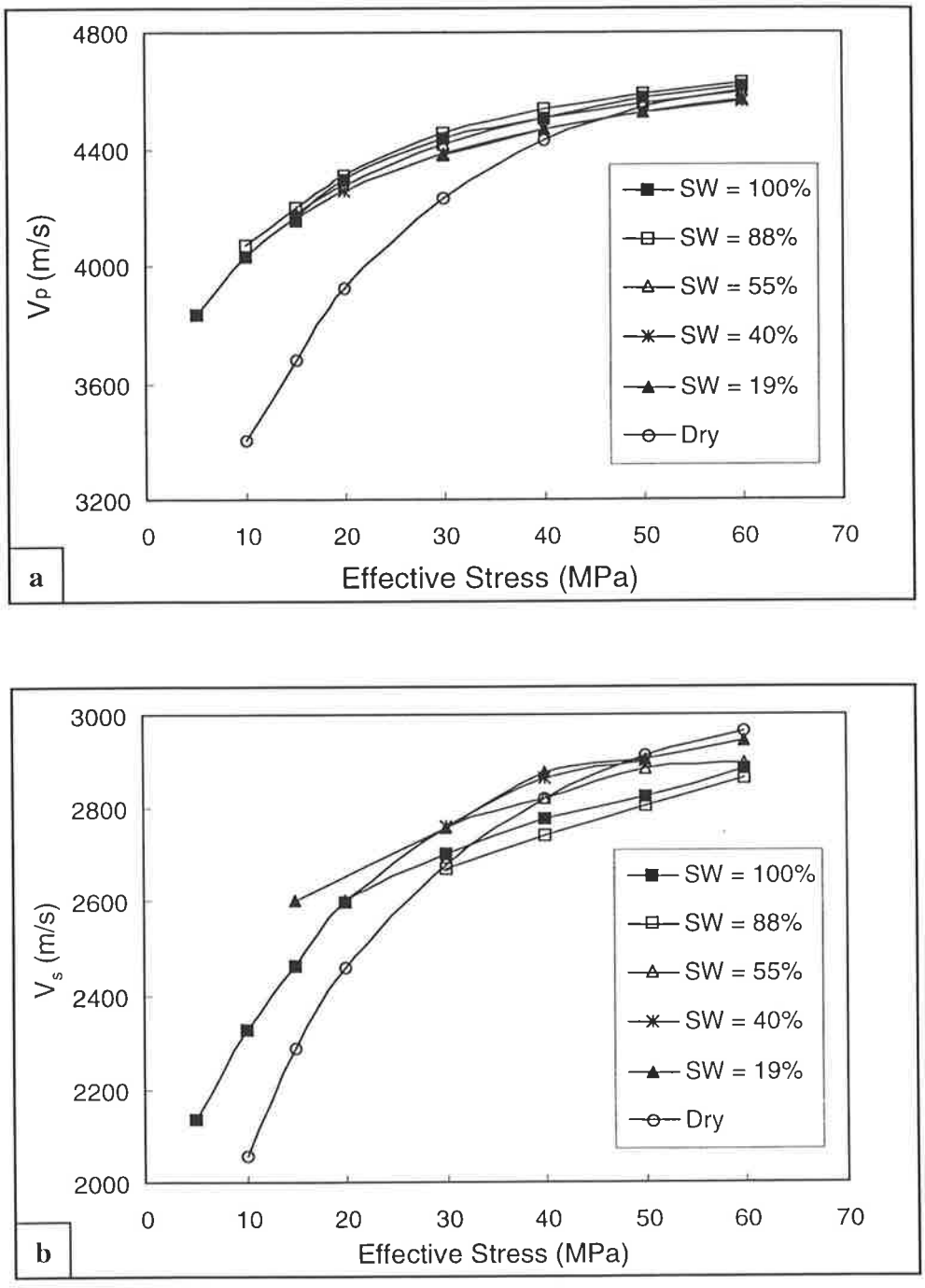

Figure 9.7. Variation of V_p (a) and V_s (b) with effective stress in sample D4 at different water saturation conditions.

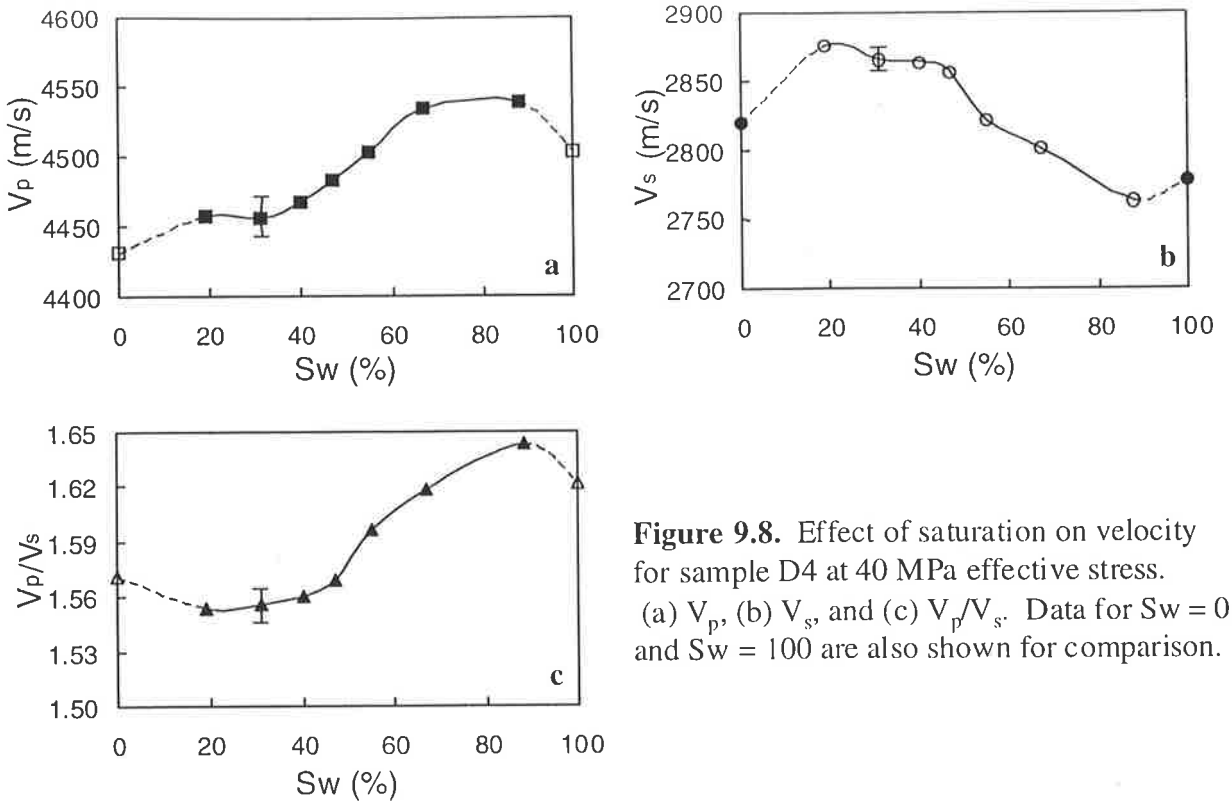

Figure 9.8. Effect of saturation on velocity for sample D4 at 40 MPa effective stress. (a) V_p, (b) V_s, and (c) V_p/V_s. Data for Sw = 0 and Sw = 100 are also shown for comparison.

9.3.3. Sample D6

Sample D6 has a permeability of 30.5 mD and was found to undergo desaturation easily. The sample approached irreducible water saturation at Sw = 8% at maximum capillary pressure of 235 kPa. Measurements were made at eight saturation levels between 86% and 8%. Figures 9.9a and b show relationship between velocities and effective stress for the sample at eight saturation stages. The V_p-effective stress curves for saturation of Sw > 15% are almost identical indicating similar stress sensitivity for V_p at this saturation range. As saturation approaches zero the stress sensitivity of V_p increases particularly at low effective stresses. Apart from saturation conditions of Sw = 100% and Sw = 0%, the velocity-effective stress trends for V_s generally are similar over entire partial saturation range.

Figure 9.10 shows the changes in V_p, V_s and V_p/V_s with saturation at 40 MPa for sample D6. V_p decreases with decreasing saturation over saturation range between 86% and 0%. However the rate of velocity decrease with saturation decrease is not similar over the saturation range. At high and moderate saturation levels the reduction rate is higher where the V_p drops exceed 117 m/s at saturation range between 86%and 38%. Over a saturation range of 15% < Sw < 38% the V_p decrease is not significant (within the error limit of the experiments, which is 0.3% for both V_p and V_s and 0.6% for V_p/V_s). V_p decreases sharply at low saturation levels (Sw < 15%). V_s increases with saturation decrease over the entire

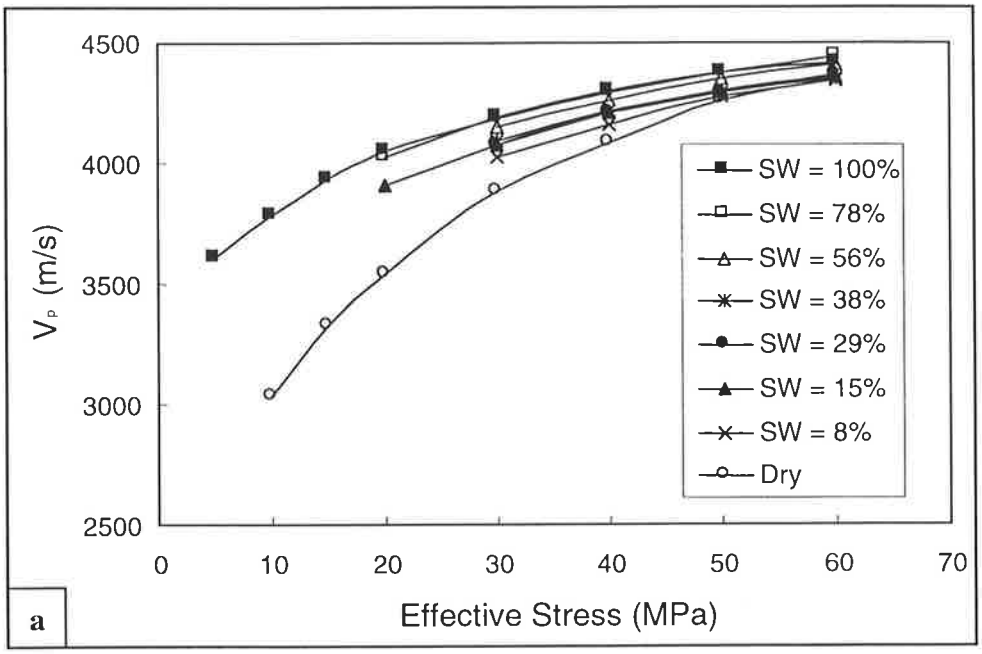

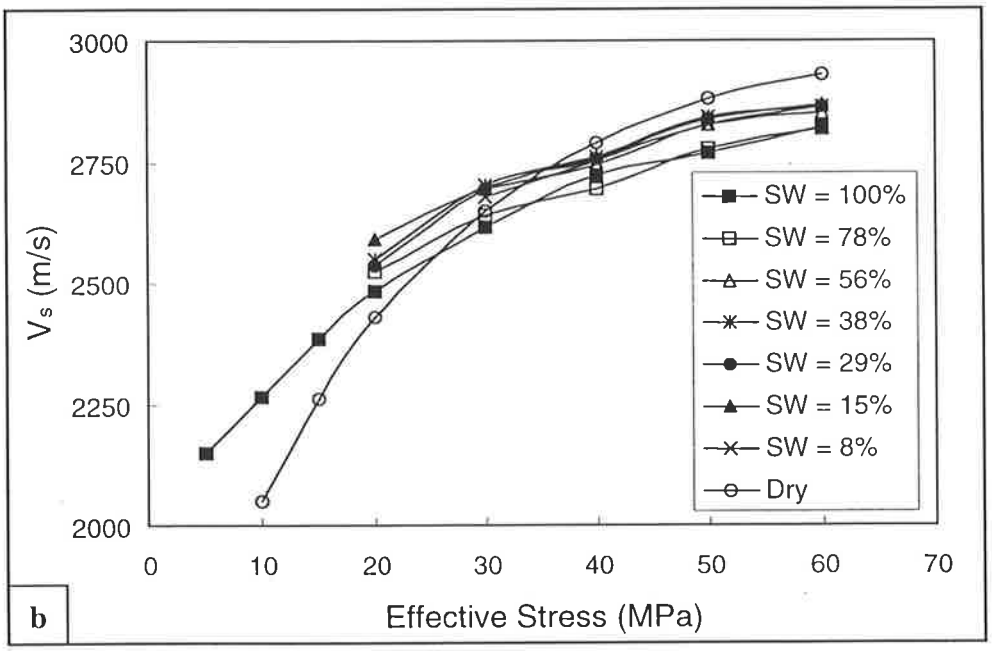

Figure 9.9. Variation of V_p (a) and V_s (b) with effective stress in sample D6 at different water saturation conditions.

partial saturation range with a sharp increase between Sw = 8% and 0% (Figure 9.10b). The value of V_p/V_s decreases from 1.57 to 1.52 over the saturation range between 100% and 38% and it remains constant between 38% and 8% followed by a sharp drop to 1.46 under dry conditions (Figure 9.10c). The general trend of the variation of velocities and their ratios with saturation in sample D6 is consistent over the measured effective stress range.

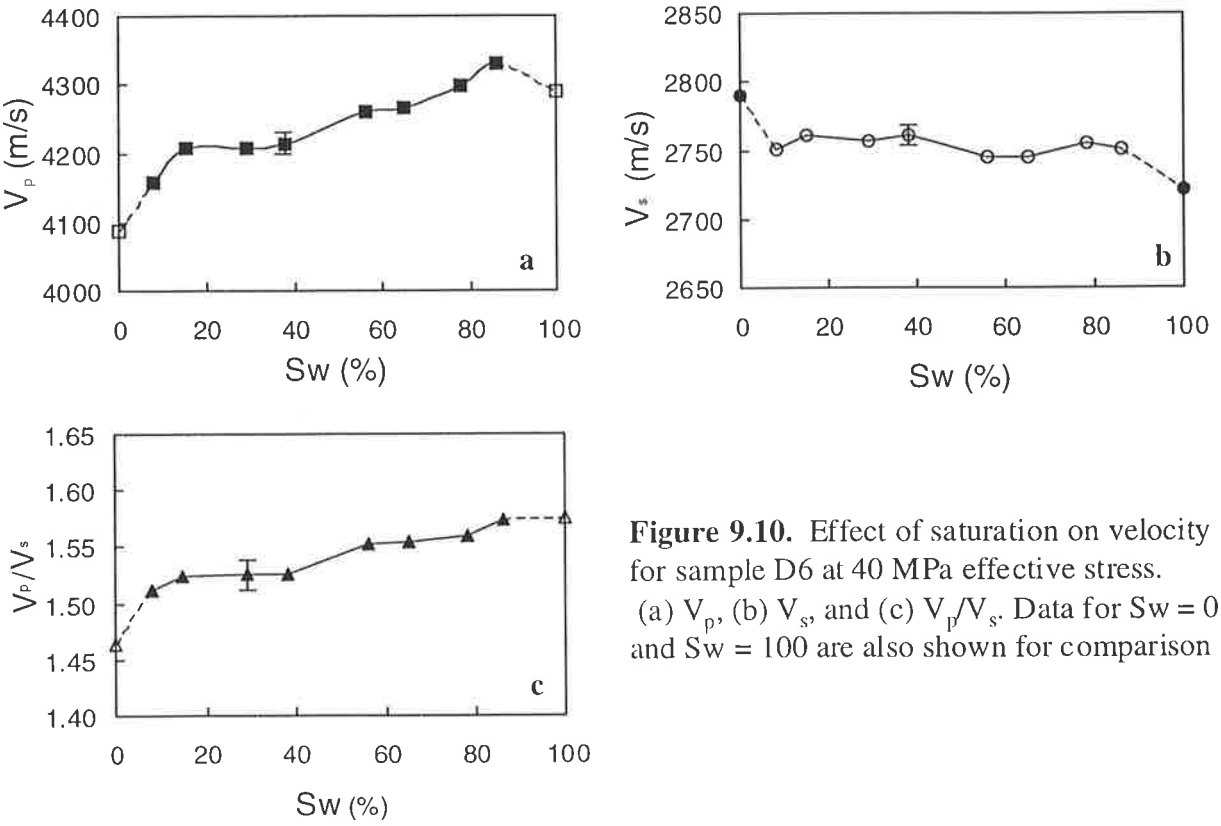

Figure 9.10. Effect of saturation on velocity for sample D6 at 40 MPa effective stress. (a) V_p, (b) V_s, and (c) V_p/V_s. Data for Sw = 0 and Sw = 100 are also shown for comparison

9.3.4. Sample S1

Sample S1 has a low permeability (0.2 mD) and the sample reached a water saturation of 34% at the highest possible capillary pressure of the porous extraction plate vessel (1 MPa). Therefore no data were acquired between the dry state and Sw = 34%. Measurements were made at four different saturation levels between 78% and 34%. Figures 9.11a and b show the experimental results of velocities versus effective stress for this sample. Figure 9.11a indicates that the stress sensitivity of V_p does not change under partial and full water saturation and only the dry sample shows a higher velocity gradient versus effective stress. The velocity-effective stress relationship for V_s remains relatively similar over the entire saturation range including dry condition (Figure 9.11b).

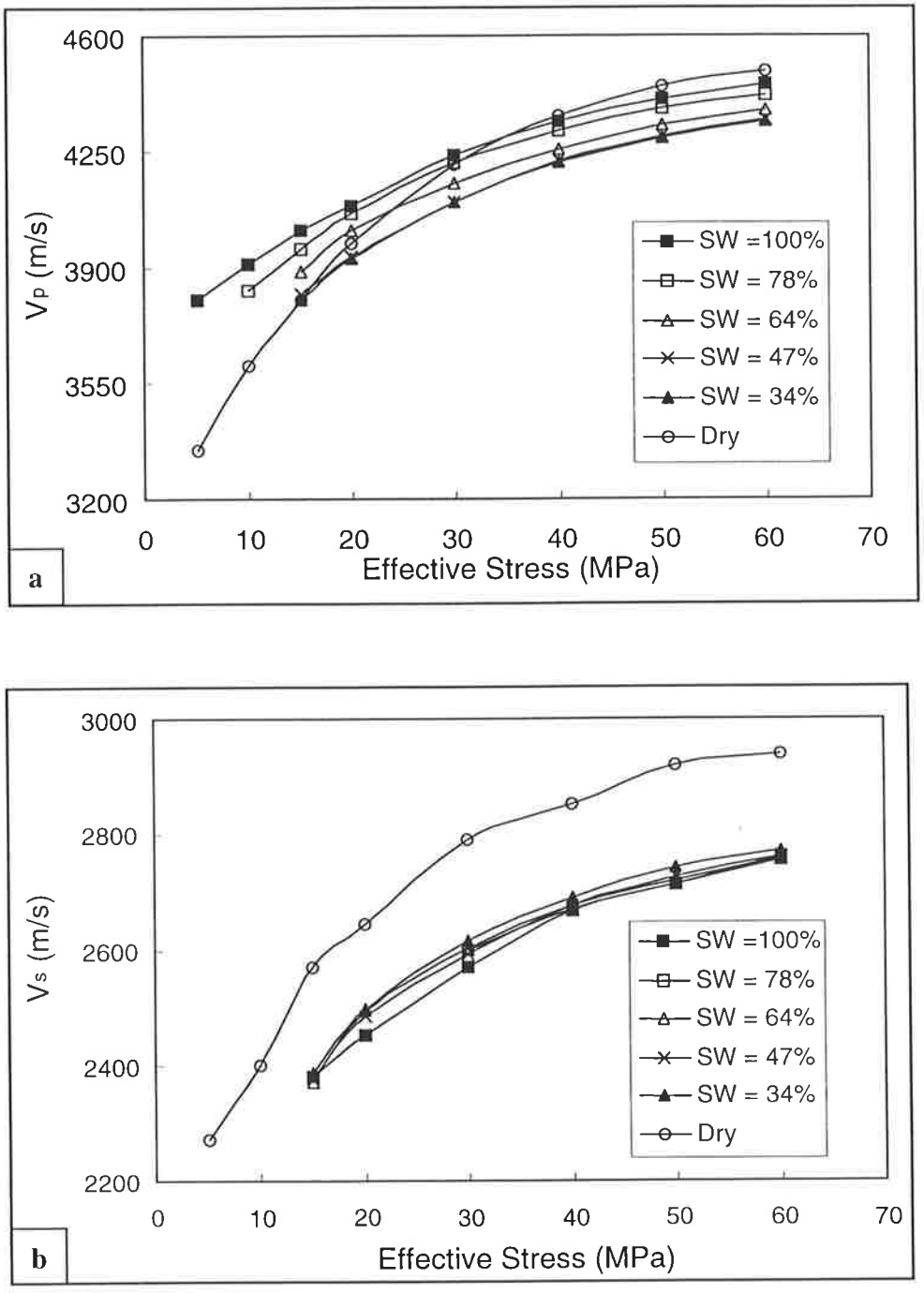

Figure 9.11. Variation of V_p (a) and V_s (b) with effective stress in sample S1 at different water saturation conditions.

Figure 9.12 shows the variation of V_p, V_s and V_p/V_s with saturation at 40 MPa effective stress for sample S1. V_p decreases by 128 m/s with decreasing saturation over the saturation range between 100% and 34%, and rises again under dry conditions by 161 m/s. V_s increases slightly (within the error limit) with saturation change from fully saturation to Sw = 34%, but increase sharply (by 183 m/s) under dry conditions. The velocity ratio for sample S1 steadily reduces from 1.63 to 1.56 with the saturation decrease from 100% to 34%, whereas under dry conditions it reaches a minimum value of 1.52. The variation of velocities and their ratios over the measured partial saturation at other stress conditions is consistent with the observed trend at 40 MPa effective stress.

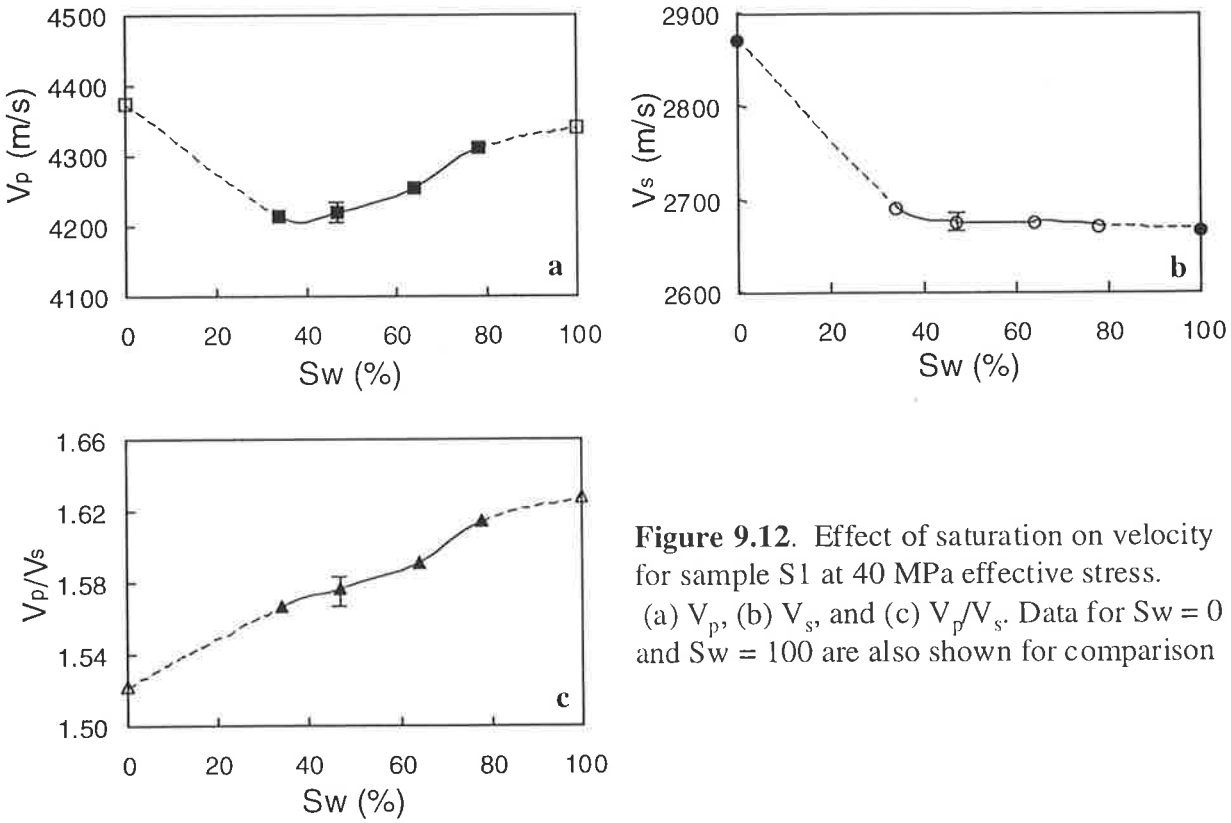

Figure 9.12. Effect of saturation on velocity for sample S1 at 40 MPa effective stress. (a) V_p, (b) V_s, and (c) V_p/V_s. Data for Sw = 0 and Sw = 100 are also shown for comparison

9.3.5. Sample M2

Sample M2 has a very low permeability (0.07 mD) and the sample equilibrated slowly in the porous plate extraction vessel. The sample reached a saturation of 37% at the highest possible capillary pressure within the vessel. Therefore no data exist between Sw = 37% and dry condition. Measurements were made at five different saturation levels between 90% and 37%. Figures 9.13a and b show experimental results for velocity variation with effective stress at different saturation stages for this sample. The general velocity-effective stress relationships for both V_p and V_s at different saturation levels are similar to those of

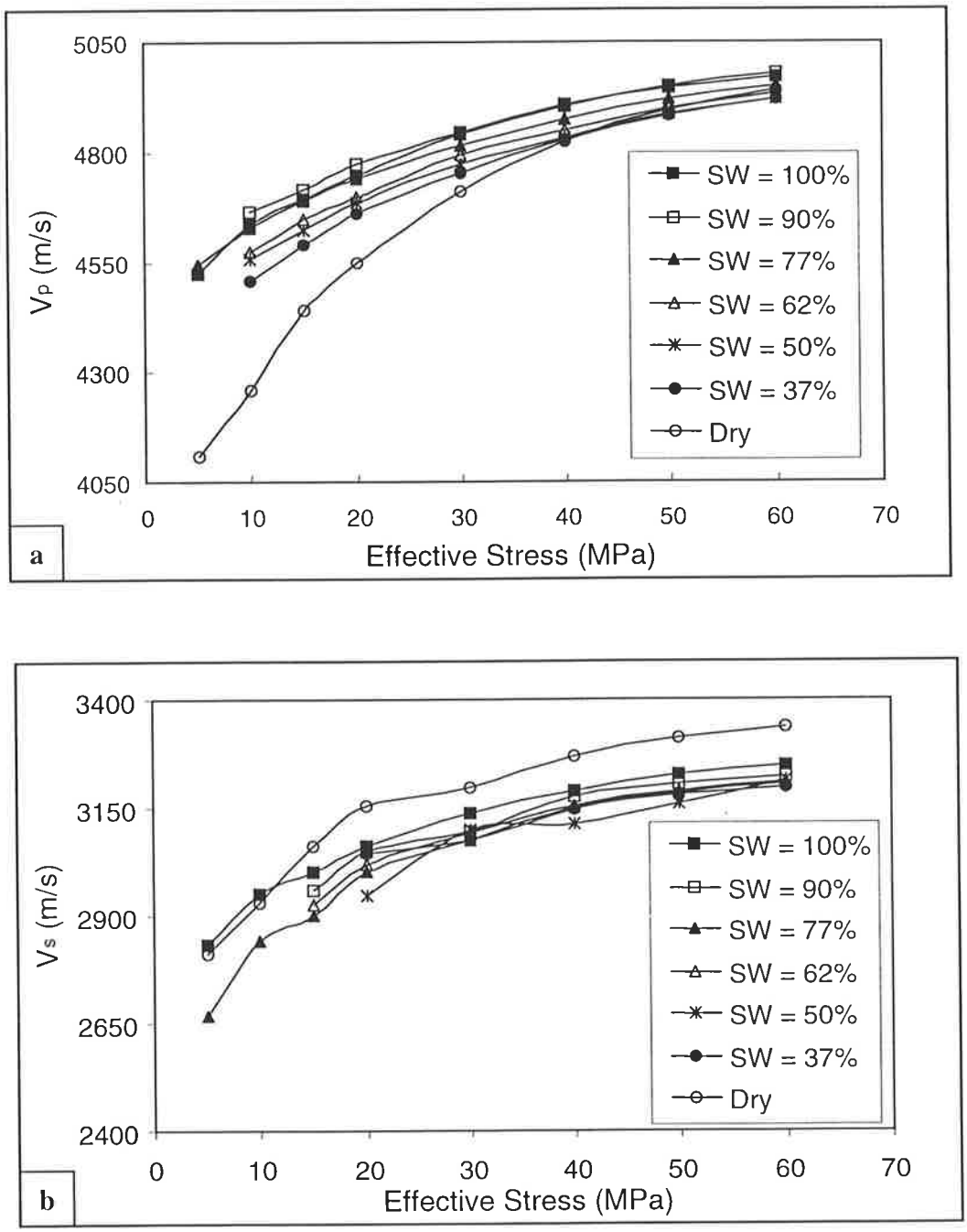

Figure 9.13. Variation of V_p (a) and V_s (b) with effective stress in sample M2 at different water saturation conditions.

sample S1 described above, with an exception for V_s in sample M2 which shows a higher stress sensitivity at low stresses under dry conditions.

Figure 9.14 shows the variation of velocities and V_p/V_s ratio at 40 MPa effective stress for the sample M2. V_p decreases by 64 m/s as saturation decreases from 90% to 37%, indicating a lesser sensitivity to saturation compared with the samples mentioned above. V_p increases slightly with saturation decrease between 100% and 90%. V_s decreases with saturation decrease over the saturation range between 100% and 77% and remains relatively unchanged as saturation falls from 77% to 37%. V_s increases by 160 m/s with decreasing saturation over the range 0% < Sw < 37%. V_p/V_s values in the sample vary between 1.53 and 1.54 with no apparent change with saturation decrease from full saturation to Sw = 37%.

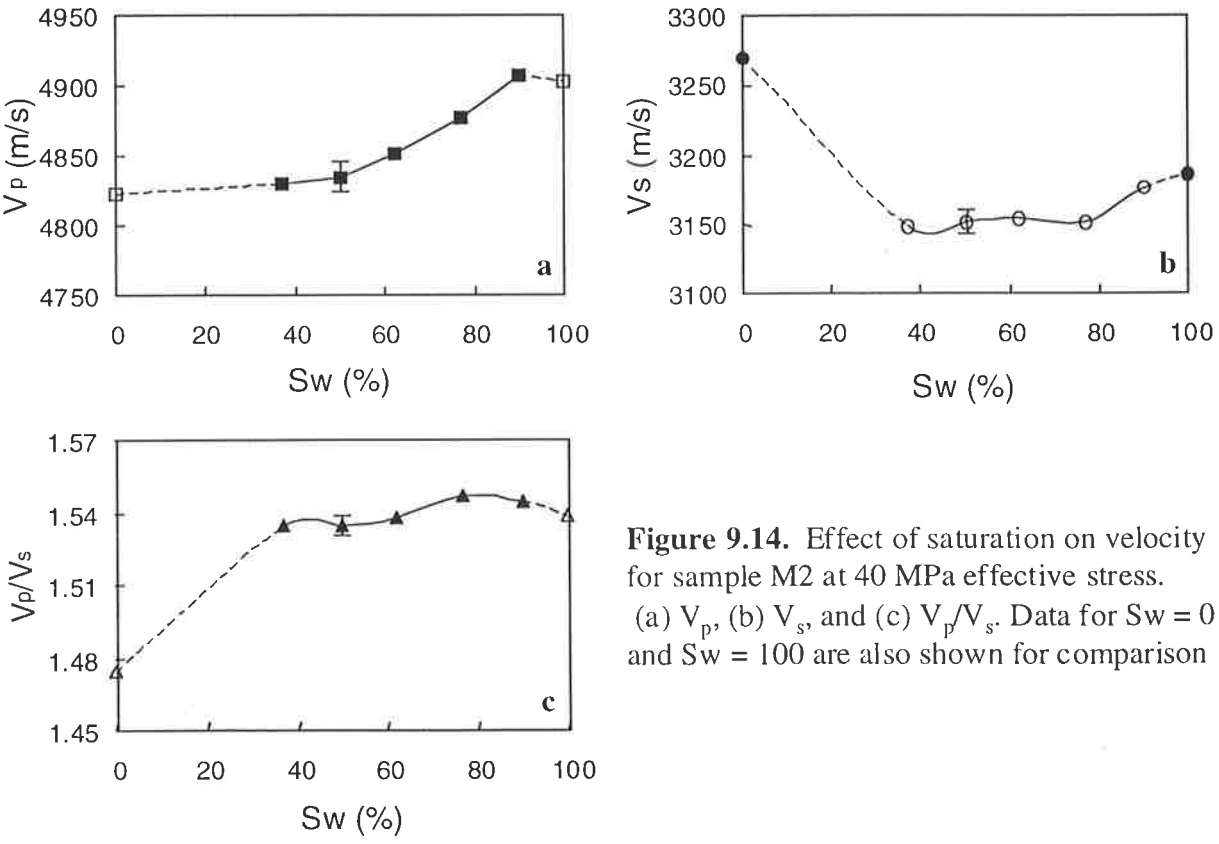

Figure 9.14. Effect of saturation on velocity for sample M2 at 40 MPa effective stress. (a) V_p, (b) V_s, and (c) V_p/V_s. Data for Sw = 0 and Sw = 100 are also shown for comparison

9.3.6. Sample M8

Sample M8 is a very tight sandstone with 0.03 mD permeability, and required high capillary pressures for desaturation of the core plug. The sample reached Sw = 79% at the maximum possible pressure of 1 MPa using the porous plate technique. Measurements were made at only two partial saturations of 86% and 79%. Figures 9.15a and b show the

experimental results for velocities versus effective stress at different saturation conditions for this sample.

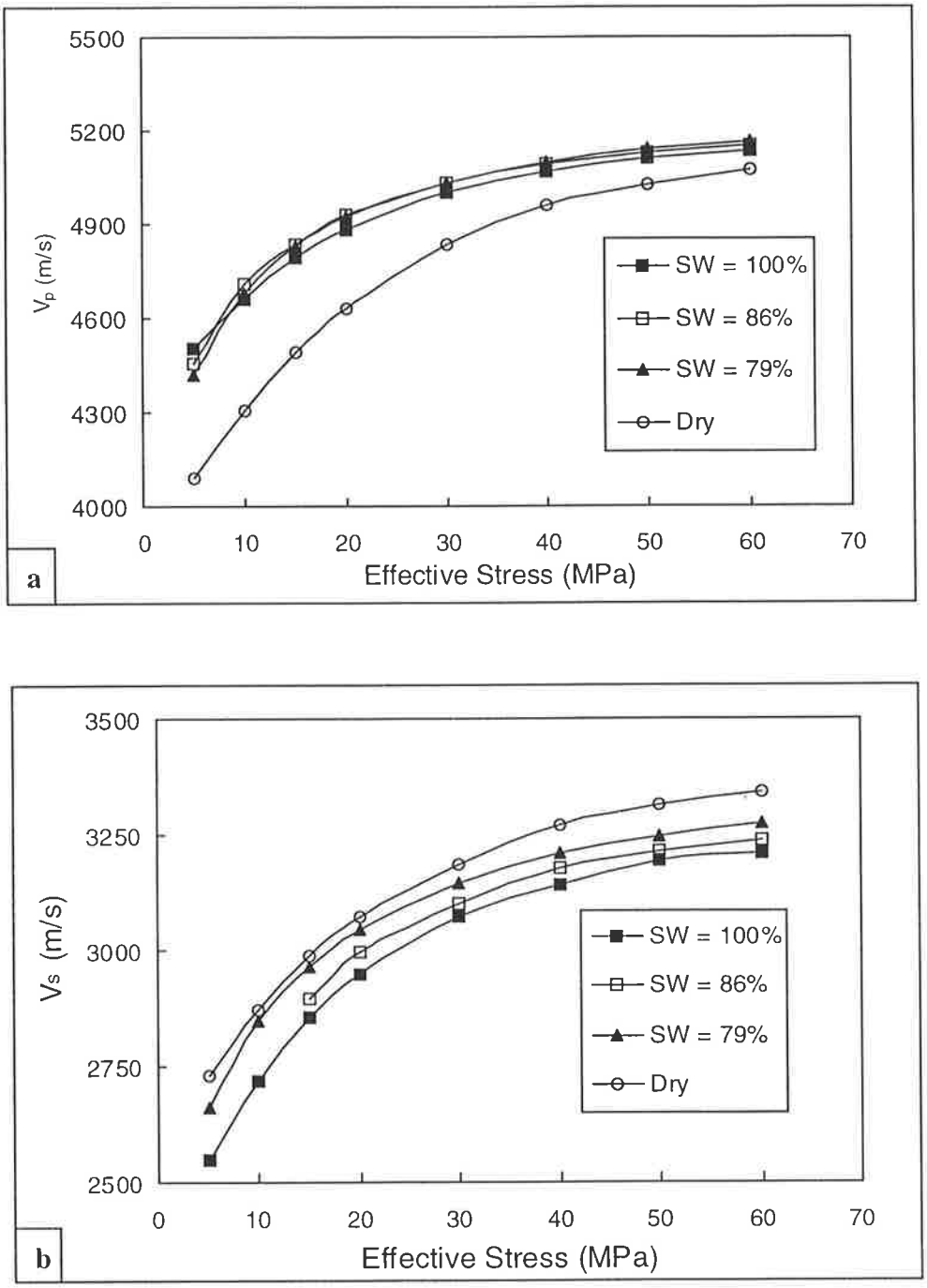

Figure 9.15. Variation of V_p (a) and V_s (b) with effective stress in sample M8 at different water saturation conditions.

The general velocity-effective stress relationship for sample M8 is similar to those shown for sample M2. Stress sensitivity of velocities at partial and fully saturated conditions are similar whereas the dry sample shows higher stress sensitivity particularly at low effective stresses.

Figure 9.16 shows the variation of V_p, V_s and V_p/V_s with saturation at 40 MPa effective stress for the sample M8. V_p increases by 33 m/s with saturation decrease from full saturation to 79% and decreases by 128 m/s under dry conditions. In contrast, V_s increases by 67 m/s as saturation changes from 100% to 79%. The value of V_p/V_s in sample M8 decrease from 1.61 to 1.59 with saturation decrease from 100% to 79%. Similar trends between velocities and saturation exist for sample M8 at other effective stresses.

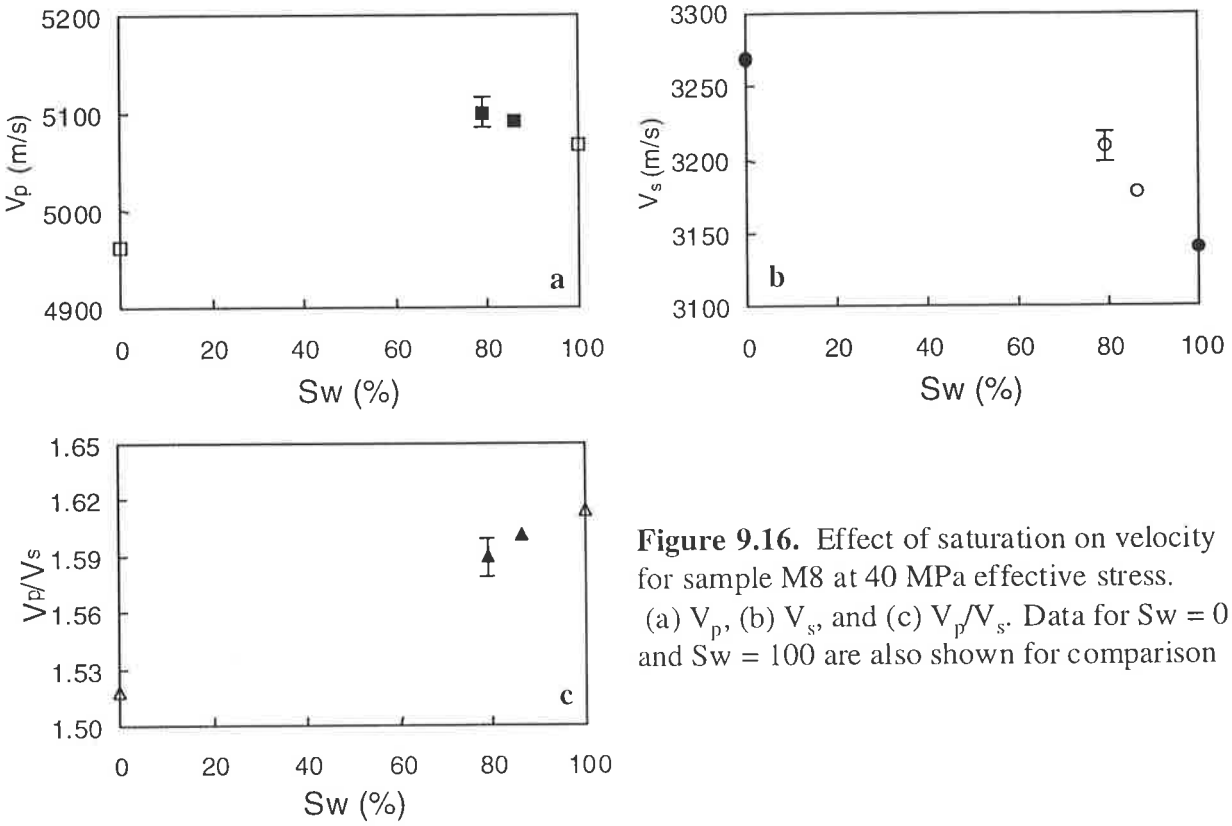

Figure 9.16. Effect of saturation on velocity for sample M8 at 40 MPa effective stress. (a) V_p, (b) V_s, and (c) V_p/V_s. Data for Sw = 0 and Sw = 100 are also shown for comparison

9.4. Discussion

9.4.1. Scale of Saturation Heterogeneity

It is known that saturation heterogeneity may influence acoustic velocities if the scale of the heterogeneity is greater than the wavelength, λ, of the elastic wave (Bourbie et al. (1987). The heterogeneity in fluid distribution in porous rocks may appear at three different scales. These are; pore-scale, sample-scale and reservoir-scale heterogeneity. Pore-scale heterogeneity is related to microstructure, pore type and geometry within the rock. Sample-scale heterogeneity results from significant lithology variation such as interbedded shale and sandstone intervals, or open/cemented fractures both at millimetre to centimetre scale. Reservoir-scale heterogeneity in saturation is caused by lithologies with

varying rock properties such as capillary pressure, permeability and porosity over the reservoir interval (meter scale). Each of these three saturation heterogeneities could influence acoustic velocities in different ways and magnitudes.

To interpret the variation of velocity with saturation for individual samples the pore-scale and sample-scale saturation heterogeneities should be taken into account. Reservoir-scale heterogeneity will be discussed later in the chapter by comparing the velocity-saturation relationships within samples collected from similar wells. In acoustic measurements performed in the current study the wavelength λ varies between 3 mm to 5 mm. Visual, thin section and SEM examinations of the samples showed no heterogeneities at the sample scale since the rock components including minerals, rock fragments and pores are randomly distributed throughout the samples with no observable lamination or fracture. Further, during the desaturation process all samples were kept under constant capillary pressure for at least two weeks at each saturation level prior to acoustic measurement. The assumption is that the desaturation process using the porous plate technique is slow enough to generate a homogeneous distribution of gas and water within the samples at the sample-scale.

Capillary pressure data for the studied samples however suggest that there is a pore-scale saturation heterogeneity within the samples under partial saturation. Although the pore geometries of the studied samples do not resemble the capillary tubes showed in Figure 9.1, one could assume that pores associated with small throats remain water saturated (or at least water-wet) over a relatively large range of saturation and only at very low saturations (high capillary pressures) and close to a dry state will be filled by gas. In contrast, pores associated with large effective throats are easily accessible by gas at relatively low capillary pressures. In addition, at high capillary pressures water will remain coating the solid internal surfaces of the pore spaces and as a coating ring at grain contacts. This pore-scale saturation heterogeneity may explain the variation of velocity with saturation in experimental data. The following generalisations could be made on the effect of partial saturation on V_p and V_s and their stress sensitivity in the Cooper Basin samples taking into account the pore-scale saturation heterogeneity.

9.4.2. Stress Sensitivity and Partial Saturation

Partial saturation has minimal influence on the stress sensitivity of velocities in the studied samples. Over a large range of saturation conditions the velocity-effective stress relationships are found to be similar to those at full saturation. Only at very low saturation (Sw < 10%) the stress sensitivity increases and gradually approaches that under dry conditions. As discussed in Chapter 8 the saturation status of the crack-like pores is the key parameter in controlling the stress sensitivity of acoustic velocities under dry and fully saturated conditions over low effective stress ranges (P_e less than 30-40 MPa). At low saturation ranges, as saturation decreases the water in small pores, (at grain contacts, in crack-like pores and coating the surfaces) begins to be replaced by gas. The change of saturation status of microcracks from water-wet to fully dry increases the total pore and fluid compressibility of the sample. Therefore, at very low saturations the whole rock becomes more pressure sensitive compared to that in moderate-to-high partial and fully saturated conditions. With the closure of microcracks at high effective stresses the velocity-effective stress relationship becomes independent of saturation status.

9.4.3. Velocity-Saturation Relationship

As mentioned in Chapter 3 the effect of pore fluid saturation on acoustic velocities is through its influence on both bulk density and elastic moduli. In order to separate the density effect from the elastic moduli effect the variation of bulk and shear moduli with saturation are discussed here. Equations 3.1 and 3.3 and the measured bulk density of partial saturated samples were used to calculate the bulk and shear moduli of the samples respectively using experimental results presented in section 9.3. For the purpose of generalisation of observations, discussion is concentrated on those samples which have acoustic data over a wider range of saturation.

Under constant effective stress, the variation of bulk modulus with saturation does not follow a consistent trend over the entire saturation range. At high and moderate saturation levels as saturation decreases bulk modulus falls (Figure 9.17). For samples S3, D4 and D6 this saturation interval coincides with zone I of the capillary pressure curves which is characterised by a rapid replacement of water with gas. In this stage the introduction of gas into pores causes a steady decrease in the bulk modulus while no significant change occurs in shear modulus. The steady decrease of bulk modulus with saturation decrease over the high and moderate saturation levels may imply a simultaneous drainage of water from the

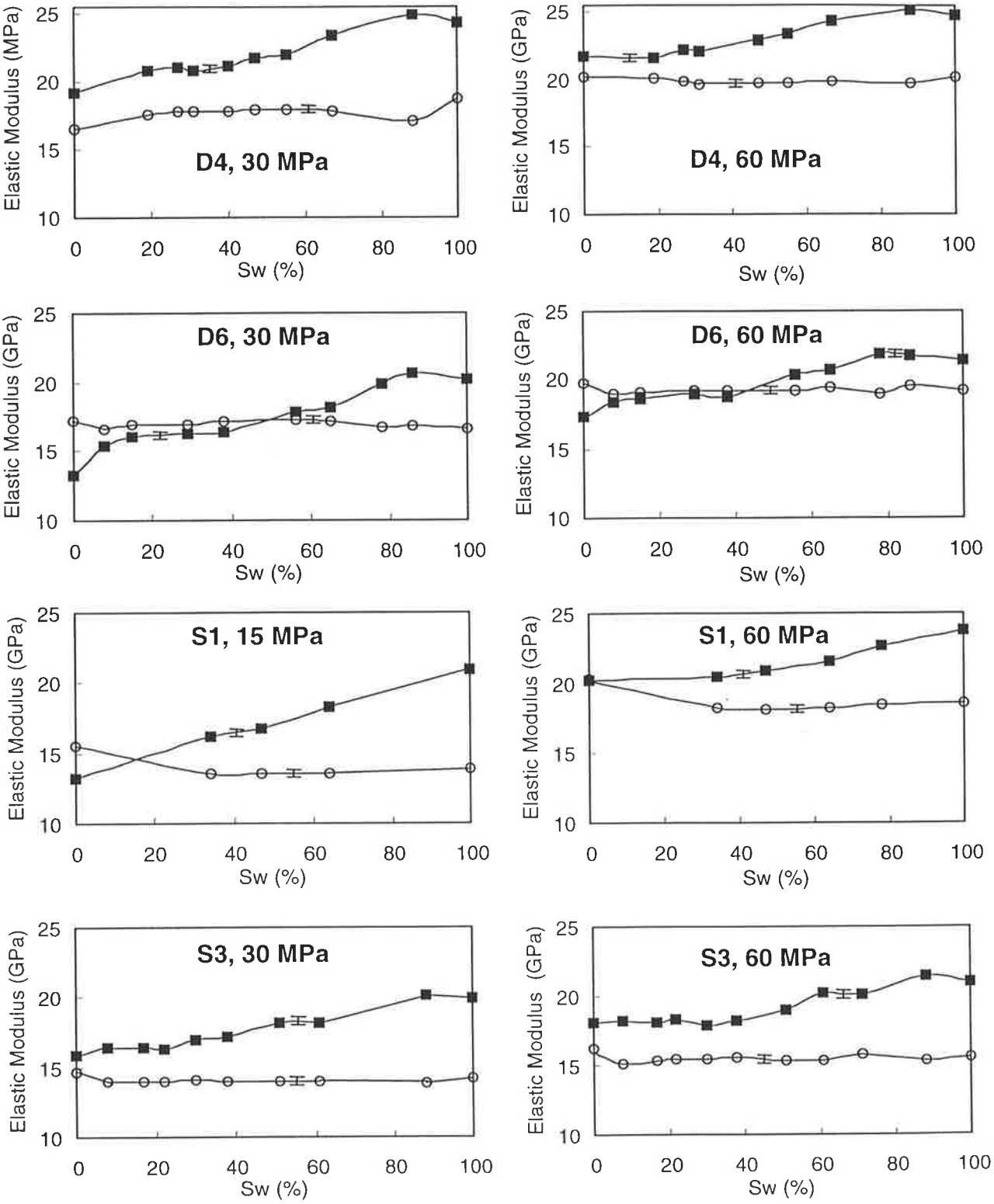

Figure 9.17. Bulk (filled square)and shear (void circle) moduli versus water saturation at different effective stresses for samples D4, D6, S1, and S3.

entire pore space with a preference for crack-like pores to retain water. The simultaneous drainage of all pores continues until the saturation approaches the irreducible status corresponding to the zone II of the capillary pressure curves. Further saturation decrease and drainage of partially drained pores has a minor effect on the bulk modulus while the bulk density slightly decreases and thus V_p remains approximately constant over low saturation range.

At high effective stresses where the presence of crack-like pores in the rock is minimal there is no variation in bulk modulus under dry conditions and low saturation ranges. At low saturation levels (near irreducible status) water becomes a disconnected phase and presents only as adsorbed layers on pore walls and grain surfaces. At low effective stress conditions, where the crack-like pores are still open, elastic moduli show a sharp decrease under dry conditions. The decrease in bulk modulus of rock at low effective stresses may be attributed to removal of water from crack-like pores and grain boundaries. The relationship between bulk modulus and saturation at low saturation to dry conditions is consistent for all samples except sample D6. For this sample the bulk modulus decreases sharply under dry conditions even at high effective stresses. Sample D6 shows a relatively high crack-closure stress (90 MPa) compared with other samples indicating that a greater number of low aspect ratio pores remain open over a larger stress range.

The shear modulus stays almost constant (within 1%) over the entire partial saturation range. The increase of V_s with saturation decrease is therefore assigned to the decrease of bulk density as gas replaces water in the pore space. Between low saturation levels and dry conditions the shear modulus increases sharply in all samples, except D4. For other samples the increase of shear modulus under dry conditions, which occurs over the entire measured effective stress range, varies between 4% to 10%. The change of shear modulus could be related to the interaction of water and grains particularly clay minerals and muddy rock fragments resulting in a matrix softening which lowers rigidity of the rock with water saturation. In the case of sample D4, either there is no such influence on shear modulus by water, or the influence exists but it is masked by crack closure at low saturations. Experimental data reported by Jones (1996) also showed a decrease in shear modulus with introduction of water in the pore space for a number of his sandstone samples. These observations suggest that the assumption that pore fluid saturation has no effect on shear modulus made in theoretical models such as Biot and Gassmann theories is not valid for

the studied samples. Wang and Nur (1992) pointed out that one reason for the discrepancy between experimental data and theoretical prediction for shear velocities in sandstones is that the influence of water on shear modulus is neglected by theoretical models.

9.5. Pore Geometry Model

The above discussion of the velocity-saturation relationship has focused on the role of pore scale fluid distribution. Pore geometry is the primary factor influencing the velocity-saturation relationships, the distribution of fluid during the desaturation process and the shape of capillary pressure curves in porous rocks. Here a simple qualitative pore geometry model is proposed to relate the pore scale fluid distribution and the variation of elastic moduli with saturation for the Cooper Basin samples.

The pore space of Cooper Basin sandstone is modelled by inclusions with a range of aspect ratios. High and intermediate aspect ratio inclusions represent macropores. Crack-like and connective pores are represented by low aspect ratio inclusions. Figure 9.18(a and b) shows a fluid distribution scenario during a desaturation process generated by capillary forces. Figure 9.18c illustrates a model for the variation of elastic moduli with saturation under fluid saturation scheme shown in Figure 9.18 (a and b). The fluid distribution scheme under partial saturation can be divided into two main stages. In the first stage of the desaturation process corresponding to the zone I of the capillary pressure curve all pores are successively and partially drained. Bulk modulus decreases steadily throughout this stage due to introduction of gas into pores until the sample approaches the irreducible stage. In the second stage the saturation level in partially drained pores is reduced toward dry condition. At high effective stresses where no low aspect ratio pores exist within the pore space the full drainage of the sample has a minimal effect on bulk modulus but the shear modulus may increase due to matrix softening effect. At low effective stresses the bulk modulus may fall by drainage of low aspect ratio pores.

This simple pore geometry model is in good agreement with the general velocity-saturation observed on experimental data for the Cooper Basin samples. The model is also consistent with the observed variation in the stress sensitivity of velocities with the saturation change in the studied sample.

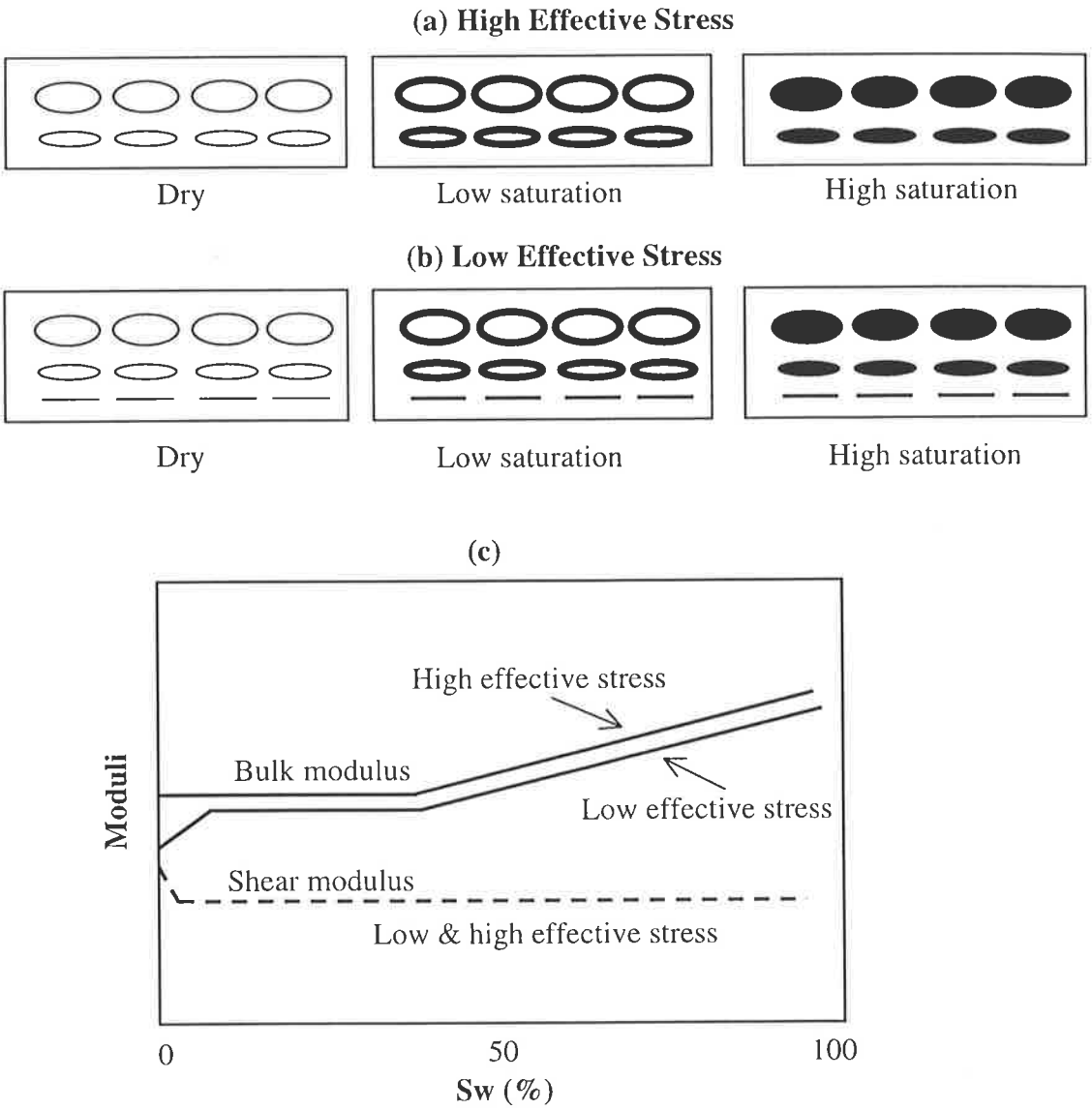

Figure 9.18. Schematic illustration of a simple pore geometry model for Cooper Basin samples and the fluid distribution during the desaturation process. The pores are represented in three groups of inclusions with high to very low aspect ratios. Water is shown in black and gas in white. (a) Pore fluid distribution at high effective stresses. (b) Pore fluid distribution at low effective stresses. (c) Generalised moduli-saturation curves for the studied samples..

9.6. Comparison with Previous Studies

Gregory (1976) examined velocity-saturation relationship in 20 different sandstones under 5000 psi (~ 35 MPa) effective stress. He generalised variation of velocities with saturation based on the sample porosities (Figure 9.19). The saturation behaviour of V_s observed for Cooper Basin samples agrees well with Gregory's idealised curve for $\phi < 10\%$ showing a slight increase in V_s with saturation decrease and sharp rise at low saturation ranges. The observed V_p-saturation relationship in the Cooper Basin samples at high effective stresses is consistent with the Gregory's generalised curve for samples within a moderate porosity range ($10 < \phi < 25\%$).

There are, however, some discrepancies between the two data sets. Sample M2 with 6.2% porosity show a V_p-saturation relationship similar to that for other samples, but in Gregory's model for low porosity samples, velocity decreases at low saturation ranges as sample approaches dry condition. This may be due to different pore geometry in low porosity samples within the two data sets. Gregory's model for low porosity samples resembles the velocity-saturation relationship observed for the Cooper Basin samples at low effective stress ranges. The velocity versus saturation behaviour differs between the two studies at high saturations. Gregory (1976) shows that V_p falls as saturation decreases between the fully water-saturated condition and Sw = 80% whereas in the present study V_p appears to remain constant or slightly increases with the saturation decrease. This may be due to differences in the saturation heterogeneity between the two studies. Cadoret et al. (1998), using X-ray tomography, showed that water is heterogeneously distributed throughout the pore space during evaporative drying at the highest saturations. They commented that at extreme saturation levels, the fluid distribution appears to be controlled only by the intrinsic properties of the rock sample and not by sample pore geometry.

Geortz and Knight (1998) used the numerical approach of Enders and Knight (1989) to investigate the interaction between the microgeometry of the pore space and the evaporative drying process (under room pressure and temperature) which can influence the form of the velocity-saturation relationship. They qualitatively modelled laboratory velocity data versus saturation measured under atmospheric pressure for three different rocks (limestone, dolomite and sandstone) in terms of pore geometry and fluid distribution. They found that the velocity-saturation relationships are different in form for each rock type because of differences in pore space microgeometry. Bulk and shear moduli in

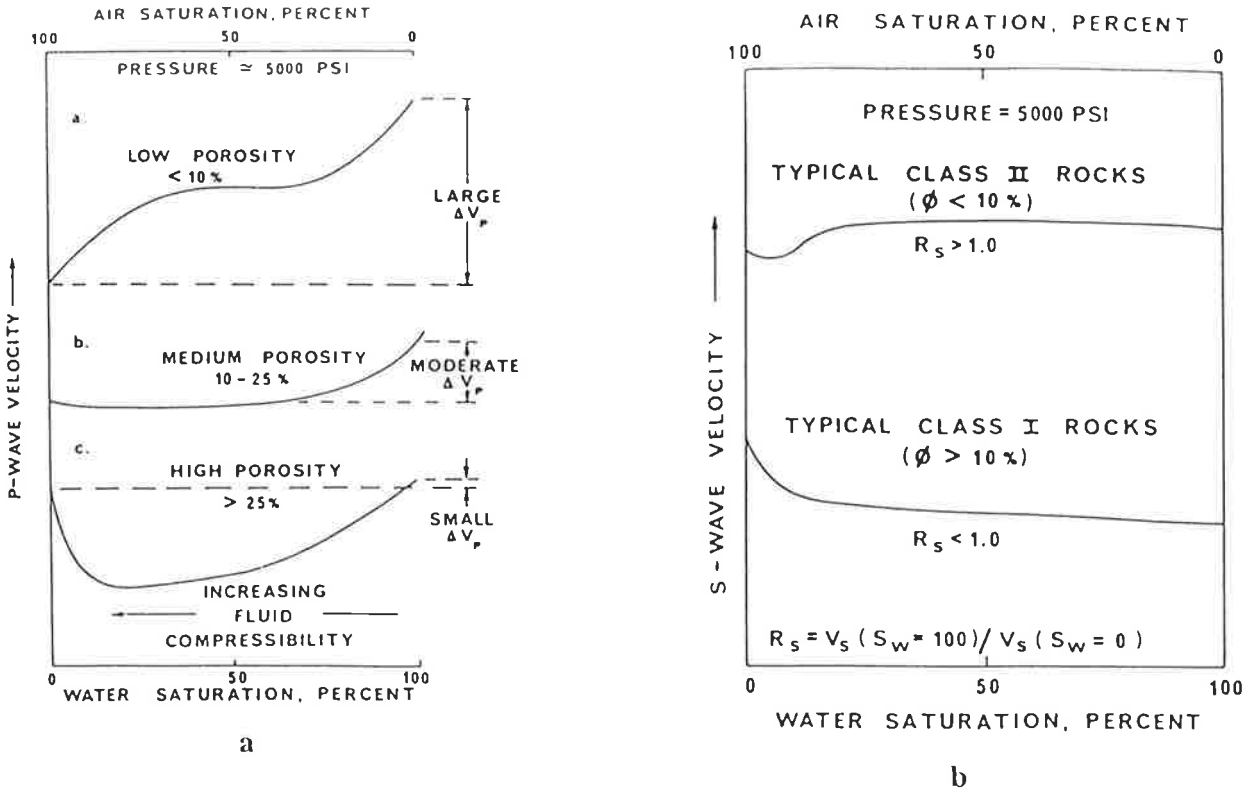

Figure 9.19. Generalised velocity-saturation relationships, (a) V_p, (b) V_s, for sandstones under 5000 psi (~ 35 MPa) confining pressure (from Gregory, 1976).

limestone and sandstone showed significant decrease at low saturation due to the drainage of crack-like pores and grain contacts (Figure 9.20a and b). In contrast, the absence of these pore geometries in the dolomite results in essentially no changes in the moduli at low saturations (Figure 9.20c). the pore geometry model and the generalised elastic moduli-saturation relationship at high effective stresses proposed for the Cooper Basin samples (Figure 9.18) is consistent with the model for dolomite proposed by Geortz and Knight (1998). Whereas the model proposed for their sandstone sample (Berea sandstone) is in general agreement with the model suggested here for the Cooper Basin samples under low effective stress conditions.

There is also a general agreement between the form of the velocity-saturation relationship observed in the Cooper Basin samples and laboratory data reported by Jones (1996), the drying experiment in Murphy (1984), the drainage experiment of Knight and Nolen-Hoeksema (1990) and the flow experiment in Domenico (1977). This similarity in velocity-saturation relationships implies that three different desaturation processes namely; (I) the evaporative drying under room conditions also used by Gregory (1976), (II) the drainage (flow) process and, (III) the porous plate extraction technique also used by Jones (1996), could basically generate similar pore scale fluid distribution in sandstones.

9.7. Heterogeneity at Reservoir Scale

Work by Murphy (1984) on tight sandstones at 5 kHz frequency and atmospheric pressure showed that V_p and V_p/V_s are sensitive to partial saturation and that bore-hole acoustic measurements may delineate the range of partial gas saturation. The magnitude of change in velocities with saturation observed for samples used in the current study appears not to be practically significant (around 2% for V_p). This suggests that, at ultrasonic frequency, the degree of saturation can not reliably be inferred from V_p or V_s only. The V_p/V_s ratio, however, shows a noticeable decrease in magnitude over the saturation range from high to low saturation near irreducible saturation. For instance under 40 MPa effective stress the velocity ratio in sample S3 drops from 1.66 at high saturation (Sw = 88%) to 1.55 as rock approaches to irreducible saturation (Sw = 8%). Combining capillary pressure information with the form of V_p/V_s–saturation for Cooper Basin samples suggests that laboratory velocity measurements may be used as an indicator of saturation status and as means of

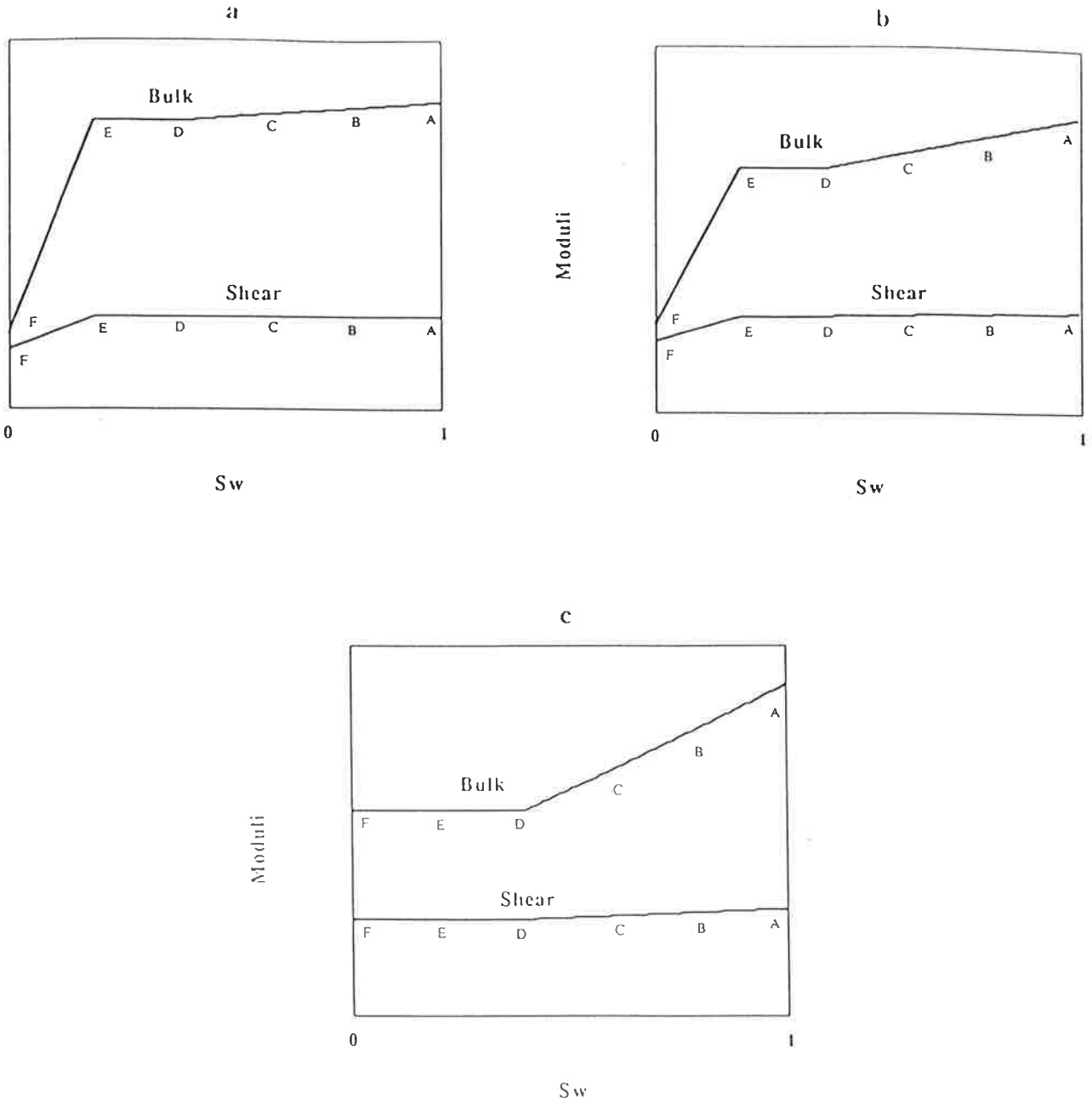

Figure 9.20. Forms of elastic modulus-saturation relationships for (a) a limestone sample, (b) Berea sandstone and (c) a dolomite sample from ultrasonic laboratory measurements at room pressure condition using evaporative drying process (from Goertz and Knight, 1998).

characterising the pore geometry and the distribution of pore fluid within the pore space of rocks.

Assuming a capillary equilibrium status in the reservoir, different rock types may show different saturation depending on their petrophysical properties. Thus there are high saturation zones neighbouring low saturation zones. For example samples S1 and S3 represent two different rock types in terms of capillary pressure characteristics over a 1.5-meter thick interval of single reservoir sandstone. At the same capillary pressure of 100 kPa sample S1 remains fully water saturated whereas sample S3 would have a partial saturation of about 25%.

If the V_p/V_s-saturation relationship observed at ultrasonic frequency exists at sonic log frequency then acoustic data in conjunction with lithological information could determine the saturation status of the various regions of the reservoir. This observation is consistent with the modelling work of Knight et al. (1998) in which the relationship between V_p and water saturation at seismic frequency is determined for reservoir models with patchy distribution of gas and water. They showed that saturation heterogeneity results in velocity changes across a large saturation range, distinctly different from the case of uniform saturation (Biot-Gassmann model) where there is only a large change in velocity close to the point of full water saturation.

9.8. Summary and Conclusions

The relationships between velocities, saturation and effective stress were investigated in a suite of six Cooper Basin sandstone samples. Experimental data indicate that there is a link between the velocity-saturation relationship and pore-scale fluid distribution. Petrographic information, capillary pressure curves, and acoustic data were incorporated into a simple pore geometry model to interpret the velocity-saturation relationship and stress sensitivity under partially saturated conditions for the studied samples.

As saturation decreases, V_p generally decreases over the range from high to moderate saturation, while V_s generally increases over the entire saturation range. The steady decrease of V_p as saturation decreases over the range from high to moderate saturation suggests a simultaneous drainage of water from pores with a variety of high to moderate

aspect ratios, while crack-like (low aspect ratio) pores retain water. Under high effective stresses, within the moderate to low saturation range, and as samples approach irreducible saturation, V_p remains effectively constant. At low effective stresses V_p decreases significantly between low saturation and dry conditions. Partial saturation has minimal influence on the stress sensitivity of velocities in the studied samples and only at very low saturation (near to dry condition) does the stress sensitivity of velocities gradually increase as saturation decreases. Closure and degree of saturation of the low aspect ratio pores controls the velocity-pressure and velocity-saturation relationships at low saturation and pressure conditions. The similarity of velocity-saturation relationships observed in the current study with of those published in the literature suggests that three different desaturation processes; flow (drainage), evaporating drying and porous plate extraction techniques, may generate similar pore-scale fluid saturation distribution in rock samples.

Experimental data presented in this chapter confirm that ultrasonic velocity measurements in the laboratory may be used as an indicator of saturation status and as a means of characterising pore geometry and the distribution of pore fluid in reservoir rocks. Further investigation is needed to verify this observation at sonic log and seismic frequencies, and for other rock types.

Chapter 10

Implications for Hydrocarbon Exploration and Development

10.1. Introduction

This chapter elaborates on some of the implications of the experimental results discussed in previous chapters, for hydrocarbon exploration and development. Examples are provided from the Cooper Basin. First the dependence of velocities on frequency is investigated using the Gassmann (1951) equation. In the second part, the influence of changes in reservoir pressure on the porosity determined from velocity data is shown and a mechanism is presented for calibration of sonic log readings for the pressure variation in the Cooper Basin. The potential of velocity ratio (V_p/V_s) for detection of fluid type at in situ reservoir effective stress is shown. Finally, the implications of the study for reservoir monitoring using time lapse seismic are addressed.

10.2. Velocity Dispersion

It is known that the acoustic velocities in fluid saturated rocks are dispersive. That is, the velocities are frequency dependent. The magnitude of velocity dispersion need to be known if acoustic data obtained from laboratory measurements at ultrasonic frequencies are to be used for log analysis and seismic interpretation. Comparison of laboratory ultrasonic velocities with the low frequency wave propagation model of Biot (1956a) and Gassmann (1951) may give estimates of total velocity dispersion between low frequency and measurement frequency. Assuming that the dry velocities are independent of frequency (Winkler, 1985), Biot-Gassmann equations are used to calculate the low frequency velocities (or elastic moduli) in the fully saturated rocks. The difference between the measured velocities and the calculated low frequency velocities may be interpreted as indication of dispersion (Winkler, 1985 and 1986).

To derive the input parameters for the Gassmann equation (equation 3.4) experimental results on V_p and V_s measurements on dry samples were used in conjunction with density measurements to derive bulk (k_d) and shear (μ_d) moduli of the samples. Empirical relations for acoustic velocity of water at different pressures and temperatures quoted by Schon (1996) were used to calculate the bulk modulus of water (k_f) at different confining pressures (Table 10.1). Bulk modulus of the matrix (k_m) was determined from an extrapolation to zero porosity of the regression curve of k_d versus porosity at 60 MPa confining pressures (Figure 10.1). Wang and Nur (1992) suggested a value of 35 GPa for k_m in shaly sandstone which is consistent with the k_m = 34.95 GPa assigned from the cross plot shown in Figure 10.1 for the Cooper Basin samples.

Pressure (MPa)	V_p (m/s)	Bulk Modulus (GPa)
0	1509	2.27
10	1527	2.33
20	1545	2.38
30	1563	2.44
40	1581	2.50
50	1599	2.55
60	1617	2.61

Table 10.1. Elastic properties of water used in dispersion analysis.

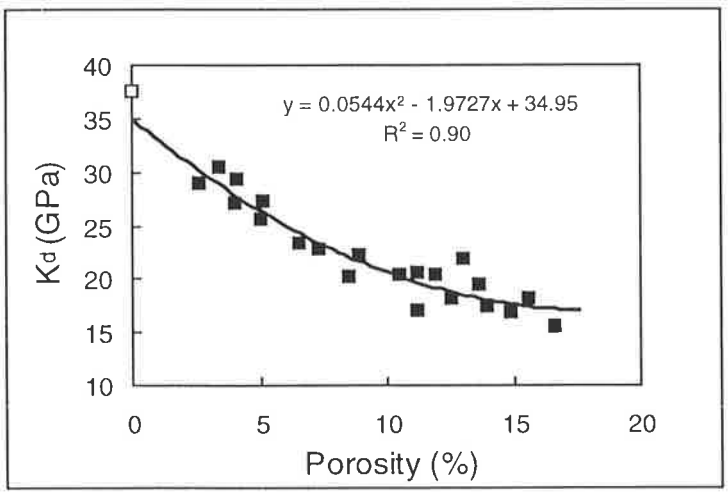

Figure 10.1. Bulk modulus of dry samples versus porosity at 60 MPa confining stress. Void Square shows the bulk modulus of pure quartz, 37.6 GPa quoted from Schon (1996).

Figure 10.2 illustrates the plot of computed bulk modulus for fully water saturated samples at 40 MPa confining stress using Gassmann's relation versus measured data. The computed low frequency bulk modulus for water saturated samples is, in general, less than the measured values in particular for low porosity (higher bulk modulus) samples. Deviations of data from the perfect (1:1) correlation showed by the dashed line in the plot may be considered estimates of bulk modulus dispersion with frequency from near zero to one MHz range. The absolute deviation of predicted values from measured data within the samples ranges between 1% to 10% with an average of 4.3%.

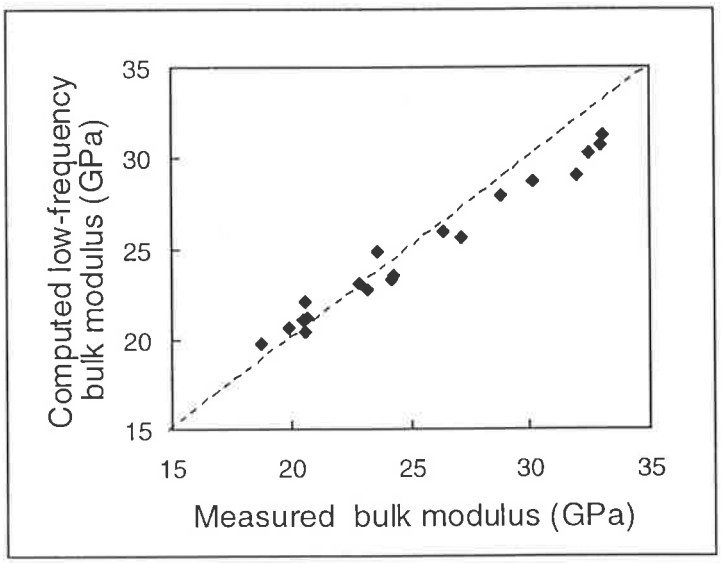

Figure 10.2. The plot of computed bulk modulus for fully water-saturated samples at 40 MPa confining stress using Gassmann's equation versus measured data. Dashed line shows perfect (1:1) correlation.

Figure 10.3 shows the calculated near zero-frequency versus measured V_p and V_s for data shown in Figure 10.2. Figure 10.3 indicates the calculated low-frequency velocities are systematically greater than measured velocities. The average of absolute deviation of calculated velocities from the measured values is 1.3% and 2.8% for V_p and V_s respectively. The Biot-Gassmann model assumes that shear modulus is independent of pore fluid (equation 3.5) and its value is similar for a given rock at dry and water-saturated conditions. However, several investigators (for example; Gregory (1976), Winkler (1986), Wang et al. (1991)) along with the experimental results presented in Chapter 9 of the current study have indicated that introduction of water to a extremely dry sample will reduce the rigidity of the rock through chemical interaction between water and the rock's

components. This would increase the calculated low-frequency saturated velocity by a few percent and therefore the true velocity dispersion may be masked if the shear modulus of the extremely dry samples were used for calculation of low-frequency saturated V_p. Hence, the negative velocity dispersions (ultrasonic velocity greater than low frequency velocity) shown in Figure 10.3 are artificial.

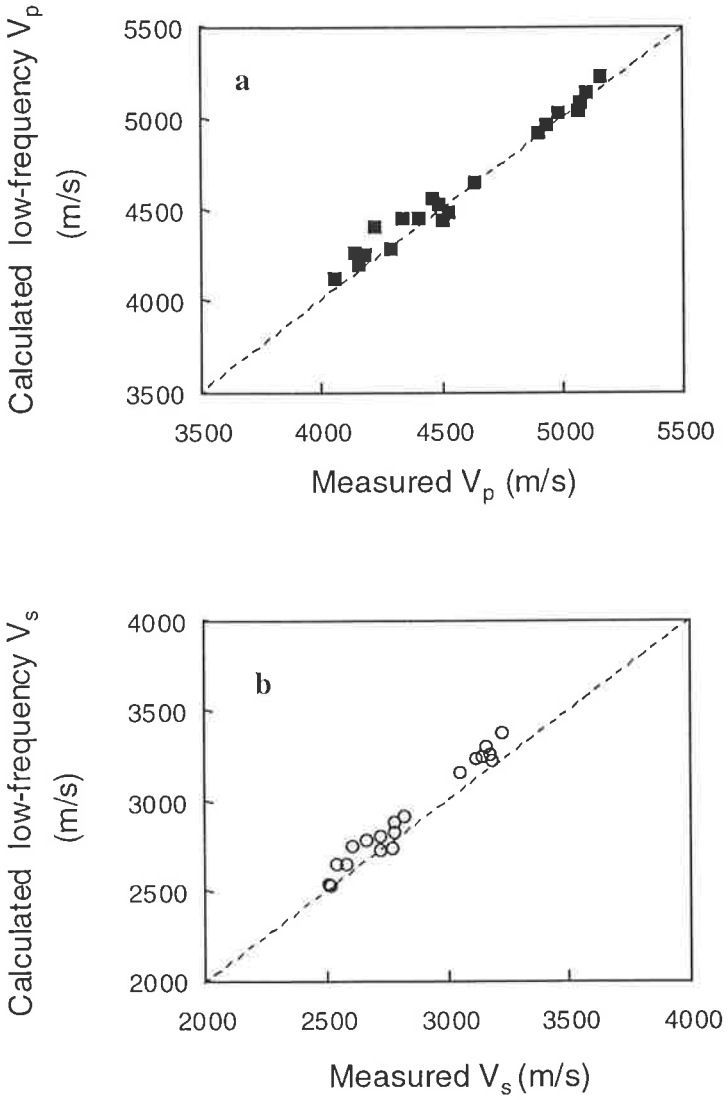

Figure 10.3. Calculated low-frequency velocities using Gassmann's equation versus measured velocities. Dashed line shows perfect (1:1) correlation. (a) V_p, (b) V_s.

Figure 10.4 illustrates calculated low frequency V_p considering water-wet shear modulus as input parameter for velocity calculations. Biot-Gassmann calculated velocities fit the measured ultrasonic frequency adequately well with an average of 1% dispersion. Wang and Nur (1992) commented that a 2% difference between Biot-Gassmann calculated low–

frequency and the measured velocities should be considered as a perfect fit for practical purposes. It is concluded that velocities measured in the laboratory at ultrasonic frequencies on water saturated Cooper Basin samples can be treated as low-frequency data and therefore may be used with confidence for sonic log and seismic interpretations.

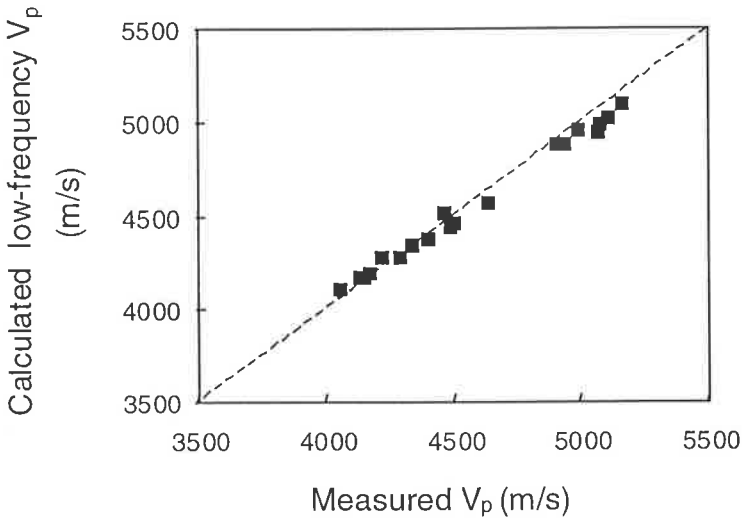

Figure **10.4.** Calculated low-frequency V_p using Gassmann's equation versus measured V_p, considering water-wet shear modulus as input parameter for velocity calculations. Dashed line shows perfect (1:1) correlation.

10.3. Sonic Log-Derived Porosities and In Situ Effective Stress

Direct hydrocarbon detection, reservoir characterisation and monitoring are the main goals of exploration seismology and are dependent on an understanding of rock properties under varying reservoir conditions. The in situ effective stress in a hydrocarbon reservoir may vary during production. Depletion of the reservoir can increase the in situ effective stress. In a multi-layer reservoir, different reservoirs may have various pressures due to different production rates or different pore pressure gradients. Knowledge of the magnitude of such variation is essential for the exploration of new reserves and optimisation of the performance of existing fields. Lumley et al. (1997) commented that the effects of variation of in situ reservoir pressure during production are more seismically visible than previously thought.

As mentioned in Chapter 3, the stress dependent nature of wave velocities could influence porosity values derived from sonic transit times in reservoir rocks. That is, for a reservoir

rock at a certain depth and with a given porosity, the sonic log will indicate varying transit time as the reservoir pressure changes. Consequently log-derived or apparent porosity would change with time. This may be particularly true for reservoir rocks with high-stress sensitivity at or beyond the upper boundaries of the velocity-effective stress relationship generalised by Dvorkin et al. (1996). Experimental data presented in Chapter 6 indicates that the stress sensitivity of acoustic velocities in some of Cooper Basin samples is higher than those reported in the literature. The in situ effective stress in the Cooper Basin reservoir is about 20-30 MPa. For the sandstone samples examined in the current study this pressure corresponds to the high-velocity gradient region in the velocity-effective stress curve. The considerable difference between in situ effective stress and the predicted microcrack-closure stress in the study area (around 81 MPa) implies that small changes in reservoir pressure may cause a significant change in the velocity of the reservoir rock.

Acoustic velocities measured in the laboratory on a Cooper Basin core with known petrophysical characteristics are used to show the magnitude of variation in porosity values assigned to a rock by calculation based on the sonic log when in situ effective stress varies. Figure 10.5 shows V_p measured at dry and fully water-saturated conditions versus effective stress for sample S1 with a 10.5% helium core porosity. The Overton-Hamilton (1986) equation which is a modified version of the time average formula (Chapter 3) is used to convert measured velocities to porosity, under dry (air-saturated) and water-saturated conditions, assuming that the sonic transit time in the well-bore environment for this rock corresponds to the ultrasonic velocity measured under laboratory conditions.

Figure 10.6 shows apparent porosities using the Overton and Hamilton equation and the actual core porosities measured at elevated effective stresses of 5 to 60 MPa. The total core porosity reduction of the sample over this pressure range is less than one-porosity unit. Similar to other conventional velocity-porosity equations the Overton-Hamilton equation does not account for the effect of pressure on acoustic velocity, and will indicate a decreasing porosity as effective stress increases. The equation underestimates the porosity by up to 3 porosity units as the in situ effective stress exceeds 30 MPa. Underestimation of the porosity leads to underestimation of hydrocarbon pore volume and artificially low reserve estimates. Where the economical cut-off is based on a porosity value, the underestimation of porosity due to the pressure effect of sonic log values may lead to partially pressure depleted, but economic, reservoirs being bypassed. In contrast, under

overpressured conditions, where the effective stress is lower than 30 MPa, neglecting the pressure effect on velocity results in overestimation of porosity. Because of the non-linear behaviour of the velocity-effective stress relationship the variation of velocity is rapid at low effective stress (overpressure zone), particularly under air-saturated conditions. For instance at an effective stress of 10 MPa (a highly over-pressured zone) the porosity assigned to the sample by conventional velocity-porosity transforms can be as high as 17.2% and 13.2% at air (gas) saturated and water saturated conditions, respectively.

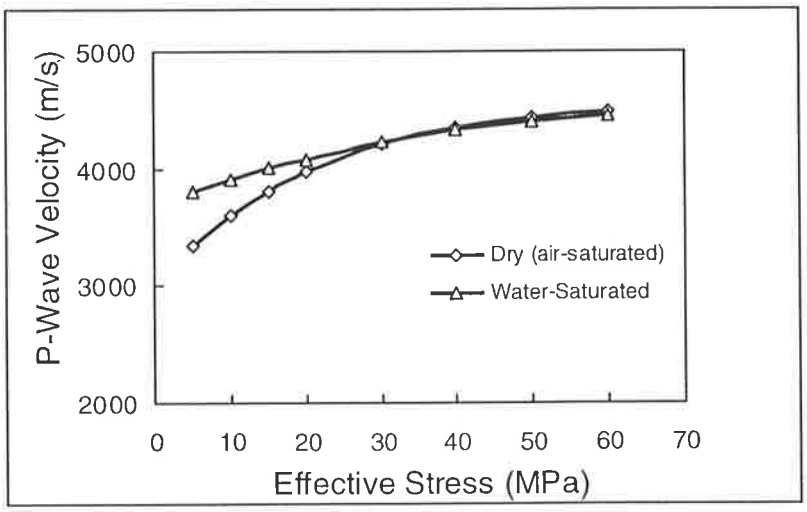

Figure 10.5. P-wave velocity measured as a function of effective stress for sample S1 with a helium porosity of 10.5%.

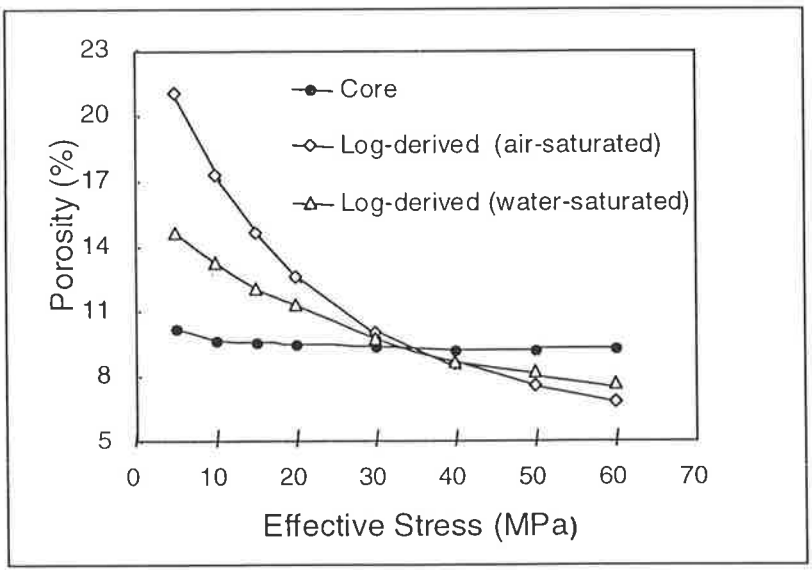

Figure 10.6. Comparison between measured and calculated porosity versus effective stress for sample S1.

It is often necessary to make correction to log data prior to using them for petrophysical evaluation. For many logging tools there are correction charts to remove environmental effects, such as temperature, mud type, salinity of the formation water and so on. Despite the pressure effects noted above there is no published correction chart for the sonic log for varying effective stress conditions. The stress sensitivity of acoustic velocities may significantly differ from one rock type to another (Khaksar et al. (1997) and Vernik (1997)). Where the other porosity tools (neutron and density logs) are not available or due to the borehole conditions are not reliable, and where the reservoir pressure varies in different wells, or even in the same well different reservoirs show varying pressures, it is necessary to calibrate the sonic tool response to the pressure variation. Petro-acoustic studies involving the measurement of acoustic velocities in representative core plugs at different pressure and saturation conditions along with the petrology and sedimentology of reservoir rocks will provide useful guides for calibration and quantitative interpretation of velocity data in hydrocarbon producing reservoirs.

Based on the velocity-effective stress relationships derived from experimental studies presented here an equation is proposed to calibrate the variation of V_p to the reservoir pressure changes in the studied samples.

$$dV_p/dP = 79.35e^{-0.05P} \qquad (10.1)$$

where V_p is in m/s and P is effective stress in MPa.
Equation (10.1) provides a basis for an empirical correction factor for the pressure effect on sonic log response in the Cooper Basin wells (Khaksar et al., 1998).

10.3.1. A Field Example

Among the wells which have been drilled in recent years in the Cooper Basin, there are a number in which reservoirs appear to have anomalously low porosity (as calculated from the sonic log) and exhibit a high level of pressure depletion. For instance almost two thirds of recoverable gas in the Toolachee Field (Chapter 2) has already been produced. Formation pressure data obtained from the Repeat Formation Tester (RFT) tool in this field indicate a variety of reservoir pressures ranging from non-depleted to moderately and highly pressure depleted, depending on the hydrocarbon production from the adjacent

wells. Hence, at a given depth different reservoirs may show different formation pressures.

The sonic log derived porosities in some of the partially pressure depleted reservoirs in the Toolachee Field show values up to 5 porosity units too low, whereas in adjacent wells similar reservoirs, but non-depleted, show normal sonic porosities. Table 10.2 shows examples of this phenomenon. The only commonly available and relatively reliable porosity device in Cooper Basin wells is the sonic tool. Figure 10.7 shows a comparison of calculated porosities from different tools where an other porosity tool (density log) is available. There is a good agreement between porosity derived from the density and sonic logs in non-depleted reservoirs but in pressure depleted reservoirs porosities derived from sonic logs show lower values.

Depth (m)	Interval	Well	Porosity from sonic log (%)	Average porosity in field (%)	Pressure depletion (%)
2218	Sand-A	T-48	7.3	12.6	67
2271	Sand-B	T-35	7.4	13.3	72
2312	Sand-C	T-39	8.4	12.6	40

Table 10.2. Examples of anomalously low log-derived porosities in partially pressure depleted sandstone gas reservoirs in the Toolachee Field, Cooper Basin.

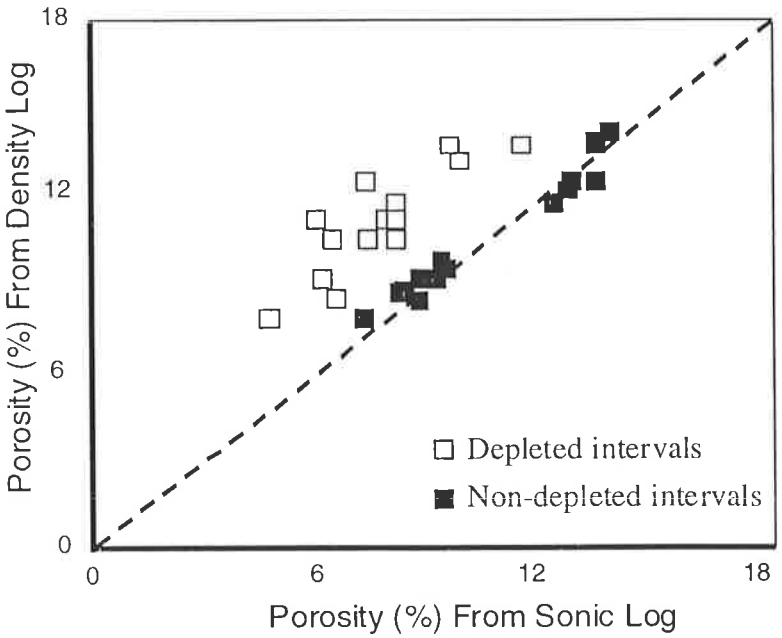

Figure 10.7. Comparison of porosity derived from sonic log and density log in non-depleted and depleted gas reservoirs in the Toolachee Field. Line shows perfect correlation (from Khaksar and Griffiths, 1996a).

In a case study Khaksar (1994) suggested that the anomalously low log-derived porosity observed in the partially pressure depleted sandstone gas reservoirs in the Toolachee Field may be caused by the influence of effective stress on the sonic transit times. Based on the available wireline log information and analogy with published laboratory data for Berea sandstone Khaksar and Griffiths (1996b) proposed an empirical equation for the calibration of sonic log readings to formation pressure variation for the Toolachee Field reservoir rocks. They showed that the porosity underestimation using the Overton-Hamilton equation due to a 7 to 21 MPa reduction in formation pressure (increase in effective stress) for samples with porosities of 17% and 8% ranges from 1.3 to 3.0 and 1.0 to 2.5 porosity units, respectively. This range of porosity underestimation has the same order of magnitude as those estimated for sample S1 at high effective stresses using laboratory data. That is, the velocity-pressure relationship obtained from laboratory data is consistent with the sonic log anomaly observed in partially pressure-depleted reservoirs in the Cooper Basin.

10.4. Information on Shear Wave Velocity

The analysis of amplitude-versus-offset (AVO); direct hydrocarbon indication techniques, and processing and interpretation of multicomponent seismic and vertical seismic profiles (VSP) need information on propagation of shear waves in the earth. Although S-wave velocity logs have now been available for many years, there are very few wells in the Cooper Basin with S-wave velocity data. Therefore prediction of V_s from other logs is necessary where measured V_s logs are not available. Several empirical and theoretical models have been published to predict S-wave velocity from other logs (for example; Han et. al (1986), Xu and White (1996)). The theoretical model of Xu and White (1996) requires a hypothetical pore aspect ratio spectrum and needs detailed rock properties information including accurate clay minerals percentages which may not be available all the time (Dutta, 1997).

The laboratory measurement of acoustic velocities indicate that for the Cooper Basin sandstones V_p and V_s are similarly affected by lithology, porosity and clay content. This is consistent with works by Castagna et al. (1985), Han et al. (1986), Freund (1992) and Vernik (1994) which demonstrated that for clastic rocks V_s is a linear function of V_p at both ultrasonic and sonic log frequencies. Figure 10.8 demonstrates the relationship

between Vs and V_p for the Cooper Basin sandstones measured under dry and water saturated conditions for effective stress of 20 MPa. Statistical analysis of experimental results indicates that a linear function of the form;

$$V_p = R\, V_s \qquad (10.2)$$

where R is constant, fits the data satisfactorily with correlation coefficients better than 0.97. Table 10.3 shows the value of R and the regression coefficient over a pressure range of 20 to 60 MPa. The value of R (V_p/V_s ratio) for dry rock is independent of effective stress whereas for water saturated samples it decreases as effective stress increases. The observation on the lack of relationship between velocity ratio and effective stress for dry rocks is consistent with data on other rocks reported by Gregory (1976) and Castagna et al. (1985). Variation of velocity ratio with effective stress for water saturated Cooper Basin samples may be explained by the different stress sensitivity of V_p under dry and water saturated conditions as discussed previously in Chapters 6 and 8.

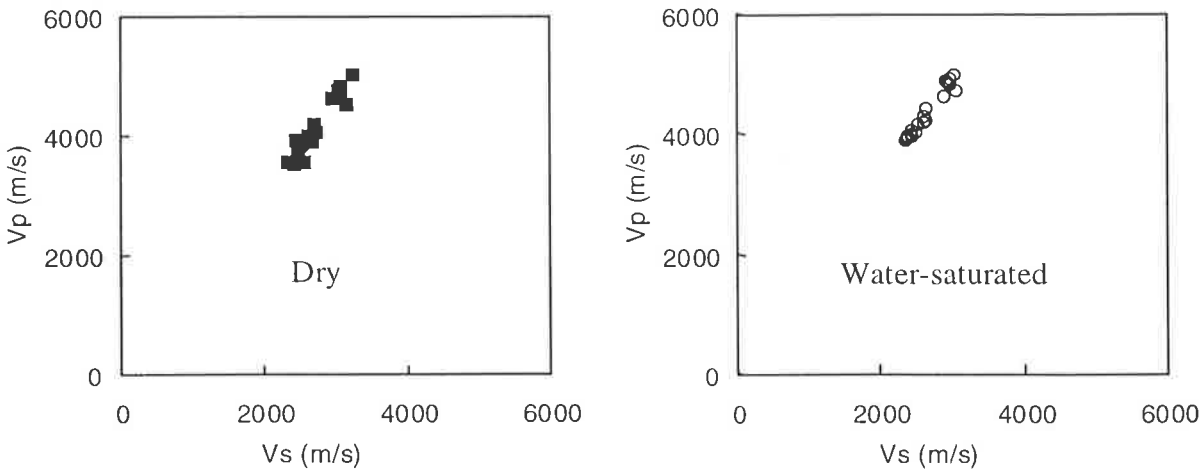

Figure 10.8. Relationship between V_s and V_p for the Cooper Basin sandstones measured under dry and water-saturated conditions for effective stress of 20 MPa.

Effective stress (MPa)	Dry	R	Water saturated	R
20	1.52	0.97	1.64	0.97
30	1.52	0.98	1.62	0.97
40	1.52	0.98	1.61	0.98
50	1.52	0.98	1.59	0.98
60	1.52	0.98	1.59	0.97

Table 10.3. V_p/V_s ratio (R) in equation (10.2) as a function of effective stress for dry and water saturated Cooper Basin sandstones. R is the regression coefficient of the best fit.

Using Kuster-Toksoz (1974a) model, Tatham (1982) showed that the pore geometry and microstructure of the rock is a major factor controlling the magnitude and stress sensitivity of the velocity ratio in sandstones. This indicates that different sandstones may show similar velocity ratios if they have similar pore geometries. Figure 10.9 shows the relationship between velocity ratio (V_p/V_s) and porosity at an effective stress of 30 MPa, under both dry and water saturated conditions. The lack of relationship between velocity ratio and porosity in the Cooper Basin samples may be explained by the fact that all samples investigated in this study are from one formation, have the same mineralogy, and demonstrate a relatively similar diagenetic history. Similar petrographic and sedimentological characteristics result in low variability of pore geometries within the samples regardless of their total porosity. In addition, the range of porosities of the studied samples is relatively small which could obscure the possible relationship between velocity ratio and core porosity shown in the literature.

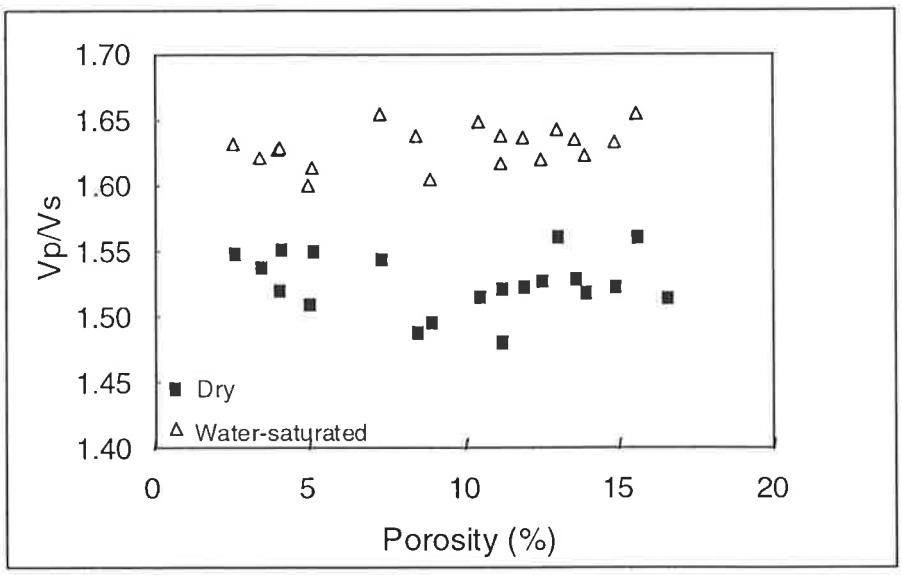

Figure 10.9. Velocity ratio versus porosity at 30 MPa effective stress for dry and water-saturated Cooper Basin sandstones.

The strong correlation between V_s and V_p implies that for the Cooper Basin rocks the S-wave velocity may be predicted from P-wave velocity with confidence. Further as indicated in Table 10.3, the V_p/V_s ratio in dry and water saturated samples is significantly different suggesting that the V_p/V_s ratio has potential for detecting gas saturated intervals under in situ reservoir pressures wherever shear wave velocity data are available. This is in agreement with acoustic data on partially saturated samples addressed in Chapter 9.

10.5. Potential for Time Lapse Seismic

As reservoir fluids are produced or injected during enhanced oil recovery, the reservoir's dynamic properties may change. If these changes are large enough, repetitive seismic surveys can map fluid distributions, changes in reservoir pressure and temperature and fluid fronts. Reports of successful reservoir monitoring using time lapse seismic are increasing (for example: Nur (1989), Watts et al. (1996), Waite and Sigit (1997)). Before shooting repetitive seismic surveys the feasibility of such work should be investigated. The feasibility of reservoir monitoring using time lapse seismic has two aspects: the petrophysical and the seismic. The former can be studied through rock physics, which focuses on the acoustic properties of reservoir rocks. The latter includes selection of seismic methods, acquisition design and parameters, seismic resolution, processing, etc. Petro-acoustical measurements are essential to investigate the petrophysical aspects of feasibility studies of seismic reservoir monitoring allowing the modelling of possible variation in acoustic properties with changes in reservoir pressure and saturation with time (Wang, 1997).

The strong stress sensitivity and the distinct V_p/V_s values for dry and water-saturated Cooper Basin cores measured at ultrasonic frequencies suggest that the dynamic changes in pressure and saturation of the reservoir rocks may also be detectable from acoustic impedance or travel time at seismic and sonic log frequencies. Figure 10.10 shows typical results from acoustic velocity measurements for a Cooper Basin sample. The graph shows the changes in acoustic impedance for changes in effective stress, for air (dry) and fully water saturated conditions. As the fluid pressure decreases the effective stress increases and acoustic impedance rises. The initial in situ pressure in gas producing Cooper Basin reservoirs is between 20 to 30 MPa which can be increased to 50 MPa in some highly pressure depleted reservoirs. This leads to around a 17% rise in the acoustic impedance which may be detectable on seismic data. A change in fluid from gas to water results in an increase of acoustic impedance of around 23%. However, these results do not completely simulate the actual reservoir conditions since there is a partial fluid saturation condition within the reservoir.

Partial saturation changes appear to have a smaller effect on acoustic impedance in these rocks. Figure 10.11 shows the sensitivity of acoustic properties of the same sample shown in Figure 10.10 to the variations in both effective stress and fluid saturation. The P-wave

acoustic impedance and velocity are strongly dependent on effective stress at both low (Sw = 15%) and high (Sw = 80%) water saturation levels whereas V_s is less sensitive to pore fluid changes.

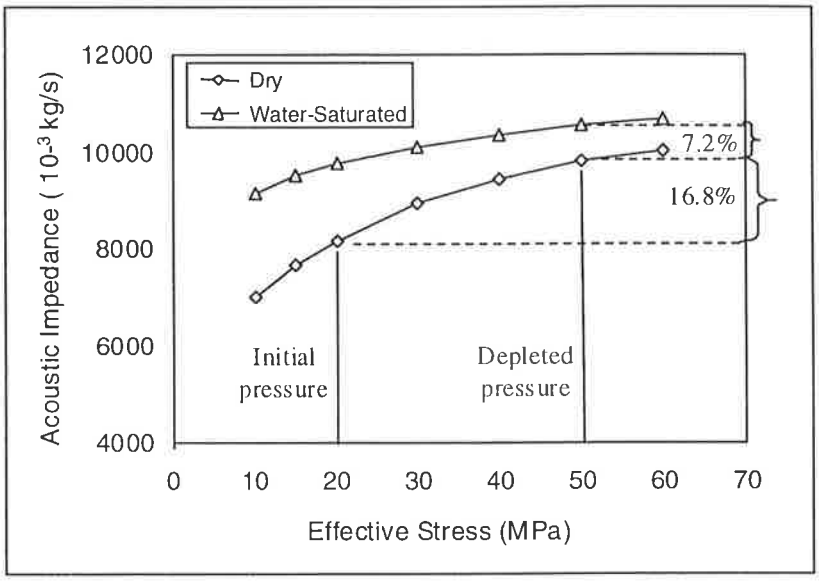

Figure 10.10. Acoustic impedance versus effective stress for a sample D6 with a helium porosity of 11.2%.

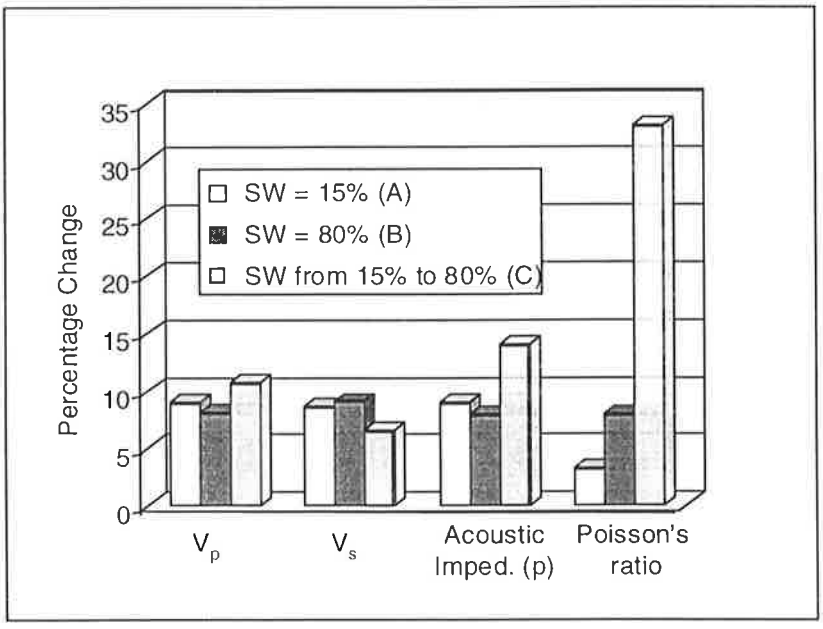

Figure 10.11. Variation of elastic properties as a result of the increase of in situ effective stress from 20 to 50 MPa at three saturation conditions for the sample D6. (A) pressure depleted, gas saturated with no saturation change; (B) pressure depleted, water-saturated with no saturation change and (C) pressure depleted with increasing water saturation from 15 to 80 percent.

In contrast Poisson's ratio (or V_p/V_s ratio) is more sensitive to the variation of water saturation than to changes in reservoir pressure. This implies that over an interval with known rock properties in a gas producing reservoir while the temporal changes in acoustic impedance of a reservoir may enable the pressure depleted regions to be tracked, time-differential V_p/V_s and AVO analysis may also be effective in tracking the flood front. This suggests that time-lapse seismic reservoir monitoring might indeed be feasible in the Cooper Basin. A robust core-log based forward modelling of the changes in pressure and saturation with time in the study area is needed to predict the change in acoustic impedance and Poisson's ratio compatible with seismic resolutions.

10.6. Conclusions

In this chapter some of implications of the experimental results presented in previous chapters were addressed for hydrocarbon exploration and development in the Cooper Basin. Comparison of velocities measured at ultrasonic frequencies on studied core samples with theoretical low-frequency predictions by Gassmann's equation suggests that velocity dispersion due to frequency effect is negligible in these samples. It is concluded that acoustic velocity data derived from laboratory measurements at ultrasonic frequencies can be used with confidence for sonic log and seismic interpretations in the Cooper Basin.

The stress dependent nature of acoustic velocities in rocks requires that when the sonic log is used to determine the porosity of reservoir rocks with varying pressure conditions, the in-situ pressure should be taken into account. It was shown that for two abnormal pressure conditions, overpressured and pressure-depleted, neglecting the pressure effect results in anomalously high and low sonic porosities, respectively. Based on the experimental results on the studied samples a velocity-pressure relationship is defined which provides a basis for an empirical correction factor for the pressure effect on sonic log response in the Cooper Basin wells. Further, the potential of the velocity ratio (V_p/V_s) for detection of fluid type at in situ reservoir pressure, and prediction of V_s from V_p, were demonstrated for the Cooper Basin rocks. The strong stress sensitivity and the distinct V_p/V_s values for dry and water saturated Cooper Basin cores measured at ultrasonic frequencies, suggest that the dynamic changes in pressure and saturation of the reservoir rocks might also be detectable from acoustic impedance or travel time at seismic and sonic log scales.

Chapter 11

Summary and Conclusions

11.1. Overview and Summary of Results

This chapter summarises the findings of the research and gives recommendations for further investigations for verification and extension of the project results.

The primary objective of this study was to investigate the influence of effective stress, fluid saturation, porosity and clay content on the velocity of compressional and shear waves in a set of low to moderate porosity sandstones. The research integrated field data and petrography with laboratory measurements of acoustic velocities of representative rock samples from the Permian sandstones of the Cooper Basin, South Australia.

In Chapter 3, data from the Toolachee Field, a gas producing field in the southern Cooper Basin were compared to published experimental data. It was confirmed that, as well as porosity, other factors such as clay and fluid content are also important (and should be considered) when sonic logs are used for porosity determination. None of the experimentally derived velocity-porosity equations examined in Chapter 3 provide a globally applicable method for porosity calculation from sonic logs. The shortcomings of these equations are more pronounced when applied to gas-bearing shaly sandstone formations. It was also shown that the common velocity-porosity methods do not account for the variation of velocity due to reservoir pressure change. Neglecting the stress-dependent nature of velocity may result in an erroneous prediction of porosity from velocity and errors in other applications of velocity data in a reservoir with varying effective stresses.

Systematic laboratory measurements were carried out to investigate the effects of effective stress on ultrasonic compressional and shear wave velocities in a set of low to moderate

porosity samples from Cooper Basin sandstone reservoirs. Experimental results showed that acoustic velocities in dry (Chapter 6) and water-saturated (Chapter 8) samples increase non-linearly with effective stress over the pressure range of 5 to 60 MPa. The increase of wave velocities with effective stress is stronger below 40 MPa. Above 40 MPa the velocity gradient decreases significantly in both dry (100% air-saturated) and water-saturated rocks. In general the stress sensitivity of water-saturated samples is less than that for dry rocks particularly at low effective stress ranges. A regression equation in the form of $V = A - Be^{-DP}$ describes empirically the velocity-effective stress relationship for the Cooper Basin rocks under both dry and water-saturated conditions. In this equation V is the wave velocity in m/s, P is effective stress in MPa, A is the crack-free velocity, D shows the rate of crack closure and the difference between A and B is the velocity at zero effective stress. This equation gives improved prediction of velocities at high effective stress ranges compared to an alternative equation suggested by Eberhart-Phillips et al. (1989) (Chapter6). The non-linear velocity-pressure equation was also found to be applicable to the acoustic data reported by Freund (1992). The predicted crack-closure stresses, $P_{closure}$, of the samples range from 70 MPa to 95 MPa with insignificant correlation with porosity, permeability and clay content. It was found that there is a positive correlation between the velocity gradient and core porosity, but this trend is weak and diminishes as pressure increases. The volume fraction clay content has an insignificant correlation with the velocity gradient for both dry and water-saturated samples.

The variations of compressional and shear wave velocities and quality factors Q_p and Q_s, with confining stress (P_c) and pore pressure (P_p) have also been measured on a Cooper Basin sandstone (Chapter 7). The experimental results show that wave velocities and quality factors of the sample are sharply dependent on differential pressure, P_d, defined as the arithmetic difference between P_c and P_p, and less dependent on pore pressure changes at constant P_d. Thus equal increments of pore pressure and confining stress do not have a precisely zero effect on the measured acoustic properties. It has been shown that V_p, V_s, Q_p and Q_s in the Cooper Basin sandstone sample depend on effective stress, defined as $P_e = P_c - nP_p$, with $n \leq 1$. The value of the effective stress coefficients for V_p and V_s approach unity at high differential pressures whereas the pore-pressure dependency of Q_p and Q_s for the sample increases as the differential pressure increases. No data have previously been published on the effect of pore pressure on the Q_s in rocks. The observation of the effective

stress coefficient for Q_s in sandstone, as shown in Chapter 7, is the first time that it has been reported in the literature.

As published by others (for example, Tosaya and Nur (1982), Han et al. (1986) and Klimentos (1991)) analysis of experimental data in the current study (Chapter 8) suggests that considering a clay content term would improve the velocity-porosity transform. However a simple plot of clay content versus both V_p and V_s for the studied samples shows no significant correlation (in contrast to the studies mentioned above).

In Chapter 9, the effect of partial saturation on V_p and V_s was investigated for a suite of six Cooper Basin sandstone samples under varying confining stress. As water saturation decreases, V_p generally decreases over the range from high to moderate saturation, while V_s generally increases over the entire saturation range. Under high effective stresses, within the moderate to low saturation range, and as samples approach irreducible saturation, V_p remains effectively constant. At low effective stresses V_p decreases dramatically between the low saturation and dry condition (100% air-saturated). Partial saturation has minimal influence on the stress sensitivity of velocities in the studied samples and only at very low water saturation (near to dry condition) does the stress sensitivity of velocities gradually increase as water saturation decreases (Figure 9.17).

11.2. Discussions and Conclusions

11.2.1. Velocity-Effective Stress Relationship

The rapid increase in velocity over an effective stress range of 5 to 40 MPa in the studied samples results from the closure of microcracks (connective pores) which act as defects in the solid framework of the rock. The closure of microcracks, which hardly changes the rock porosity, improves the grain contact conditions in the rock skeleton and increases the rock's stiffness and elastic moduli. Experimental results indicate that pore geometry and inter-grain contacts may be more appropriate than total porosity in describing the stress sensitivity of sandstones under in-situ effective stress condition. It is also concluded that the distribution and location of clay particles within the rock framework (quartz grains) may be more important than the total volumetric clay content in the pressure dependency of velocity in shaly sandstones (Figures 6.12 and 6.14).

11.2.2. Effective Stress Coefficient for Velocities and Quality Factors

While small changes in pore fluid compressibility may partly explain the slight increase of V_p with pore pressure increase at constant P_d, it does not explain the increase of V_s under similar conditions. The strong dependence of quality factor on pore pressure particularly at high P_d implies that the experimental data cannot be fully explained by crack closure. The deviation of effective stress coefficient from unity for compressional and shear wave quality factors at high P_d is attributed to the heterogeneity in elastic properties of the main rock components (quartz and clay) and pore geometry.

11.2.3. Velocity versus Porosity and Clay Content

The lack of correlation between clay content and velocity in the Cooper Basin sandstones is preliminary attributed to the textural characteristics and the type of clay distribution within the studied samples. Although considering a clay content term in velocity-porosity transforms in shaly sandstones is essential, the effect of clay minerals on velocities may not adequately be explained if only the volume fraction of clay is taken into account. Nevertheless, the total clay content in sandstone reservoirs as is routinely derived from the gamma ray log may be underestimated where kaolinite is present.

11.2.4. Velocity-Saturation Relationship

Experimental results presented in Chapter 9 confirm that acoustic velocities in partially water/gas saturated rocks strongly depend on the spatial scales of heterogeneous fluid distribution. The saturation heterogeneity at pore-scale, shown by capillary pressure analysis, controls the velocity-saturation relationships in the samples studied. The steady decrease of V_p as saturation decreases from the high saturation range to near irreducible conditions suggests a simultaneous drainage of water from pores with a variety of high to moderate aspect ratios, while microcracks (low aspect ratio) pores retain water. Closure and degree of saturation of the low aspect ratio pores controls the velocity-effective stress and velocity-saturation relationships under low saturation and low effective stress conditions. A simple comparison between the capillary pressure data and the shape of the V_p/V_s–saturation curve suggest that laboratory velocity measurements may be used as an indicator of saturation condition and as a means of characterising the pore geometry and the distribution of pore fluid within the pore space of rocks.

11.3. Applications

The second aspect of this research was to investigate the use of laboratory measurements of acoustic properties on core samples for the evaluation of hydrocarbon reservoirs from sonic log and surface seismic. The following are some of the major implications arising from this study for hydrocarbon exploration and development. The study has demonstrated that:

- The velocity dispersion due to frequency difference between ultrasonic laboratory measurements on cores and theoretical low (seismic) frequency is about 1%. Thus the acoustic velocity data derived from laboratory measurements at ultrasonic frequencies can be considered to be low-frequency data according to Biot-Gassmann theory. This means that laboratory measured velocities may be comparable with the sonic log and seismic data in the Cooper Basin. This finding needs to be tested in the field.

- Where the in situ reservoir pressure is much less than the microcrack-closure pressure of the reservoir rocks, the variation of reservoir pressure could cause significant changes in velocity of the reservoir rocks. For instance, anomalously high velocities (low sonic transit times) have been reported by Watts et al. (1996) in pressure depleted gas reservoirs in the Magnus Field, North Sea. It was shown that, for two abnormal pressure conditions, overpressured (low effective stress) and pressure-depleted (high effective stress), neglecting the pressure effect results in anomalously high and low sonic porosities, respectively. Sonic log data in partially pressure-depleted Cooper Basin gas fields are consistent with the velocity-effective stress relationship obtained from the laboratory measurements. An empirical correction factor is proposed for the pressure effect on sonic log response in the Cooper Basin wells ($dV_p/dP_e = 79.35e^{-0.05P}$, where V_p is in m/s and P is effective stress in MPa).

- The potential exists to use the velocity ratio (V_p/V_s) to detect fluid type and saturation status under in situ reservoir effective stress. The possibility of predicting of V_s from V_p, was demonstrated for both air- and water-saturated conditions over a range of effective stresses for the sandstone reservoirs of the study area.

- The strong stress sensitivity and the distinct V_p/V_s values for air- and water-saturated Cooper Basin cores indicate that dynamic changes in pressure and saturation of the

reservoir rocks might also be detectable from sonic travel time and time lapse seismic (4D).

Although these results refer specifically to Cooper Basin reservoir rocks, the methods used and results of this study have direct implications for reservoir rocks elsewhere.

11.4. Future Studies

Within the time constraint of a PhD study a number of interesting and practically important observations were made on the influence of effective stress and fluid saturation on acoustic velocities in low to moderate porosity shaly sandstones. There is still much to be done within this field to refine and extend the work presented in this thesis. The following are a few suggestions for further work.

- Although the influence of effective stress on acoustic velocities in rocks has been known for many years there is no published calibration chart to correct sonic log readings for the variation of in situ reservoir pressure. **It would be very useful to generate an atlas of velocity-pressure plots for different rock types saturated with different pore fluids and under various saturation conditions.** The outcome not only would help petrophysicists and log analysts in more accurate interpretation of sonic log data but also could be useful in pore pressure prediction from seismic and reservoir monitoring through time lapse seismic (4D).

- This thesis qualitatively showed the importance of pore geometry and grain contacts on the velocity of elastic waves in rocks. **A future study should focus on defining parameter(s) which could provide quantitative description of the pore geometry of the rock samples to used to link the acoustic and petrographical properties.** Petrographic image analysis (PIA) techniques should be very useful for this purpose.

- **The observation that velocity ratio (V_p/V_s) is related to the degree of saturation has been demonstrated for the first time in this study and should be investigated further.** The use of capillary pressure curves and wettability data to describe the scale of saturation heterogeneity and its relationship to acoustic velocities may provide useful

information on the saturation status of reservoir rocks from seismically derived interval velocities.

- Although a study of wave attenuation was not within the objectives of the present project, data on compressional and shear wave attenuation were also collected during laboratory measurements. Investigation of wave attenuation characteristics may reveal such information as lithology, type and degree of saturation, and permeability. **It is recommended that attenuation data be compared to petrophysical and lithological properties of all studied samples**. The identification of effective stress coefficients for the wave quality factors presented in Chapter 7 is novel and **more studies are recommended for other rock types under a wide range of frequencies to verify this observation.**

- **Robust theoretical models are needed to extrapolate the ultrasonic data to other frequencies and spatial scales.** Laboratory results presented in this thesis provide a useful set of acoustic data for modelling and theoretical development.

REFFERENCES

Apak, S.N., 1994: Structural development and control on stratigraphy and sedimentation in the Cooper Basin. PhD Thesis, The University of Adelaide.

Ament, W.S., 1953: Sound propagation in gross mixtures. The Journal of Acoustical Society of America **25**, 638-641.

Anstey, N.A., 1991: Velocity in thin section. First Break **9**, 449-457.

Assefa, S., 1994: Seismic and petrophysical properties of carbonate reservoir rocks. PhD thesis, The University of Reading, England.

Battersby, D.G., 1976: Cooper Basin oil and gas fields. In Leslie, R.B., H.J. Evans and C.L. Knight (eds.) Economical geology of Australia and New Guinea, 3, Petroleum Australia, Australian Institute of Mining and Metallurgy Monograph **7**, 321-70.

Benson , G,C. and Kiyohara, O., 1974: tabulation of some integral functions of describing diffraction effects in the ultrasonic field of a circular piston source. The Journal of Acoustical Society of America **55**, 184-185.

Best, A.I., 1992: The prediction of reservoir properties of sedimentary rocks from seismic measurements. PhD Thesis, The University of Reading, England.

Best, A.I., 1997: The influence of pressure on ultrasonic velocity and attenuation in near-surface sedimentary rocks. Geophysical Prospecting **45**, 345-364.

Best, A.I. and McCann C., 1995: Seismic attenuation and pore-fluid viscosity in clay-rich reservoir sandstones. Geophysics **60**, 1386-1397.

Best, A.I. and Sam, M.S., 1997: Compressional wave velocity and attenuation at ultrasonic and sonic frequencies in near-surface sedimentary rocks. Geophysical Prospecting **45**, 327-344.

Best, A.I., McCann, C. and Sothcott, J., 1994: The relationships between the velocities, attenuations and petrophysical properties of reservoir sedimentary rocks. Geophysical Prospecting **42**, 151-178.

Biot, M.A., 1956a: Theory of propagation of elastic waves in fluid-saturated porous solid. 1-Low frequency range. The Journal of Acoustical Society of America **28**, 168-178.

Biot, M.A., 1956b: Theory of propagation of elastic waves in a fluid-saturated porous solid. 2-Higher frequency range. The Journal of Acoustical Society of America **28**, 179-191.

Biot, M.A., 1962: Generalised theory of acoustic propagation in porous dissipative media. The Journal of Acoustical Society of America **34**, 1254-1264.

Bourbie, T., Coussy, O. and Zinszner, B., 1987: Acoustics of porous media. Gulf Publishing Company. Texas.

Cadoret, T., Marion, D. and Zinszner, B., 1993: Influence of frequency and fluid distribution on acoustic velocity in partially saturated limestones. SEG 63rd Annual Meeting Expanded Abstracts. Paper S3.9

Cadoret, T., Mavko, G. and Zinszner, B., 1998: Fluid distribution effect on sonic attenuation in partially saturated limestones. Geophysics **63**, 154-160.

Caruso, L., Simmons, G. and Wilkens, R., 1985: The physical properties of a set of sandstones-part I the samples. International Journal of Rock Mechanics, Mineral sciences and Geomechanics Abstracts **22**, 381-392.

Castagna, J.P., Batzle, M.L. and Eastwood, R.L., 1985: Relationships between compressional-wave and shear-wave velocities in clastic silicates. Geophysics **50**, 571-581.

Chaney, A.J., Cubitt, C.J. and, Williams, B.P.J., 1997: Reservoir potential of glacio-fluvial sandstones; Merrimellia Formatiom, Cooper Basin, South Australia. The APPEA Journal **37**, 154-177.

Cheng, C.H. and Toksoz, M.N., 1979: Inversion of seismic velocities for the pore aspect ratio spectrum of a rock. Journal of Geophysical Research **84**, 7533-7543.

Christensen, N.I and Wang, H.F., 1985: The influence of pore pressure and confining pressure on dynamic elastic properties of Berea sandstone. Geophysics **50**, 207-213.

Domenico, S.N., 1974: Effect of water saturation on seismic reflectivity of sand reservoirs encased in shale. Geophysics **39**, 759-769.

Domenico, S.N., 1976: Effect of brine-gas mixture on velocity in an unconsolidated sand reservoir. Geophysics 41, 882-894.

Domnico, S.N., 1977, Elastic properties of unconsolidated porous sand reservoirs. Geophysics **42**, 1339-1368.

Domenico, S.N., 1984: Rock lithology and porosity determination from shear and compressional wave velocity. Geophysics **49**, 1188-1195.

Dutta, N.C., 1997: A new procedure to generate pseudo-shear wave log construction-methods, results and road ahead. 59th EAGE Conference Extended Abstracts, paper F32.

Dvorkin, J. and Nur, A., 1993: Dynamic poroelasticity; A unified model with the squirt and the Biot mechanisms. Geophysics **58**, 524-533.

Dvorkin, J., Mavko, G. and Nur, A., 1995: Squirt flow in fully saturated rocks. Geophysics **60**, 97-107.

Dvorkin, J., Nolen-Hoeksema, R. and Nur, A., 1994: The squirt-flow mechanism; Macroscopic description. Geophysics **59**, 428-438.

Dvorkin, J., Nur, A. and Chaika, C., 1996: Stress sensitivity of sandstones. Geophysics **61**, 444-455.

Eberhart-Phillips, D, Han, D-H and Zoback, M.D., 1989: Empirical relationships among seismic velocity, effective pressure, porosity, and clay content in sandstone. Geophysics **54**, 82-89.

Ehrlich, R., Crabtree, S.J., Horkowitz, K.O, and, Horkowitz, J.P., 1991: Petrology and reservoir physics, I- objectives classification of reservoir porosity. The American Association of Petroleum Geologists Bulletin **75**, 1547-1562.

Ehrlich, R. and Davis, D.K., 1989: Image analysis of pore geometry; relationship to reservoir engineering and modeling. SPE 19054.

Enders, A. and Knight, R. 1989: The effect of microscopic fluid distribution on elastic velocities. The Log Analyst **30,** 434-444.

Fatt, I. 1958: Compressibility of sandstones at low to moderate pressures. The American Association of Petroleum Geologists Bulletin **42**, 1924-57.

Folk, R.K., 1974: Petrology of sedimentary rocks. Hemphill Publishing Company, Texas.

Freund, D., 1992: Ultrasonic compressional and shear velocities in dry clastic rocks as a function of porosity, clay content, and confining pressure. Geophysical Journal International **108**, 125-135.

Gassmann, F., 1951: Elastic waves through a packing of spheres. Geophysics **16**, 673-685.

Gatehouse, C.G., 1972: Formations of Gidgealpa Group in the Cooper Basin. Australian Oil and Gas Review **18** (12), 10-15.

Geertsma, J. and Smith, D.C., 1961: Some aspects of elastic wave propagation in fluid-saturated porous solids. Geophysics **26**, 169-181.

Goertz, D, and Knight, R.J., 1998: Elastic wave velocities during evaporative drying. Geophysics **63**, 171-183.

Gregory, A.R., 1976: Fluid saturation effects on dynamic elastic properties of sedimentary rocks. Geophysics **41**, 895-921.

Griffiths C.M., 1982: A proposed geologically consistent segmentation and reassignment algorithm for petrophysical borehole logs. In Cubitt, J.M. and Reyment, R.A. (eds.), Quantitative stratigraphic correlation. John Whily & Sons, 287-298.

Han, D-H., Nur, A. and Morgan, D., 1986: Effects of porosity and clay content on wave velocities in sandstones. Geophysics **51**, 2093-2107.

Hardy , R. and Tucker, M., 1991: X-ray powder diffraction of sediments. In Tucker, M. (ed.) Techniques in sedimentology. Blackwell Scientific Publications, 191-228.

Hashin, Z. and Shtrikman, S., 1963: A variational approach to the theory of the elastic behavior of multiphase materials. Journal of Mechanics and Physics Solids **11**, 127-140.

Heath, R., 1989: Exploration in the Cooper Basin. The APEA Journal **29**, 366-378.

Hicks, W.G and Berry, J.E., 1956: Application of continuous velocity logs to determination of fluid saturation of reservoir rocks. Geophysics **21**, 739-754.

Hottman, C.E. and R.K. Johnson, 1965: Estimation of formation pressure from log-derived shale properties. Journal of Petroleum Technology **17**, 717-22.

Houseknecht, D.W., 1987: Assessing the relative importance of compaction processes and cementation to reduction of porosity in sandstones. . The American Association of Petroleum Geologists Bulletin **71**, 633-42.

Hughes, D.S., Blnkenship, E.B. and Mims, R.L., 1950, Variation of elastic moduli and wave velocity with pressure and temperature in plastics. Journal of Applied Physics **21**, 294-297.

Hunt, J.W., Heath, R.S. and Mckenzie, P.E., 1989: Thermal and maturity and other geological controls on the distribution and composition of Cooper Basin hydrocarbon. In O'Neil, B.J. (ed.), The Cooper and Eromanga Basins, Australia. Proceedings of Petroleum Exploration Society of Australia, Society of Petroleum Engineers and Australian Society of Exploration Geophysics South Australian Branches, Adelaide, 509-523.

Jenkins, C.C., 1989: Geochemical correlation of source rocks and crude oils from the Cooper and Eromanga Basins. In O'Neil, B.J. (ed.), The Cooper and Eromanga Basins, Australia. Proceedings of Petroleum Exploration Society of Australia, Society of Petroleum Engineers and Australian Society of Exploration Geophysics (South Australian Branches), Adelaide, 525-539.

Jizba, D. and Marion, D., 1994: Heimdal Monitoring I; establishing feasibility from cores and logs. SEG 64th Annual meeting Expanded Abstracts, paper DP4.4.

Jones, S.M., 1996: The effects of confining pressure, pore-fluid salinity and saturation on the acoustic properties of sandstones. PhD Thesis, University of Reading, England.

Kappel, A.J., 1966: The Cooper Creek Basin. The APEA Journal **6**, 71-75.

Kappel, A.J., 1972: The geology of the Patchawarra area Cooper Basin. The APEA Journal **12**, 53-57.

Khaksar, A., 1994: Techniques for improving the petrophysical evaluation of the Patchawarra Formation in the Toolachee Field, Cooper Basin South Australia. MSc Thesis, The University of Adelaide, Australia.

Khaksar, A. and Griffiths, C.M., 1996a: Influence of effective stress on acoustic velocity and log derived porosity. SPE 36981.

Khaksar, A. and Griffiths, C.M., 1996b: Velocity-porosity transforms and effective stress in gas bearing reservoirs, a case study. 58th EAGE Conference Expanded Abstracts, paper E10.

Khaksar, A. and Griffiths, C.M., 1998a: Porosity from sonic log in gas-bearing shaly sandstone; field data versus empirical equations. Exploration Geophysics **29**, 440-446.

Khaksar, A, and Griffiths, C.M. 1998b: Acoustic velocities as a function of effective pressure in low to medium porosity shaly sandstones, part 1- experimental results. Exploration Geophysics **29**, 447-455.

Khaksar, A. and Griffiths, C.M., 1998c: Acoustic velocities as a function of effective pressure in low to medium porosity shaly sandstones, part 2- implications for hydrocarbon exploration. Exploration Geophysics **29**, 456-461.

Khaksar, A. Griffiths, C.M. and McCann, C., 1998, A petro-acoustic study of Cooper Basin sandstones. The APPEA Journal **38,** 874.

Khaksar, A., McCann, C., Griffiths, C., Sothcott, J., and Khazanehdari, J., 1997: Stress sensitivity of P-and S-wave velocities in a set of low to medium porosity dry sandstones. 59th EAGE Conference Extended Abstracts, paper F31.

Khaksar, A. and Mitchell, A., 1995: An improvement in lithology interpretation from well logs in the Patchawarra Formation, Toolachee Field, Cooper Basin, South Australia. Exploration Geophysics **26**, 347-53.

King, M.S., 1966: Wave velocities in rocks as function of changes in overburden pressure and pore fluid saturation . Geophysics **31**, 50-73.

Kinsler, L.E. and Frey, A.R., 1962: Fundamental of acoustics. John Wiley & Sons. NewYork.

Klemme, H.D., 1980: Petroleum basins, Classifications and characteristics. Journal of Petroleum Geology **3**, 187-207.

Klimentos, T., 1991: The effects of porosity, permeability and clay content on the velocity of compressional waves. Geophysics **56**, 1930-1939.

Klimentos, T. and McCann, C., 1990: Relationships among compressional wave attenuation, porosity, clay content, and permeability in sandstones. Geophysics **55**, 998-1014.

Klinkenberg, L.J., 1941: The permeability of porous media to liquids and gases. American Petroleum Institute, Drilling and Production Practice **2**, 200-213

Knight, R., Dvorkin, J, and, Nur, A., 1998: Acoustic signatures of partial saturation. Geophysics **63**, 132-138.

Knight, R. and Nolen-Hoeksema, R., 1990: A laboratory study of the dependence of elastic wave velocities on pore-scale fluid distribution. Geophysical Research Letters **17**, 1529-1532.

Kuster, G.T., and Toksoz, M.N., 1974a: Velocity and attenuation of seismic waves in two-phase media; part I theoretical formulations. Geophysics **39**, 587-606.

Kuster, G.T., and Toksoz, M.N, 1974b: Velocity and attenuation of seismic waves in two-phase media; part II Experimental results. Geophysics **39**, 607-618.

Lumley, D.E., Behrens, R.A. and, Wang, Z., 1997: Assessing the technical risk of a 4-D seismic project. The Leading Edge **16**, 1287-1291.

Maerefat, N., Baldwin, B.A., Chaves, A.A., LaTorraca, G.A. and Swanson, B.F., 1990: SCA guidelines for sample preparation and porosity measurement of electrical resistively samples; part IV-guidelines for saturating and desaturating core plugs during electrical resistively measurements. The Log Analyst **30**, 68-75.

Marion, D. and Nur, A., 1991: Pore-filling material and its effect on velocity in rocks. Geophysics **56**, 225-230.

Martin, K.R., 1967: Gidgepla and Merrimeli Formations in Cooper's Creek Basin. Australian Oil and Gas Journal **14**. 29-35.

Mavko, G.M. and Nur, A., 1979: Wave attenuation in partially saturated rocks. Geophysics **44**, 161-178.

McCann, C. and Sothcott, J., 1992: Laboratory measurements of the seismic properties of sedimentary rocks. In Hurst, A, Griffiths, C.M. and Worthington, P.F. (eds.) Geological applications of wire -line logs 2. Geological Society Special Publication No. **65**, 285-297

McCann, C., Sothcott, J. and Assefa, S., 1997: Prediction of petrophysical properties from seismic quality-factor measurements. In Lovell, M.A and Harvey, P.K. (eds.), Developments in petrophysics, Geological, Society Special Publication No. **122,** 121-130.

McDonough, R.C.M., 1998: Economics of gas field developments. In Gravestock, D.I., Hibburt, J.F. and Drexel, J.F. (eds.) The petroleum geology of South Australia Volume 4, Cooper Basin. Primary Industries and Resources South Australia, 199-204.

MESA, 1992: Petroleum exploration and development in South Australia. 8th edition, 96-101.

MESA, 1993, Petroleum exploration and development in South Australia. 9th edition, 84-87.

MESA, 1997, Petroleum exploration and development in South Australia. 11th edition, 79-81.

Middleton, M.F. and Hunt, J.W., 1988: Influence of tectonics on Permian coal rank patterns in Australia. Cooper Basin Producers, unpublished report.

Minear, J.W., 1982: Clay models and acoustic velocities. SPE 11031.

Morton, J.G.G., 1989: Petrophysics of Cooper Basin reservoirs in South Australia. In O'Neil B.J. (ed.), The Cooper and Eromanga Basins, Australia. Proceedings of Petroleum Exploration Society of Australia, Society of Petroleum Engineers and Australian Exploration Geophysicists SA branches, 153-163.

Morton, J.G.G., 1998: Undiscovered petroleum resources. In Gravestock, D.I., Hibburt, J.F. and Drexel, J.F. (eds.) The petroleum geology of South Australia Volume 4, Cooper Basin. Primary Industries and Resources South Australia, 205-211.

Murphy III, W.F., 1982: Effect of partial water saturation on attenuation in Massilon sandstone and vycor porous glass. The Journal of Acoustic Society of America **71**, 1458-1468.

Murphy III, W. F., 1984: Acoustic measurements of partial gas saturation in tight sandstones. Journal of Geophysical Research **89**, 11549-11559.

Murphy, III, W.F., Winkler, K.W. and Kleinberg, R.L, 1986: Acoustic relaxation in sedimentary rocks; dependence on grain contacts and fluid saturation. Geophysics **51**, 757-766.

Nadeau, P.H. and Hurst, A., 1991: Application of back-scattered electron microporosity in sandstones. Journal of Sedimentary Petrology **61**, 921-925.

Nur, A., 1989: Four-dimensional seismology and (true) direct detection of hydrocarbon; the petrophysical basis. The Leading Edge **8** No. 9, 30-36.

Nur, A. and Byrelee, J.D., 1971: An exact effective stress law for elastic deformation of rock with fluids. Journal of Geophysical Research **76**, 6414-6419.

Nur, A. and Simmons, G., 1969: The effect of saturation on velocity in low porosity rocks. Earth Planetary Science Letters **7**, 183-193.

O'connell, R. and Budiansky, B., 1977: Viscoelastic properties of fluid-saturated cracked solids. Journal of Geophysical Research **82**, 5719-5725.

Overton, M., and Hamilton, N., 1986: A petrophysical review of unit fields, Cooper Basin, South Australia. Santos Ltd. unpublished internal report.

Papadakis, E.P., 1972: Ultrasonic diffraction loss phase change for broad-band pulses. The Journal of Acoustical Society of America **52**, 847-849.

Papalia, N., 1969: The Nappamerri Formation. The APEA Journal **9**, 108-110.

Plona, T.J., 1980: Observation of a second bulk compressional wave in a porous medium ultrasonic frequencies. Applied Physics Letters **36**, 259-261.

Pittman, E.D. and Thomas, J.B, 1979: Some application of scanning electron microscopy to the study of reservoir rock. Journal of Petroleum Technology **31**, 1375-80.

Prasad, M. and Manghnani, M.H., 1997: Effect of pore and differential pressure on compressional wave velocity and quality factor in Berea and Michigan sandstones. Geophysics **62**, 1163-1176.

Raymer, L.L., Hunt, E.R. and Gardner, J.S., 1980: An Improved sonic transit time-to-porosity transform. SPWLA 25th Annual Logging Symposium, paper P.

Rezaee, M.R.,1996: Reservoir characterisation of the Tirrawarra sandstone in the Moorari and Fly Lake fields, southern Cooper Basin, South Australia. PhD Thesis. The University of Adelaide, Australia.

Rider, & M.H., 1986: The geological interpretation of well logs. Blackie, Scotland.

Ringstad, C and Fjaer, E., 1997: The effect of pore pressure on acoustic velocities. EAGE 59th Conference Extended Abstracts, paper F29.

Ruhovets, N and Fertl, W.H., 1982: Digital shaly sand analysis based on Waxman-Smits Model and log-derived clay typing. In Shaly sands, SPWLA Special Volume, V107-V134.

Schon, J. H., 1996: Physical properties of rocks, fundamentals and principles of petrophysics. handbook of Geophysical Exploration, Seismic Exploration Vol. 18. Pergamon. UK.

Schulz-Rojahn, J.P., 1991: Origin, evolution and controls of Permian reservoir sandstones in the southern Cooper Basin, South Australia. PhD Thesis, The University of Adelaide, Australia.

Stanmore, P.J. 1989: Case studies of stratigraphic and fault traps in the Cooper Basin. The APEA Journal 29, 361-369.

Stuart, W.J., 1976: The genesis of Permian and Lower Triassic reservoir sandstones during phases of southern Cooper Basin development. The APEA Journal **16**, 37-47.

Stuart, W.J., Farrow, B.B., Tingate, P.R., Schulz-Rojhan, J.P., Apak, A., Lemon, N.M. and Luo, P., 1992: Porosity and permeability in Permian sandstones; Southern Cooper Basin. The University of Adelaide, ERDC project No. 1407 final report.

Stuart, W.J., Kennedy, S., and Thomas, A.D., 1988: The influence of structural growth and other factors on the configuration of fluviatile sandstones, Permian Cooper Basin. The APEA Journal **28**, 255-266.

Sun, X., 1997; Structural style of the Warburton Basin and control in the Cooper and Eromanga Basins, South Australia. Exploration Geophysics **28**, 333-339.

Tao, G. and King, M.S., 1993: Porosity and pore structure from acoustic well logging data. Geophysical Prospecting **41**, 435-451.

Tao, G., King, M.S. and Nabi-Bidhendi, M., 1995: Ultrasonic wave propagation in dry and brine-saturated sandstones as a function of effective stress; laboratory measurements and modeling. Geophysical Prospecting **43**, 299-327.

Tatham, R.H., 1982: V_p/V_s and lithology. Geophysics **47**, 336-344.

Terzaghi, K., 1943: Theoretical soil mechanics. Wiley, New York.

Thornton, R.C.N., 1979, Regional stratigraphic analysis of the Gidgealpa Group southern Cooper Basin Australia. The Geological Survey of South Australia Bulletin **49**.

Todd, T. and Simmons, G., 1972: Effect of pore pressure on the velocity of compressional waves in low-porosity rocks. Journal of Geophysical Research **77**, 3731-3743.

Toksoz, M.N, Cheng, C.H. and Timur, A., 1976: Velocities of seismic waves in porous rocks. Geophysics **41**, 621-645.

Tosaya, C. and Nur, A., 1982: Effect of diagenesis and clay on compressional velocities in rocks. Geophysical Research Letters **9**, 5-8.

Trewin, N., 1991: Use of scanning electron microscope in sedimentology. In Tucker, M., (ed.) Techniques in sedimentology, Blackwell Scientific Publications, 229-273

Tutuncu, A.N., Podio, A.L. and Sharma, M.M., 1994: An experimental investigation of factors influencing compressional- and shear-wave velocities and attenuations in tight gas sandstones. Geophysics **59**, 77-86.

Vavra, C.L., Kaldi, J.G. and Sneider-R.M., 1992: Geological applications of capillary pressure; a review. The American Association of Petroleum Geologists Bulletin **76**, 840-850.

Veevers, J.J., 1984: Phanerozoic earth history of Australia. Oxford Geological Science Series, Oxford University Press, New York.

Vernik, L., 1994: Predicting lithology and transport properties from acoustic velocities based on petrophysical classification of siliciclastics. Geophysics **59**, 420-427.

Vernik, L., 1997: Predicting porosity from acoustic velocities in siliciclastics; a new look. Geophysics **62**, 118-128.

Vernik, L. and Nur, A., 1992: Petrophysical classification of siliciclastics for lithology and porosity prediction from seismic velocities. The American Association of Petroleum Geologists Bulletin **76**, 1295-1309.

Waite, M.W. and Sigit, S., 1997: Seismic monitoring of the Duri steamflood, application to reservoir management. The Leading Edge **16**, 1275-1278.

Wang, Z., 1997: Feasibility of time-lapse seismic reservoir monitoring: the physical basis. The Leading Edge **16**, 1327-1329.

Wang, Z., Hirsche, W.K. and Sedgwick, G., 1991: Seismic monitoring of water floods?-A petrophysical study. Geophysics **56**, 1614-1623.

Wang, Z. and Nur, A., 1990: Wave velocities in hydrocarbon- saturated rocks; experimental results. Geophysics **55**, 723-733.

Wang, Z. and Nur, A., 1992: Elastic wave velocities in porous media, A theoretical recipe SEG Reprint Series No. **10 (2)**, 1-35.

Watt, J.P., Davis, G.F. and O'Connel, R.J., 1976: The elastic properties of composite materials. Reviews of Geophysics and Space Physics **14**, 541-563.

Watts, G.F., T., Jizba, D., Gawith, D.E. and, Gutteridge, P., 1996: Reservoir monitoring of the Magnus Field through 4D time-lapse seismic analysis. Petroleum Geoscience **2**, 361-372.

White, J.E., 1983: Underground sound. Elsevier, New York.

Williams, B.P.J., E.K. Wild and R.J. Suttill, 1985, Paraglacial aeolianites, potential new hydrocarbon reservoirs, Gidgealpa Group, Southern Cooper Basin. The APEA Journal **25,** 291-310

Wilkens, R.H., Simmons, G., Wissler, T.M. and Caruso, L., 1986; The physical properties of a set of sandstones-part III, the effects of fine-grained pore-filling material on compressional wave velocity. International Journal of Rock Mechanics, Mining Science &Geomechanics Abstracts **23,** 313-325.

Winkler, K.W., 1985: Dispersion analysis of velocities and attenuation in Berea sandstone. Journal of Geophysical Research **90**, 6793-6800.

Winkler, K.W., 1986: Estimates of velocity dispersion between seismic and ultrasonic frequencies. Geophysics **51**, 183-189.

Winkler, K.W., Plona, T.J., 1982: Techniques for measuring ultrasonic velocities and attenuation spectra in rocks under pressure. Journal of Geophysical Research **87**, 10776-10780.

Wyllie, M.R., Gregory, A.R. and Gardner, L.W., 1956: Elastic wave velocities in heterogeneous and porous media. Geophysics **21**, 41-40.

Wyllie, M.R., Gregory, A.R. and Gardner, G.H.F., 1958: An experimental investigation of factors affecting elastic wave velocities in porous media. Geophysics **23**, 459-493.

Xu, S. and, White, R.E., 1995: A new velocity model for clay-sand mixtures. Geophysical Prospecting **43**, 91-118.

Xu, S. and, White, R.E., 1996: A physical model for shear-wave velocity prediction. Geophysical Prospecting **44**, 687-717.

Yassir, N.A, and Bell, J.S., 1994: Relationships between pore pressure, stress, and present-day geodynamics in the Scotian Shelf, offshore Eastern Canada. The American Association of Petroleum Geologists Bulletin **78**, 1863-1890.

Yew , C.C. and Mills, A.A., 1989: The occurrence and search for Permian oil in the Cooper Basin, Australia. The APEA Journal **29**, 339-359.

Yin, H. and Nur, A. 1993: Porosity, permeability, and acoustic velocity in granular materials. SEG 63rd Annual Meeting Expanded Abstracts, 775-778.

Yu, G., Vozoff, K. and Durney D.W., 1991: Effect of pore pressure on compressional wave velocity in coals. Exploration Geophysics **22**, 475-480.

Zemanek, J. and Rudnick, I. 1961: Attenuation and dispersion of elastic waves in a cylindrical bar. The Journal of Acoustical Society of America **33**, 1283-1288.

Zimmerman R.W., 1991: Compressibility of sandstones. Development in Petroleum Science, **29**, Elseiver, Amsterdam.

Zoback, M.D. and Byerlee, J.D., 1974: Permeability and effective stress. The American Association of Petroleum Geologists Bulletin **59**, 154-158.

Appendix A

Nomenclature

Symbol	Description	Unit
α	Aspect ratio	
a	Attenuation coefficient	dB/cm
Δa	attenuation coefficient increment	
P	Average pressure (helium porosimetry	Pa
ρ	Bulk density	g/cm^3
k	Bulk modulus	GPa
k_d	Bulk modulus of dry rock	GPa
k_f	Bulk modulus of fluid	GPa
k_m	Bulk modulus of matrix	GPa
P_{cap}	Capillary pressure	kPa
v_s	Chamber volume (helium porosimetry)	cm^3
v_{cl}	Clay content	%, fraction
M	Compressional modulus	GPa
P_c	Confining stress	MPa
θ	Contact angle	Radian
R	Correlation coefficient	
$P_{Closure}$	Crack-closure stress	MPa
f_c	Critical wave frequency	Hz
$\rho(br)$	Density of buffer-rod	g/cm
ρ_0	Density of buffer-rod at atmospheric pressure	g/cm
ρ_w	Density of water	g/cm^3
P_d	Differential pressure	MPa
H	Diffracting ability factor	
φ	Diffraction phase shift	
z	Distance from transducer	
P_e	Effective stress	MPa
N	Effective stress coefficient	
Q	Flow rate	cm^3/s
ρ_f	Fluid density	g/cm^3
Gr_{sand}	Gamma ray log in sandstone	API
Gr_{shale}	Gamma ray log in shale	API
Gr_{log}	Gamma ray log reading	API

K_g	Gas permeability	mD
ρ_m	Grain density	g/cm^3
v_m	Grain volume	cm^3
τ	Interfacial tension	N
K_l	Liquid permeability	mD
a'	Measured attenuation coefficient	
t'	Measured travel time	s
mmstb	Million standard barrel	
S_m	Normalised distance for the mth echoes	cm
S_n	Normalised distance for the nth	cm
S	Normalised distance from transducer	cm
π	number (~3.14)	
Δx	Path length (pulse)	cm
K	Permeability	mD
$\Delta\varphi$	Phase difference	
P_p	Pore pressure	MPa
v_{pore}	Pore volume	Cm^3
ϕ	Porosity	%, fraction
Δp	Pressure fall	Pa
p'	Pressure fall (helium porosimetry	Pa
Q_p	P-wave quality factor	
V_p	P-wave velocity	m/s
$V_p(br)$	P-wave velocity in buffer-rod	m/s
V_f	P-wave velocity in fluid	m/s
V_m	P-wave velocity in matrix	m/s
r_c	Radius of capillary	cm
p_r	Reference pressure (helium porosimetry	Pa
v_r	Reference volume (helium porosimetry	cm^3
R(f)	Reflection coefficient	
A, B, D, K	Regression coefficients in velocity-stress equation	
L	Sample length	cm
m_d	Sample mass (dry)	g
m_{ps}	Sample mass (partially saturated)	g
v_{pore}	Sample pore volume	cm^3
A	Sample surface area	cm^2
vt	Sampler bulk volume	cm^3
μ	Shear modulus	GPa
G	Shear modulus	GPa
μ_d	Shear modulus of dry rock	GPa
V(f)	Single frequency velocity	m/s
$A_2(f)$	Spectral amplitude (bottom reflection)	

$A_1(f)$	Spectral amplitude (top reflection)	
Q_s	S-wave quality factor	
V_s	S-wave velocity	m/s
$V_s(br)$	S-wave velocity in buffer-rod	m/s
a	Transducer diameter	cm
Δt	Travel time difference (pulse)	
tcf	Trillion cubic feet (10^{12} ft^3)	
dV/dP	Velocity gradient	
VGR	Velocity gradient ratio	
V_p/V_s	Velocity ratio	
η	Viscosity	cP
Sw	Water saturation	%
f	Wave frequency	Hz
Q	Wave quality factor	
Dt	Wave transit time	µs/m
Dt_f	Wave transit time in fluid	µs/m
Dt_m	Wave transit time in matrix	µs/m
V	Wave velocity	m/s
λ	Wavelength	cm
W	Weight	fraction
I	Principle peak height (XRD)	mm

Appendix B

List of core and log data used in Chapter 3

Well name: Toolachee-3

Depth (m)	D_t (µs/m)	ϕ Core (%)	V_{cl} (fraction)	Sw (%)
2197.6	241.0	11.9	0.5	53.0
2197.9	240.6	5.7	0.5	53.0
2198.2	242.8	10.5	0.5	53.0
2198.5	239.2	12.2	0.4	53.0
2198.8	238.1	12.9	0.4	53.0
2199.1	247.9	11.9	0.3	53.0
2199.4	249.5	12.5	0.3	38.0
2199.7	250.6	11.5	0.3	38.0
2199.7	250.6	10.1	0.2	38.0
2200.0	248.4	14.2	0.2	38.0
2200.3	247.7	19.8	0.2	38.0
2200.6	256.1	23.4	0.1	27.0
2200.9	271.4	14.0	0.2	27.0
2201.5	257.6	11.7	0.3	31.0
2218.4	254.7	14.1	0.3	31.0
2218.9	263.5	14.0	0.2	31.0
2219.2	271.5	14.1	0.2	31.0
2219.7	255.4	11.8	0.2	31.0
2220.0	245.6	10.4	0.1	14.0
2220.5	276.8	18.8	0.1	14.0
2220.9	302.1	21.9	0.1	14.0
2221.3	289.0	13.9	0.1	13.5
2221.6	282.6	14.5	0.0	13.5
2221.9	291.4	13.4	0.0	10.0
2222.1	292.3	22.6	0.0	10.0
2222.4	294.7	18.9	0.0	10.0
2223.0	299.2	19.0	0.0	15.0
2223.4	285.5	17.4	0.1	15.0
2223.7	282.5	19.9	0.1	15.0
2224.0	276.7	17.0	0.1	15.5
2224.9	300.1	22.9	0.2	15.5
2225.2	292.1	18.2	0.2	17.5
2225.5	286.0	15.9	0.5	83.0
2228.9	245.6	11.3	0.4	83.0
2229.2	242.7	8.5	0.4	83.0
2229.3	242.6	7.8	0.3	83.0
2229.5	246.1	11.0	0.2	83.0
2229.8	261.8	13.3	0.2	46.0
2230.2	278.3	16.3	0.2	46.0
2230.4	258.7	13.9	0.2	40.0
2230.8	268.2	14.3	0.2	40.0
2230.9	265.4	12.8	0.2	36.0
2231.2	267.2	17.6	0.1	33.0
2231.6	263.8	12.7	0.1	33.0
2231.7	260.8	11.4	0.1	33.0
2231.7	262.2	14.3	0.1	33.0
2231.8	266.2	12.5	0.1	28.0

Toolachee-3 Continued:

Depth (m)	D_t (µs/m)	ϕ Core (%)	V_{cl} (fraction)	Sw (%)
2232.0	272.1	14.8	0.1	28.0
2232.3	284.4	15.4	0.3	89.0
2237.4	247.8	12.9	0.3	89.0
2237.7	253.9	14.9	0.3	89.0
2238.0	255.8	14.3	0.3	89.0
2238.1	254.9	13.8	0.3	89.0
2238.6	250.3	10.8	0.3	89.0
2238.8	254.4	13.7	0.3	39.0
2239.2	277.8	15.5	0.2	39.0
2239.5	276.2	13.9	0.1	39.0
2239.6	271.2	14.9	0.1	39.0
2239.8	267.2	16.1	0.1	39.0
2240.0	279.7	19.8	0.1	26.0
2240.5	289.5	13.5	0.1	26.0
2240.8	288.2	22.1	0.1	26.0
2241.1	283.8	18.6	0.0	23.5
2241.5	280.3	17.9	0.0	23.5
2241.9	279.3	19.6	0.3	74.0
2261.1	252.6	10.7	0.3	74.0
2261.3	254.1	11.9	0.3	74.0
2261.9	240.8	10.0	0.4	76.0
2261.9	238.7	10.7	0.5	76.0
2262.2	237.2	7.3	0.5	76.0
2262.5	254.2	12.3	0.2	76.0
2263.1	263.5	11.0	0.2	76.0
2263.4	252.1	12.1	0.4	80.0
2263.9	236.7	8.1	0.2	80.0
2264.6	251.7	12.6	0.2	80.0
2264.8	251.1	12.8	0.2	80.0
2265.1	249.4	13.5	0.1	80.0
2265.3	259.0	13.7	0.0	80.0
2265.6	264.1	10.8	0.0	80.0
2265.9	265.2	18.2	0.0	80.0
2266.1	259.0	17.6	0.0	80.0
2266.4	254.2	14.2	0.5	80.0
2266.7	253.2	12.1	0.6	100.0
2275.2	243.3	10.1	0.5	100.0
2275.6	243.1	9.5	0.4	100.0
2276.1	244.5	11.6	0.1	100.0
2276.6	263.5	13.5	0.1	100.0
2276.8	262.5	13.1	0.1	100.0
2277.2	250.8	14.1	0.1	100.0
2277.5	253.5	13.7	0.1	100.0
2277.8	266.7	15.5	0.1	100.0
2278.0	268.3	17.1	0.1	100.0
2278.4	269.1	15.9	0.1	100.0

Well Name: Toolachee-6

Depth (m)	D_t (µs/m)	ϕ Core (%)	V_{cl} (fraction)	Sw (%)
2277.1	243.6	8.4	0.5	42.0
2277.4	246.9	11.7	0.5	42.0
2277.7	244.5	9.8	0.3	42.0
2278.0	265.4	12.3	0.3	42.0
2278.7	290.2	16.0	0.2	31.5
2279.0	295.3	18.1	0.2	31.5
2279.3	285.8	17.8	0.1	18.0
2279.6	269.9	16.6	0.1	18.0
2279.9	276.3	19.1	0.1	18.0
2280.2	303.4	15.5	0.1	17.5
2280.5	296.4	18.3	0.1	17.5
2280.8	282.4	18.0	0.2	17.5
2281.1	249.5	12.7	0.2	16.0
2303.2	241.7	9.0	0.2	17.0
2303.5	244.7	8.7	0.1	17.0
2303.8	260.0	13.9	0.1	17.0
2304.3	270.6	13.8	0.1	16.3
2304.7	242.6	19.1	0.1	6.0
2304.9	243.3	15.4	0.2	6.0
2305.6	260.1	13.2	0.1	9.7
2305.8	263.2	21.3	0.1	7.5
2306.6	255.6	20.4	0.1	7.5
2306.7	267.3	20.3	0.1	7.9
2313.0	267.7	17.1	0.0	19.0
2313.3	251.6	16.7	0.0	19.0
2313.7	259.9	16.9	0.0	18.7
2315.2	253.6	20.5	0.1	17.0
2315.5	260.9	17.8	0.1	15.7
2315.9	261.4	16.4	0.1	15.7
2316.2	262.3	15.0	0.1	15.7
2316.5	252.8	13.2	0.1	18.7
2316.8	238.1	8.7	0.2	18.7
2317.1	241.9	13.8	0.2	50.5
2317.4	248.7	10.0	0.2	50.5
2317.7	235.8	10.7	0.2	50.5
2318.0	233.8	12.8	0.3	50.5
2318.3	250.6	13.8	0.2	88.0
2318.6	260.1	11.4	0.2	88.0
2318.9	255.3	11.9	0.2	50.5
2319.2	245.3	10.1	0.2	50.5
2319.8	236.8	13.0	0.3	63.0
2320.1	244.0	11.5	0.3	66.0
2320.4	248.7	9.4	0.3	66.0
2320.7	233.8	6.1	0.4	66.0
2321.0	225.9	3.1	0.4	66.0
2321.1	225.7	8.5	0.4	71.0
2321.3	234.5	13.2	0.3	71.0

Toolachee-6Continued:

Depth (m)	D_t (µs/m)	ϕ Core (%)	V_{cl} (fraction)	Sw (%)
2321.6	232.8	7.3	0.3	64.0
2322.0	239.0	13.0	0.3	64.0
2322.6	249.6	9.5	0.2	46.0
2322.9	243.2	12.1	0.3	46.0
2323.2	233.5	7.0	0.3	46.0
2323.5	225.7	8.6	0.3	78.0
2323.8	233.0	14.2	0.2	78.0
2324.1	253.1	14.6	0.2	78.0
2324.4	255.0	13.3	0.2	43.5
2324.7	232.4	4.4	0.2	43.5
2325.0	239.9	12.8	0.2	52.5
2325.3	262.2	16.8	0.2	43.0
2325.6	272.9	15.4	0.2	43.0
2325.9	265.6	16.0	0.1	43.0
2326.2	264.5	15.8	0.1	43.0
2326.5	260.8	14.2	0.1	47.5
2326.8	253.9	8.8	0.2	47.5
2327.1	252.8	14.1	0.2	58.0
2327.4	256.8	14.1	0.2	58.0
2327.7	264.8	13.8	0.2	58.0
2328.4	246.1	12.2	0.2	57.5
2328.7	240.7	14.5	0.2	80.0
2329.0	252.5	15.3	0.2	80.0
2329.3	243.3	11.8	0.2	71.0
2329.6	229.6	12.4	0.2	71.0
2329.9	230.1	14.9	0.1	75.0
2330.2	240.4	14.0	0.1	82.0
2330.5	236.0	10.9	0.1	82.0
2330.8	229.5	13.6	0.1	82.0
2331.4	245.4	14.1	0.1	98.0
2331.7	250.8	15.6	0.1	81.0
2332.0	246.5	12.3	0.3	81.0

Appendix C

Acoustic velocities in dry samples

Sample Name: D1

P_c (MPa)	V_p (m/s)	V_s (m/s)	V_p/V_s	G (GPa)	k (GPa)
60	4671	3052	1.53	22.6	22.8
50	4629	3018	1.53	22.1	22.5
40	4555	2964	1.53	21.3	21.9
30	4423	2865	1.54	19.9	20.9
20	4208	2716	1.54	17.9	19.1
15	4060	2626	1.54	16.7	17.6
10	3860	2495	1.54	15.1	16.0
5	3623	2364	1.53	13.6	13.8

Sample Name: D2

P_c (MPa)	V_p (m/s)	V_s (m/s)	V_p/V_s	G (GPa)	k (GPa)
60	4535	3017	1.50	21.8	20.2
50	4477	2991	1.50	21.4	19.4
40	4371	2935	1.49	20.6	18.2
30	4184	2839	1.47	19.3	16.2
20	3895	2670	1.46	17.0	13.5
15	3687	2547	1.45	15.5	11.8
10	3436	2371	1.45	13.4	10.3
5	3124	2154	1.45	11.1	8.5

Sample Name: D3

P_c (MPa)	V_p (m/s)	V_s (m/s)	V_p/V_s	G (GPa)	k (GPa)
60	4282	2819	1.52	18.2	17.7
50	4227	2783	1.52	17.8	17.3
40	4145	2723	1.52	17.0	16.7
30	4009	2625	1.53	15.8	15.8
20	3793	2472	1.53	14.0	14.3
15	3604	2346	1.54	12.6	13.0
10	3379	2188	1.54	11.0	11.5

Sample Name: D4

P_c (MPa)	V_p (m/s)	V_s (m/s)	V_p/V_s	G (GPa)	k (GPa)
60	4603	2965	1.55	20.2	21.8
50	4543	2912	1.56	19.5	21.5
40	4431	2819	1.57	18.3	20.8
30	4233	2678	1.58	16.5	19.2
20	3925	2460	1.60	13.9	16.9
15	3683	2288	1.61	12.0	15.1
10	3407	2057	1.66	9.7	13.7

Sample Name: D6

P_c (MPa)	V_p (m/s)	V_s (m/s)	V_p/V_s	G (GPa)	k (GPa)
60	4340	2930	1.48	19.8	17.0
50	4257	2878	1.48	19.1	16.3
40	4086	2791	1.46	18.0	14.6
30	3886	2649	1.47	16.2	13.3
20	3539	2428	1.46	13.6	10.8
15	3323	2259	1.47	11.8	9.8
10	3035	2050	1.48	9.7	8.3

Sample Name: D7

P_c (MPa)	V_p (m/s)	V_s (m/s)	V_p/V_s	G (GPa)	k (GPa)
60	4529	2971	1.52	20.6	20.4
50	4477	2938	1.52	20.1	19.9
40	4390	2882	1.52	19.4	19.1
30	4250	2792	1.52	18.2	17.9
20	4002	2632	1.52	16.2	15.8
15	3781	2485	1.52	14.4	14.2
10	3580	2355	1.52	12.9	12.7
5	3218	2126	1.51	10.5	10.1

Sample Name: D8

P_c (MPa)	V_p (m/s)	V_s (m/s)	V_p/V_s	G (GPa)	k (GPa)
60	4595	3020	1.52	20.9	20.5
50	4530	2981	1.52	20.4	19.9
40	4411	2896	1.52	19.2	19.0
30	4257	2798	1.52	17.9	17.6
20	3984	2606	1.53	15.6	15.6
15	3774	2472	1.53	14.0	14.0
10	3564	2299	1.55	12.1	13.0

Sample Name: D10

P_c (MPa)	V_p (m/s)	V_s (m/s)	V_p/V_s	G (GPa)	k GPa)
60	4192	2713	1.55	16.12	17.00
50	4132	2704	1.53	16.01	16.04
40	4016	2617	1.53	15.00	15.32
30	3835	2520	1.52	13.90	13.68
20	3574	2329	1.53	11.88	12.14

Sample Name: M1

P_c (MPa)	V_p (m/s)	V_s (m/s)	V_p/V_s	G (GPa)	k (GPa)
60	5064	3384	1.50	28.4	25.7
50	5025	3350	1.50	27.8	25.5
40	4947	3292	1.50	26.9	24.9
30	4817	3191	1.51	25.2	23.9
20	4619	3034	1.52	22.8	22.5
15	4487	2939	1.53	21.4	21.4
10	4306	2815	1.53	19.6	19.8
5	4099	2749	1.49	18.7	16.7

Sample Name: M2

P_c (MPa)	V_p (m/s)	V_s (m/s)	V_p/V_s	G (GPa)	k (GPa)
60	4941	3338	1.48	27.3	23.4
50	4896	3311	1.48	26.9	22.9
40	4824	3270	1.48	26.2	22.1
30	4711	3197	1.47	25.0	21.0
20	4549	3154	1.44	24.4	18.2
15	4441	3060	1.45	22.9	17.7
10	4260	2931	1.45	21.0	16.4
5	4110	2811	1.46	19.4	15.6

Sample Name: M7

P_c (MPa)	V_p (m/s)	V_s (m/s)	V_p/V_s	G (GPa)	k (GPa)
60	5107	3323	1.54	28.3	29.0
50	5074	3303	1.54	27.9	28.7
40	5016	3254	1.54	27.1	28.3
30	4910	3170	1.55	25.7	27.4
20	4751	3028	1.57	23.5	26.5
15	4638	2923	1.59	21.9	25.9
10	4509	2802	1.61	20.1	25.2
5	4385	2695	1.63	18.6	24.4

Sample Name: M8

P_c (MPa)	V_p (m/s)	V_s (m/s)	V_p/V_s	G (GPa)	k (GPa)
60	5073	3344	1.52	28.1	27.2
50	5025	3314	1.52	27.6	26.7
40	4962	3269	1.52	26.9	26.1
30	4836	3183	1.52	25.5	24.8
20	4629	3072	1.51	23.7	22.2
15	4490	2987	1.50	22.4	20.8
10	4308	2869	1.50	20.7	19.1
5	4090	2731	1.50	18.8	17.1

Sample Name: M10

P_c (MPa)	V_p (m/s)	V_s (m/s)	V_p/V_s	G (GPa)	k (GPa)
60	5219	3411	1.53	29.2	29.4
50	5186	3381	1.53	28.7	29.2
40	5116	3328	1.54	27.8	28.6
30	5018	3234	1.55	26.2	28.2
20	4846	3084	1.57	23.9	27.1
15	4723	2952	1.60	21.9	26.8
10	4587	2817	1.63	19.9	26.2
5	4435	2703	1.64	18.3	24.9

Sample Name: M11

P_c (MPa)	V_p (m/s)	V_s (m/s)	V_p/V_s	G (GPa)	k (GPa)
60	5295	3472	1.53	30.8	30.5
50	5261	3439	1.53	30.2	30.4
40	5214	3400	1.53	29.5	30.1
30	5139	3343	1.54	28.5	29.4
20	5020	3251	1.54	27.0	28.4
15	4948	3216	1.54	26.4	27.3
10	4860	3182	1.53	25.9	25.8
5	4760	3105	1.53	24.6	25.0

Sample Name: M13

P_c (MPa)	V_p (m/s)	V_s (m/s)	V_p/V_s	G (GPa)	k (GPa)
60	5038	3282	1.54	26.7	27.3
50	4998	3252	1.54	26.2	27.0
40	4926	3193	1.54	25.2	26.4
30	4820	3110	1.55	23.9	25.6
20	4643	2962	1.57	21.7	24.4
15	4531	2865	1.58	20.3	23.7
10	4380	2710	1.62	18.2	23.3
5	4199	2602	1.61	16.8	21.3

Sample Name: S1

P_c (MPa)	V_p (m/s)	V_s (m/s)	V_p/V_s	G (GPa)	k (GPa)
60	4490	2940	1.53	20.2	20.2
50	4445	2920	1.52	20.0	19.6
40	4355	2850	1.53	19.0	19.0
30	4210	2790	1.51	18.2	17.2
20	3970	2645	1.50	16.4	15.1
15	3800	2570	1.48	15.5	13.2
10	3600	2400	1.50	13.5	12.4
5	3350	2200	1.52	12.1	10.2

Sample Name: S2

P_c (MPa)	V_p (m/s)	V_s (m/s)	V_p/V_s	G (GPa)	k (GPa)
60	4602	3031	1.52	22.0	21.4
50	4553	3006	1.51	21.7	20.8
40	4464	2964	1.51	21.0	19.7
30	4300	2874	1.50	19.8	17.9
20	4051	2739	1.48	18.0	15.4
15	3855	2629	1.47	16.6	13.5
10	3674	2513	1.46	15.1	12.2
5	3429	2358	1.45	13.3	10.4

Sample Name: S3

P_c (MPa)	V_p (m/s)	V_s (m/s)	V_p/V_s	G (GPa)	k (GPa)
60	4276	2730	1.57	16.2	18.1
50	4230	2710	1.56	15.9	17.6
40	4118	2650	1.55	15.2	16.5
30	4050	2600	1.56	14.7	16.0
20	3810	2510	1.52	13.7	13.3
15	3654	2334	1.57	11.8	13.2

Sample Name: S4

P_c (MPa)	V_p (m/s)	V_s (m/s)	V_p/V_s	G (GPa)	k (GPa)
60	4120	2689	1.53	15.42	15.63
50	4094	2673	1.53	15.23	15.44
40	4033	2644	1.53	14.90	14.80
30	3914	2585	1.51	14.24	13.67
20	3698	2473	1.50	13.03	11.78
15	3532	2379	1.48	12.06	10.51
10	3322	2225	1.49	10.55	9.46

Sample Name: S5

P_c (MPa)	V_p (m/s)	V_s (m/s)	V_p/V_s	G (GPa)	k (GPa)
60	4282	2799	1.53	17.3	17.5
50	4244	2776	1.53	17.0	17.1
40	4175	2739	1.52	16.6	16.4
30	4059	2674	1.52	15.8	15.4
20	3851	2543	1.51	14.3	13.7
15	3698	2443	1.51	13.2	12.7
10	3491	2294	1.52	11.6	11.4
5	3188	2051	1.55	9.3	10.1

Sample Name: S6

P_c (MPa)	V_p (m/s)	V_s (m/s)	V_p/V_s	G (GPa)	k (GPa)
60	4413	2856	1.55	18.48	19.49
50	4381	2840	1.54	18.27	19.13
40	4330	2812	1.54	17.91	18.61
30	4221	2761	1.53	17.27	17.35
20	3959	2617	1.51	15.52	14.82
15	3754	2489	1.51	14.04	13.22
10	3499	2314	1.51	12.13	11.56

Sample Name: S7

P_c (MPa)	V_p (m/s)	V_s (m/s)	V_p/V_s	G (GPa)	k (GPa)
60	4016	2848	1.41	18.7	12.3
50	3995	2813	1.42	18.3	12.5
40	3942	2784	1.42	17.9	12.0
30	3827	2727	1.40	17.2	10.9
20	3576	2577	1.39	15.3	9.1
15	3404	2471	1.38	14.1	8.0
10	3191	2324	1.37	12.5	6.9
5	2834	2084	1.36	10.0	5.2

Appendix D

Acoustic velocities of water-saturated samples

Sample Name: D1

P_c (MPa)	V_p (m/s)	V_s (m/s)	V_p/V_s	G (GPa)	k (GPa)
60	4709	2922	1.61	21.3	27.0
50	4680	2879	1.63	20.7	27.1
40	4635	2825	1.64	19.9	27.1
30	4572	2765	1.65	19.1	26.8
20	4444	2633	1.69	17.3	26.3
15	4350	-	-	-	-
10	4239	-	-	-	-
5	4096	-	-	-	-
0	3774	-	-	-	-

Sample Name: D2

P_c (MPa)	V_p (m/s)	V_s (m/s)	V_p/V_s	G (GPa)	k (GPa)
60	4592	2885	1.59	20.6	24.7
50	4560	2822	1.62	19.7	25.2
40	4487	2785	1.61	19.2	24.2
30	4393	2682	1.64	17.8	24.0
20	4241	2555	1.63	16.7	22.3
15	4082	2431	1.66	15.0	21.3
10	3921	-	-	-	-
5	3775	-	-	-	-

Sample Name: D3

P_c (MPa)	V_p (m/s)	V_s (m/s)	V_p/V_s	G (GPa)	k (GPa)
60	4257	2669	1.59	17.2	20.8
50	4228	2642	1.60	16.9	20.7
40	4178	2582	1.62	16.1	20.7
30	4104	2534	1.62	15.5	20.0
20	3987	2426	1.64	14.2	19.5
15	3901	-	-	-	-

Sample Name: D4

P_c (MPa)	V_p (m/s)	V_s (m/s)	V_p/V_s	G (GPa)	k (GPa)
60	4615	2884	1.60	20.2	24.8
50	4573	2823	1.62	19.4	25.0
40	4503	2777	1.62	18.7	24.3
30	4436	2701	1.64	17.7	24.2
20	4296	2599	1.65	16.4	23.0
15	4166	2464	1.69	14.8	22.5
10	4033	2327	1.73	13.2	22.0
5	3834	2134	1.80	11.1	21.0

Sample Name: D6

P_c (MPa)	V_p (m/s)	V_s (m/s)	V_p/V_s	G (GPa)	k (GPa)
60	4413	2821	1.56	19.2	21.5
50	4372	2768	1.58	18.5	21.5
40	4289	2721	1.58	17.9	20.6
30	4180	2617	1.60	16.6	20.2
20	4047	2485	1.63	14.9	19.7
15	3932	2384	1.65	13.7	19.1
10	3786	2266	1.67	12.4	18.1
5	3610	2148	1.68	11.2	16.6

Sample Name: D7

P_c (MPa)	V_p (m/s)	V_s (m/s)	V_p/V_s	G (GPa)	k (GPa)
60	4499	2797	1.61	19.5	24.5
50	4468	2771	1.61	19.2	24.3
40	4404	2728	1.61	18.6	23.6
30	4325	2642	1.64	17.4	23.5
20	4190	2510	1.67	15.7	22.9
15	4093	2471	1.66	15.2	21.5
10	3980	-	-	-	-
5	3831	-	-	-	-

Sample Name: D8

P_c (MPa)	V_p (m/s)	V_s (m/s)	V_p/V_s	G (GPa)	k (GPa)
60	4635	-	-	-	-
50	4586	--	--	--	--
40	4532	-	-	-	-
30	4435	-	-	-	-
20	4281	-	-	-	-
15	-	-	-	-	-
10	-	-	-	-	-

Sample Name: D10

P_c (MPa)	V_p (m/s)	V_s (m/s)	V_p/V_s	G (GPa)	k GPa)
60	4202	2635	1.59	16.2	19.6
50	4155	2616	1.59	16.0	19.0
40	4060	2517	1.61	14.8	18.8
30	3976	2500	1.59	14.6	17.5
20	3899	2355	1.66	13.0	18.3
10	3829	2250	1.70	11.8	18.5

Sample Name: M1

P_c (MPa)	V_p (m/s)	V_s (m/s)	V_p/V_s	G (GPa)	k (GPa)
60	5084	3280	1.55	27.2	29.0
50	5044	3245	1.55	26.6	28.8
40	4989	3181	1.57	25.5	28.8
30	4928	3115	1.58	24.5	28.6
20	4843	2985	1.62	22.5	29.2
15	4792	2949	1.63	21.9	28.7
10	4756	-	-	--	-

Sample Name: M2

P_c (MPa)	V_p (m/s)	V_s (m/s)	V_p/V_s	G (GPa)	k (GPa)
60	4971	3246	1.53	26.5	26.8
50	4945	3224	1.53	26.1	26.6
40	4903	3186	1.54	25.5	26.4
30	4842	3137	1.54	24.7	26.0
20	4751	3059	1.55	23.5	25.4
15	4697	3004	1.56	22.7	25.2
10	4638	2951	1.57	21.9	24.9
5	4526	2831	1.60	20.2	24.7

Sample Name: M7

P_c (MPa)	V_p (m/s)	V_s (m/s)	V_p/V_s	G (GPa)	k (GPa)
60	5092	3153	1.61	25.7	32.7
50	5061	3092	1.64	24.7	33.2
40	4989	3055	1.63	24.1	32.1
30	4929	2978	1.66	22.9	32.2
20	4815	2908	1.66	21.8	30.8
15	4646	2779	1.67	19.9	29.1
10	4357	-	-	-	-

Sample Name: M8

P_c (MPa)	V_p (m/s)	V_s (m/s)	V_p/V_s	G (GPa)	k (GPa)
60	5132	3209	1.60	26.3	32.2
50	5109	3192	1.60	26.0	32.0
40	5067	3140	1.61	25.2	32.0
30	5001	3071	1.63	24.1	31.8
20	4882	2947	1.66	22.2	31.3
15	4789	2856	1.68	20.8	30.8
10	4660	2716	1.72	18.9	30.4
5	4501	2550	1.77	16.6	29.6

Sample Name: M10

P_c (MPa)	V_p (m/s)	V_s (m/s)	V_p/V_s	G (GPa)	k (GPa)
60	5165	3236	1.60	26.7	32.4
50	5142	3224	1.60	26.5	32.1
40	5104	3160	1.62	25.5	32.5
30	5031	3088	1.63	24.3	32.1
20	4895	2920	1.68	21.7	32.1
15	4813	-	-	-	-
10	4722	-	-	-	-
5	4571	-	-	-	-

Sample Name: M11

P_c (MPa)	V_p (m/s)	V_s (m/s)	V_p/V_s	G (GPa)	k (GPa)
60	5234	3297	1.59	28.1	33.4
50	5209	3272	1.59	27.7	33.3
40	5163	3225	1.60	26.9	33.1
30	5102	3147	1.62	25.6	33.2
20	4997	3023	1.65	23.7	33.1
15	4938	2935	1.68	22.3	33.4
10	4875	-	-	-	-
5	4852	-	-	-	-

Sample Name: M13

P_c (MPa)	V_p (m/s)	V_s (m/s)	V_p/V_s	G (GPa)	k (GPa)
55	4981	3097	1.61	24.2	30.4
45	4938	3055	1.62	23.6	30.2
35	4853	2996	1.62	22.7	29.3
25	4712	2948	1.60	22.0	26.8
20	4633	-	-	-	-
15	4594	-	-	-	-
10	4519	-	-	-	-
5	4452	-	-	-	-
0	4405	-	-	-	-

Sample Name: S1

P_c (MPa)	V_p (m/s)	V_s (m/s)	V_p/V_s	G (GPa)	k (GPa)
60.0	4451	2753	1.62	18.53	23.74
50.0	4407	2713	1.62	18.01	23.50
40.0	4341	2667	1.63	17.39	22.90
30.0	4236	2570	1.65	16.15	22.36
20.0	4083	2451	1.67	14.70	21.17
15.5	4013	2381	1.69	13.87	20.90
10.8	3910	-	-	-	-
4.8	3799	-	-	-	-

Sample Name: S2

P_c (MPa)	V_p (m/s)	V_s (m/s)	V_p/V_s	G (GPa)	k (GPa)
60	4557	2855	1.60	20.0	24.3
50	4528	2833	1.60	19.7	24.1
40	4466	2785	1.60	19.1	23.6
30	4369	2722	1.60	18.2	22.6
20	4230	2624	1.61	16.9	21.4
15	4141	2563	1.62	16.1	20.6
10	4037	2473	1.63	15.0	20.0
5	3892	-	-	-	-

Sample Name: S3

P_c (MPa)	V_p (m/s)	V_s (m/s)	V_p/V_s	G (GPa)	k (GPa)
60	4235	2582	1.64	15.5	21.0
50	4183	2546	1.64	15.1	20.6
40	4154	2514	1.65	14.7	20.5
30	4087	2469	1.66	14.2	20.0
20	3965	2371	1.67	13.1	19.2
15	3878	2313	1.68	12.5	18.4
10	3757	2145	1.75	10.7	18.6

Sample Name: S5

P_c (MPa)	V_p (m/s)	V_s (m/s)	V_p/V_s	G (GPa)	k (GPa)
60	4225	2618	1.61	16.1	20.5
50	4189	2592	1.62	15.8	20.2
40	4138	2547	1.62	15.3	19.9
30	4060	2502	1.62	14.7	19.1
20	3944	2387	1.65	13.4	18.7
15	3856	2322	1.66	12.7	18.1
10	3753	2201	1.71	11.4	17.9
5	3593	-	-	-	-

Sample Name: S6

P_c (MPa)	V_p (m/s)	V_s (m/s)	V_p/V_s	G (GPa)	k (GPa)
60	4303	2654	1.62	16.6	21.6
50	4271	2636	1.62	16.4	21.2
40	4218	2606	1.62	16.0	20.6
30	4141	2533	1.63	15.2	20.3
20	4016	2435	1.65	14.0	19.4
15	3908	2334	1.67	12.9	18.9
10	3711	-		-	-

Sample Name: S7

P_c (MPa)	V_p (m/s)	V_s (m/s)	V_p/V_s	G (GPa)	k (GPa)
60	3933	2687	1.46	17.5	14.1
50	3897	2665	1.46	17.2	13.8
40	3832	2604	1.47	16.4	13.7
30	3743	2552	1.47	15.8	12.9
20	3570	2431	1.47	14.3	11.8
15	-	2371	-	13.6	-

Appendix E

Acoustic velocities of partially water-saturated samples

Sample Name: D4

P_e (MPa)	V_p (m/s)	V_s (m/s)	V_p/V_s	G (GPa)	k (GPa)	Sw (%)
60	4569	2943	1.55	20.0	21.6	19
50	4527	2903	1.56	19.5	21.4	19
40	4467	2876	1.55	19.1	20.7	19
30	4375	2759	1.59	17.6	20.8	19
15	4151	2601	1.60	15.7	19.0	19
60	4553	2903	1.57	19.6	22.1	31
50	4512	2885	1.56	19.4	21.6	31
40	4456	2865	1.56	19.1	20.8	31
30	4375	2763	1.58	17.8	20.9	31
20	4239	-	-	-	-	31
15	4119	2581	1.60	15.5	18.8	31
60	4563	-	-	-	-	40
50	4525	2899	1.56	19.7	21.7	40
40	4467	2863	1.56	19.2	21.1	40
30	4383	2762	1.59	17.8	21.2	40
20	4257	-	-	-	-	40
15	4159	-	-	-	-	40
60	4577	2897	1.58	19.7	22.9	47
50	4539	2880	1.58	19.5	22.4	47
40	4483	2857	1.57	19.2	21.7	47
30	4405	2761	1.60	17.9	21.7	47
20	4265	-	-	-	-	47
15	4181	-	-	-	-	47
60	4595	2896	1.59	19.8	23.4	55
50	4557	2886	1.58	19.6	22.8	55
40	4503	2822	1.60	18.8	22.8	55
30	4414	2758	1.60	17.9	22.0	55
20	4274	2602	1.64	16.0	21.8	55
15	4181	-	-	-	-	55
60	4624	2890	1.60	19.8	24.3	67
50	4587	2865	1.60	19.5	24.0	67
40	4534	2801	1.62	18.6	24.0	67
30	4459	2744	1.63	17.9	23.4	67
20	4310	2589	1.66	15.9	22.9	67
15	4201	-	-	-	-	67
60	4628	2865	1.62	19.7	25.1	88
50	4589	2806	1.64	18.9	25.3	88
40	4538	2743	1.65	18.1	25.4	88
30	4456	2669	1.67	17.1	24.9	88
20	4309	-	-	-	-	88
15	4195	-	-	-	-	88
10	4068	-	-	-	-	88

Sample Name: D6

P_e (MPa)	V_p (m/s)	V_s (m/s)	V_p/V_s	G (GPa)	k (GPa)	Sw (%)
60	4345	2863	1.52	19.0	18.4	8
50	4272	2827	1.51	18.5	17.6	8
40	4157	2751	1.51	17.5	16.6	8
30	4023	2677	1.50	16.6	15.3	8
60	4360	2867	1.52	19.1	18.7	15
50	4297	2838	1.51	18.7	17.9	15
40	4207	2761	1.52	17.7	17.5	15
30	4074	2697	1.51	16.9	16.0	15
20	3910	2590	1.51	15.1	15.3	15
60	4364	2865	1.52	19.2	19.0	29
50	4295	2837	1.51	18.8	18.1	29
40	4209	2757	1.53	17.8	17.7	29
30	4077	2693	1.51	17.0	16.3	29
20	-	2536	-	15.0	-	29
60	4351	2864	1.52	19.3	18.8	38
50	4294	2845	1.51	19.0	18.0	38
40	4214	2760	1.53	17.9	17.8	38
30	4088	2704	1.51	17.2	16.4	38
20	-	2549	-	15.3	-	38
60	4407	2851	1.55	19.3	20.4	56
50	4346	2825	1.54	18.9	19.6	56
40	4259	2745	1.55	17.9	19.2	56
30	4146	2696	1.54	17.2	17.8	56
60	4425	2858	1.55	19.4	20.7	65
50	4365	2829	1.54	19.1	19.9	65
40	4267	2745	1.55	17.9	19.4	65
30	4156	2687	1.55	17.2	18.2	65
60	4439	2817	1.58	19.0	21.9	78
50	4379	2778	1.58	18.5	21.3	78
40	4296	2695	1.59	17.4	21.0	78
30	4192	2639	1.59	16.7	19.9	78
20	4026	2525	1.59	15.3	17.6	78
60	4460	2850	1.56	19.5	21.8	86
50	4403	2781	1.58	18.6	21.8	86
40	4330	2751	1.57	18.2	20.8	86
30	4230	2647	1.60	16.9	20.6	86

Sample Name: M2

P_e (MPa)	V_p (m/s)	V_s (m/s)	V_p/V_s	G (GPa)	k (GPa)	Sw (%)
60	4923	3195	1.54	25.2	26.3	37
50	4883	3180	1.54	25	25.6	37
40	4830	3148	1.53	24.5	25.0	37
30	4752	3074	1.55	23.4	24.7	37
20	4662	3045	1.53	22.9	23.2	37
15	4593	-	-	-	-	37
10	4507	-	-	-	-	37
60	4920	3214	1.53	25.6	25.9	50
50	4887	3158	1.55	24.7	26.3	50
40	4835	3110	1.55	24.0	26.0	50
30	4775	3098	1.54	23.8	24.8	50
20	4686	2947	1.59	21.5	25.7	50
15	4627	-	-	-	-	50
10	4557	-	-	-	-	50
60	4933	3207	1.54	25.6	26.4	62
50	4900	3186	1.54	25.3	26.1	62
40	4851	3154	1.54	24.8	25.6	62
30	4794	3091	1.55	23.8	25.5	62
20	4702	3019	1.56	22.7	24.8	62
15	4648	2925	1.59	21.3	25.4	62
10	4576	-	-	-	-	62
60	4949	3207	1.54	25.7	27	77
50	4923	3183	1.55	25.3	26.8	77
40	4877	3152	1.55	24.8	26.3	77
30	4816	3075	1.57	23.6	26.5	77
20	4741	3003	1.58	22.5	26.1	77
15	4691	2900	1.62	21.0	27.0	77
10	4627	2842	1.63	20.2	26.6	77
5	4546	2668	1.70	17.8	27.9	77
60	4980	3222	1.55	26.0	27.5	90
50	4950	3203	1.55	25.7	27.1	90
40	4907	3177	1.54	25.3	26.6	90
30	4846	3097	1.56	24.0	26.8	90
20	4774	3049	1.57	23.3	26	90
15	4718	2958	1.59	21.9	26.5	90
10	4665	-	-	-	-	90

Sample Name: M8

P_e (MPa)	V_p (m/s)	V_s (m/s)	V_p/V_s	G (GPa)	k (GPa)	Sw (%)
60	5165	3275	1.58	27.4	31.6	79
50	5137	3247	1.58	26.9	31.5	79
40	5100	3209	1.59	26.3	31.3	79
30	5033	3146	1.60	25.2	30.9	79
20	4927	3045	1.62	23.6	30.4	79
15	4830	2962	1.63	22.4	29.7	79
10	4681	2847	1.64	20.7	28.3	79
5	4418	2662	1.66	18.1	25.7	79
60	5154	3239	1.59	26.8	32.1	86
50	5126	3215	1.59	26.4	31.9	86
40	5091	3179	1.60	25.8	31.8	86
30	5029	3099	1.62	24.5	31.9	86
20	4930	2998	1.64	22.9	31.5	86
15	4834	2861	1.69	20.9	31.8	86
10	4709	-	-	-	-	86
5	4456	-	-	-	-	86

Sample Name: S1

P_e (MPa)	V_p (m/s)	V_s (m/s)	V_p/V_s	G (GPa)	k (GPa)	Sw (%)
60	4340	2770	1.57	18.2	20.4	34
50	4287	2742	1.56	17.8	19.8	34
40	4214	2690	1.57	17.2	19.2	34
30	4094	2613	1.57	16.2	18.2	34
20	3923	2498	1.57	14.8	16.8	34
15	3799	2388	1.59	13.5	16.2	34
60	4347	2760	1.58	18.2	20.8	47
50	4295	2725	1.58	17.7	20.4	47
40	4220	2676	1.58	17.1	19.7	47
30	4095	2591	1.58	16	18.6	47
20	3931	2484	1.58	14.7	17.2	47
15	3815	2380	1.60	13.5	16.7	47
60	4373	2759	1.59	18.3	21.6	64
50	4327	2717	1.59	17.7	21.3	64
40	4255	2674	1.59	17.2	20.6	64
30	4155	2602	1.60	16.3	19.8	64
20	4011	2496	1.61	15	18.7	64
15	3883	2370	1.64	13.5	18.2	64
60	4418	2761	1.60	18.4	22.6	78
50	4377	2713	1.61	17.8	22.6	78
40	4313	2671	1.61	17.2	22	78
30	4213	2599	1.62	16.3	21.1	78
20	4061	-	-	-	-	78
15	3955	-	-	-	-	78
10	3826	-	-	-	-	78

Sample Name: S3

P_e (MPa)	V_p (m/s)	V_s (m/s)	V_p/V_s	G (GPa)	k (GPa)	Sw (%)
60	4200	2638	1.59	15.1	18.2	8
50	4158	2623	1.59	15.0	17.7	8
40	4094	2600	1.57	14.7	16.9	8
30	3998	2520	1.59	13.8	16.4	8
60	4196	2648	1.58	15.4	18.1	17
50	4143	2631	1.57	15.2	17.4	17
40	4085	2607	1.57	14.9	16.7	17
30	4001	2527	1.58	14.0	16.4	17
60	4210	2654	1.59	15.5	18.3	22
50	4156	2636	1.58	15.3	17.6	22
40	4089	2601	1.57	14.9	16.9	22
30	3989	2521	1.58	14.0	16.3	22
20	3857	-	-	-	-	22
60	4174	2647	1.58	15.5	17.9	30
50	4153	2635	1.58	15.3	17.7	30
40	4081	2593	1.57	14.9	17.0	30
30	4015	2520	1.59	14.0	16.9	30
60	4187	2644	1.58	15.5	18.2	38
50	4145	2633	1.57	15.4	17.6	38
40	4086	2606	1.57	15.1	17.0	38
30	4012	2509	1.60	14.0	17.1	38
60	4196	2618	1.60	15.4	19.0	51
50	4157	2598	1.60	15.1	18.6	51
40	4105	2544	1.61	14.5	18.4	51
30	4050	2493	1.62	13.9	18.2	51
60	4237	2602	1.63	15.3	20.2	61
50	4174	2578	1.62	15.0	19.3	61
40	4118	2527	1.63	14.4	19.1	61
30	4037	2488	1.62	14.0	18.2	61
60	4250	2633	1.61	15.8	20.1	71
50	4212	2554	1.65	14.8	20.6	71
40	4158	2541	1.64	14.7	19.7	71
30	4101	2424	1.69	13.4	20.4	71
60	4264	2581	1.65	15.3	21.4	88
50	4245	2567	1.65	15.2	21.2	88
40	4186	2510	1.67	14.5	21.0	88
30	4100	2459	1.67	13.9	20.1	88

Appendix F

Publications

1. Refereed Papers

Khaksar, A. and Griffiths, C.M., 1996a: Influence of effective stress on acoustic velocity and log derived porosity. SPE 36981. Proceedings of the Asia Pacific Oil and Gas Conference, Society of Petroleum Engineers, Adelaide, Australia (in press in the SPE Reservoir evaluation and Engineering).

Khaksar, A. and Griffiths, C.M., 1998a: Porosity from sonic log in gas-bearing shaly sandstone; field data versus empirical equations. Exploration Geophysics **29**, 440-446.

Khaksar, A, and Griffiths, C.M. 1998b: Acoustic velocities as a function of effective pressure in low to medium porosity shaly sandstones, part 1- experimental results. Exploration Geophysics **29**, 447-455.

Khaksar, A. and Griffiths, C.M., 1998c: Acoustic velocities as a function of effective pressure in low to medium porosity shaly sandstones, part 2- implications for hydrocarbon exploration. Exploration Geophysics **29**, 456-461.

2. Conference and Seminar Presentations

Khaksar, A., 1998a: Petro-Acoustic of Cooper Basin Sandstones. Geological Society of Australia, Abstracts **52**. 25. The Winner of the Australian Petroleum Cooperative Research Centre Award for the best petroleum related presentation at the 12th Victorian Universities Geoscience Conference, Melbourne, Australia.

Khaksar, A., 1998b: Acoustic properties of Cooper Basin sandstones. Oral presentation for the CSIRO-Petroleum. Melbourne, Australia.

Khaksar, A., 1998c: Acoustic responses in tight gas sandstone, A Cooper Basin Example. Oral presentation for the Boral Energy. Adelaide, Australia.

Khaksar, A. Griffiths, C.M and. McCann, C., 1998, A petro-acoustic study of Cooper Basin sandstones. 38th APPEA Conference poster session Canberra, Australia. Published in the APPEA Journal **38**, 874.

Khaksar, A., McCann, C., Griffiths, C., Sothcott, J. and Khazanehdari, J., 1997a: Stress sensitivity of P-and S-wave velocities in a set of low to medium porosity dry

sandstones. 59th EAGE Conference Extended Abstracts, paper F31, Geneva, Switzerland.

Khaksar, A., McCann, C., Griffiths, C., Sothcott, J. and Khazanehdari, J., 1997b: Ultrasonic compressional and shear velocities as a function of effective pressure in dry and water saturated sandstones. Oral presentation, 21st UK Geophysical Assembly, Southampton, England.

Khaksar, A. and C.M. Griffiths, 1996b: Velocity-porosity transforms and effective stress in gas bearing reservoirs, a case study. 58th EAGE Conference Expanded Abstracts, Paper E10, Amsterdam, The Netherlands.

Khaksar, A., and Griffiths, C.M, (1998) Porosity form sonic log in gas-bearing shaly sandstones: field data versus empirical equations.
Exploration Geophysics, v. 29 (4), pp. 440-446

Khaksar, A., and Griffiths, C. (1998) Acoustic velocities as a function of effective pressure in low to moderate porosity shaly sandstones, Part 1 - experimental results. *Exploration Geophysics, v. 29 (4), pp. 447-455*

Khaksar, A., and Griffiths, C. (1998) Acoustic velocities as a function of effective pressure in low to moderate porosity shaly sandstones, Part 2- Implications for hydrocarbon exploration.
Exploration Geophysics, v. 29 (4), pp. 456-461

Khaksar, A., and Griffiths, C. M. (1999) Influence of Effective Stress on the Acoustic Velocity and Log-Derived Porosity.
SPE Reservoir Evaluation & Engineering, v. 2 (1), pp. 69-74